

MATERIALS PHYSICS AND MECHANICS

Vol. 52, No. 4, 2024

125

MATERIALS PHYSICS AND MECHANICS

Principal Editors:

Alexander Belyaev

Andrei Rudskoi

Institute for Problems in Mechanical Engineering of the Russian Academy of Science (RAS), Russia

Peter the Great St. Petersburg Polytechnic University, Russia

Founder and Honorary Editor: Ilya Ovid'ko (1961-2017)

Institute for Problems in Mechanical Engineering of the Russian Academy of Sciences (RAS), Russia

Associate Editor:

Anna Kolesnikova

Artem Semenov

Institute for Problems in Mechanical Engineering of the Russian Academy of Sciences (RAS), Russia

Peter the Great St. Petersburg Polytechnic University, Russia

Editorial Board:

E.C. Aifantis

Aristotle University of Thessaloniki, Greece

K.E. Aifantis

University of Florida, USA

U. Balachandran

Argonne National Laboratory, USA

A. Bellosi

Research Institute for Ceramics Technology, Italy

S.V. Bobylev

Institute for Problems in Mechanical Engineering (RAS), Russia

A.I. Borovkov

Peter the Great St.Petersburg Polytechnic University, Russia

G.-M. Chow

National University of Singapore, Singapore

Yu. Estrin

Monash University, Australia

A.B. Freidin

Institute for Problems in Mechanical Engineering (RAS), Russia

Y. Gogotsi

Drexel University, USA

I.G. Goryacheva

Institute of Problems of Mechanics (RAS), Russia

D. Hui

University of New Orleans, USA

G. Kiriakidis

IESL/FORTH, Greece

D.M. Klimov

Institute of Problems of Mechanics (RAS), Russia

G.E. Kodzhaspirov

Peter the Great St. Petersburg Polytechnic University, Russia

S.A. Kukushkin

Institute for Problems in Mechanical Engineering (RAS), Russia

T.G. Langdon

University of Southampton, U.K.

V.P. Matveenko

Institute of Continuous Media Mechanics (RAS), Russia

A.I. Melker

Peter the Great St. Petersburg Polytechnic University, Russia

Yu.l. Meshcheryakov

Institute for Problems in Mechanical Engineering (RAS), Russia

N.F. Morozov

St. Petersburg State University, Russia

R.R. Mulyukov

Institute for Metals Superplasticity Problems (RAS), Russia

Yu.V. Petrov

St. Petersburg State University, Russia

N.M. Pugno

Politecnico di Torino, Italy

B.B. Rath

Naval Research Laboratory, USA

A.E. Romanov

Ioffe Institute (RAS), Russia

A.M. Sastry

University of Michigan, Ann Arbor, USA

B.A. Schrefler

University of Padua, Italy

N.V. Skiba

Institute for Problems in Mechanical Engineering (RAS), Russia

A.G. Sheinerman

Institute for Problems in Mechanical Engineering (RAS), Russia

R.Z. Valiev

Ufa State Aviation Technical University, Russia

K. Zhou

Nanyang Technological University, Singapore

"Materials Physics and Mechanics" Editorial Office:

Phone: +7(812)552 77 78, ext. 224 E-mail: mpmjournal@spbstu.ru Web-site: http://www.mpm.spbstu.ru

International scientific journal "Materials Physics and Mechanics" is published by Peter the Great St. Petersburg Polytechnic University in collaboration with Institute for Problems for Mechanical Engineering in the Russian Academy of Sciences in both hard copy and electronic versions. The journal provides an international medium for the publication of reviews and original research papers written in English and focused on the following topics:

- Mechanics of composite and nanostructured materials.
- Physics of strength and plasticity of composite and nanostructured materials.
- Mechanics of deformation and fracture processes in conventional materials (solids).
- Physics of strength and plasticity of conventional materials (solids).
- Physics and mechanics of defects in composite, nanostructured, and conventional materials.
- Mechanics and physics of materials in coupled fields.

Owner organizations: Peter the Great St. Petersburg Polytechnic University; Institute of Problems of Mechanical Engineering RAS.

Materials Physics and Mechanics is indexed in Chemical Abstracts, Cambridge Scientific Abstracts,
Web of Science Emerging Sources Citation Index (ESCI) and Elsevier Bibliographic Databases (in particular, SCOPUS).

© 2024, Peter the Great St. Petersburg Polytechnic University © 2024, Institute for Problems in Mechanical Engineering RAS



МЕХАНИКА И ФИЗИКА МАТЕРИАЛОВ

Materials Physics and Mechanics

Том 52, номер 4, 2024 год

Учредители:

Редакционная коллегия журнала Главные редакторы:

д.ф.-м.н., чл.-корр. РАН А.К. Беляев Институт проблем машиноведения Российской академии наук (РАН)

д.т.н., академик РАН А.И. Рудской Санкт-Петербургский политехнический университет Петра Великого

Основатель и почетный редактор: д.ф.-м.н. И.А. Овидько (1961-2017)

Институт проблем машиноведения Российской академии наук (РАН)

Ответственные редакторы

д.ф.-м.н. А.Л. Колесникова

Институт проблем машиноведения Российской академии наук (РАН)

д.ф.-м.н. А.С. Семенов Санкт-Петербургский политехнический университет Петра Великого

Международная редакционная коллегия:

д.ф.-м.н. С.В. Бобылев

Институт проблем машиноведения РАН, Россия

к.т.н., проф. А.И. Боровков

Санкт-Петербургский политехнический ун-т Петра Великого, Россия

д.ф.-м.н., проф. Р.З. Валиев

Уфимский государственный технический университет, Россия

д.ф.-м.н., академик РАН И.Г. Горячева

Институт проблем механики РАН, Россия

д.ф.-м.н., академик РАН Д.М. Климов

Институт проблем механики РАН, Россия

д.т.н., проф. Г.Е. Коджаспиров

Санкт-Петербургский политехнический ун-т Петра Великого, Россия

д.ф.-м.н., проф. С.А. Кукушкин

Институт проблем машиноведения РАН, Россия

д.ф.-м.н., академик РАН В.П. Матвеенко

Институт механики сплошных сред РАН, Россия

д.ф.-м.н., проф. А.И. Мелькер

Санкт-Петербургский политехнический ун-т Петра Великого, Россия

д.ф.-м.н., проф. Ю.И. Мещеряков

Институт проблем машиноведения РАН, Россия

д.ф.-м.н., академик РАН Н.Ф. Морозов

Санкт-Петербургский государственный университет, Россия

д.ф.-м.н., чл.-корр. РАН Р.Р. Мулюков

Институт проблем сверхпластичности металлов РАН, Россия

д.ф.-м.н., чл.-корр. РАН Ю.В. Петров Санкт-Петербургский государственный университет, Россия

д.ф.-м.н., проф. А.Е. Романов

Физико-технический институт им. А.Ф. Иоффе РАН, Россия д.ф.-м.н. **Н.В. Скиба**

Институт проблем машиноведения РАН, Россия

д.ф.-м.н., проф. А.Б. Фрейдин

Институт проблем машиноведения РАН, Россия

д.ф.-м.н. А.Г. Шейнерман

Институт проблем машиноведения РАН, Россия

Prof., Dr. E.C. Aifantis

Aristotle University of Thessaloniki, Greece

Dr. K.E. Aifantis

University of Florida, USA

Dr. U. Balachandran

Argonne National Laboratory, USA

Dr. A. Bellosi

Research Institute for Ceramics Technology, Italy

Prof., Dr. G.-M. Chow

National University of Singapore, Singapore

Prof., Dr. Yu. Estrin Monash University, Australia

Prof., Dr. Y. Gogotsi

Drexel University, USA

Prof., Dr. **D. Hui**

University of New Orleans, USA

Prof., Dr. G. Kiriakidis

IESL/FORTH. Greece

Prof., Dr. T.G. Langdon

University of Southampton, UK

Prof., Dr. N.M. Pugno

Politecnico di Torino, Italy

Dr. B.B. Rath

Naval Research Laboratory, USA

Prof., Dr. A.M. Sastry

University of Michigan, Ann Arbor, USA

Prof., Dr. B.A. Schrefler

University of Padua, Italy

Prof., Dr. K. Zhou Nanyang Technological University, Singapore

Тел.: +7(812)552 77 78, доб. 224 E-mail: mpmjournal@spbstu.ru Web-site: http://www.mpm.spbstu.ru

Тематика журнала

Международный научный журнал "Materials Physics and Mechanics" издается Санкт-Петербургским политехническим университетом Петра Великого в сотрудничестве с Институтом проблем машиноведения Российской академии наук в печатном виде и электронной форме. Журнал публикует обзорные и оригинальные научные статьи на английском языке по следующим тематикам:

- Механика композиционных и наноструктурированных материалов.
- Физика прочности и пластичности композиционных и наноструктурированных материалов.
- Механика процессов деформации и разрушения в традиционных материалах (твердых телах).
- Физика прочности и пластичности традиционных материалов (твердых тел).
- Физика и механика дефектов в композиционных, наноструктурированных и традиционных материалах.
- Механика и физика материалов в связанных полях.

Редколлегия принимает статьи, которые нигде ранее не опубликованы и не направлены для опубликования в другие научные издания. Все представляемые в редакцию журнала "Механика и физика материалов" статьи рецензируются. Статьи могут отправляться авторам на доработку. Не принятые к опубликованию статьи авторам не возвращаются.

Журнал "Механика и физика материалов" ("Materials Physics and Mechanics") включен в систему цитирования Web of Science Emerging Sources Citation Index (ESCI), SCOPUS и РИНЦ.

Contents

Accelerated degradation by mechanical load of HIT solar cells encapsulated in flexible plastic A.V. Bobyl, R.V. Davydov, O.I. Konkov, A.V. Kochergin, D.A. Malevsky, S.E. Nikitin	1-8
MEMS gas sensor of resistive type for detection of hydrogen sulfide down to low concentrations I.M. Komarevtsev, A.S. Kondrateva, A.N. Kazakin, Ya.B. Enns, I.A. Lazdin, P.A. Karaseov, U.D. Akulshin	9-22
First-principles investigations of physical properties of Nd doped FeSi compour A. Kumar, R. Kumar, A. Kumar, V.K. Nautiyal, N. Iram	ıd 23–32
The influence of low frequency electric field on the coalescence of water drops in emulsion shear flow R.R. Galeev, A.I. Mullayanov, A.A. Musin, L.A. Kovaleva	33-40
Surface modification by laser cladding: state-of-the-art and future prospects R. Ranjan, A.K. Das	41-51
Ultrasonic layer-by-layer treatment of PN85Y15 coating as a way to increase wear resistance of friction pair with bronze I.S. Syundyukov, M.A. Skotnikova, A.Yu. Ryabikin	52-62
Thermal analysis of wear of polymer-polymer friction pairs in vacuum and atmosphere conditions A.O. Pozdnyakov, E.B. Sedakova	63-80
Structure and strength of Mg-Zn-Zr alloy subjected to high pressure torsion D.A. Aksenov, M.A. Shishkunova, R.N. Asfandiyarov, Y.R. Sementeeva	81-90
The effect of martensite stabilization in titanium nickelide after various methods of pre-deformation: simulation with a single set of constants A.E. Volkov, F.S. Belyaev, N.A. Volkova, E.A. Vukolov, M.E. Evard, T.V. Rebrov	91-99
Interface shear damage of novel biocomposite materials based on polyhydroxyalkanoates biopolymer matrix A. Mokaddem, M. Belkheir, M. Rouissat, B. Doumi, A. Boutaous	100-113
Hybrid of a nonlinear Maxwell-type viscoelastoplastic model with the linear viscoelasticity constitutive constitutive equation and properties of crossbred creep and stress-strain curves A.V. Khokhlov	114-140

Synthesis of WO _{2.72} :Fe thin films via ammonium tungstate precursor by spray pyrolysis technique and annealing E. Ouadah, N. Hamdadou	141-151
Fiberglass thermal barrier for building safety S.V. Fedosov, A.A. Lazarev, A.N. Maltsev, M.V. Toropova, I.A. Bogdanov	152-162
Quasi-static thermal response of a circular plate due to the influence of memory-dependent derivatives N.K. Lamba	163-172
Comprehensive studies of pipes metal to identify the causes of failure in the gas pipeline of the gas lift system of an oil and gas condensate field A.M. Kunakova, V.A. Svintsov, V.A. Olenev, D.A. Gogolev, L.R. Sayfutdinova, M.S. Solodovnikova	173-182

Submitted: July 2, 2024 Revised: July 19, 2024 Accepted: August 21, 2024

Accelerated degradation by mechanical load of HIT solar cells encapsulated in flexible plastic

A.V. Bobyl ¹, R.V. Davydov ², O.I. Konkov ¹, A.V. Kochergin ³,

D.A. Malevsky ¹, S.E. Nikitin ¹

ABSTRACT

The degradation of plastic-encapsulated silicon HIT solar cells ($156 \times 156 \text{ mm}^2$) with Ag and Cu metallization was studied under mechanical load with a soft rod with a radius of 25 mm (Ball-on-Ring) up to a maximum 400 kPa. Local 2D photo- and electroluminescence, as well as measurements of dark and light current-voltage characteristics were used. Three phases were detected: (1) an increase in power by 2-4% due to a decrease in leakage currents with pressures up to 125 kPa, (2) accumulation of deformations completed by the avalanche-like formation of a volumetric defect in the substrate with a radius of up to 10 μ m with a drop in power by 3-5%, (3) formation of a system of cracks with a width of < 1 μ m, with an increase in their total length during under maximum mechanical load to 4000 ÷ 4100 mm and a decrease in of solar cell power to 12 ÷ 16 %.

KEYWORDS

accelerated degradation • mechanical load • avalanche-like • crack • photoluminescence • electroluminescence **Citation:** Bobyl AV, Davydov RV, Konkov OI, Kochergin AV, Malevsky DA, Nikitin SE. Accelerated degradation by mechanical load of HIT solar cells encapsulated in flexible plastic. *Materials Physics and Mechanics*. 2024;52(4): 1–8. http://dx.doi.org/10.18149/MPM.5242024_1

Introduction

An important area of long-term forecasting of silicon solar cell (SC) technology development is to increase their service life. In the next 10 years, according to M. Fischer, Annual report ITRPV for PV 2023, 40-year module technical lifetimes are expected. When studying the SC degradation, we will consider the following circumstances:

- 1. The importance of accelerated testing of materials and various devices is noted [1]. In particular, 7-day bench tests can accelerate the rate of degradation by 30 times compared to their climatic tests [1]. There is a so-called scientific direction Service Life Prediction (SLP) [2], aimed at developing new test methods for testing with an applied engineering (commercial) task to guarantee the quality of products (goods), in particular, solar modules [3].
- 2. According to [4], as SLP parameters become more stringent, studies can be divided into two groups: training and testing samples, which are prototypes of standard industrial standards (GOST) [5] and more detailed specialized test methods [6], respectively.
- 3. Among more than 50 existing SC degradation mechanisms [7], 14 % of failures occur under mechanical load and about 35 % with thermal cyclic deformations, i.e. in total, this

¹ loffe Institute, St. Petersburg, Russia

² Peter the Great St. Petersburg Polytechnic University, St. Petersburg, Russia

³ STC Thin Film Technologies in Power Engineering, St. Petersburg, Russia

[™] davydovroman@outlook.com

is almost half of the SC failures due to the mechanical damage of substrate and contact system.

- 4. Cracking processes are usually studied using a Ring-on-Ring bending test [8], 3 or 4 point bending tests [9].
- 5. Flexible silicon SC were chosen for following reasons:
- 5.1. They are the most widespread in the long term [7].
- 5.2. The market for flexible SC is expected to increase to 25 % of all SC [10].
- 5.3. For more effective research, it is necessary to conduct them at large deflections, as well as in the presence of SC mechanically strong protection.

Thus, standard and accelerated strength studies of SC degradation are an important stage in substantiating the reliability of their long-term forecasts. The methods must reproduce the actual operation of the solar energy system.

Materials and Methods

To obtain silicon HIT-type SC, (100) wafers ($156 \times 156 \text{ mm}^2$) of Cz-silicon produced by LONGi were used with an oxygen concentration of $8 \cdot 10^{17}$ cm⁻³, carbon ~ $5 \cdot 10^{16}$ cm⁻³, and a dislocation density of 500 cm⁻². The SC technology included: cleaning, pyramidal texturing, PECVD deposition of amorphous silicon, conductive electrodes (indium tin oxide) and the formation of Ag or Cu fingers by screen printing or electrochemical deposition, respectively [11,12]. Double-sided lamination was used with CVF film based on polyolefins (DNS company), thickness ~ 600 µm and the formation of layers of polyethylene terephthalate (PET), thickness ~ 350 ÷ 400 µm (Fig. 1).

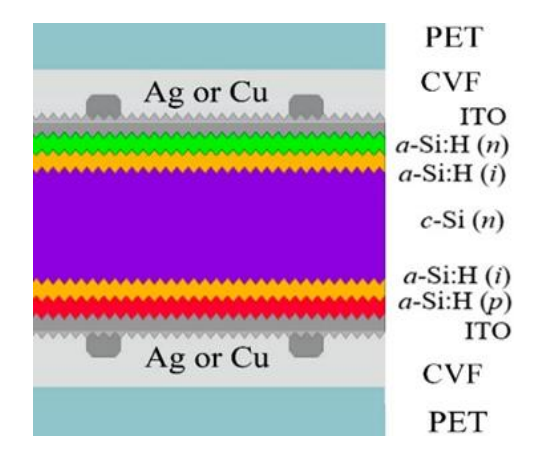


Fig. 1. Cross-section structure of HIT-type silicon SC and protective layers

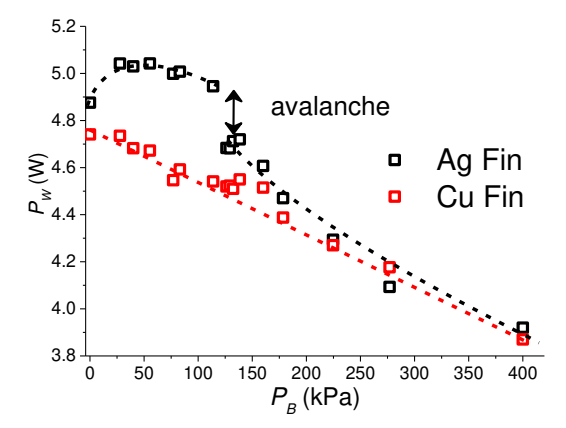


Fig. 2. Power dependences of two SC on the bending pressure P_B . The point of an avalanche-like drop in the power of SC with Ag fingers is marked

The dimensions of the laminated SC with protective layers were $\sim 220 \times 220 \times 2.2 \text{ mm}^3$. They were placed in the corners on 4 supports with a soft layer thickness of 1.5 cm and an area of $2 \times 2 \text{ cm}^2$, with a diagonal 180 mm distance between the supports. The test design followed a combination of the previously used Ball-on-Ring and Ring-on-Ring methods [8,11]. Static axial load in the range $P_B = 0 \div 400 \text{ kPa}$ was applied at the geometric center to the plate through $\Delta t = 200 \text{ h}$ to maximum P_{BM} and $t_M = 3325 \text{ h}$. SC power degradation were measured on HalmcetisPV-Moduletest3 equipment at AM 1,5 (Fig. 2).

Results

EL and PL measurements

The SC were monitored at room temperature by 2D photo- and electroluminescence (PL and EL). When studying EL, external direct displacement was used. PL studies were carried out on the LumiSolarCell System (Fig. 3), and EL on the MBJ SolarModule EL-quickline 4.0 (Fig. 4).

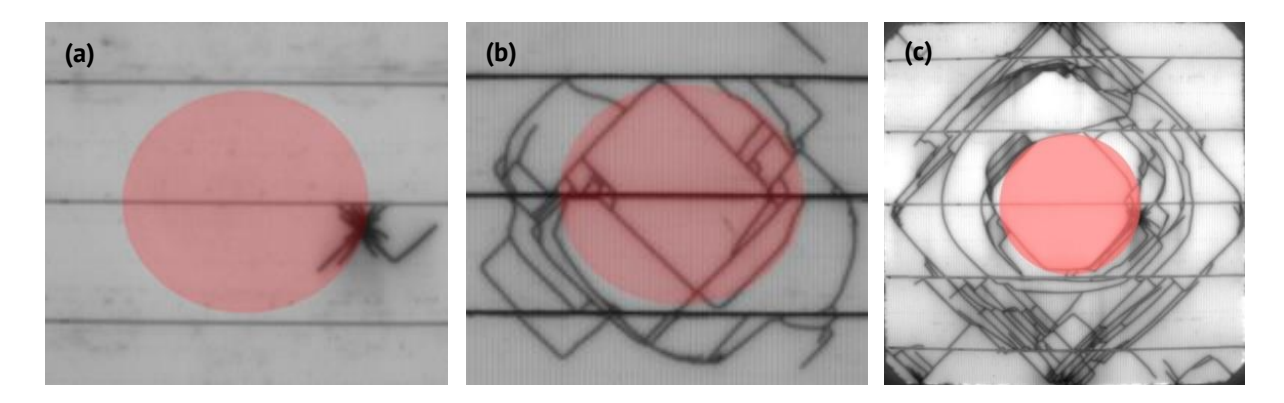


Fig. 3. (a) PL image after the occurrence of an avalanche at PB = 125 kPa in sample with Ag fingers; (b) accumulation of cracks up to PB =125 kPa in the Cu sample by fingers; (c) accumulation of cracks in the Cu sample by fingers at PBM = 400 kPa. The red disk is the pressure area

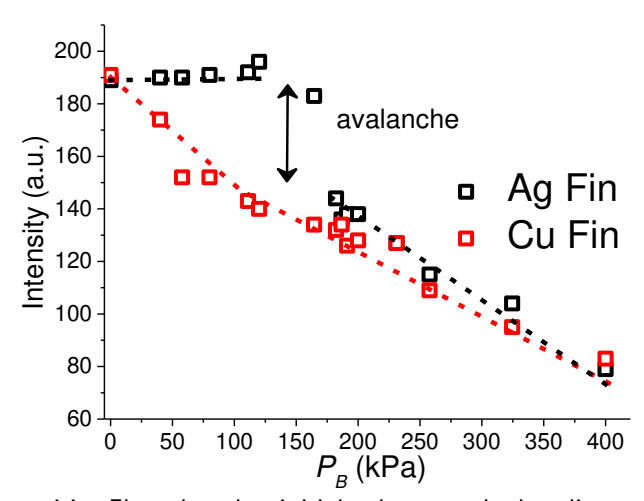


Fig. 4. Intensities EL, reduced to initial values, on the bending pressure P_B . The point of an avalanche-like drop in EL intensity of SC with Ag fingers is marked

Comparing Fig. 2 and 3 it can be seen that on the sample with Ag fingers 3 phases were detected:

- 1. increase in power with pressures up to 125 kPa;
- 2. the increase power in this sample will end with an avalanche-like appearance of a volumetric substrate defect with a radius of up to $10 \mu m$;
- 3. formation of a system of cracks appearance with a width < 1 μ m, and an increase in their total length at P_{BM} up to 4000 mm, and a decrease in power. On Cu finger sample, even at small P_B values, cracks appear with an increase in its total length to a slightly larger value of 4100 mm.

From Fig. 2 and 4 can be seen that for both samples their powers and EL intensities converge at large P_B , which indicates a common mechanism of SC degradation - the occurrence of cracks in the substrate.

Current-voltage characteristics measurements

According to [13], to describe degradation processes under conditions of significant changes in the current-voltage characteristics (CVC), a single-diode electrical model with series R_S and parallel R_{SH} resistances can be used. The first value will be associated with the degradation of the contact grid, and the second with parasitic leakage currents through the volume of the SC. It is obvious that measurements are necessary in both the light and dark states of SC due to significant differences in their nonlinearity. Programs for calculating dark CVC [14] and light CVC [15] have been developed using Python. In particular, dark CVCs are described by the implicit equation:

$$I = I_0 \left\{ exp\left(\frac{q(V - R_S I)}{kT}\right) - 1 \right\} + \frac{V - R_S I}{R_{SH}}.$$
 (1)

Measurements of load and dark CVC were carried out before and after exposure to mechanical loads. The calculation results of CVC measurements are shown in Table 1.

Table 1. Power P_W (W), its changes ΔP_W (%), fill factor FF (%), R_S (ohm) and R_{SH} (ohm) SC with Ag and C	ū
fingers for load and dark CVC. P_B (kPa) values are indicated	

Finger				Load	CVC	Dark CV	
metals,	P_{W}	FF	ΔP_{W}	Rs	R_{SH}	Rs	R_{SH}
pressure				Νς	V2H	Λς	V2H
Ag							
$P_{\rm B}$ =0	4.88	73.6	0,0	0.0182	0.82	0.313	10600
P _B =100	5.04	76.36	+3.40	0.0177	1.13	0.327	12600
P _B -100	5.04	72.34	-0.40	0.0177	0.73	0.327	156
$P_{\rm B}=P_{\rm BM}$	4.09	67.1	-16.1	0.0227	0.53	0.420	29.25
Cu							
$P_{\rm B}=0$	4.74	74.0	0.0	0.0184	0.87	0.316	52.46
P _B =100	4.68	73.6	-1.24	0.0174	0.80	0.320	66.09
$P_{\rm B}=P_{\rm BM}$	4.18	69.4	-12.0	0.0211	0.60	0.320	57.96

Discussion

A discussion of the experimental results on the type and dependence of the number of cracks on pressure is carried out in the following sequence.

SC with Aq fingers at P_B < 125 kPa

There is an improvement in its efficiency by 3.49 %. The positive effects of heterogeneity of impurities in semiconductors are known from the work on Si p-n junctions by Goetzberger and Shockley [16] and solar silicon by Kvedera [17]. Improvements in parameters under bending loads [18], in the presence of radiation effects on GaAs [19] and Si [20], during current forming of PERC [21] and light-induced other [22,23] solar cells are also known. The ambiguity of the short-term improvement of the latter in [24] is associated with the presence of a starting "infant" stage of operation, in particular at this stage there is a rapid significant drop in power up to 5 % [7].

SC with Ag Fingers at P_B ~ 125 kPa

The appearance of a large dendrite-like [7] or cross-like [25] crack system can be explained by the presence of elastic energy accumulation stag and its avalanche-like release. A volumetric substrate defect with a radius of up to 10 µm is formed with a 4 % power drop. Only the mechanism of internal avalanche corrosion is possible [26] due to two reasons: 1) under our experiment conditions, the so-called Sustained-load cracking or delayed fracture (pressure is applied and a significant delay with its subsequent increase) [27,28], 2) experimental temperatures are much lower than Si brittle-to-ductile transition temperatures (~ 550 °C) [29]. This mechanism was also previously observed during the embrittlement of metals with hydrogen [27], in brittle solids [30], and in Si at high temperatures [31].

SC with Cu fingers at P_B from 0 to P_{BM} , SC with Ag fingers at $P_B > 125$ kPa and up to P_{BM}

As can be seen from Fig. 3(c), two areas can be distinguished: near the pressure application contour and at its periphery. Usually, images of curved and rounded cracks are observed [7,32], and much less often cases are observed with a change in the angle of their growth by 90° [33], which is associated with the anisotropy of the potential at the end of the crack [34]. The presence of this anisotropy is probably important for the formation of the small rectangular shapes that we observed, but for the large rounded squares, a more likely reason is the corresponding symmetry of the strain distribution [35]. In general, the length of the cracks and the nature of their growth as the pressure increases are fully consistent with the Sustained-load cracking and brittle fracture of metals methods described and consisting of 3 stages [36,37]: the occurrence of cracks, their growth and destruction of the sample. At the same time, for SC, the presence of a large number of cracks and a power drop of up to 10 % for several solar cells in a module is considered quite acceptable in conditions of mass industrial production [38–40].

Conclusion

The usefulness and reliability of the results of studies of SC degradation mechanisms is largely determined by their methodology and its proximity to real operating conditions. The following circumstances are important:

- 1. carrying out accelerated degradation in accordance with the concept of Service Life Prediction (SLP) [3];
- 2. testing in a wide range of external influences;
- 3. conducting strength tests because in total, this is almost half of the SC failures due to the mechanical damage of substrate and contact system;
- 4. for more effective research is necessary to conduct them on flexible SC. The following results were obtained:
- 1. Three phases of power changes were detected: (i) an increase in SC power by 2-4% at low pressure, (ii) accumulation of deformations completed by the avalanche-like substrate damage with a drop in power by 3-5%, (iii) formation of crack system with an

increase in their total length at P_{BM} to 4000 ÷ 4100 mm and a decrease in of SC power to 12 ÷ 16 %.

- 2. The ambiguity of the short-term SC power improvement is associated with the presence of a starting "infant" effect.
- 3. The appearance of a large dendrite-like or cross-like crack system can be explained by the presence of elastic energy accumulation stage and its avalanche-like release.
- 4. For both SC samples with Ag and Cu fingers their powers and EL intensities converge at large P_B , which indicates a common mechanism of SC degradation the occurrence of cracks in the substrate.
- 5. The factor for accelerating degradation (AD) by ML using developed method can be calculated within the range AD = $25 \div 50$.
- 6. Combined Ball-on-Ring and Ring-on-Ring scheme made it possible to carry out accelerated degradation of solar cells parameters by $12 \div 16 \%$ in 140 days, close to corresponding degradation values over 10-20 years of their operation in natural (field) conditions.
- 7. The use of local 2D photo- and electroluminescence methods, measurements of dark and light (load) current-voltage characteristics make it possible to fully describe the degradation processes of both the SC electric contact grid and the volume of the active photovoltaic part of the SC.

References

- 1. Nelson HA, Schmutz FC. Accelerated weathering. A consideration of some fundamentals governing its application. *Trans. Roy. Soc. London.* 1926;18(12): 1222–1227.
- 2. Martin JW, Ryntz RA, Chin J, Dickie RA. (eds.) *Service life prediction of polymeric materials: global perspectives*. Springer; 2009.
- 3. Jordan DC, Kurtz SR. *Photovoltaic degradation rates: an analytical review.* National Renewable Energy Laboratory; 2012.
- 4. James G, Witten D, Hastie T, Tibshirani R. An Introduction to Statistical Learning with Applications. NY: Springer; 2013.
- 5. Standard IEC. IEC 61215-1-1:2021. *Terrestrial photovoltaic (PV) modules Design qualification and type approval- Part 1: Test requirements.* International Electrotechnical Commission; 2021.
- 6. Standard MIL-STD-810H. Environmental engineering considerations and laboratory tests. 2014.
- 7. Köntges M, Kurtz S, Packard CE, Jahn U, Berger KA, Kato K, Friesen T, Liu H, Van Iseghem M, Wohlgemuth J, Miller D, Kempe M, Hacke P, Reil F, Bogdanski N, Herrmann W, Buerhop-Lutz C, Razongles G. Friesen G. *Review of failures of photovoltaic modules*. Report IEA-PVPS T13-01:2014, 2014.
- 8. Nikitin SE, Shpeizman VV, Pozdnyakov AO, SI Stepanov, RB Timashov, VI Nikolaev, Terukov EI, Bobyl AV. Fracture strength of silicon solar wafers with different surface textures. *Materials Science in Semiconductor Processing*. 2022;140: 106386.
- 9. Borrero-Lopez O, Vodenitcharova T, Hoffman M, Leoz AJ Fracture strength of polycrystalline silicon wafers for the photovoltaic industry. *J. Am. Ceram. Soc.* 2009;92(11): 2713–2717.
- 10. Li X, Li P, Wub Z, Luo D, Yu HY, Lu ZH. Review and perspective of materials for flexible solar cells. *Materials Reports: Energy.* 2021;1(1): 100001.
- 11. Abolmasov S, Kochergin A, Terukov EI, Shelopin G. Conducting climatic and mechanical tests for solar modules made of heterojunction PV cells with a copper contact grid. *Adv. Eng. Res.* 2022;213: 39–44.
- 12. Shetty DK, Rosenfield AR, McGuire P, Bansal GK, Duckworth WH. Biaxial flexure test for ceramics. *Amer. Ceramics Soc. Bull.* 1980;59(12): 1193–1197.
- 13. Humada AM, Hojabri M, Mekhilef S, Hamada HM. Solar cell parameters extraction based on single and double-diode models: A review. *Renewable and Sustainable Energy Reviews*. 2016;56: 494–509.
- 14. Würfel P, Würfel U. Physics of Solar Cells. Wiley-VCH Verlag GmbH & Co; 2016.

- 15. Celik AN, Acikgoz N. Modelling and experimental verification of the operating current of monocrystalline photovoltaic modules using four- and five-parameter models. *Applied Energy*. 2007:84(1): 1–15.
- 16. Goetzberger A, Shockley W. Metal precipitates in Silicon pn junctions. J. Appl. Phys. 1960;31: 1821–1824.
- 17. Kveder V, Schroter W, Sattler A, Seibt M. Simulation of Al and phosphorus diffusion gettering in Si. *Materials Science and Engineering*. 2000;71(1-3): 175–181.
- 18. Sawada R, Karaki T, Watanabe J. Gettering of crystalline defects in Si by bending. *Applied Physics Letters*. 1981;38: 368–369.
- 19. Grusha SA, Evstigneev AM, Ismailov KA, Konakova RV, Krasiko AN, Sinishchuk IK, et. al. Electric field effect on radiation-induced gettering of defects in GaAs. *Phys. Stat. Sol. (A)*, 1984;86(1): 83–87.
- 20. Zhang Y, Qin L, Hou R, Ma N, He Y, Chen X, Yao L, Xu W, Qin G. Room-temperature gettering of Au in Si wafers with surface defects under small dose γ-ray radiation. *J. Phys. D: Appl. Phys.* 2015;48: 105101.
- 21. Wang Z, Shen H, Hu D, Wei Q, Ni Z, Li Y, Sun L, Qian H. Influence of double current injection annealing on anti-LID effect in mono-like silicon PERC solar cells. *Journal of Materials Science: Materials in Electronics.* 2020;31: 3221–3227.
- 22. Wright M, Stefani BV, Soeriyadi A, R Basnet, C Sun, W Weigand, Z Yu, Z Holman, Macdonald D, Hallam B. Progress with Defect Engineering in Silicon Heterojunction Solar Cells. *Physica Status Solidi (RRL)*. 2021;15(9): 2100170.
- 23. Boudjemila L, Davydov VV, Aleshin AN, VM Malyshkin, EI Terukov. Electrical characteristics of CsPbI3 and CsPbBr3 lead halide Pervoskvite nanocrystal films deposited on Si-c solar cells for high-efficiency photovoltaics. *St. Petersburg State Polytechnical University Journal: Physics and Mathematics.* 2022;15(3.2): 91–96.
- 24. Madumelu C, Wright B, Soeriyadi A, Wright M, Chen D, Hoex B, Hallam B. Investigation of light-induced degradation in N-type silicon heterojunction solar cells during illuminated annealing at elevated temperatures. *Solar Energy Materials and Solar Cells*. 2020;218: 110752.
- 25. Köntges M, Morlier A, Eder G, Fleiß E, Kubicek B, Lin J. Review: ultraviolet fluorescence as assessment tool for photovoltaic modules. *IEEE Journal of Photovoltaics*, 2020, 10(2): 616–633.
- 26. Segbefia OK, Akhtar N, Sætre TO. Moisture induced degradation in field-aged multicrystalline silicon photovoltaic modules. *Solar Energy Materials and Solar Cells*. 2023;258: 112407.
- 27. Landes JD, Wie RP. The kinetics of subcritical crack growth under sustained loading. *International Journal of Fracture*. 1973;9(3): 277 293.
- 28. Storgärds E, Simonsson K. Crack length evaluation for cyclic and sustained loading at high temperature using potential drop. *Experimental Mechanics*. 2015;55(3): 559–568.
- 29. Samuels J, Roberts SG, Hirsch PB. The brittle-to-ductile transition in silicon. *Materials Science and Engineering: A.* 1988;105–106(1): 39–46.
- 30. Barés J, Bonamy D. Crack growth in heterogeneous brittle solids: intermittency, crackling and induced seismicity. *Phil. Trans. R. Soc. A.* 2019;377(2136): 20170386.
- 31. Tanner BK, Garagorri J, Gorostegui-Colinas E, Elizalde MR, Bytheway R, McNally PJ, Danilewsky AN. The geometry of catastrophic fracture during high temperature processing of silicon. *Int J Fract.* 2015;195: 79–85.
- 32. Papargyri L, Theristis M, Kubicek B, Krametz T, Mayr C, Papanastasiou P, Georghiou GE. Modelling and experimental investigations of 1 microcracks in crystalline silicon photovoltaics: A review. *Renewable Energy*. 2020;145: 2387–2408.
- 33. Dhimish M, Hu Y. Rapid testing on the effect of cracks on solar cells output power performance and thermal operation. *Sci Rep.* 2022;12: 12168.
- 34. Alam MS, Wahab MA. A new approach for modeling of fatigue crack growth in welded cruciform and curve T joint structures. In: *ASME 2005 International Mechanical Engineering Congress and Exposition*. ASME; 2008. p.351–360.
- 35. Espitia-Mesa G, Hernández-Pedraza E, Molina-Tamayo S, Mejía-Gutiérrez R. Design, analysis, and modeling of curved photovoltaic surfaces using composite materials. *TecnoLógicas*. 2022;25(53): e2171.
- 36. Liu D, Pons DJ. Crack propagation mechanisms for creep fatigue: a consolidated explanation of fundamental behaviours from initiation to failure. *Metals*. 2018;8(8): 623.
- 37. Köntges M, Kunze I, Kajari-Schröder S, Breitenmoser X, Bjørneklett B. The risk of power loss in crystalline silicon based photovoltaic modules due to micro-cracks. *Solar Energy Materials and Solar Cells*, 2011;95(4): 1131–1137.
- 38. Morlier A, Haase F, Köntges M. Impact of cracks in multicrystalline silicon solar cells on PV module power a simulation study based on field data. *IEEE Journal of Photovoltaics*. 2015, 5(6): 1735–1741

39. Boudiemila L, Davydov V, Malyshkin V. Quantum-mechanical methods for processing the results of classical experiments as an alternative to kalman filter. In: *Proceedings of the 2021 International Conference on Electrical Engineering and Photonics*. EExPolytech; 2021. p.256–259.

40. Rud V, Melebaev D, Krasnoshchekov V, Ilyin I, Terukov E, Diuldin M, Andreev A, Shamuhammedowa M, Davydov V. Photosensitivity of nanostructured Schottky barriers based on GaP for solar energy applications. *Energies.* 2023;16(5): 2319.

About Authors

Alexander V. Bobyl 🗓 Sc

Doctor of Physical and Mathematical Sciences Leading Researcher (Ioffe Institute, St. Petersburg, Russia)

Roman V. Davydov D Sc

Candidate of Physical and Mathematical Sciences
Associate Professor (Peter the Great St. Petersburg Polytechnic University, St. Petersburg, Russia)

Oleg I. Konkov D Sc

Candidate of Physical and Mathematical Sciences Senior Researcher (loffe Institute, St. Petersburg, Russia)

Artem V. Kochergin D Sc

Technologist (STC Thin Film Technologies in Power Engineering, St. Petersburg, Russia)

Dmitry A. Malevsky D Sc

Senior Researcher (loffe Institute, St. Petersburg, Russia)

Sergey E. Nikitin D Sc

Candidate of Chemical Sciences Senior Researcher (loffe Institute, St. Petersburg, Russia) Submitted: March 14, 2024 Revised: May 6, 2024 Accepted: May 28, 2024

MEMS gas sensor of resistive type for detection of hydrogen sulfide down to low concentrations

I.M. Komarevtsev ¹, A.S. Kondrateva ¹, A.N. Kazakin ¹, Ya.B. Enns ¹,

I.A. Lazdin ², P.A. Karaseov ², U.D. Akulshin ²

ABSTRACT

The technological route to manufacture a resistive-type MEMS gas sensor for low analyte concentration detection is proposed and the main characteristics of the device are demonstrated. MEMS consists of a silicon substrate with nickel interdigital electrodes acting as a microheater, on top of which a thin (100 nm) gassensitive layer of nickel oxide (NiO) is deposited. The silicon substrate is etched from the back side of the device to achieve a membrane of about 50 microns. The operating temperature of the sensitive layer in measurement mode is 130–205 °C. The proposed device shows the effect of introducing hydrogen sulfide in a gas mixture from 1 to 100 ppm on the conductivity of the sensing layer.

KEYWORDS

microelectromechanical system • nickel oxide • microelectromechanical resistive gas sensor • hydrogen sulfide **Acknowledgements.** The results of the article were obtained with the financial support of State Budget FSRM-2023-0009. Topic: New approaches to obtaining hybrid micro- and nanostructures for nonlinear optics and sensors.

Citation: Komarevtsev IM, Kondrateva AS, Kazakin AN, Enns YaB, Lazdin IA, Karaseov PA, Akulshin UD. Microelectromechanical gas sensor of resistive type for detection of hydrogen sulfide down to low concentrations. *Materials Physics and Mechanics*. 2024;52(4): 9–22.

http://dx.doi.org/10.18149/MPM.5242024_2

Introduction

Microelectromechanical systems (MEMS) are used in applications ranging from gyroscopes and accelerometers to air pollution detection systems [1-5]. At the same time, high-performance gas sensors with high sensitivity, selectivity, and low response time to small changes in gas concentration are still needed to improve reliability. Compact and MEMS sensors with low power consumption are one of the options for solving this problem.

The main difficulty in the application of MEMS as high-performance gas sensors of resistive type is the selection of the material of the gas-sensitive element, which can be thin films of metal oxides, metal-organic composites, nanocomposites and other materials [4-7]. The development of new topologies of microsystems and the search for the best materials for the sensitive layer is the actual task. At the same time, the choice of material for the sensitive layer of the gas sensor is based on the gas to be detected, thus, the study of sensitivity to different gases of different elements and compounds is also extremely important [8-10].

¹ Alferov University, St. Petersburg, Russian Federation

² Peter the Great St. Petersburg Polytechnic University, St. Petersburg, Russian Federation

[™] bitbooks8@gmail.com

Hydrogen sulfide is a neurotoxic gas that causes poisoning if the content of the compound exceeds 50 ppm. The maximum permissible, or low, concentrations are less than 7 ppm for the work area and 0.008 ppm for the residential area. For measuring in the range of operating area concentrations of 1–1000 ppm, electrochemical sensors are used. They have low response rate, low resolution, and a bulky design, as well as low energy efficiency (only a few watts). Other methods of studying the concentration of gases in the mixture, such as mass spectrometry, chromatography and optical methods, are not suitable for conditions of continuous air quality monitoring, as they require special sample preparation and do not allow full automation of the process without the use of highly qualified personnel.

In turn among MEMS devices for detection of hydrogen sulfide the sensors based on tin oxide, tantalum oxide with various doping were used. It is shown that the presence of metal inclusions (zinc, copper, nickel, indium) increases the sensitivity and selectivity to this gas due to the formation of sulfides of these metals on the surface. The application of these sensors is limited by the long recovery time (it takes several hours for desorption) and/or degradation of the active layer [11]. The presence of oxidation centers on a sensitive layer is also important in detection of hydrogen sulfide. The presence of such centers is associated with both the crystallinity of a film, and the roughness of its surface.

One of the options for the material of the sensing element is nickel oxide. For films of nickel oxide, which acts as an active center for the addition of hydrogen sulfide, the possibility of achieving greater surface roughness was shown in the study of electrochromic properties [12]. In addition, the p-type conductivity of nickel oxide suggests a decrease in the conductivity of the material through the adsorption of hydrogen sulfide on its surface [13].

Thus, the purpose of this work was to create a MEMS gas sensor of resistive type with a thin-film sensing element of nickel oxide, suitable for detection in a gas mixture with a concentration of hydrogen sulfide from 1 to 100 ppm.

Methodology of manufacturing MEMS gas sensor

Functional diagram and design of the sensitive element

For manufacturing the laboratory prototype of the sensitive element (SE) of the MEMS hydrogen sulfide gas sensor, the classical functional scheme of resistive gas sensors [5] was chosen. It contains a heating element and a sensitive layer based on a semiconductor film that changes its conductivity by interaction with analyte molecules during adsorption and desorption of gas from the surface of the active layer [11].

The SE is made of monocrystalline silicon with a thickness of 0.4 mm and a size of 10×10 mm in the horizontal plane. In the central part, the silicon is thinned to a membrane with a thickness of about 50 µm to reduce power consumption and increase the SE performance (Fig. 1(b)). On the membrane, there are a heater and two interdigital electrodes separated by an insulating dielectric and made by thin-film technology from metal having an ohmic contact to the semiconductor layer of nickel oxide (Fig. 1(a)). For p-type NiO, nickel and gold, which have a high work function, can act as contacts. The heater is designed in the form of a meander, whose paths between the protrusions of the interdigital electrodes, and is covered with a protective dielectric from above, unlike the

protrusions of the electrodes [14]. The length of the protrusions of the interdigital electrodes is 2 mm, the distance between the protrusions is 300 μ m, and the width of the heater track is 100 μ m. The sensitive layer (NiO) is located on the membrane above all the elements and is in electrical contact only with the protrusions of the electrodes acting as a measuring element. With this configuration of the SE, the entire surface of the sensitive layer is open for interaction with the molecules of the analyzed gas, and the maximum heating is carried out directly between the protrusions of the measuring electrodes [15].

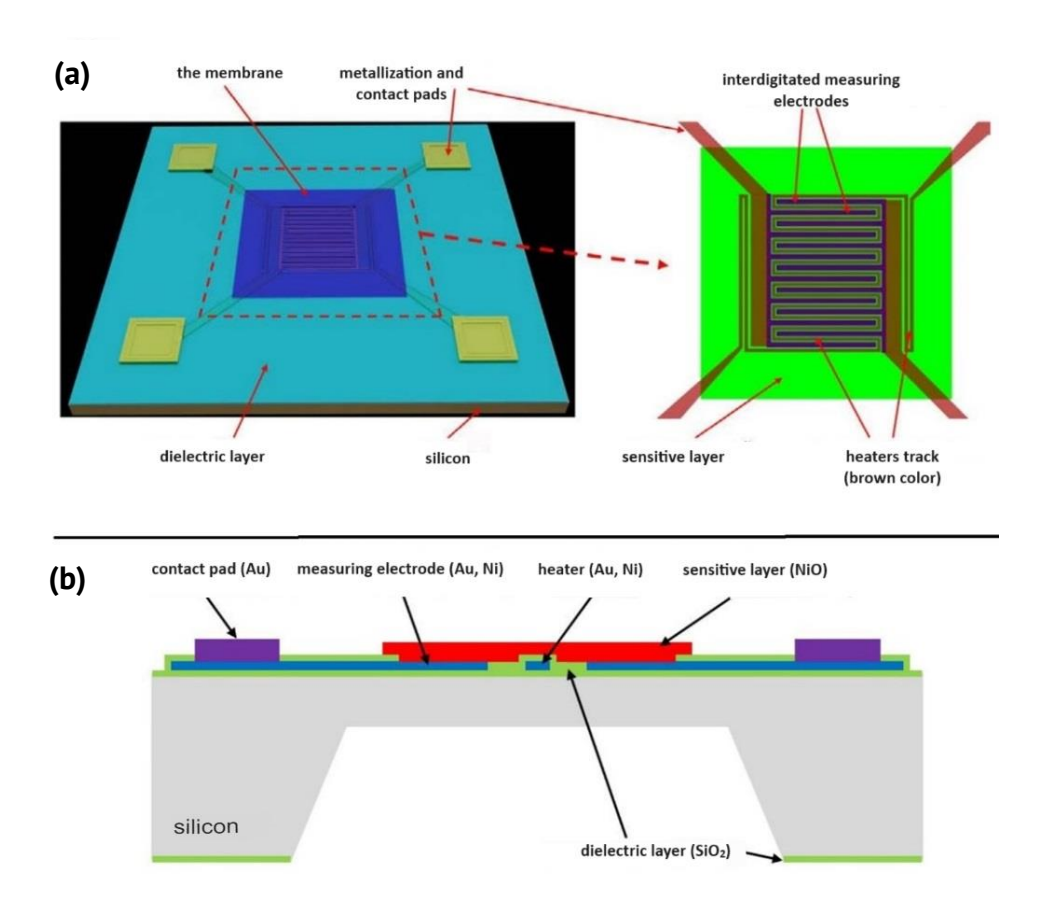


Fig. 1. Schematic diagram of the SE chip: (a) top view: chip size $10 \times 10 \times 0.4$ mm; (b) side view (not to scale)

The performance, sensitivity, and selectivity of such a SE to the analyzed gas depend on the thickness and crystal structure of the NiO layer [15], regulated by the modes of its vacuum deposition and subsequent high-temperature annealing, as well as on the temperature mode of the SE operation, set by the heater [16,17].

The technological route presented in Fig. 2 was chosen for the fabrication of SE laboratory models. The presented route is universal, as it is suitable for the use of various gas-sensitive materials, such as nickel, titanium, molybdenum, tin oxides and others [8,9,18–20] with the use of metallization system based on noble metals and a plasma method of membrane formation. In addition, a nickel metallization system can be used to create an electrical contact to the gas-sensitive layer, and alkaline etching of silicon in potassium hydroxide solutions can be used to form a silicon membrane with low heat capacity.

Manufacturing MEMS hydrogen sulfide gas sensor

To precisely position the elements during the technological process, special marks were created on the plates for subsequent precise alignment of the elements located on the front (top) side of the plate and the back (bottom) side of the plate (Fig. 2). A ~ 100 nm thick SiO_2 oxide layer, grown by thermal oxidation for four hours at 950 °C, was coated with a positive photoresist, followed by double-sided photolithography. This was followed by etching the oxide in a standard SiO_2 buffer etchant for 1 min and 5 μ m mark burial by wet etching of the silicon in 25 % tetramethylammonium hydroxide (TMAH) solution for 10 min at 70 °C. This was followed by cleaning aggregates from the surface and repeated thermal oxidation of the silicon for 4 h at 950 °C.

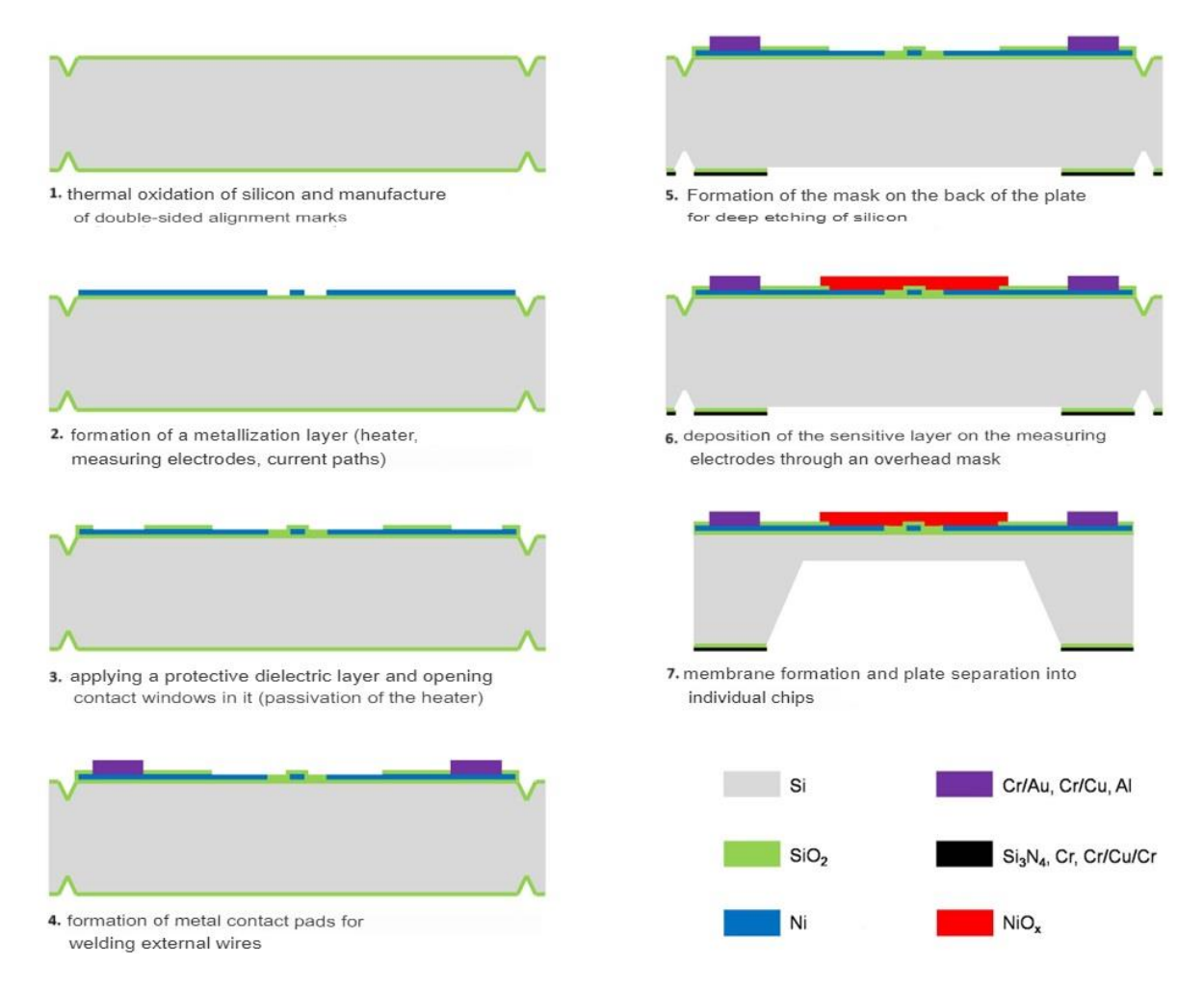


Fig. 2. Technological route to manufacture MEMS gas sensor

At the second stage (Fig. 2), the topology of the metallization layer was formed, including heating elements, measuring interdigital electrodes, contact pads and connecting paths. Vacuum DC-magnetron sputtering of pure nickel with a thickness of 100 nm was used to apply the metal coating. Next, the topology was formed on the metal layer using direct photolithography. The type of photomasks used is shown in Fig. 3. Nickel etching was carried out in 30 % nitric acid solution.

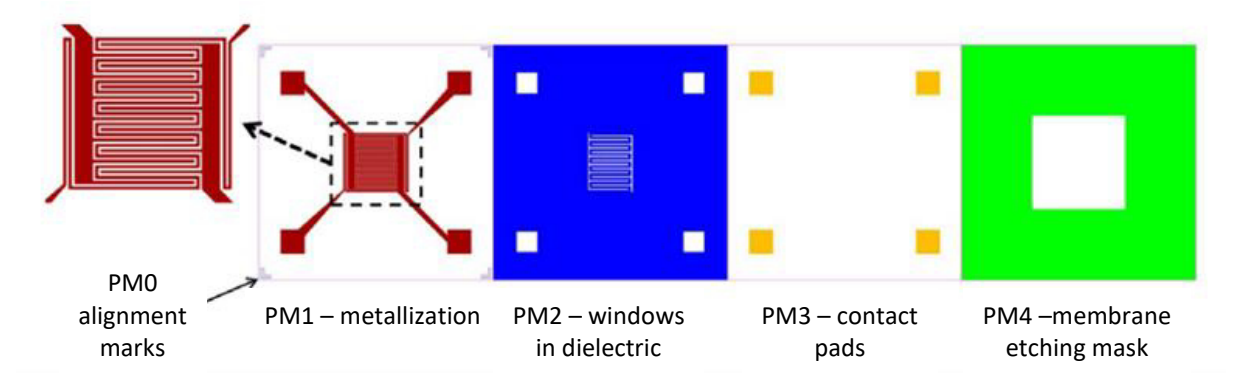


Fig. 3. Topology of used photomasks

To insulate the heater, a SiO_2 dielectric film with a thickness of 300 nm was deposited on the surface of the heating element. This operation was performed using the lift-off photolithography method exposed to PM2 "windows in dielectric" mask. The SiO_2 layer was deposited by vacuum reactive DC-magnetron sputtering of a pure silicon target in an oxygen and argon atmosphere (1:1) at a pressure of 2 mTorr and a discharge power of 150 W at a rate of 2 nm/min. The photoresist was removed in a boiling solution of dimethylformamide and monoethanolamine (1:1), resulting in the formation of contact windows in the deposited dielectric film above the measuring electrodes and microwire bonding pads. To ensure guaranteed heater insulation, the procedure with the application of the insulating layer was performed twice. In addition, to improve the contact pads located at the edges of the chip, a repeated nickel metallization procedure using the lift-off photolithography and vacuum magnetron sputtering of metal.

The penultimate step of the technological route was the etching of the silicon membrane. The topology of the mask was formed using the PM4 "mask for membrane" (Fig. 3). The choice of a specific method of membrane fabrication, as well as modes of silicon etching and chemical reagents used, was made in accordance with the chemical resistance of the elements on the front surface.

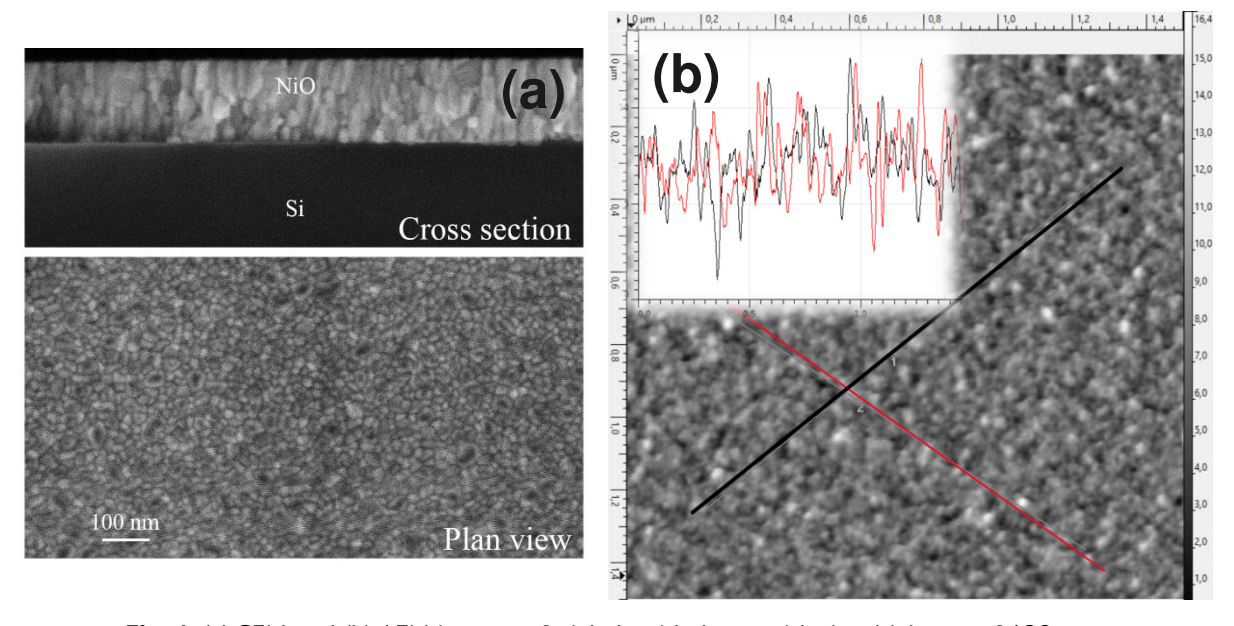


Fig. 4. (a) SEM and (b) AFM images of nickel oxide layer with the thickness of 120 nm

Deposition of the gas-sensitive NiO layer on the central area of the chips was performed through an overlay mask made of a silicon plate with laser-cut square holes (Fig. 2). Vacuum reactive DC-magnetron sputtering of a nickel target with a diameter of 100 mm [21] and a thickness of 1 mm in an atmosphere consisting of 30 % oxygen and 70% argon (O_2 flow rate of 6 sccm, Ar flow rate of 14 sccm) [22] was used for the deposition. The operating pressure during sputtering was 3 mTorr, the discharge power was about 100 W (0.3 A, 340 V), and the distance from the target to the chip substrate holder was 20 cm. The NiO deposition rate was 2 nm/min. The thickness of the deposited coating varied from 30 to 120 nm, and the thin film morphology is shown in Fig. 4 [6,14,15].

To increase the proportion of the crystal phase in the deposited NiO films, annealing was performed at 300-550 °C [23-26]. The annealing temperature was limited to 400 °C, since at higher temperatures significant degradation of the metallization system occurred.

Results and discussion

To study the gas sensitivity of the MEMS SEs, they were placed for mounting in metallized ceramic boards (Fig. 5(a)), which have low thermal conductivity to reduce overall power consumption. The use of such layouts for mounting contacts allowed to protect the metal contacts of SE, as the most vulnerable to the effects of hydrogen sulfide, and to provide flip-chip mounting of SE. The chip in the case is shown in Fig. 5(b).

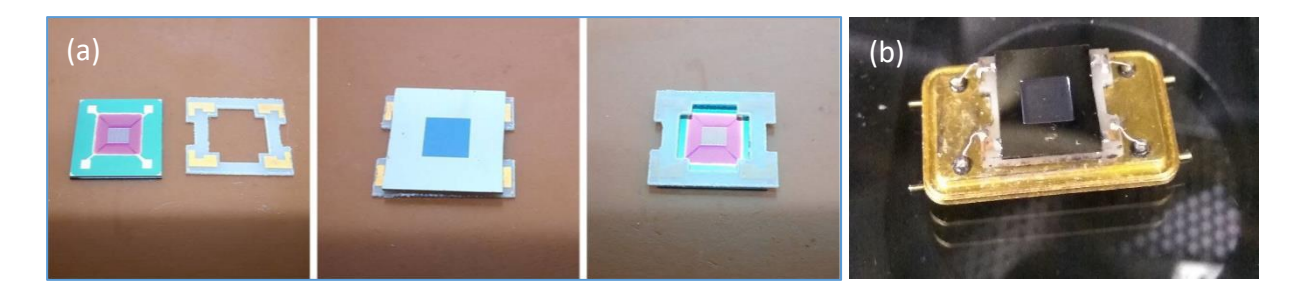


Fig. 5. Polycor boards, MEMS sensor before (a) and after (b) mounting

Measuring the main electrical parameters of the MEMS sensor

Before determining the sensitivity to the presence of hydrogen sulfide of known concentration, the basic electrical parameters of the laboratory MEMS sensor prototypes were measured, such as the resistance of the heater and gas-sensitive layer at different temperatures.

During the measurements, each chip with the MEMS sensor was subjected to slow heating and cooling. During this time, the resistance values of the nickel heater and the NiO sensitive layer between the measuring interdigital electrodes were measured. The chips both with and without annealing were used for the measurements. Figure 6 shows the characteristic temperature dependences of the resistances for five SEs with nickel oxide layer with a thickness of 120 nm, differing in high-temperature annealing modes.

Subsequently, the parameters of the obtained calibration curves allowed estimating the temperature of the sensor's operating zone by extrapolating the obtained dependencies to the entire temperature range.

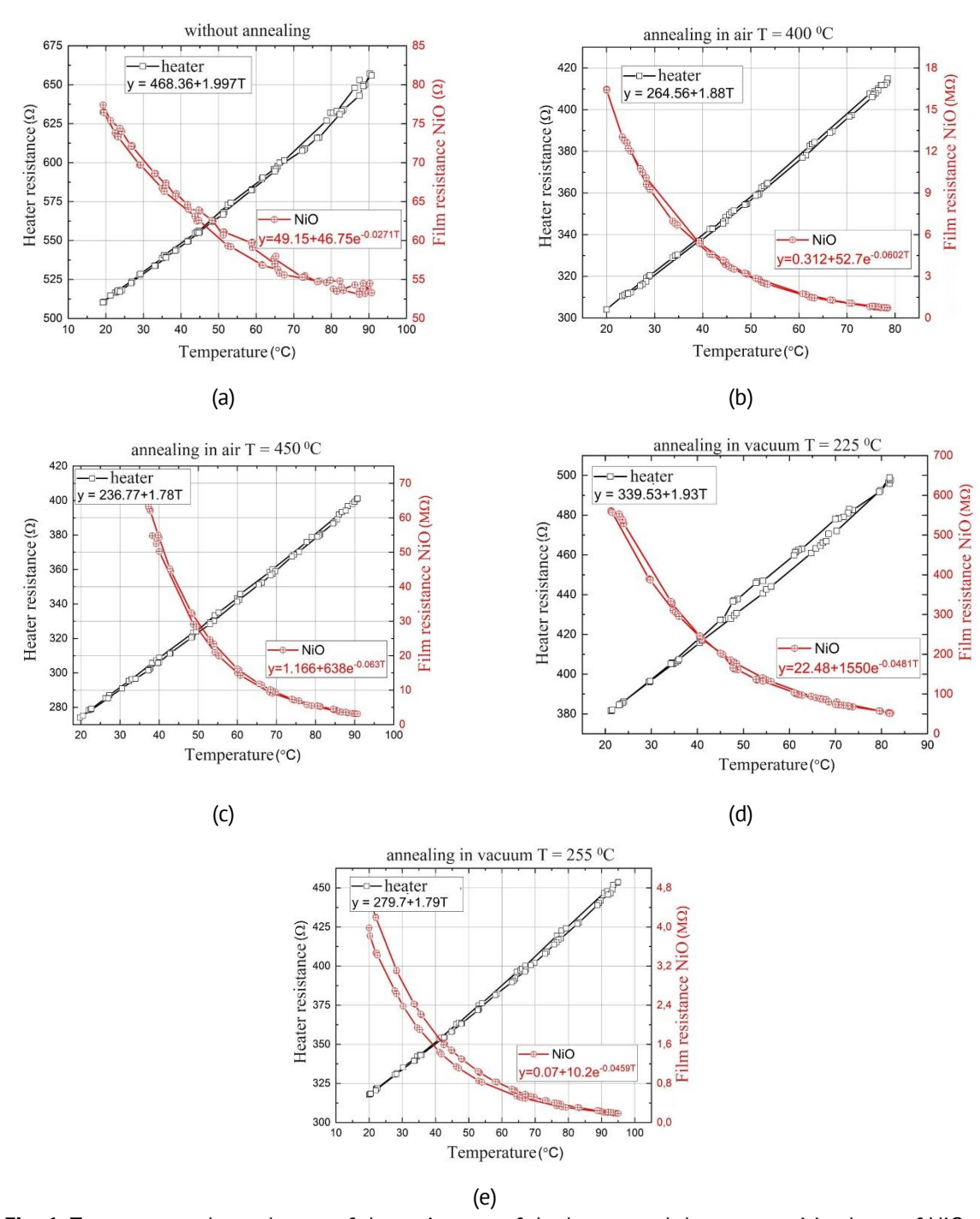


Fig. 6. Temperature dependences of the resistance of the heater and the gas-sensitive layer of NiO without annealing (a), with vacuum annealing (residual pressure 10^{-6} Pa) (b,c) and annealing in air (d,e)

Effect of annealing temperature on the electrical parameters of the active layer

All annealed SE samples are characterized by a linear temperature dependence of the measured resistance (conductivity) in semi-logarithmic coordinates (Fig. 7(b)), which indicates the formation of a high-quality polycrystalline layer of semiconductor NiO and the ohmic nature of the metal contacts burned into it [15,17]. For the SE without annealing, this dependence is nonlinear, which may indicate either an amorphous state of the gas-sensitive layer or poor quality of the contacts [27].

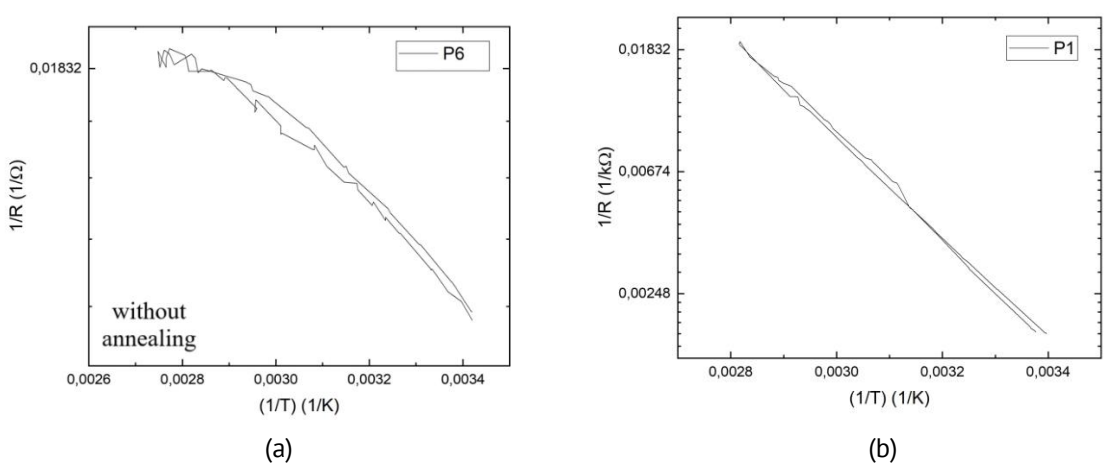


Fig. 7. Temperature dependences of the conductivity of the gas-sensitive layer of the SE in semi-logarithmic coordinates before (a) and after (b) annealing of NiO

The absolute value of the resistance of the nickel heater decreases with increasing annealing temperature in each series of experiments, in the range from 850 to 500 ohms, and its temperature coefficient of resistance is almost constant in the studied temperature range [28].

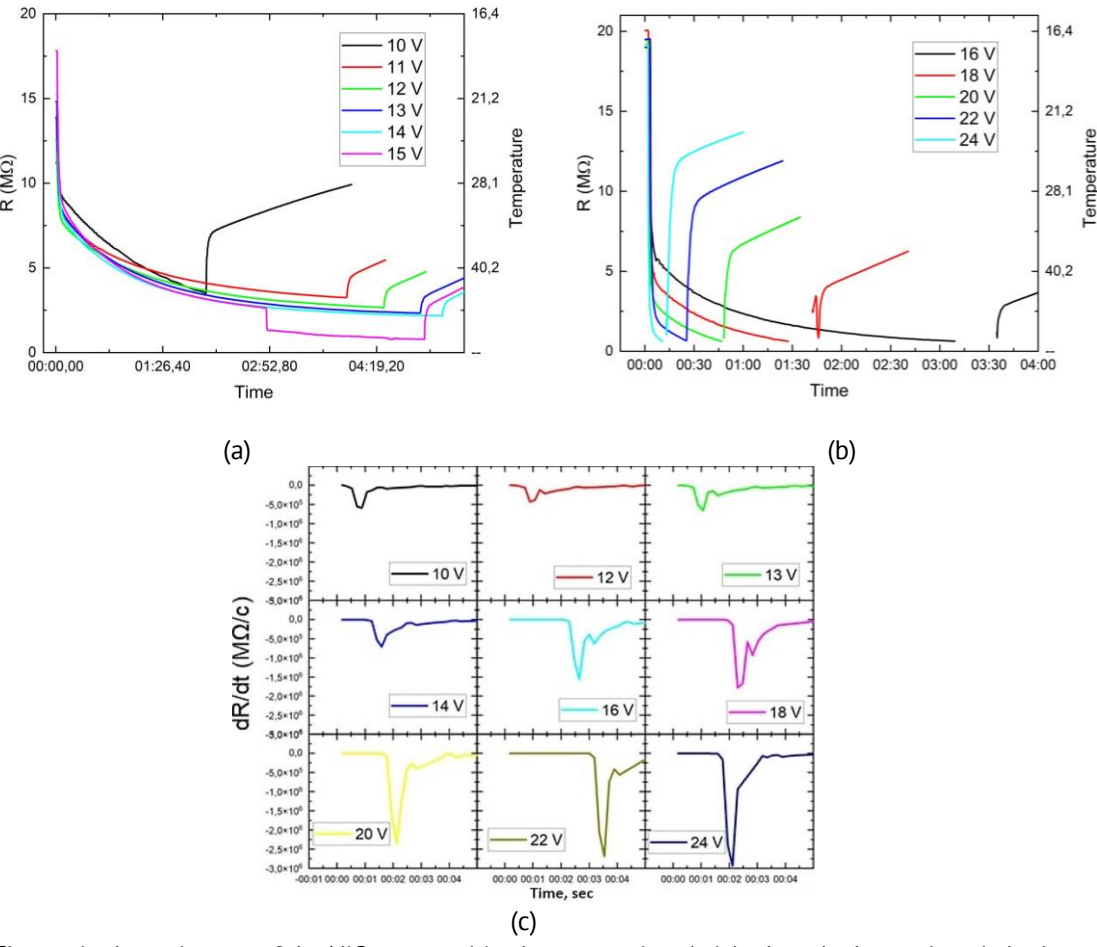


Fig. 8. Change in the resistance of the NiO gas-sensitive layer over time (min) when the heater is switched on and off at different voltages on the heater: (a) heating/cooling time of the sensor when applying voltage to the heater from 10 to 15 V (power < 1 W); (b) heating/cooling time of the sensor when applying voltage to the heater from 16 to 24 V (power > 1 W); (c) derivative of the heater resistance when applying voltage in pulse mode

Sensor response time

Figure 8 shows the experimental time characteristics of one of the laboratory models of the SE at different values of voltage supplied to the heater. These dependencies are characterized by two time intervals both on the heating curve and on the cooling curve – a rapid change [22,29] in the temperature of NiO at the initial moment of the response time (t_{90}) of several seconds and slow thermal stabilization of the SE within several minutes after switching on or off the supply voltage.

Power consumption parameters for different operating temperatures

The power consumption of the formed SE was from 0.5 to 1.5 W (Fig. 9) in the operating temperature range. During the study, it was found that despite the presence of the membrane, during heating, the sample case is strongly heated. In order to reduce the heating, it was proposed to use additional "legs" for thermal decoupling of the sample. The "legs" were metal pins on the back surface of the case, which were supposed to improve heat dissipation. However, the presence of "legs" did not give the expected results. The reason for this may be the strong influence of convective heating of the case due to the large area of the heater and the small gap in the case.

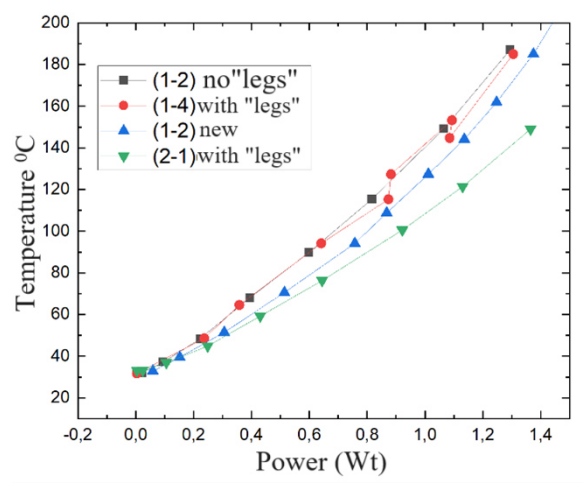


Fig. 9. Experimental dependences of the heater temperature on the power supply for different installation conditions in the case (with and without "legs")

Study of the sensitivity of a gas sensor to hydrogen sulfide

For *p*-type semiconductors, interaction with gases by the reduction mechanism leads to a decrease in resistance, which is caused by an increase in the number of holes in the valence band due to a decrease in the number of electrons as a result of chemical sorption of gas on the surface. The reverse mechanism is observed with the oxidation mechanism. This changes the geometric size of the space charge region and other parameters of the semiconductor film related to its conductivity. This is demonstrated schematically in Fig. 10. In the case of the nickel oxide film, an increase in the resistance of the active layer is expected with increasing temperature when interacting with hydrogen sulfide.

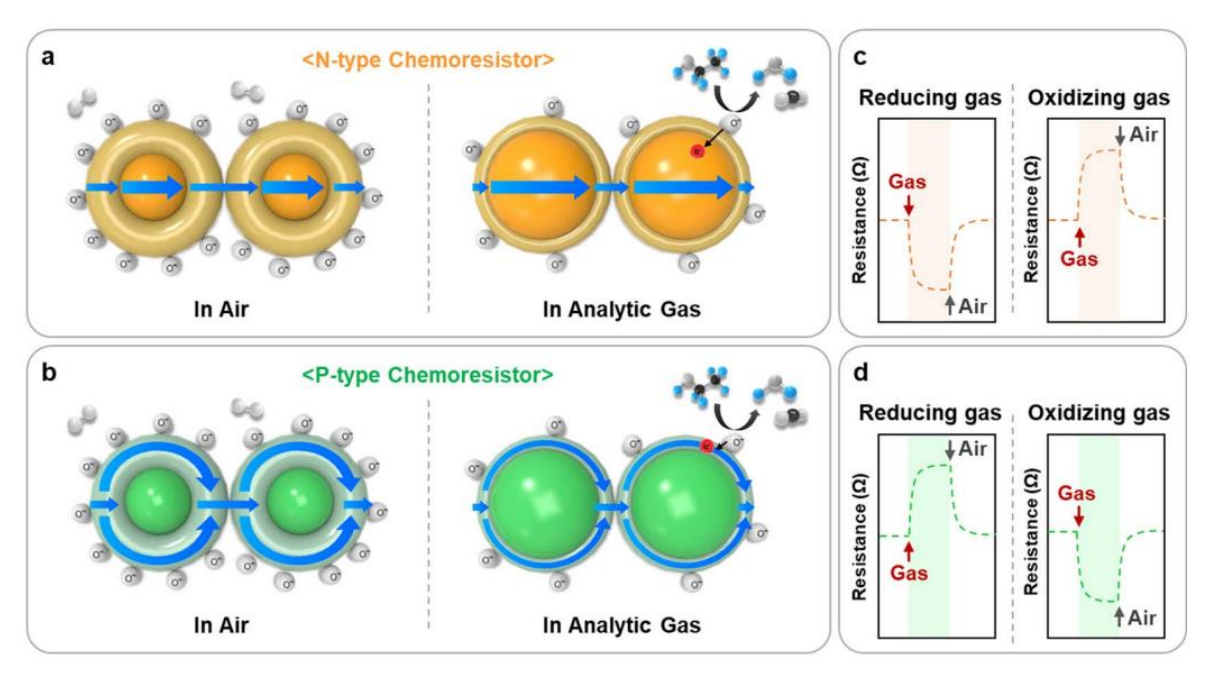


Fig. 10. Gas detection mechanism and transient resistance changes of *n*-type (a,c) and *p*-type (b,d) chemoresistive gas sensors

The tests of the manufactured MEMS sensor elements were carried out using a measuring stand consisting of a chamber, a gas distribution system for hydrogen sulfide (with a maximum hydrogen sulfide concentration in the chamber of 100 ppm), a reference hydrogen sulfide sensor "ATOM MIRAX", and the corresponding electronic equipment for signal recording. Resistance measurements were carried out using a resistive divider circuit [30] based on precise calibration resistances (Fig. 11).

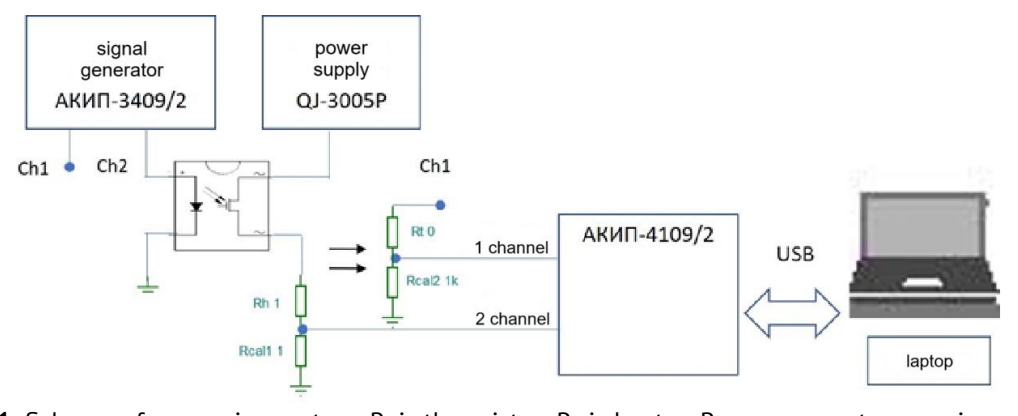


Fig. 11. Scheme of measuring system: R_t is thermistor; R_h is heater, R_{cal} are current measuring resistors

The SE was tested at heater operating temperatures from 130 to 205 °C to exclude the influence of changes in the registered signal from the flow rate. In the measurements, the gas flow rate was maintained constant using two GMFCs; the total flow was 3.6 l/h. Figure 12 shows an example of the dependences of hydrogen sulfide influence on the sensor resistance in comparison with the reference hydrogen sulfide sensor for different gas supply ratios at the operating temperature, and also indicates the heater temperature drift during measurements at 130, 170, 205 °C. The formed SE allowed to detect from 1 to 100 ppm of hydrogen sulfide.

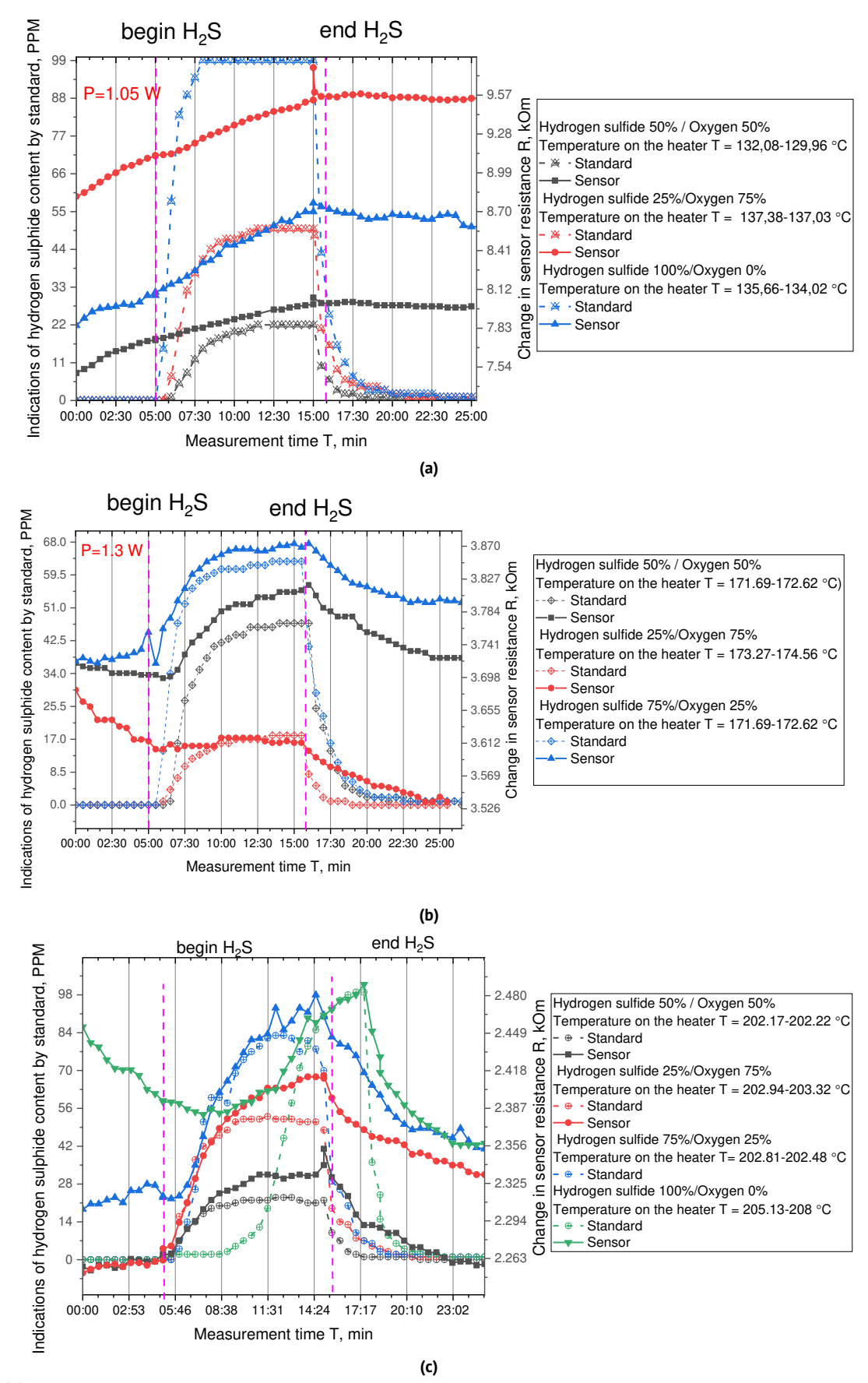


Fig. 12. Dependencies of the influence of hydrogen sulfide on the resistance of the sensor in comparison with the reference sensor for different gas supply ratios (as a percentage of the total volume of gases in the mixture), at different operating temperatures: (a) 130 °C, (b) 170 °C, (c) 205 °C

Figure 12 shows that the nickel oxide-based gas sensor manufactured using the proposed MEMS technology allows detecting hydrogen sulfide in the range from 1 to 100 ppm. The most effective operating temperature for detecting hydrogen sulfide is 205 °C (Table 1). The operating power of the sensor is 1.45 W. Moreover, the built-in microheater provides a simultaneous heating function without the need for any external heating device. However, a systematic study requires consideration of the selectivity of the sensor when gases other than hydrogen sulfide are also present in the air.

Table 1. Sensor parameters at different operating temperatures

Operating temperature of	Response to hydrogen	Power, W	Recorded concentrations,
the sensor, °C	sulfide, sec	POWEI, W	ppm
130	-	1.05	_
170	30	1.30	15–100
205	10	1.45	1–100

Conclusion

The article proposes and tests a technology for manufacturing MEMS hydrogen sulfide sensors with a sensitive layer of nickel oxide. The sensitive layer of nickel oxide (NiO) showed sensitivity to hydrogen sulfide from 1 to 100 ppm, for annealed films at a temperature of 300 to 400 °C, the optimal operating temperature was 205 °C. The presence of a silicon membrane made it possible to reduce energy consumption to several watts, due to a decrease in the heat capacity of the chip while maintaining the size and design of the heater. The MEMS sensor showed a thermal stabilization time of about a minute, under the condition of a sharp primary heating of about 1 sec.

This resistive-type MEMS sensor with a self-heating thin NiO film is suitable for energy-efficient gas sensor applications but requires testing for selectivity.

References

- 1. Dong Y, Gao W, Zhou Q, Zheng Y, You Z. Characterization of the gas sensors based on polymer-coated resonant microcantilevers for the detection of volatile organic compounds. *Analytica Chimica Acta*. 2010;671(1–2): 85–91.
- 2. Zampolli S, Elmi I, Ahmed F, Passini M, Cardinali GC, Nicoletti S, Dori L. An electronic nose based on solid state sensor arrays for low-cost indoor air quality monitoring applications. *Sensors and Actuators B: Chemical.* 2004;101(1–2): 39–46.
- 3. Tomchenko AA, Harmer GP, Marquis BT, Allen JW. Semiconducting metal oxide sensor array for the selective detection of combustion gases. *Sensors and Actuators B: Chemical.* 2003;93(1–3): 126–134.
- 4. He L, Jia Y, Meng F, Li M, Liu J. Development of sensors based on CuO-doped SnO_2 hollow spheres for ppb level H_2S gas sensing. *Journal of Materials Science*. 2009;44(16): 4326–4333.
- 5. Kanan SM, El-Kadri OM, Abu-Yousef IA, Kanan MC. Semiconducting Metal Oxide Based Sensors for Selective Gas Pollutant Detection. *Sensors*. 2009;9: 8158–8196.
- 6. Park SJ, Lee SM, Oh MH, Huh YS, Jang HW. Food quality assessment using chemoresistive gas sensors: achievements and future perspectives. *Sustainable Food Technology*. 2024;2: 266–280.
- 7. Wang C, Yin L, Zhang L, Xiang D, Gao R. Metal Oxide Gas Sensors: Sensitivity and Influencing Factors. *Sensors*. 2010;10(3): 2088.
- 8. Santhosh S, Balamurugan K, Mathankumar M, Shankar K, Subramanian B. Electrochromic and optical studies on Nb_2O_5 –NiO mixed oxide films for smart window applications. *Optical Materials*. 2023;135: 113248. 9. Huang X, Meng F, Pi Z, Xu W, Liu J. Gas sensing behavior of a single tin dioxide sensor under dynamic
- temperature modulation. Sensors and Actuators B: Chemical. 2004;99(2-3): 444-450.

- 10. Hyodo T, Nishida N, Shimizu Y, Egashira M. Preparation and gas-sensing properties of thermally stable mesoporous SnO₂. Sensors and Actuators B: Chemical. 2002;83(1–3): 209–215.
- 11. Kondrateva AS, Bespalova PG, Filatov LA, Tanklevskaya EM, Pavlov SI, Alexandrov SE. Gas-sensitive properties of thin nickel oxide films. Russian Journal of Applied Chemistry. 2017;90(6): 846–852.
- 12. Chen H, Ma H, Zhu Y, Zhao M, Chen Z, Zhang L. Novel approach for improving electrochromic and mechanical properties of NiO film: Experiment and molecular dynamics simulation. Applied Surface Science. 2023;609: 155209.
- 13. Lee CY, Chiang CM, Wang YH, Ma RH. A self-heating gas sensor with integrated NiO thin-film for formaldehyde detection. Sensors and Actuators B: Chemical. 2007;122(2): 503-510.
- 14. Sun YF, Liu SB, Meng FL, Liu JY, Jin Z, Kong LT, Liu JH. Metal oxide nanostructures and their gas sensing properties: A review. Sensors. 2012;12(3): 2610-2631.
- 15. Lee CY, Hsieh PR, Lin CH, Chou PC, Fu LM, Chiang CM. MEMS-based formaldehyde gas sensor integrated with a micro-hotplate. *Microsystem Technologies*. 2006;12: 893–898.
- 16. Wang Y, Liu C, Wang Z, Song Z, Zhou X, Han N, Chen Y. Sputtered SnO₂:NiO thin films on self-assembled Au nanoparticle arrays for MEMS compatible NO₂ gas sensors. Sensors and Actuators B: Chemical. 2019;278: 28–38.
- 17. Gatty HK, Stemme G, Roxhed N. A miniaturized amperometric hydrogen sulfide sensor applicable for bad breath monitoring. *Micromachines*. 2018;9(12): 612.
- 18. Bonaccorsi L, Malara A, Donato A, Donato N, Leonardi SG, Neri G. Effects of UV Irradiation on the Sensing Properties of In₂O₃ for CO Detection at Low Temperature. *Micromachines*. 2019;10(5): 338.
- 19. Donato N, Grassini S. Editorial for the Special Issue on Nanostructure Based Sensors for Gas Sensing: from Devices to Systems. Micromachines. 2019;10(9): 591.
- 20. Wang F, Jia J, Zhao W, Zhang L, Ma H, Li N, Chen Y. Preparation and electrochromic properties of NiO and ZnO-doped NiO thin films. Materials Science Semiconductor Processing. 2022;151: 106986.
- 21. Tan S, Gao L, Wang W, Gu X, Hou J, Su G. Preparation and black-white electrochromic performance of the non-contact ZnO@NiO core-shell rod array. Surfaces and Interfaces. 2022;30: 101889.
- 22. Zhang L, Zhao M, Chen Y, Chen H, Wang F, Ma L, Ma H. Effect of sputtering pressure on the electrochromic properties of flexible NiO films prepared by magnetron sputtering. *Materials Letters*. 2024;354: 135317.
- 23. Tuna Ö, Mak AK, Öztürk O, Karabulut M. Influence of oxygen partial pressure on the structural, optical and electrochromic properties of NiO thin films grown by magnetron sputtering. *Applied Physics A.* 2023;129(12): 820.
- 24. Choi D, Son M, Im T, Ahn SH, Lee CS. Microstructure control of NiO-based ion storage layer with various sized NiO particles to evaluate the electrochromic performance. *Materials Chemistry and Physics*. 2020;249; 123121.
- 25. Li Z, Yu Z, Wang W, Hou J, Gao L, Gu X, Su G. Nickel oxide film with tertiary hierarchical porous structure and high electrochromic performance and stability. Materials Chemistry Physics. 2021;269: 124738.
- 26. Ivanova T, Harizanova A, Koutzarova T, Vertruyen B. Preparation and Investigation of Sol Gel TiO₂-NiO Films: Structural, Optical and Electrochromic Properties. Crystals. 2024;14(2): 192.
- 27. Goel R, Jha R, Ravikant C. Nickel oxide (NiO) nano-triangles with enhanced electrochromic and photovoltaics properties. Chemical Papers. 2023;77(5): 2885-2903.
- 28. Wruck DA, Rubin M. Structure and Electronic Properties of Electrochromic NiO Films. Journal of the Electrochemical Society. 1993;140: 1097.
- 29. Jia J, Chen Y, Zhang W, Wang Z, Wang F, Zhang L, Ma H. Experimental study and simulation of electrochromic properties of TiO₂-doped NiO films. Ceramics International. 2024;50(9): 15065-15075.
- 30. Niu G, Zhuang Y, Hu Y, Liu Z, Wang F. Selective Discrimination of Ppb-level Vocs Using Mos Gas Sensor in Pulse-Heating Mode with the Modified Hill's Model. In: Proceedings of the IEEE International Conference on Micro Electro Mechanical Systems (MEMS). Institute of Electrical and Electronics Engineers Inc.; 2023: 826–829.

About the Authors

Ivan M. Komarevtsev D Sc

Researcher (Alferov University, St. Petersburg, Russia)

Anastasia S. Kondrateva 🔟 Sc

Candidate of Chemical Sciences Associate Professor (Alferov University, St. Petersburg, Russia)

Alexei N. Kazakin 🗓 Sc

Engineer (Alferov University, St. Petersburg, Russia)

Yakov B. Enns D Sc

Researcher (Alferov University, St. Petersburg, Russia)

Ilya A. Lazdin 🗓 Sc

Engineer (Peter the Great St. Petersburg Polytechnic University, St. Petersburg, Russia)

Platon A. Karaseov D Sc

Doctor of Physical and Mathematical Sciences Professor (Peter the Great St. Petersburg Polytechnic University, St. Petersburg, Russia)

Yurie D. Akulshin D Sc

Lead Engineer (Peter the Great St. Petersburg Polytechnic University, St. Petersburg, Russia)

Submitted: August 23, 2023 Revised: May 28, 2024 Accepted: July 22, 2024

First-principles investigations of physical properties of Nd doped FeSi compound

A. Kumar ^{1\infty}, ¹⁰ R. Kumar ², R. Kumar ³, A. Kumar ⁴¹⁰, V. K. Nautiyal⁵, N. Iram ⁶

- ¹ Swami Vivekanand Subharti University, Meerut, Uttar Pradesh, India
- ² Subharti Polytechnic College, Swami Vivekanand Subharti University, Meerut, Uttar Pradesh, India
- ³ K.V. Subharti College of Science, Swami Vivekanand Subharti University, Meerut, India
- ⁴ Mahamaya Government Degree College, Sherkot, Bijnore, India
- ⁵ Chaudhary Charan Singh University, Meerut, Uttar Pradesh, India
- ⁶ Bahauddin Zakariya University, Multan, Pakistan
- [™] 01amankumar@gmail.com

ABSTRACT

The structural, electronic, magnetic and thermodynamics properties of the NdFeSi intermetallic compound are studied using the full potential linearized augmented plane wave plus local orbital method, which is based on the theoretical framework of the density functional theory. We calculated the structural properties, in terms of the lattice constant, bulk modulus, first derivative of bulk modulus, and minimum volume. We calculated the electronic properties by considering the band structure, as well as the total and partial density of states. Electronic properties are confirmation that the NdFeSi intermetallic compound exhibits a metallic nature due to Nd-f state. The magnetic properties correlate with the magnetic moment. We determined that this compound's magnetic moment is 7.02610 μ B. We investigated thermal behavior in terms of the Grüneisen parameter γ , the bulk modulus β_0 , the Debye temperature θ_D , and the entropy S with different temperatures and pressure ranges. All these results indicate that the NdFeSi compound is used in spintronic applications.

KEYWORDS

DFT • electronic properties • density of state • rare earth element

Citation: Kumar A, Kumar R, Kumar A, Nautiyal V.K., Iram N., First-principles investigations of physical properties of Nd doped FeSi compound. *Materials Physics and Mechanics*. 2024;52(4): 23–32. http://dx.doi.org/10.18149/MPM.5242024_3

Introduction

Researchers have been exploring the unique and exciting properties of rare-earth intermetallic compounds, which include a high melting point, good temperature ductility, high strength, hardness, low specific weight, corrosion resistance, various temperature mechanical properties, and the use of electronic and magnetic properties [1]. Compounds such as the RETX eSolid-state physics contains compounds such as the RETX equalatomic ratio stoichiometry arrangement and approximately 2,000 combinations [2], types of crystal structures in crystallography [3]. Researcher-led exploration exercises and further development in this field are ongoing. This has improved human society. The study of RETX-type materials has explored electronic, magnetic, and thermodynamic behavior, and these materials show different kinds of industrial applications. It has much potential in multiple sectors, such as aviation, automobiles, spintronics, electrical, and

electronics industries [4,5]. Rare-earth intermetallic compounds have a magnetic nature because they contain incompletely filled 4-f electron orbitals. When the temperature rises above room temperature, they show a ferromagnetic core with high spin polarization [5]. Previous publications demonstrated that the magnetic nature of NdFeSi, GdFeSi, TbFeSi, and LaFeSi materials, as well as REFeSi (RE=Nd, Gd, and Tb), exhibits a ferromagnetic nature at Curie temperature T_c = 25 K for NdFeSi, 135 K for GdFeSi, and 125 K for TbFeSi, while LaFeSi exhibits a paramagnet nature [6]. All elements of the lanthanide's series have paired and unpaired electrons in their inner 4-f orbits. There are 4-f uncompleted subshells in the electronic configuration of Nd ([Xe] $4f^4$ $6s^2$) due to the uncompleted 4-f electron orbitals. RETX rare-earth intermetallic compounds show a magnetic nature due to the uncompleted 4-f electron orbital's

In this research paper, we have examined the electronic, magnetic, and thermal behaviours of the NdFeSi compound using the density functional theory (DFT), which relies on fundamental concepts such as the Kohn-Sham (KS) equation and the self-consistent field (SCF) [7,8]. We conducted structural, electronic, and magnetic calculations using the WIEN-2K software [9], and we also utilized this software to investigate the thermal behaviour. However, this was only feasible when we interfaced WIEN-2K with GIBBS2 software. GIBSS2 software is based on the Debye model [10]. The NdFeSi compound has a CeFeSi-type tetragonal crystal structure, and the space group is p4/nmm [11,12]. We looked at the crystal structure, energy E - volume V curves, bulk modulus B_0 , and a derivative of bulk modulus B_0 . We studied the electronic behaviour using band diagrams and the total and partial density of state (TDOS and PDOS, respectively). We also looked at the thermal behaviour using the Gruneisen parameter γ , the bulk modulus B_0 , the Debye temperature (θ_0), and the entropy (S). We studied this over a wide range of temperatures and pressures.

Method of calculations

In this paper, a computational approach was used. We studied the NdFeSi material's electronic, magnetic, and thermodynamic properties using the FPLAPW+LO method and the general gradient approximation (GGA) based on DFT [13-15]. We used the Birch-Murnaghan equation (EOS) to find the structural properties of the NdFeSi material [16]. We selected a cutoff energy of 6.0 Ry and three k-mess points under the high-symmetry Brillouin zone for the SCF calculation. ne. In this process, we choose a charge of approximately 0.0001 ec for crystal convergence. The muffin tin sphere radius (RMT) is the small atomic electron cloud sphere radius in a unit cell. RMT plays an important role in the calculation of physical properties. If we need more plane waves, then we require a large RMT. Many plane waves contribute significantly to the calculation's accuracy. However, if we heavily rely on RMT, the surface charge will leak. Given that no center charge should be present, its value must be minimal. Its value should be meager, as there is no core charge leaking from its surface. If the charge leaks, the RMT's value fluctuates, either increasing or decreasing. This on the core surface, there is no charge leakage. We keep the RMT value low to allow for the retention of more plane waves. In our calculation, we have taken RMT 2.50 a.u. for Nd and 2.00 a.u. for Fe and Si. For our SCF calculations, we have chosen lattice parameters $a_0 = b_0 = 4.031$ Å and $c_0 = 6.828$ Å for NdFeSi (CeFeSi type tetragonal crystal structure) shown in Table 1. We found the Fermi energies to be 0.64630 electron volts (Table 2). We investigated the magnetic properties of the material using GGA and DFT. We used GIBBS2 software for the material's thermal behaviour. It's based on the Debye model.

Table 1. Crystallography data of NdFeSi compound such as space group, lattice parameter and atomic position

Compound	Space group	Lattice parameter, Å	Nd	Fe	Si
NdFeSi	p4/nmm (129)	$a_0=b_0=4.031$ $c_0=6.828$	(0.25, 0.25, 0.67)	(0.75, 0.25, 0)	(0.25, 0.25, 0.20)

Table 2. Lattice parameters (a_0, c_0) , bulk modulus B_0 , the derivative of bulk modulus B'_0 , minimum energy E_{\min} , the volume of unit cell V_0 , and the Fermi energy E_F at 0 K for NdFeSi compound

S.N.	Parameter	Symbols	Value	Experimental data
1 Lattice parameters, Å		$a_0 = b_0$	4.069	4.031 [18]
		<i>C</i> ₀	6.918	6.828 [18]
2	The bulk modulus of material, GPa	B_0	103.7584	
3	derivative of bulk modulus of material, GPa	B_0'	4.3393	
4	The energy at equilibrium condition, Ryd	E_{min}	-44771.811751	
5	Unit cell volume at equilibrium condition, a.u. ³	V_0	749.9931	
6	Fermi energy, eV	E_{F}	0.64630	

Results and Discussion

Structural properties

VESTA software was used to generate the unit cell structure (Fig. 1) of the NdFeSi material [17]. The NdFeSi compound shows a CeFeSi-type tetragonal crystal structure. Birch-Murnaghan equations (EOS) have helped determine structural properties in terms of E-V curve, B_0 , and B_0 . Table 2 displays the determined values of the structural parameter for the NdFeSi compound. The determined estimations of the lattice constant show remarkable concurrence with experimental values [18–26]. B_0 is an essential parameter

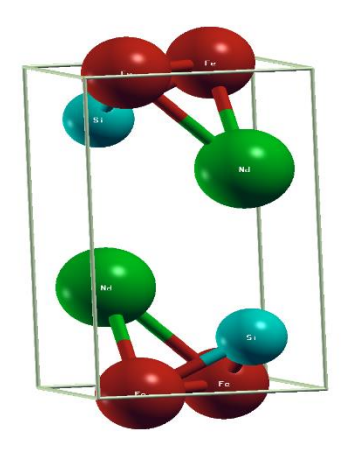


Fig. 1. Unit cell crystal structure of NdFeSi compound used VESTA software

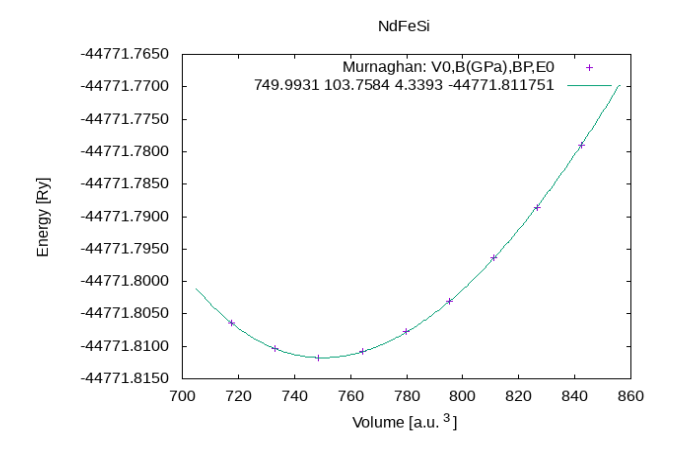


Fig. 2. Variation of total energy with unit cell volume of NdFeSi compound

of materials in material science and a measure of the material's resistance to compression. The degree of resistance value also increases when B_0 is increased, as shown in Table 2. The literature does not contain any experimental B_0 values. As a result, our measured results are considered predicted; we can use them in future research work. The material's E-V curve, as depicted in Fig. 2, provides information about the structural stability curves. Such curves offer NdFeSi compound stability.

Electronic and magnetic properties

Now we are discussing the electronic properties of the NdFeSi compound in terms of band structure, TDOS, and PDOS. We have determined the electronic band diagrams of the NdFesi compound along with spin up and spin down the channel in high symmetry Brillouin zone direction using GGA approximation. In the electronic band diagrams, Fig. 3(a,b) for the NdFeSi compound displays the Fermi level at the origin. In-band graphs, most of the bands lie from -9.5 to 0 eV for the spin-up channel below the Fermi level shown in Fig. 3(a). Similarly, most of the bands lie from -9.0 to 0 eV for the spin-down channel below the Fermi level shown in Fig. 3(b). From Fig. 3(a,b) in the band diagram, we see that the valance and conduction bands overlap among themselves. Therefore, the NdFeSi compound exhibits a metallic character. This result primarily accounts for the unfailing of the Nd-4f ([Xe] 4f46s2) electronic shell. The result is clear, our combination has a metallic nature. We are discussing TDOS and PDOS of the NdFeSi compound shown in Fig. 4. In Fig. 4(a), we can see there are three sharp peaks in the valence and conduction bands.

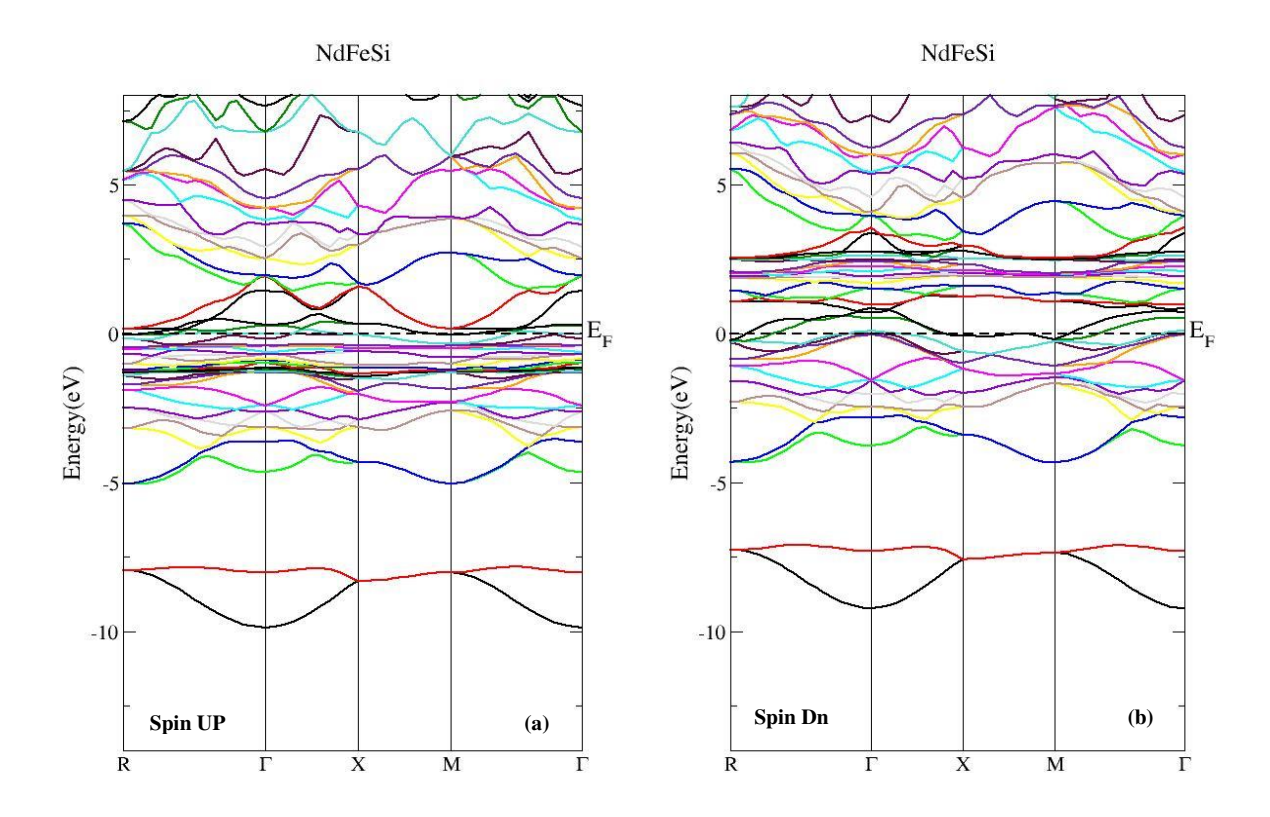


Fig. 3. Electronic band structures of (a) NdFeSi for spin up and (b) NdFeSi for spin down (Dn) using GGA approach

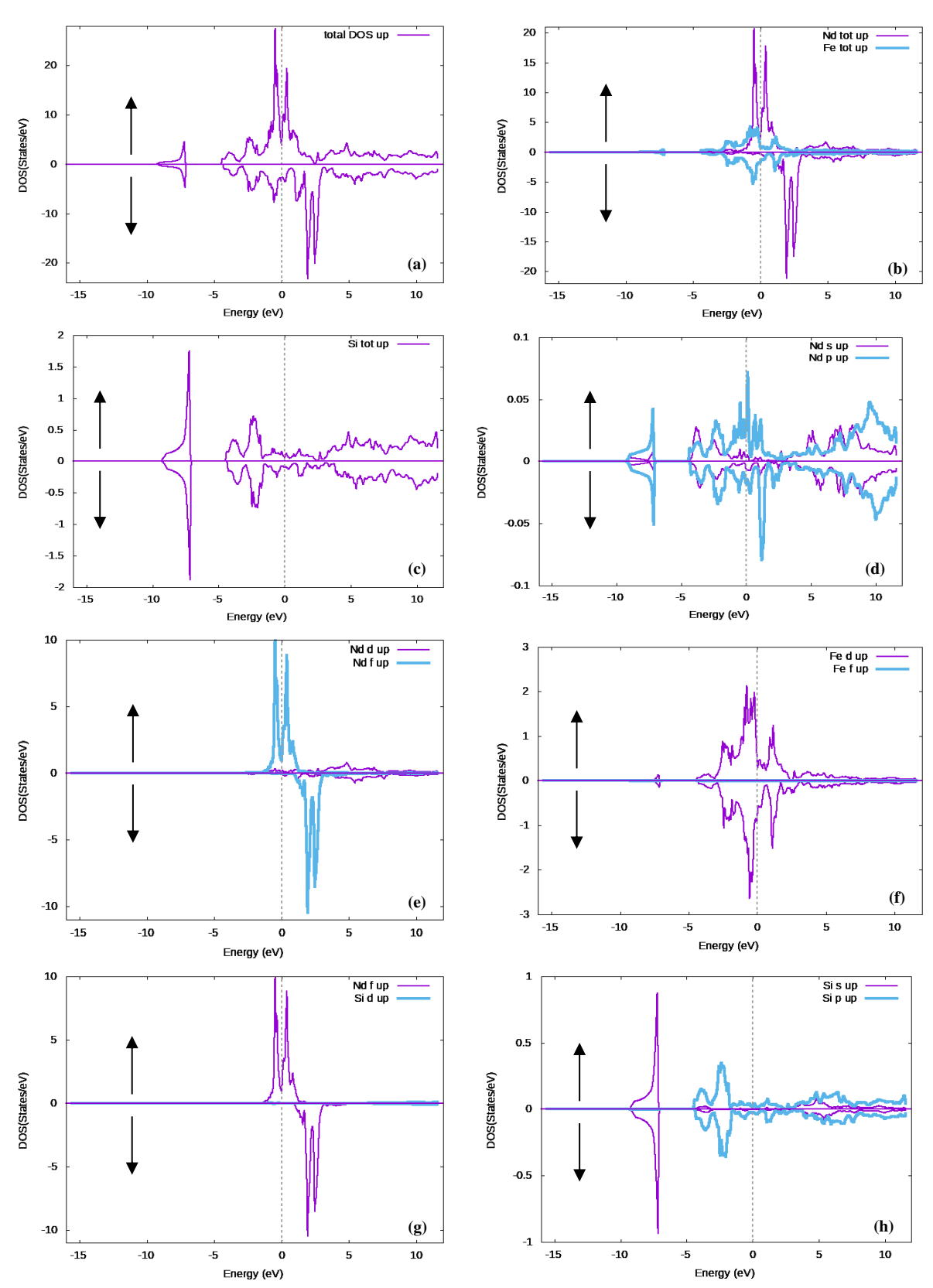


Fig. 4. Density of states(DOS) along with spin up and spin down of (a) NdFeSi-total DOS, (b) Nd-total DOS and Fe- total DOS, (c) Si-total DOS, (d) Nd-s partial DOS, and Nd-p partial DOS, (e) Nd-d partial DOS and Nd-f partial DOS, (f) Fe-d partial DOS and Fe-f partial DOS, (g) Nd-f partial DOS and Si-d partial DOS, (h) Si-s partial DOS and Si-p partial DOS

The first peaks in the valance band correspond approximately to -7.1 eV for the spin-down channel below the Fermi levels, and another two peaks correspond approximately to -7.1 and -0.62 eV for the spin-up channel below the Fermi level. Similarly, in the conduction band, the first peaks approximately belong to 0.63 eV for the spin-up channel above the Fermi level, and another two peaks approximately belong to 1.87 and 2.5 eV for the spin-down channel above the Fermi level.

The sharp peak between -0.62 and 0.63 eV is responsible for the Nd-f electronic shell (Fig. 4(e)), with a minor role for the Fe-d electronic shell (Fig. 4(f)). The sharp peak of -7.1 eV is responsible for the Si-S electronic shell (Fig. 4(h)), with a minor role for the Nd-p electronic shell (Fig. 4(d)). The sharp peaks of ~ 1.87 and ~ 2.5 eV is responsible for the Nd-f electronic shell (Fig. 4(e)). They can observe the different curves of TDOS and PDOS due to the electronic Nd-4f shell for the NdFeSi compound. $E_{\rm F}$ is shown in Table 1. The TDOS and PDOS for the NdFeSi component demonstrate their metallic nature. Table 3 displays the calculated magnetic moments of the NdFeSi compound, as well as the magnetic moments of the interstitial region and individual atoms (Fe, Si). The individual moment of Nd3+ dominates the total magnetic moment of the NdFeSi compound. The Nd-4f electronic shell is responsible for the magnetic moment.

Table 3. Magnetic properties (µ_B) in of NdFeSi compound

	Spin magnetic moments $\mu_{ extsf{B}}$
Interstitial region of magnetic moment	1.23229
Magnetic moment of Nd	3.40766
Magnetic moment of Fe	-0.51018
Magnetic moment of Si	-0.00057
Total Magnetic moment of NdFeSi	7.02610

Thermodynamic behavior

We are discussing thermal behaviour at a wide temperature and pressure, which gives us valuable information about the material. We determined the thermal behaviour by combining the GIBBS2 software with the WIEN2k software, which uses the Debye model. When the atoms of a crystal vibrate, it changes some of its thermodynamic properties inside the crystal, which also changes some of the thermodynamic parameters of the materials that we have observed. We looked at how heat behaves in terms of the Grüneisen parameter (ν), the bulk modulus (B_0), the Debye temperature (θ_0), and the entropy (S) at a range of temperatures and pressures. We used wide temperature (0-300 K) and pressure ranges (0-50 GPa) in the present research work to calculate all thermal parameters for NdFeSi. In a thermal system, entropy (S) is defined as energy and matter dispersal. This is also defined as the calculation of disorder for a system on a microscopic level. It is based on the compound NdFeSi temperature- and pressuredependent parameters, as shown in Figs. 5(a) and 5(e), respectively. In Fig. 5(a), the vibration energy decreases as the temperature increases, causing the value of S to also decrease. The entropy (S) is mainly responsible for the vibrations in the atoms, resulting in the internal energy of the atomic orbital also increasing. Figure 5(e) illustrates the influence of pressure on entropy (S). When pressure rises, the material's entropy (S)

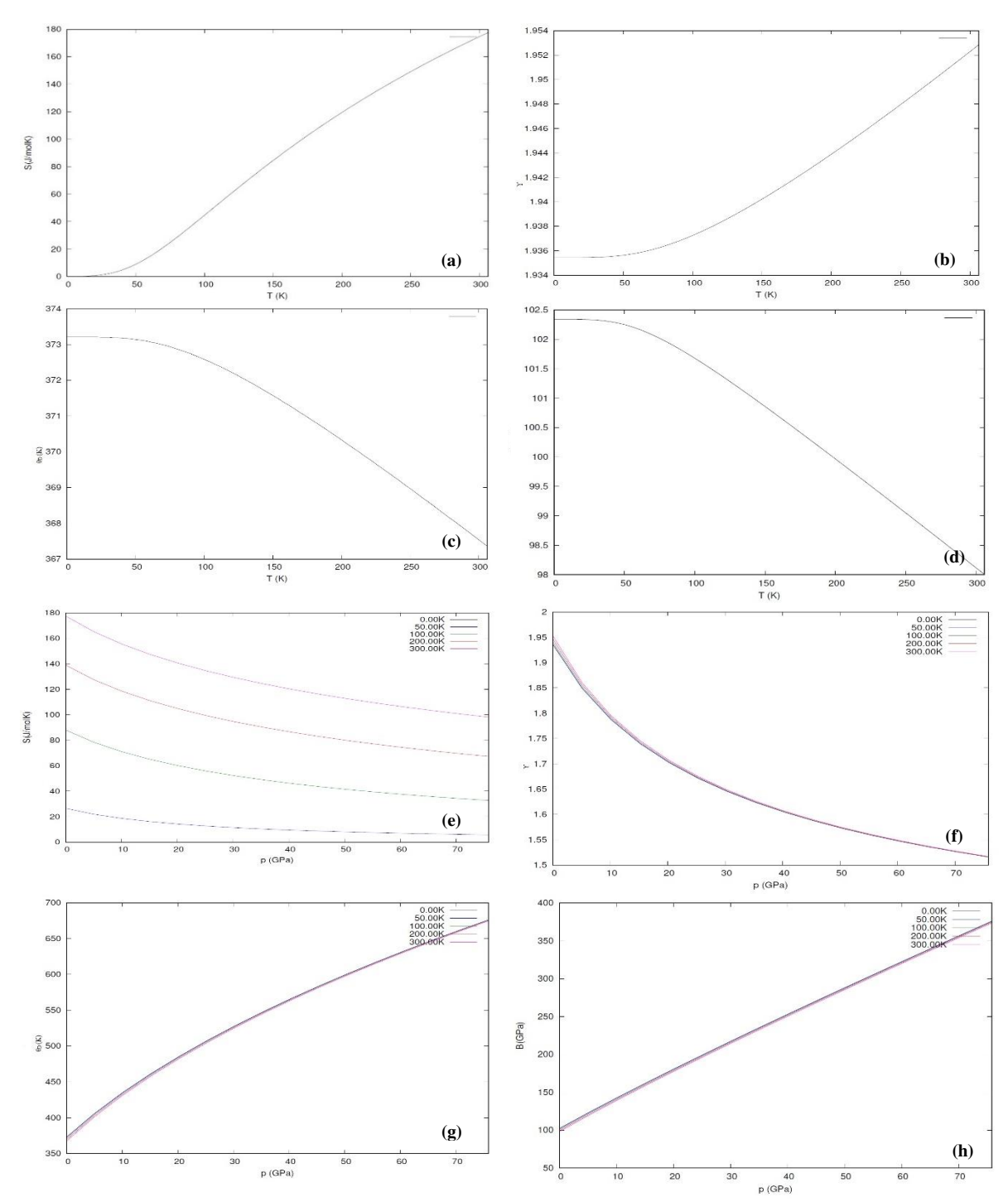


Fig. 5. (a) Variation in temperature Vs entropy S, (b) variation in temperature Vs the Grüneisen parameter γ , (c) variation in temperature Vs the Debye temperature θ_D , (d) variation in temperature Vs the bulk modulus B, and (e) variation in pressure Vs entropy S, (f) variation in pressure Vs the Grüneisen parameter γ , (g) variation in pressure Vs the Debye temperature θ_D , (h) variation in pressure Vs the bulk modulus B, for NdFeSi

decreases at a slow rate. Therefore, the volume of the unit cell decreases, and the internal energy of the material increases, resulting in reduced entropy (S). The effect of different temperatures on the Grüneisen parameter (γ) is shown in Fig. 5(b). The Grüneisen parameter is a function of the crystal lattice; it's defined as anharmonicity. Figure 5(b) indicates that the value of γ was found to be nonzero at T=0 K, but when the temperature increases, the value of γ also increases. This shows that the anharmonicity of crystal lattices rises with

temperature. Figure 5(f) illustrates the effect of different pressures on y. It has been found to decrease the value of y when pressure is increased. As you can see in Fig. 5(c,q), the NdFeSi changes its Debye temperature (θ_D) at different temperature ranges (0-300 K) and pressure ranges (0–50 GPa). At T = 0 K, the value of θ_D is found at ~ 366.25 K. It is seen in Fig. 5. Figure 5(c) demonstrates that an increase in temperature leads to a decrease in the value. We are discussing thermal behaviour at a wide temperature and pressure, which gives us valuable information about the material. We determined the thermal behaviour by combining the GIBBS2 software with the WIEN2k software, which uses the Debye model. When the atoms of a crystal vibrate, it changes some of its thermodynamic properties inside the crystal, which also changes some of the thermodynamic parameters of the materials that we have observed. We looked at how heat behaves in terms of the Grüneisen parameter (y), the bulk modulus (B_0), the Debye temperature (θ_D), and the entropy (S) at a range of temperatures and pressures. We have used wide temperature ranges (0-300 K) and pressure ranges (0-50 GPa) in our present research work to calculate all thermal parameters for NdFeSi. In a thermal system, entropy (S) is defined as energy and matter dispersal. This is also defined as the calculation of disorder for a system on a microscopic level. It is based on the compound NdFeSi's temperature- and pressure-dependent parameters, as shown in Fig. 5(a,e). In Fig. 5(a), the vibration energy decreases as the temperature increases, causing the value of S to also decrease. The entropy (S) is mainly responsible for the vibrations in the atoms, resulting in the internal energy of the atomic orbital also increasing. Figure 5(e) illustrates the influence of pressure on entropy (S). When pressure rises, the material's entropy (S) decreases at a slow rate. Therefore, the volume of the unit cell decreases, and the internal energy of the material increases, resulting in reduced entropy (S). The effect of different temperatures on the Grüneisen parameter (γ) is shown in Fig. 5(b). γ is a function of the crystal lattice; it's defined as anharmonicity. Figure 5(b) indicates that the value of y was found to be nonzero at T = 0 K, but when the temperature increases, the value of γ also increases. This shows that the anharmonicity of crystal lattices rises with temperature. Figure 5(f) illustrates the effect of different pressures on y. It has been found to decrease the value of y when pressure is increased. As you can see in Fig. 5(c,g), the NdFeSi compound changes its Debye temperature (θ_D) at different temperature ranges (0–300 K) and pressure ranges (0–50 GPa). At T = 0 K, the value of θ_D is found at ~ 366.25 K. It is seen in Fig. 5. Figure 5(c) illustrates that an increase in temperature results in a decrease in the value of θ_D decreases to ~ 50 K, and then the value of θ_D gradually decreases with the increase in temperature. However, when T exceeds 50 K, the temperature rapidly decreases the value of θ_D . The temperature decreases to approximately 50 K, after which the value of θ_D gradually decreases with an increase in temperature. However, when T exceeds 50 K, the temperature rapidly decreases the value of θ_D .

Figure 5(g) illustrates the pressure's impact on the θ_D . In Table 3, we find the value of θ_D at 366 to 368 K at P=0 with various temperature ranges (0–300 K). As a result, the value of θ_D also increases gradually with the increase in pressure. Another part of the NdFeSi compound's thermal behaviour is shown in Fig. 5(d,h), which show the bulk modulus (B_D) at different temperatures (0–300 K) and pressures (0–50 GPa). The value of B_D offers details about the material, how it affects the degree of resistance (DOR) of materials, and how hard or soft the material is. At this point, when the compound

temperature increases, the degree of resistance decreases, and the compound becomes more flexible as the temperature rises. Figure 5(d) illustrates that an increase in temperature leads to a decrease in the value of B_0 for the NdFeSi compound, resulting in a change in its unit cells. At T = 0 K, the value of B_0 is found at ~ 40 GPa, but after T = 40 K, the value of B_0 decreases rapidly for the NdFeSi compound. Analysis of these results reveals that the B_0 changes with temperature, solely due to changes in the crystal's unit cell. Figure 5(h) illustrates the pressure's impact on the B_0 . Table 3 finds the value of B_0 at approximately 96 to 98 GPa at P = 0, across various temperature ranges (0–300 K). As a result, the value of B_0 also increases gradually with the increase in pressure. As a result, the value of B_0 also increases slowly with the increase in pressure. The degree of resistance then rises, and our compound becomes inflexible (hard).

Conclusions

We have calculated the structural, electronic, magnetic, and thermal properties of the NdFeSi compound using the DFT method and the FPAPW+LO technique, with the assistance of WIEN2K software. We have investigated the structural and electronic properties of the NdFeSi material, obtaining information on the lattice constant, bulk modulus, a derivative of bulk modulus, band diagrams, and the total and partial density of states (TDOS and PDOS), respectively. In terms of electronic properties, our compound has a metallic nature because of the Nd-4f electronic shell. Similarly, the magnetic behaviour of the NdFeSi compound shows that the magnetic personality due to the Nd-4f electronic shell is responsible for its magnetic nature. A lot of different temperatures and pressures (0-50 GPa) were used to study the thermal behaviour of different materials. The Grüneisen parameter (y), the bulk modulus (B_0) , the Debye temperature (θ_0) , and the entropy (S) were investigated. We have discussed the bulk modulus (B_0). As a result, when the temperature of the material increases, the material's softness also increases, but when the pressure of the material increases, the material's hardness also increases. In the case of Debye temperature (θ_D), pressure is more effective than temperature. As a result, the material's energy density increases, consuming a large amount of energy within a small space, leading to a decrease in the material's entropy (S).

References

- 1. Gschneidner Jr K, Russell A, Pecharsky A, Morris J, Zhang Z, Lograsso T, Hsu D, Lo CHC, Ye Y, Slager A, Kesse D. A family of ductile intermetallic compounds. *Nature Mater*. 2003;2: 587–591.
- 2. Villars P, Calvert LD. *Pearsons's Handbook of Crystallographic Data for Intermetallic Compounds*. American Society or Metals: 1997. 3. Fornasini ML, Merlo F. Equiatomic temary phases formed by alkaline earths and rare earths. *J. Alloys Compd.* 1995;219(1–2):63–68.
- 4. Wolf SA, Awschalom DD, Buhrman RA, Daughton JM, von Molnár S, Roukes ML, Chtchelkanova AY, Treger DM. Spintronics: a spin-based electronics vision for the future. *Science*. 2001;294(5546): 1488–1495.
- 5. Asadabadi S J, Cottenier S, Akbarzadeh H, Saki R, Rots M. Valency of rare earths in RIn3 and RSn3: Ab initio analysis of electric-field gradients. *Phys. Rev. B.* 2002;66(19): 195103.
- 6. Welter R., Venturini G, Malaman B. Magnetic properties of RFeSi (RLa-Sm, Gd-Dy) from susceptibility measurements and neutron diffraction studies. *Journal of Alloys and Compounds*. 1992;189(1): 49–58.
- 7. Singh DJ, Nordstrom L. Plane Waves Pseudo Potentials and the LAPW Method. New York: Springer; 2006.
- 8. Schwarz K. DFT calculations of solids with LAPW and WIEN2k. J. Solid State Chemistry. 2003;176(2): 319–328.
- 9. Blaha P, Schwarz K, Madsen G K H, Kuasnicka D, Luitz J. *WIEN2k An Augmented Plane Wave-Local Orbitals Program for Calculating Crystal Properties*. Wien, Austria: K. Schwarz Technical Universitat; 2001.

- 10. Otero-De-La-Roza A, Abbasi-Pérez D, Luaña V. GIBBS2: A new version of the quasi-harmonic model code. II. Models for solid-state thermodynamics, features, and implementation. *Computer Physics Communications*. 2011;182(10): 2232–2248.
- 11. Welter R, Venturini G, Malaman B, Ressouche E. Crystallographic data and magnetic properties of new RTX compounds (R≡La-Sm, Gd; T≡Ru, Os; X≡Si, Ge). Magnetic structure of NdRuSi. *Journal of Alloys and Compounds*. 1993;202(1–2): 165–172.
- 12. Guzik A. The magnetic and transport properties of the new GdTiSb compound *J. Alloys Compd.* 2006;423(1–2): 40–42.
- 13. Larabi A, Mebarki M, Abdellaoui I, Mahmoudi A, Merazga S, Gabouze N. Ab initio study of Hydrogen and Lithium behaviors in Cu2O. *Materials Physics and Mechanics*. 2023;51(4): 172–185.
- 14. Blaha P, Schwarg K, Sorantin P, Tricky SB. Full potential, linearized augmented plane wave programs for crystalline systems. *Computer. Phys. Commun.* 1990;59(2): 399–415.
- 15. Perdew JP, Burke K, Ernzerhof M. Generalized Gradient Approximation Made Simple. Phys. Rev. Lett. 1997;77(18): 3865.
- 16. Wedepohl PT. Comparison of a simple two-parameter equation of state with the Murnaghan equation, *Solid State Communications*. 1971;10(10): 947–951.
- 17. Momma K, Izumi F. VESTA 3 for Three-Dimensional Visualization of Crystal, Volumetric and Morphology Data. *Journal of Applied Crystallography*. 2011;44: 1272–1276.
- 18. Welter R, Venturini G, Ressouche E, Malaman B. Magnetic properties of RCoSi (R= La—Sm, Gd, Tb) compounds from susceptibility measurements and neutron diffraction studies. *Journal of Alloys and Compounds*. 1994;210(1–2): 279–286.
- 19. Kumar A, Guatam R, Chand S, Kumar A, Singh RP. First principle electronic, magnetic and thermodynamic characterization of heavy fermion ternary rare earth metal alloys. *Materials Physics and Mechanics*. 2019;42(1):112–130.
- 20. Gautam R, Kumar A, Singh R. First Principal Investigations on Electronic, Magnetic, Thermodynamic, and Transport Properties of TlGdX₂ (X= S, Se, Te). *Acta Physica Polonica A*. 2017;132(4): 1371–1378.
- 21. Gautam R, Kumar A, Kumar A, Singh PK, Singh RP. Magneto-optical effects in half metallic ferromagnets: Rare earth thallium tellurides (TlXTe2; X = Tb-Er). *Optik.* 2020;223: 165317.
- 22. Kumar A, Kumar A, Kumar K, Singh RP, Singh R, Kumar R. The Electronic and Thermodynamic Properties of Ternary Rare Earth Metal Alloys. *East European Journal of Physics*. 2023:1:109–117.
- 23. Kumar A, Gautam R, Singh RP, Kumar A. DFT Investigations of Electronic, magnetic and Thermodynamic properties of ternary rare earth transition metal alloys. *International Journal of Advanced Science and Technology.* 2020;29(08): 1150–1158. 24. Kumar A, Kumar A, Pundir SK, Singh N. First Principal Study for Concentration Profile of Mn Doped ZnSnAs2. *TWIST*. 2024;19(1): 377–381.
- 25. Singh NK, Kumar A, Kiran A. Optical Properties of Indium Chalcogenide In2Se3xTe3(1-X) Vacuum Evaporated Polycrystalline Thin Films. *TWIST*. 2024;19(1): 338–341.
- 26. Kumar A, Kumari K, Sharma SK. Theoretical Study of Structural and Electronic Properties of Rare Earth Transition Metal Gallides. *TWIST*. 2024;19(1): 275–280.

About Authors

Aman Kumar 🔟 🔀

PhD, Assistant Professor (Swami Vivekanand Subharti University, Meerut, Uttar Pradesh, India)

Rahul Kumar

PhD, Assistant Professor (Subharti Polytechnic College, Swami Vivekanand Subharti University, Meerut, Uttar Pradesh, India)

Rajiv Kumar

PhD, Assistant Professor (K.V. Subharti College of Science, Swami Vivekanand Subharti University, Meerut, India)

Anuj Kumar 🔟 Sc

PhD, Assistant Professor (Mahamaya Government Degree College, Sherkot, Bijnore, India)

Vivek Kumar Nautiyal Sc

PhD, Assistant Professor (CCS University Meerut, Uttar Pradesh, India)

Nazia Iram Sc

PhD, Assistant Professor (Bahauddin Zakariya University, Multan, Pakistan)

Submitted: December 1, 2023 Revised: February 28, 2024 Accepted: June 11, 2024

The influence of low frequency electric field on the coalescence of water drops in emulsion shear flow

R.R. Galeev [™], A.I. Mullayanov [®], A.A. Musin, L.A. Kovaleva [®]

Ufa University of Science and Technology, Ufa, Russia

[™] galeevr93@gmail.com

ABSTRACT

Crude oil often mixes with water to form water-in-oil emulsions as a result of factors such as high shear at the production wellhead and surfactants that are naturally present in crude oil. The present study is aimed at determining the conditions leading to electrocoalescence of water droplets in the flow of the emulsion. An important part of this preliminary work concerns the creation of an experimental cell and installation designed to study the massive coalescence of droplets in a shear flow of an emulsion under the action of an applied inhomogeneous alternating electric field. The flow of the emulsion through the cell is created by a syringe pump. We determine the effect of exposure by the volume of the separated phases of the emulsion in the drainage tank. Further research will be related to the study of various emulsions with varying concentration and flow rate and possibly the frequency of the applied field. The research results will be useful for creating devices for electrocoalescence in the flow.

KEYWORDS

electrocoalescence • nonuniform • electric field • ITO glass • photolitography

Acknowledgements. The reported study was funded by the grant of the Russian Science Foundation (project No. 19-11-00298). **Citation:** Galeev RR, Mullayanov AI, Musin AA, Kovaleva LA. The influence of low frequency electric field on the coalescence of water drops in emulsion shear flow. *Materials Physics and Mechanics*. 2024;52(4): 33–40. http://dx.doi.org/10.18149/MPM.5242024_4

Introduction

Refining crude oil often requires the extraction of large amounts of water. Crude oil often mixes with water to form water-in-crude emulsions as a result of factors such as high shear at the production wellhead and surfactants that are naturally present in crude oil [1,2]. These emulsions are undesirable and required emulsification to remove dispersed water and associated inorganic salts in accordance with manufacturing and shipping specifications. In addition, demulsifying these crude oil emulsions reduces corrosion and catalyst poisoning and invariably maximizes the overall profitability of crude oil recovery. Recently, there has been a growing research interest in developing effective solutions to the problems associated with the transportation and processing of crude oil emulsions, as well as restrictions on the discharge of produced water [3,4]. There are various methods for the separation of emulsions [5-7]. Moreover, a more efficient demulsification process can be achieved through the use of synergistic effects by combining one or more of these methods. The undisputed favorite among them is the electric method. This method includes both exposure to direct current, alternating (LF, RF, MW) field [8-10]. Electrical methods can be used at any stage of emulsion separation. However, it is advisable to use these methods immediately before or during centrifugation because it obtains the greatest efficiency. Most of the work is aimed at studying electrocoalescence at low frequencies. In electrocoalescence, an electric field is applied to a dispersion of conductive water droplets in a poorly conductive oil to force the droplets to coalesce in the direction of the field [11]. As a rule, the behavior of coalescence can be described in three stages: the droplets approach each other, the film thinning / drying process, and film rupture, leading to the coalescence of droplets-droplets. However, there are other mechanisms, such as the formation of droplet chains, dipole – dipole coalescence, electrophoresis, dielectrophoresis and random collisions. The type of electric field, such as alternating, direct and pulsed direct current, plays a significant role depending on the design and setup of the system. Other factors, such as the average droplet size and the residence time of the liquid mixture under the influence of the electric field, stand out due to the efficiency of coalescence [12]. One of these is the conductivity of the water phase. Dielectric parameters are important characteristics, which depend both on the content of the dispersed phase and on the parameters of the electromagnetic field [2,13]. Experiments have been reported using silicone oils, vegetable oils and hydrocarbons in a droplet fixer that allows the use of low viscosity oils [14,15]. Another factor is the nature and concentration of surfactants at the drop-oil interface [16,17]. It was found that the time of electrocoalescence decreases with increasing interfacial tension. This study shows that increasing the interfacial tension gradient will shorten the coalescence time, which is important for improving the mixing efficiency of the droplets [18,19]. The influence of oil viscosity and energy consumption on the rate of coalescence was also investigated [20,21]. In this case, the viscosity of the dispersed system depends on both temperature and the content of the dispersed phase [22,23]. Much attention is paid to the numerical modeling of electrocoalescence using molecular dynamics (MD) modeling [24]. The results showed that the merging of droplets depended on the strength of the electric field [25]. The deformation of a water drop in a dielectric oil phase in the presence of external pulsating electric fields is numerically analyzed by the finite element method [26]. Proprietary software Comsol Multiphysics is used for modeling.

Materials and Methods

Emulsion preparation

An emulsion consisting of water microdroplets suspended in tetradecane was chosen as the object of the study (Fig. 1). Deionized water, purified by the Milli-Q Advantage A10 system (EMD Millipore), was emulsified in tetradecane C (Reachim) using a stirrer.

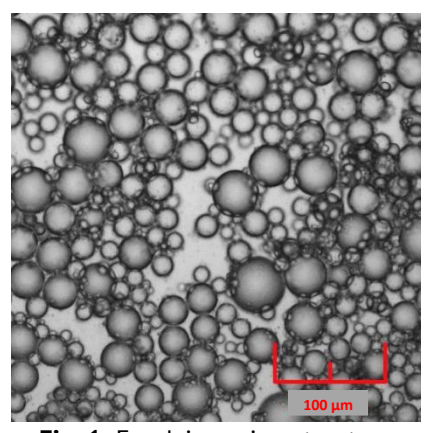


Fig. 1. Emulsion microstructure

To stabilize the emulsion, a nonionic surfactant, sorbitanmonooleate (SPAN 80, Sigma-Aldrich), at a weight concentration of 0.5 % was previously dissolved in tetradecane.

Using digital image processing in the ImageJ program, the diameters and the number of droplets were obtained and a graph of the probability density of the droplet size distribution was plotted. The data were fitted with a log normal distribution, from which an average droplet size of 9 μ m was determined.

Experimental setup

For the research, a laboratory setup (Fig. 2) was assembled based on an Olympus IX71 optical microscope, with an integrated high-speed camera Photron FASTCAM SA5. The experimental cell is installed on the table of an optical microscope. An Agilent 33522A signal generator is used to generate an electric field in the cell, followed by amplification through a Tabor Electronics 9100 high-voltage low-frequency amplifier.

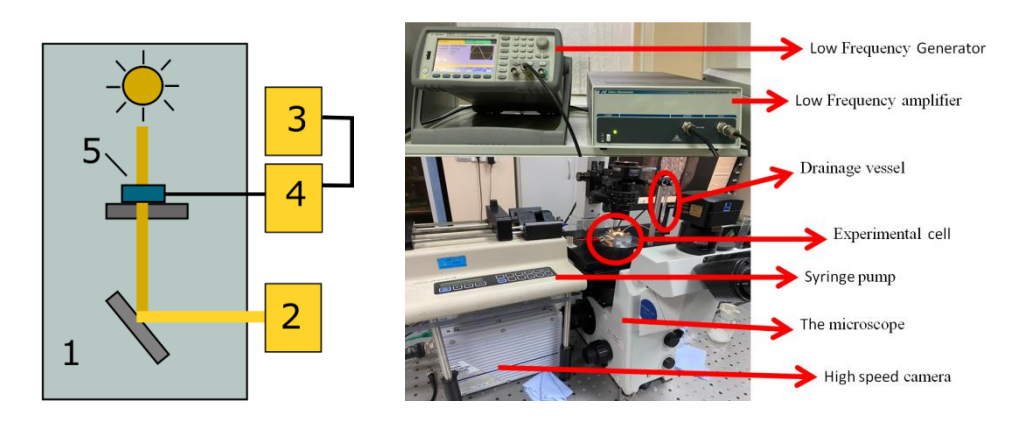


Fig. 2. Laboratory setup diagram: 1 - microscope; 2 - camera; 3 - signal generator; 4 - amplifier; 5 - experimental cell

The cell for electrocoalescence was placed on the stage of an optical microscope. The cell is a sandwich of two glasses between which a Teflon gasket 100 μ m thick was installed in which a channel was cut. Glass with an electrically conductive layer of indium tin oxide ITO (Indium TinOxide) was used as the lower substrate, on the surface of which sawtooth electrodes with a distance of 200 μ m between the tops were etched by the photolithography method. An alternating bipolar voltage was applied to the electrode system from a 33522A arbitrary waveform generator (Agilent Technologies), amplified with a Tabor 9100 amplifier (Tabor Electronics Ltd.).

Experimental cell

The main part of the laboratory setup is an experimental cell, which is a sandwich of two glasses with a Teflon gasket 100 μ m thick between them. A channel 1 mm wide and 10 mm long is cut into the Teflon gasket. Holes were made on the upper substrate for the movement of the liquid under study. Electrically conductive glass with an indium-tin oxide layer (ITO glass) was used as the lower substrate, on the surface of which a sawtooth microelectrode system was etched using the photolithography technique. For this, a negative photoresist (Allresist AR-N 4400-50) was applied to the glass using a

centrifuge for smooth distribution of the substance (Spin 150) at 1000 rpm for 120 sec. After that, the photoresist layer was dried in an oven (WiseStir MSH - 20D) at 90 °C for 90 min under a laminar flow cabinet. Next, the stage of exposure under ultraviolet light was performed through a film mask, which was made by the method of photo output. Thereafter, the glass substrate was heated in an oven at 100 °C for 10 min to re-cure. After the steps described above, the non-exposed areas of the photoresist were washed off. The next stage of manufacturing involves etching an electrically conductive layer not protected by a photoresist; for this, a 10 % aqueous solution of hydrochloric acid was prepared, where a glass substrate with a previously applied thin layer of zinc was placed. Then, after etching the electrically conductive layer, the areas of the exposed photoresist were removed using methylpyrrolidone. After that, the required configuration of microelectrodes was obtained on the glass surface. To protect the electrodes, a protective layer of electrically insulating acrylic varnish (PLASTIK-71) was applied to the glass surface. To connect the microelectrodes to the amplifier output, a place was left, and then elastic conductive tape was glued. After that, the cell was assembled by gluing the glasses together using epoxy glue.

The measuring cell is a flat channel of rectangular cross-section without geometric features (Fig. 3). Electrodynamically, the complexity of the design is due to the presence of specially shaped electrodes on the inner wall of the channel. The electrodes are located in a local area at the entrance to the channel to monitor electrocoalescence. When the emulsion flows through the channel, firstly it enters the area of action of the electric field, then continues to flow through the channel without features.

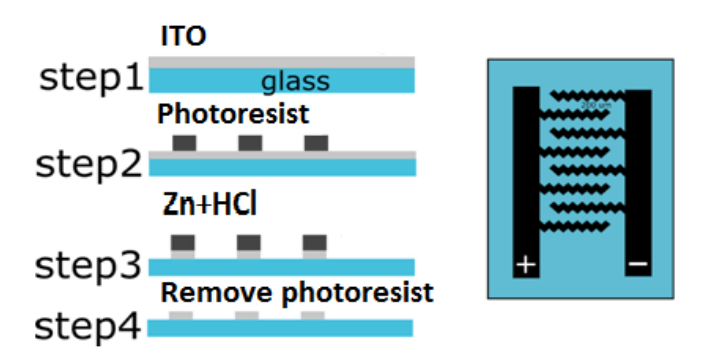


Fig. 3. Schematic of manufacturing the lower substrate of the experimental cell (left) and a system of electrodes with an interelectrode distance of 200 µm (right)

Results

The emulsion (1 ml) was pumped through the cell, where it was exposed to an inhomogeneous alternating electric field with a frequency of 500 kHz and a voltage of 300 V for all tests. At the exit, as mentioned earlier, the emulsion was collected in a tared drainage container. After passing the emulsion through the cell, we obtained separate phases of water and oil. Photographs of this process at various volumetric flow rates (1, 8 and 16 ml / h), which correspond to speeds 10, 80, 160 μ m/s obtained with a high-speed camera are shown in Figs. 4–6. The survey was carried out in the area where the

electrodes were applied. The vertical line shown in Figs. 4-6 indicates the boundary of areas with electrodes (left part) and without electrodes (right part).

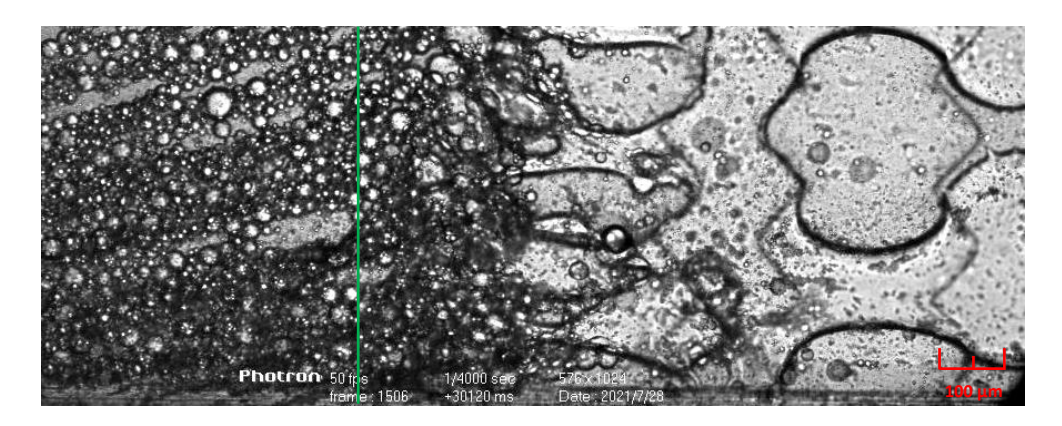


Fig. 4. The effect of an electric field on a water-in-oil emulsion at a volumetric flow rate of 1 ml/h (speed 10 μ m/s). There are no electrodes to the left of the green dividing line, and an area with electrodes to the right

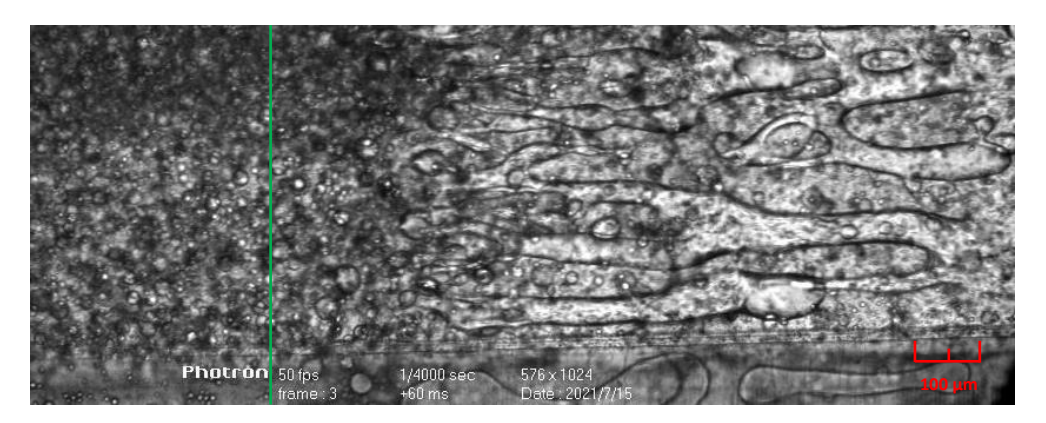


Fig. 5. The effect of an electric field on a water-in-oil emulsion at a volumetric flow rate of 8 ml/h (speed 80 μ m/s). There are no electrodes to the left of the green dividing line, and an area with electrodes to the right

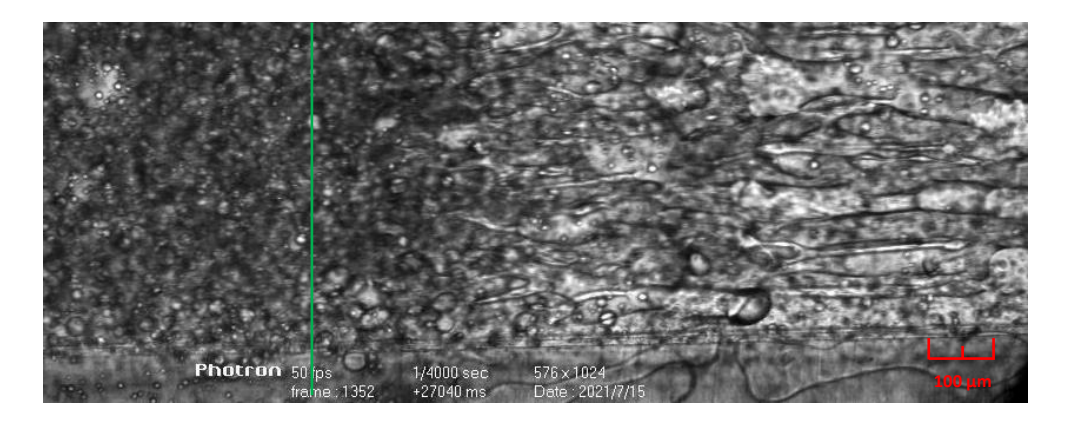


Fig. 6. The effect of an electric field on a water-in-oil emulsion at a volumetric flow rate of 16 ml/h (speed 160 μ m/s). There are no electrodes to the left of the green dividing line, and an area with electrodes to the right

As you can see in Fig. 4. the emulsion moves from left to right, and upon reaching the electrode zone, water droplets begin to coalesce, falling out into the free phase. In the case of a flow rate of 2 ml/h, small droplets are combined into large droplets of the order of $200-300 \, \mu m$.

Increasing the flow rate up to 8 and 16 ml/h (Figs. 5 and 6), the process is identical, but the coalescence of drops is worse due to the high speed of the drops, and in the electrode region, large drops are strongly deformed, and these drops are pulled out and broken into secondary drops. This is the reason for the low rate of separated water at a flow of 16 ml/h.

Based on the test results, the dependence of the separated water on the volumetric flow rate of the emulsion liquid through the cell was built. After passing through the cell, the liquid was drained into the drainage chamber and settled for 24 hours. The dependence is built on the basis of assessing the levels of liquids in the drainage chambers after settling during the day.

Figure 7 shows the dependence of the water separation on the liquid flow rate through the cell. At a volume flow of 1 ml/h, 30 % of water was separated, at 2 ml/h - 25 %, at 4 ml/h - 18 %, at 8 ml/h - 8 % and at 16 ml/h - less than 3 %. With an increase in the volumetric flow rate of the liquid, the drops do not have time to fully combine with each other, as in the case of 1 ml/h.

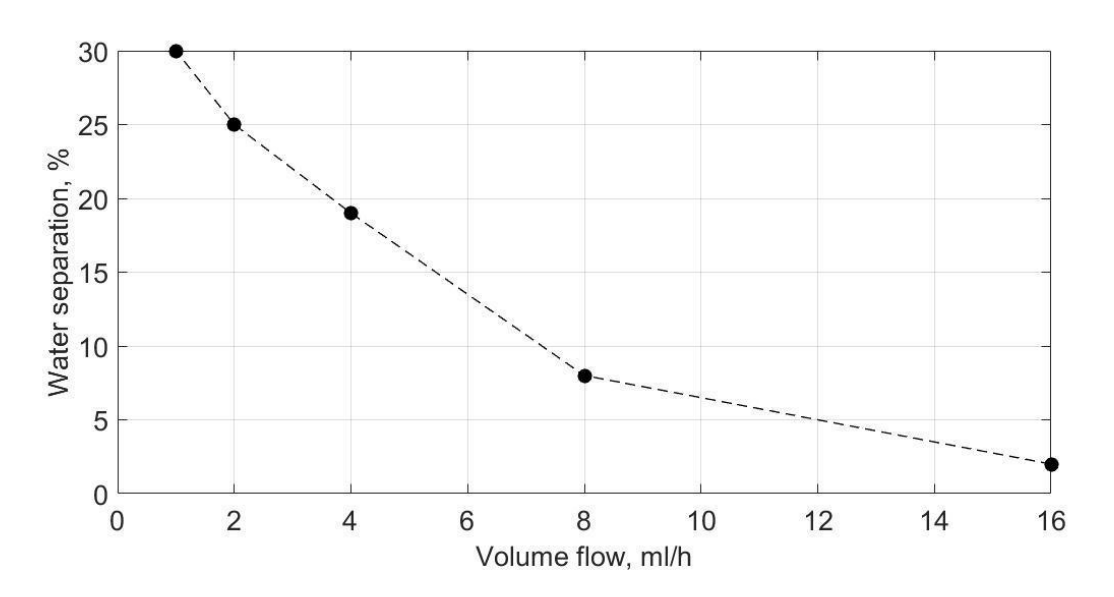


Fig. 7. Water separation from the emulsion vs volumetric flow rate

Conclusions

Based on the experiments results, we can say that this method of emulsion separation is applicable. The electric field acts on the water droplets, which leads to their coalescence in the interelectrode space. Water droplets, passing through the cell, combine and thereby increase in size, which leads to the separation of the emulsion into its constituent phases. The difference in the amount of water remaining is that as the volumetric flow rate increases, the flow rate increases, which leads to high shear flow. In this case, the drops are strongly deformed, and the connection may not occur. The formation of secondary

droplets was also observed due to the strong deformation of large droplets, which consisted in stretching along the flow and disintegrating into several small droplets. We assume that this method is appropriate because it does not require a lot of time, the use of special chemical demulsifiers, and at the exit from the cell, you can immediately get separate phases from each other. The use of this method in combination with centrifugation and the use of chemicals will increase the efficiency of emulsion separation by more than 90 %. However, the value of the indicator will greatly depend on the composition of the original emulsion and requires research in each specific case. Unfortunately, in the experiment, the concentration of emulsion droplets was not controlled, this imposes restrictions on the study of a couple of droplets or single droplets, even though we present photographs of the exposure process obtained using a microscope.

References

- 1. Goodarzi F, Zendehboudi S. A comprehensive review on emulsions and emulsion stability in chemical and energy industries. *The Canadian Journal of Chemical Engineering*. 2019;97(1): 281-309.
- 2. Zinnatullin RR, Kovaleva LA. Research of dielectric properties of oil dispersed systems depending on the ratio of asphalt-resinous substances. *Technical Physics Letters*. 2022;48(2): 77-79.
- 3. Myshov AN. Emulsions: Problems related to the destruction of emulsions in oil treatment systems. *Bulletin of science*. 2023;3(2): 206-209. (In Russian)
- 4. Kozhevnikov IO, Lipchanin DS, Popov YuYu, Meleshko MS. A new way of organizing cluster discharge and disposal of reservoir water. *Oil Gas Innovations*. 2018;9: 70-73. (In Russian)
- 5. Saad MA, Kamil M, Abdurahman NH, Yunus RM, Awad OI. An overview of recent advances in state-of-the-art techniques in the demulsification of crude oil emulsions. *Processes*. 2019;7(7): 470.
- 6. Guan Y, Cheng F, Pan Z. Superwetting polymeric three dimensional (3d) porous materials for oil/water separation: A review. *Polymers*. 2019;11(5): 806.
- 7. Eremeev AM, Elpidinsky AA. On the application of the magnetic field in the processes of destruction of oil-water emulsions. *Bulletin of the Kazan technological University*. 2013;16(2): 170-173.
- 8. Luo X, Yan H, Huang X, Yang D, Wang J, He L. Breakup characteristics of aqueous droplet with surfactant in oil under direct current electric field. *Journal of Colloid and Interface Science*. 2017;505: 460-466.
- 9. Valiullina V, Zamula Y, Mullayanov A, Iulmukhametova R, Musin A, Kovaleva L. Experimental and numerical study of the water-in-oil emulsion thermal motion in rectangular cavity with a heated bottom. In: Indeitsev DA, Krivtsov AM. (eds) *Lecture Notes in Mechanical Engineering*. Cham: Springer;2022. p.117-125.
- 10. Kovaleva L, Zinnatullin R, Musin A, Gabdrafikov A, Sultanguzhin R, Kireev V. Influence of radio-frequency and microwave electromagnetic treatment on water-in-oil emulsion separation. *Colloids and Surfaces A: Physicochemical and Engineering Aspects*. 2021;614: 126081.
- 11. Leary T, Yeganeh M, Maldarelli C. Microfluidic study of the electrocoalescence of aqueous droplets in crude oil. *ACS Omega*. 2020;5(13): 7348-7360.
- 12. Eow JS, Ghadiri M, Sharif AO, Williams TJ. Electrostatic enhancement of coalescence of water droplets in oil: a review of the current understanding. *Chemical Engineering Journal*. 2001;84(3): 173-192.
- 13. Vignesh S, Winowlin Jappes JT, Nagaveena S, Sankaranarayanan K, Krishna Sharma R, Brintha NC. A study on mechanical and dielectric properties of B4C and Al dispersed single-layered epoxy-based polymer composites fabricated through molding and curing route. *Materials Physics and Mechanics*. 2022;48(3): 328-341.
- 14. Anand V, Juvekar VA, Thaokar RM. Modes of coalescence of aqueous anchored drops in insulating oils under an electric field. *Colloids and Surfaces A: Physicochemical and Engineering Aspects*. 2019;568: 294-300.
- 15. Anand V, Juvekar VA, Thaokar RM. An experimental study on the effect of conductivity, frequency and droplets separation on the coalescence of two aqueous drops under an electric field. *Chemical Engineering Research and Design*. 2019;152: 216-225.
- 16. Trumbetova ZM, Zavodovsky AG. Investigation of the surface tension coefficient at the oil-solution asp interface for various surfactants. *News of Higher Educational institutions. oil and gas.* 2016;5: 119. (In Russian)

- 17. Mullayanov AI, Osipova RS, Musin AA, Kovaleva LA. Investigation of the process of emulsion droplets coalescence in an inhomogeneous alternating electric field in the presence of an asphaltene interfacial film at the oil-water interface. *Technical Physics Letters*. 2022;48(1): 67-69.
- 18. Luo X, Yin H, Yan H, Huang X, Yang D, He L. Electrocoalescence of two drops with different surfactant concentrations suspended in oil. *The Journal of Physical Chemistry C.* 2018;122(39): 22615-22621.
- 19. Mousavichoubeh M, Shariaty-Niassar M, Ghadiri M. The effect of interfacial tension on secondary drop formation in electro-coalescence of water droplets in oil. *Chemical Engineering Science*. 2011;66(21): 5330-5337. 20. Shahbaznezhad M, Dehghanghadikolaei A, Sojoudi H. Contactless Method for Electrocoalescence of Water in Oil. *ACS Omega*. 2021;6(22): 14298-14308.
- 21. Li B, Vivacqua V, Ghadiri M, Sun Z, Wang Z, Li X. Droplet deformation under pulsatile electric fields. *Chemical Engineering Research and Design*. 2017;127: 180-188.
- 22. Syzrantsev VV, Arymbaeva AT, Zavjalov AP, Zobov KV. The nanofluids' viscosity prediction through particle-media interaction layer. *Materials Physics and Mechanics*. 2022;48(3): 386-396.
- 23. Valiullina VI, Musin AA, Zamula YuS, Kovaleva LA. Determination of correlation dependences of emulsion viscosity on the concentration of water droplets under non-isothermal conditions. *St. Petersburg State Polytechnical University Journal. Physics and Mathematics.* 2023;16(1.2): 343-348.
- 24. Zhou Y, Dong H, Liu YH, Yang ZJ, Liu T, Li M. Molecular dynamics simulations of the electrocoalescence behaviors of two unequally sized conducting droplets. *Langmuir*. 2019;35(20): 6578-6584.
- 25. Wang Z, Dong K, Tian L, Wang J, Tu J. Numerical study on coalescence behavior of suspended drop pair in viscous liquid under uniform electric field. *AIP Advances*. 2018;8(8): 085215.
- 26. Podbereznaya IB, Lobov BN, Kovalev OF. Express method for the analysis of electromagnetic fields in non-stationary modes based on the finite element method. *News of Higher Educational Institutions*. *Electromechanics*. 2007;2: 7-9. (In Russian)

About Authors

Rushan R. Galeev

Student (Ufa University of Science and Technology, Ufa, Russia)

Almir I. Mullayanov D Sc

Engineer (Ufa University of Science and Technology, Ufa, Russia)

Airat A. Musin Sc

Candidate of Physical and Mathematical Sciences Associate Professor (Ufa University of Science and Technology, Ufa, Russia)

Liana A. Kovaleva 🗓 Sc

Doctor of Technical Sciences

Head Department of Applied Physics (Ufa University of Science and Technology, Ufa, Russia)

Submitted: September 18, 2023 Revised: March 7, 2024 Accepted: July 25, 2024

Surface modification by laser cladding: state-of-the-art and future prospects

R. Ranjan ^{1,2 | 1}, A.K. Das ²

- ¹ Dr. B.C. Roy Engineering College, Durgapur, India
- ² National Institute of Technology, Patna, India
- [™] rajeevranjan.br@gmail.com

ABSTRACT

Laser surface modification is an advanced technique utilized for the creation of robust coatings on substrates by melting and fusing pre-placed or blown powder materials. In some instances, multiple coatings are applied to achieve intricate geometries. This method serves the purpose of enhancing substrate surface properties and rectifying surface imperfections. Over the past three decades, laser surface modification has garnered significant attention due to its capacity to process a wide range of materials, because of its high energy density and rapid cooling capabilities. Researchers have extensively explored scientific aspects, including the clad-substrate inter-face, microstructure, chemical composition, mechanical properties, and tribological characteristics of deposited materials, as well as their practical applications. This article primarily focuses on the application of laser surface modification to various substrates using suitable cladding materials. Furthermore, it delves into the survey of modification parameters, such as microstructural refinement, mechanical attributes, and tribological performance, as investigated by previous scholars. Additionally, this article presents the findings of past research endeavors and offers insights into potential avenues for future investigations within the realm of laser surface modification.

KEYWORDS

surface modification • laser cladding • microstructure • microhardness • tribological properties

Citation: Ranjan R, Das AK. Surface modification by laser cladding: state-of-the-art and future prospects. *Materials Physics and Mechanics*. 2024;52(4): 41–51.

http://dx.doi.org/10.18149/MPM.5242024_5

Introduction

Many components of machines used in mining, mineral processing, manufacturing, agriculture, and many other industries need to improve their surface performance under corrosion, wear, fracture, and oxidation environments, which is unable to be satisfied through traditional methods of surfacing and coatings [1]. Due to the effects of corrosion, mechanical components often experience premature degradation and fracture before reaching their intended operational lifespan [2,3]. The wear process contributes significantly to the surface deterioration of these components, leading to increased downtime and elevated production expenses. Various types of wear, such as abrasion, impact, and corrosion, are responsible for this phenomenon. This problem is commonly encountered in the context of agricultural implements, mining machinery, and earthmoving equipment when operating on abrasive surfaces [4]. Tool steels, for example, are widely used in practically all industries to manufacture molds, dies, and other components that are subjected to exceptionally high loads [5]. These tool steels must have good wear resistance, whether they are used for cold or hot operations.

42 R. Ranjan, A.K. Das

Likewise, machinery within the chemical and petroleum sectors grapples with corrosion issues. Consequently, laser cladding emerges as a prime method for improving surface attributes. Laser cladding, an adept surface modification technique, proves invaluable in extending the operational lifespan of both weathered machine components and fresh ones, all while maintaining economical feasibility. To cultivate favorable tribological characteristics, these cladding methods are employed to amalgamate bulk materials with the substrate. In the course of this surface modification procedure, a more durable, wear-resistant material is incorporated, thereby bolstering the longevity of the component or rectifying deteriorated surfaces [6,7].

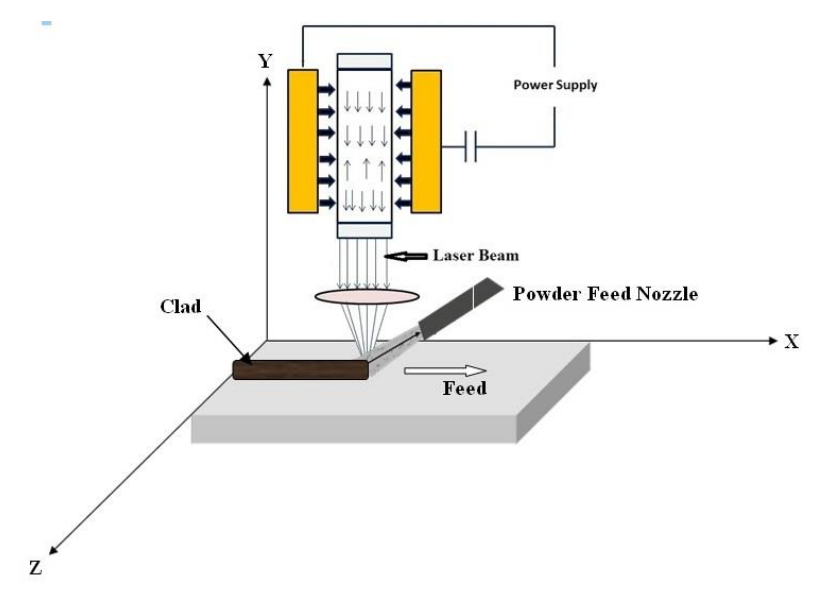


Fig. 1. Laser cladding process by powder injection

Laser cladding is a technique characterized by the fusion of a dissimilar material onto a substrate using a focused laser beam. This process involves selectively melting only a minimal layer of the substrate to establish metallurgical bonding, thereby preserving the inherent properties of the coating material [8,9]. Figure 1 illustrates the process, where a high-intensity laser beam interacts with a metallic specimen while powdered material is introduced over the molten pool. Upon solidification, this procedure results in the formation of a distinct layer referred to as the "clad". This technique uses a concentrated high-powered laser to melt the substrate's thin surface as well as the clad materials while simultaneously producing a new layer of material with specified qualities following solidification. It can produce a 0.3-5.0 mm thick coating onto a substrate, which is joined by a strong fusion bond [10,11]. Some time multi layers of coating are deposited to get complex shape geometry. The clad materials are added onto the substrate employing laser fusion of pre-placed powder or blown powders. To achieve varied qualities, a wide range of powder materials or powder combinations can be efficiently deposited onto the substrates. The deposited layer's microstructure is often exceedingly fine, resulting in excellent metallurgical characteristics. It is possible to attain excellent results, such as enhanced microstructure, mechanical and tribological properties, by selecting suitable clad materials and optimized process parameters [12]. Laser cladding has gained a lot of attention in extensive research over the past three decades because

the fast cooling rates and high-density energy make this technique suited for processing a variety of materials [13].

In this paper, we present the numerous research investigations conducted on the subject of laser cladding. The paper provides an overview of cladding processes involving diverse substrates and clad materials, highlighting distinct output parameters. Additionally, it synthesizes research outcomes from previous studies, particularly in the realms of microstructural analysis, hardness assessment, and wear resistance. The comprehensive compilation of earlier research findings is presented in Table 1 for reference. Subsequently, the essential facets of each delineated domain are expounded upon in subsequent subsections. The paper culminates with a discussion of conclusions drawn from the gathered insights and offers perspectives on future directions in the field of laser cladding.

Table 1. A Summary of studies on laser cladding (LC) technology

Table 1. /	7 Julilillal y	or studies t	nı taser ctadding	(LC) technoto	ogy –
Authors (year) [Ref.]	Substrate material	Clad materials	Investigations	Variable processing parameters	Research findings
Qian etal. (1997) [14]	AISI 1020	Colmonoy 88 nickel	Microstructure, dilution, hardness, microstructures	Powder feed rate, translation speed	Optimal cladding parameters are revealed to increase hardness and improve the microstructure of the coating.
Haemers etal. (2000) [15]	AISI 316L	Colmonoy 5	Microstructure, dilution		Microstructural analysis of the coating showed the formation of the dendritic and eutectic interdendritic phases.
Sha etal. (2001) [16]	K02600 steel	S42000 stainless steel	Microstructure, wear, microhardness		In comparison to SAW cladding, Laser cladding increased the hardness of coating about twice.
Yao etal. (2006) [17]	Medium carbon steel	CNTs	Microstructure, microhardness, wear	Beam travel speeds, laser power	Resistance to wear of the cladding is increased by three times that of the untreated substrate.
Baldridge et al. (2013) [18]	Inconel 600	Inconel 690	Microstructure, microhardness	Laser power, scanning speed, beam overlap, powder feed rate	Results revealed an admirable metallurgical bond between the substrate and the clad layer with min porosity & minute surface contamination. Higher laser power may produce the best cladding quality with the least amount of porosity and surface imperfections. Suggested optimizing Inconel 690 powder chemistry for future research.
Tanigawa et al. (2015) [19]	304 stainless steel	Ni-Cr-Si-B	Surface roughness, hardness	Overlap ratio	The hardness and roughness of the coating layer inversely depended on the overlap ratio.
Das et al. (2016) [20]	Ti-6Al-4V	Rare earth oxide (Y ₂ O ₃)	Microstructure, microhardness, wear	Laser power, scanning speed	The addition of Y_2O_3 improved the coating's microhardness and wear resistance.
Murzakov etal. (2016) [21]	C5140 steel	TaC and WC	Microstructure, wear		The cladding's microstructure and mechanical properties improved as a result of the research. When compared to the substrate, wear resistance is increased by 2–6 times.
Stanciu etal. (2016) [22]	AISI 5140	NiCrBSi, Inconel 718	Hardness, wear		Concerning the substrate, the cladding layers' wear coefficient and hardness increased.
Alam etal. (2017) [23]	AISI 1018	420 martensitic stainless steel	Microstructure, residual stresses, microhardness	Laser speed, power, powder feed rate	The rise in laser power and speed led to an augmentation in both hardness and residual stress levels.
Liu etal. (2017) [24]	Forged 300 M steel	AerMet100 steel	Microstructure, hardness, tensile properties		Results revealed a superb clad-to-substrate metallurgical bond with enhanced mechanical properties.

R. Ranjan, A.K. Das

Diensto					
Riquelme et al. (2017) [25]	AA6082 aluminum	Al/SiCp	Microstructure, mechanical properties		The cladding had better mechanical qualities than the substrate, according to the findings.
Lei et al. (2018) [26]	1Cr13 stainless steel	Carbon fibers reinforced nickel	Microstructure, microhardness, wear, corrosion	Laser scanning speed	Higher laser scanning speeds increase the coatings' wear and corrosion resistance.
Chen et al. (2019) [27]	IN718	Multi-walled carbon nanotubes (MWCNT)	Microstructure		The enhancement of graphene structure within GNSs and CNRs led to an intensified adverse effect on element segregation and the formation of Laves phase in the IN718 superalloy.
He et al. (2019) [28]	Ti-6Al-4V	TiC, CNT	Microstructure, microhardness, wear		According to the findings, the coating had a higher microhardness, a lower friction coefficient, and a much higher wear resistance than the substrate.
Sibisi et al. (2019) [29]	Ti-6Al-4V	CpTi/SiAlON	Microstructure, microhardness		Enhancement in microstructural and hardness properties as compared to the substrate.
Zhao et al. (2019) [30]	H13 mild steel	Cobalt- based alloy	Microstructure, microhardness, wear resistance		Compared Laser cladding with plasma cladding and revealed superior wear resistance and microhardness of the laser cladding.
Hulka et al. (2020) [31]	S235JR steel	WC- Co/NiCrBSi(T i)	Microstructure, corrosion resistance	Laser power, Ti-contents	The results demonstrated an excellent clad-to- substrate metallurgical bonding with fine microstructure, enhanced microhardness, and reduced Fe penetration from the substrate to the clad.
Spranger et al. (2020) [32]	Tool steel X38CrMoV5	TiB₂	Microstructure, hardness		A significant increase in hardness with the implantation of TiB ₂ particles was found.
Wang et al. (2020)	5CrNiMo steel	TiMoB ₂ , Ti,MoC, Fe ₇ Cr ₇ C ₃ with Y ₂ O ₃	Microstructure, wear	Y ₂ O ₃ contents	The mechanical properties of the cladding were enhanced by adding Y_2O_3 and got optimum values with Y_2O_3 content of 2 wt. %.
Zhu et al. (2020) [34]	Inconel 625	NiCrAlY/Ag₂ O/Ta₂O₅	Microstructure, microhardness, Friction, wear performance		Revealed 1.5 times lower coefficient of friction and 2 times lower wear rate of coating as compared to the substrate.
Chen et al. (2020) [35]	IN718	Ni-CNTs	Microstructure, tensile, wear properties		The findings revealed effective improvement in the tensile and wear quality of the clad.
Li et al. (2020) [36]	A36 mild steel	MSS with FeeNb powder	Microhardness, Tensile propt., Corrosion res.		Found remarkable enhancement in mechanical properties of the coating.
Li et al. (2020) [37]	TA1 titanium	Deloro22- Si ₃ N ₄ -B ₄ C	Microstructure, toughness		The result exhibited dense microstructure and enhanced the toughness as compared to the substrate.
Luo et al. (2020) [38]	1045 steel	Fe-Al	Microstructure, compositions, tribological properties		The coating achieved a low frictional coefficient and low rate of wear.
Ma et al. (2020) [39]	316 stainless steel	C ₄ coating	Microstructure, corrosion		Because of oxide film formation on the surface due to the C4 coating, there was an increase in corrosion resistance in sulfuric acid solution.
Mohamm ed et al. (2020) [40]	Mild steel (ASTM A36)	WT-6	Dilution ratio, hardness	Laser power, scanning speed, wire feed rate	Experimentally found optimal process parameters as laser power = 3.7 – 3.9 kW, feed rate = 75 mm/s, and scanning speed = 6 mm/s.
Savrai et al. (2020) [41]	Low carbon steel	CoNiCrW	Microstructure, phase composition, microhardness, micromechanical properties		Findings revealed remarkable enhancement in the mechanical properties of the coating.

Xiang et al. (2020) [42]	Ti	CoNiTi medium entropy alloy	Microstructure, hardness		Results revealed a superb metallurgical bond between CoNiTi MEA and Ti-substrate. Hardness measurements of the clad were found ~5 times advanced than the substrate.
Xiao et al. (2020) [43]	Q235 steel	Nb10 alloy	Microstructure, microhardness, wear resistance		An outstanding metallurgical coating, characterized by its uniformity and absence of cracks, was achieved, resulting in enhanced mechanical characteristics.
Zhang et al. (2020) [44]	A3 steel	Ni-Cu/WC- 12Co	Microstructure, microhardness, wear, corrosion resistance	WC-12Co contents	Microhardness directly depended on WC-12Co content. Optimal wear resistance was found at WC-12Co content of 20 wt.%.
Zhang et al. (2020) [45]	Ti6Al4V	Graphene reinforced Ti6Al4V	Microstructure		When Ti ₆ Al ₄ V was cladding by Graphene/Ti ₆ Al ₄ V, feathery TiC was produced.
Zhao et al. (2020) [46]	No. 45 steel	TiC/B ₄ C/Ni2 04-based	Microstructure, microhardness		Results revealed microhardness and coefficient of friction were 3.23 and 0.281 times respectively of the initial Ni ₂ O ₄ cladding when coated by 30 % TiC. On the other hand, microhardness and coefficient of friction were 4.38 and 0.752 times respectively of the previous layer when coated by 30 % B ₄ C and 5 % TiC.
Zhou et al. (2020) [47]	S355 steel	Cr-& Mo- Reinforced FeSiB	Microstructure, CoF, corrosive- wear		The result showed excellent resistance to corrosive wear of FeSiBCr coating among the three coatings namely, coating of FeSiB, coating of FeSiBCr, and coating of FeSiBCrMo. This revealed that wear resistance is mainly affected by the phase distribution.
Hu et al. (2021) [48]	5Cr₅MoSiV1 steel	Ni3Ta-TaC reinforced Ni-based	Microstructure, wear		The wear characteristics of Ni-Ta cladding and Ni- TaC cladding were found to be 2 and 4-times greater than the substrate, respectively.
Li et al. (2021) [49]	Nickel-alu minum bronze	TaC/Co- based	Microstructure, microhardness, wear, electrochemical corrosion		When compared to the substrate, the coating demonstrated a 6.2-fold increase in microhardness, a 0.303-fold drop in frictional coefficient, and a 0.4-fold drop in wear rate.
Liu et al. (2021) [50]	AISI 304	AlCoCrFeNiS i _x	Microstructure, microhardness, wear	Si - contents	The microhardness of the coating was significantly enhanced. Increased Si concentration also lowered the coating's frictional coefficient and wear rate.
Tian et al. (2021) [51]	2Cr13 steel	Inconel 625/ WC	Microstructure, microhardness, corrosion resistance	WC-contents	Optimal corrosion resistance was found at 10 wt. % WC.
Yuan et al. (2021) [52]	AISI 1045	Ni45	Microstructure, microhardness, wear, corrosion resistance		Results revealed better mechanical properties at higher-speed lasers.
Li et al. (2021) [53]	5083 aluminum	Al _x CrFeCoNi Cu	Hardness, wear	Al-contents	The hardness and the wear resistance directly depended on Al-contents.
Bartkows ki et al. (2021) [54]	Low carbon steel	Fe/WC	Macroscopic observation, microstructure, microhardness	Laser power, powder feed rate	The optimal coating was produced based on microhardness and corrosion resistance at 12.50 g/min powder feeding rate.
Liu et al. (2021) [55]	15CrMn steel	CoCrFeMnTi 0.2	Microstructure, microhardness, wear		The coating was enhanced in terms of wear resistance and microhardness. When compared to the substrate, the microhardness was raised by around 3.5 times.
Riquelme et al. (2021) [56]	ZE41 Magnesium Alloy	Al/SiC	Wear behavior, corrosion resistance		Result revealed enhancement in wear properties of the coating concerning the substrate. Also, it was concluded that wear resistance and corrosion property are improved by adding Si or Ti.
Li et al. (2022) [57]	40CrNiMo Steel	AlCoCrFeNi- xTiC	Microstructure, wear resistance	TiC- contents	The in-situ generation of TiC particles significantly enhances hardness and wear resistance.

46 R. Ranjan, A.K. Das

Ding et al. (2023) [58]	U71Mn rail	316L stainlessstee l	Grain size, Microhardness	Scanspeeds, laserpower	Grain size increases with laser power but decreases with scan speed, while hardness increases with both power and speed.
Zhang et al. (2024) [59]		NbC	Microhardness, frictioncoefficient, corrosionresistanc e	coating (A-Nh(I	•
Zhang et al. (2024) [60]	Ti6Al4V	FeCrAlMoSi _x	Micro-hardness, microstructure, wear resistance	Si- contents	Laser cladding enhances microhardness, decreases wear loss, and reduces the coefficient of friction (COF).

Substrates and clad alloys materials

Substrates

Steel serves as the predominant choice for substrate materials in the fabrication of clad components. The selection of substrates hinges on specific application demands, encompassing factors like elevated temperature resilience and resistance to corrosive and abrasive wear. Among the varied options are: (i) stainless steels, (ii) diverse grades of carbon steels, spanning high, medium, and low carbon content, (iii) high-speed steels, (iv) Inconel, (v) titanium alloys, (vi) manganese alloys, (vii) low nickel-chrome steels, (viii) cast iron, including both grey and white cast iron varieties.

Clad Alloys

Surface enhancement through cladding improves the characteristics of a component's exterior while leaving its internal properties unchanged. This technique is employed on surfaces vulnerable to deterioration, oxidation, and corrosion. Among the frequently utilized clad alloys, iron-based, titanium-based, cobalt-based, and nickel-based alloys stand out. The applications span a wide spectrum, encompassing tasks such as crushing rocks and manufacturing control valves to minimize metal-to-metal wear. In situations marked by elevated temperatures and corrosive environments, cobalt and nickel-based clad alloys find common usage.

Microstructural characterization

The composition of both the cladding material and the substrate plays a significant role in shaping the microstructural characteristics of the coating. Additionally, laser cladding parameters exert influence over these microstructural attributes. Microstructural analysis involves the examination of grain size and shape, the composition of the cladding material, and the orientation of grain structures in the heat-affected zone (HAZ), all of which are crucial for assessing their impact on tribological and mechanical properties. Traditional metallographic methods have traditionally been employed to characterize the microstructure of these coatings. However, there are various advanced tools available for evaluating the microstructure and composition of different phases within the resulting coating. These tools encompass techniques such as EPMA (electron probe microanalyzer), FESEM (field emission scanning electron microscope) equipped with EDS (energy-dispersive X-ray spectroscopy), TEM (transmission electron microscope), among others. Abrasive sheets were used to polish the samples to a near-mirror finish, followed by

diamond polishing. The microstructure was then found out by etching them with either vilella or nital solution under the optical microscope (OM). Much of the research is centered on inquiries into microstructural aspects. Some recent research concentrated on carbon nano-tubes coatings. Chen et al. [35] studied the link between IN718 substrate and Nickel-coated carbon nanotubes (Ni-CNTs) coating and found they were bonded effectively. The findings revealed that IN718/NiO- 5CNTs composite alloys' tensile and wear characteristics can be significantly enhanced. Hu et al. [48] studied Ni₃Ta-TaC reinforced Ni-based cladding on the substrate 5Cr₅MoSiV1 steel. They found Ni-Ta and Ni-TaC claddings have two and four-times the wear resistance of 5Cr₅MoSiV1 steel, respectively. Li et al. [36] examined TA1 titanium cladding by Deloro22-Si₃N₄-B₄C and the result exhibited dense microstructure and enhanced the toughness as compared to the substrate. Liu et al. [37] studied the effect of Si content on the tribological behavior of the cladding and found frictional coefficient and wear rate of the coating were reduced with an increase in Si content. Bartkowski et al. [54] produced Fe/WC cladding on low carbon steel. They got an optimal coating based on microhardness and corrosion resistance at 12.50 g/min powder feeding rate. The study-specific investigations column in Table 1 provides a breakdown of research findings derived from microstructural analyses.

Mechanical characterization

The analysis of altered surface mechanical properties was conducted by evaluating microhardness measurements and assessing tribological behavior.

Microhardness analysis

The term "hardness" denotes the material's resistance to undergoing plastic deformation due to processes like indentation, scratching, or friction. To quantify microhardness, a Vickers indenter was employed, utilizing a microhardness tester. It is noteworthy that approximately 70 % of the collective body of research pertaining to laser cladding techniques centers on investigating the hardness characteristics of the coating. Among the 43 referenced works, 30 of them specifically delve into the examination of cladding hardness behavior. The particulars of these studies predicated on hardness can be found in Table 1, within the designated "investigations" section for their respective research endeavors. Li et al. [37] studied cladding on the titanium alloy and concluded that because of the dense grain strengthening effects of CeO₂ coating, wear-resistance and microhardness were greatly enhanced. Mohammed et al. [40] investigated the three parameters, scanning speed, laser power, and wire feed rate, which have an influence on the mechanical properties of mild steel (ASTM A36) cladding. Xiang et al. [42] examined cladding of titanium using CoNiTi medium entropy alloy. Results revealed a superb metallurgical bond between CoNiTi MEA and Ti-substrate. Hardness measurements of the coating were discovered to have hardness 5 times that of the substrate. Li et al. [49] researched 5083 aluminum substrate and AlxCrFeCoNiCu clad. The results showed the hardness increases with an increase of Al-contents.

48 R. Ranjan, A.K. Das

Tribological properties analysis

When two solid surfaces interact through sliding or rolling in solid-state contact, they undergo a process known as material degradation, which is often referred to as surface wear. This phenomenon is a prevalent issue across numerous industrial sectors. Wear encompasses various factors, such as oxidation, abrasion, erosion, impact, corrosion, or a combination thereof. The pin-on-disk tribometer stands out as the primary and highly efficient instrument for conducting tests related to the tribological properties of materials. Wang et al. [33] studied the influence of rare earth oxide on the wear quality of Fe-based ceramics produced in situ and found an optimum value of Y_2O_3 content to enhance the wear properties of the cladding. Zhu et al. [34] successfully formed coating over Inconel 625 substrate and demonstrated that 1.5 times lower coefficient of friction and 2 times lower wear rate of coating as compared to the substrate. Hu et al. [48] showed the wear characteristics of Ni-Ta cladding and Ni-TaC cladding on IN718 substrate and found enhancement in the wear resistance by 2-times and 4-times respectively. Riquelme et al. [25] studied experimentally and revealed an admirable metallurgical bond between Al/SiC metal matrix composite and ZE41 magnesium alloy substrate with improvement in wear properties. Also, it was concluded that wear resistance and corrosion properties are improved by adding Si or Ti. The details of the studies are presented in Table 1.

Conclusions and future perspectives

From a comprehensive review of various research papers on laser cladding techniques, several significant observations and recommendations for future research emerge:

- 1. Laser cladding is the most suitable technique to produce an excellent metallurgical bond between the substrate and clad of thickness 50 μm to 2 mm with low dilution and defect-free coatings.
- 2. It can be applied to an extensive range of substrates to develop a high-quality coating.
- 3. It has been found that Co-based, Ni-based, WC-based, Fe-based alloys, high entropy alloy, and many other alloys can be excellently metallurgical bounded with different substrates by laser cladding technique.
- 4. Laser cladding's effectiveness mostly depends on the laser parameters (wavelength, power), process parameters (scan speed, feed rate, assist inert gas type and pressure), clad materials and their powder size, and substrate materials.
- 5. Researchers have mostly focused on studying characteristics like microhardness, wear resistance, and microstructure; relatively few research have examined how well coatings function in connection to oxidation and erosion-corrosion behavior.
- 6. In-depth research efforts are essential to gain the complex physical and chemical interactions that take place between the substrate and the materials utilized in laser cladding processes.
- 7. Not enough focus has been placed on optimizing the laser cladding technique's parameters. Because of this, researchers should work more diligently to optimize these parameters through the use of Al-driven modeling and optimization techniques.

References

- 1. Gu Y, Xia K, Wu D, Mou J, Zheng S. Technical characteristics and wear-resistant mechanism of nano coatings: a review. *Coatings*. 2020;10(3): 233.
- 2. Uhlig HH, Revie RW. Corrosion and corrosion control. 1985.
- 3. Ranjan R, Das AK. A review on surface protective coating using cold spray cladding technique. *Materials Today: Proceedings*. 2022;56: 768–773.
- 4. Ranjan R, Das AK. Recent Advancements in Surface Modification by Gas Tungsten Arc Cladding Technique: A Review. *Advanced Materials Research*. 2022;1173: 113–122.
- 5. Bajaj P, Hariharan A, Kini A, Kürnsteiner P, Raabe D, Jägle EA. Steels in additive manufacturing: A review of their microstructure and properties. *Materials Science and Engineering: A.*2020;772: 138633.
- 6. Ranjan R, Das AK. Protection from corrosion and wear by different weld cladding techniques: A review. *Materials Today: Proceedings*. 2022;57: 1687–1693.
- 7. Ranjan R. An Overview on Enhancing Materials' Tribological and Mechanical Characteristics by Using Gas Metal Arc Weld Hardfacing. *Journal of Engineering Science & Technology Review.* 2024;17(1): 54–62.
- 8. Komvopoulos K, Nagarathnam K. Processing and characterization of laser-cladded coating materials. 1990.
- 9. Ranjan R, Das AK. Improving the Resistance to Wear and Mechanical Characteristics of Cladding Layers on Titanium and its Alloys: A Review. *Tribology in Industry*. 2023;44(1): 136.
- 10. Barekat M, Razavi RS, Ghasemi A. Nd: YAG laser cladding of Co-Cr-Mo alloy on γ-TiAl substrate. *Optics & Laser Technology*. 2016;80: 145–152.
- 11. Parekh R, Buddu RK, Patel RI. Multiphysics simulation of laser cladding process to study the effect of process parameters on clad geometry. *Procedia Technology*. 2016;23: 529–536.
- 12. Guo W, Li X, Ding N, Liu G, He J, Tian L, Chen L, Zaïri F. Microstructure characteristics and mechanical properties of a laser cladded Fe-based martensitic stainless steel coating. *Surface and Coatings Technology*.2021;408:126795.
- 13. Mazumder J. Laser-aided direct metal deposition of metals and alloys. In:*Laser additive manufacturing*. Woodhead Publishing; 2017. p.21–53.
- 14. Qian M, Lim LC, Chen ZD, Chen WI. Parametric studies of laser cladding processes. *Journal of Materials Processing Technology*. 1997;63(1–3): 590–593.
- 15. Haemers TA, Rickerby DG, Lanza F, Geiger F, Mittemeijer EJ. Hardfacing of stainless steel with laser melted colmonoy. *Journal of Materials Science*. 2000;35: 5691–5698.
- 16. Sha CK, Tsai HL. Hardfacing characteristics of S42000 stainless steel by using CO2 laser. *Journal of Materials Engineering and Performance*. 2001;10: 37–41.
- 17. Yao J, Ma C, Gao M, Kong F, Zhang Q. Microstructure and hardness analysis of carbon nanotube cladding layers treated by laser beam. *Surface and Coatings Technology*. 2006;201(6): 2854–2858.
- 18. Baldridge T, Poling G, Foroozmehr E, Kovacevic R, Metz T, Kadekar V, Gupta MC. Laser cladding of Inconel 690 on Inconel 600 superalloy for corrosion protection in nuclear applications. *Optics and Lasers in Engineering*. 2013;51(2): 180–184.
- 19. Tanigawa D, Abe N, Tsukamoto M, Hayashi Y, Yamazaki H, Tatsumi Y, Yoneyama M. Effect of laser path overlap on surface roughness and hardness of layer in laser cladding. *Science and Technology of Welding and Joining*. 2015;20(7): 601–606.
- 20. Das AK, Shariff SM, Choudhury AR. Effect of rare earth oxide (Y2O3) addition on alloyed layer synthesized on Ti-6Al-4V substrate with Ti+ SiC+ h-BN mixed precursor by laser surface engineering. *Tribology International*. 2016;95: 35–43.
- 21. Murzakov MA, Chirikov SN, Markushov YV. Research on microstructure and wear resistance of coatings obtained by adding nanoparticles of refractory compounds in laser cladding. *Journal of Physics: Conference Series.* 2016;747(1): 012062.
- 22. Stanciu EM, Pascu A, Ţierean MH, Voiculescu I, Roată IC, Croitoru C, Hulka I. Dual coating laser cladding of NiCrBSi and Inconel 718. *Materials and Manufacturing Processes*. 2016;31(12):1556–1564.
- 23. Alam MK, Edrisy A, Urbanic J, Pineault J. Microhardness and stress analysis of laser-cladded AISI 420 martensitic stainless steel. *Journal of Materials Engineering and Performance*. 2017;26:1076–1084.
- 24. Liu J, Li J, Cheng X, Wang H. Microstructures and tensile properties of laser cladded AerMet100 steel coating on 300 M steel. *Journal of Materials Science & Technology*. 2018;34(4):643–652.
- 25. Riquelme A, Escalera-Rodríguez MD, Rodrigo P, Otero E, Rams J. Effect of alloy elements added on microstructure and hardening of Al/SiC laser clad coatings. *Journal of Alloys and Compounds*. 2017;727:671–682.

50 R. Ranjan, A.K. Das

26. Lei J, Shi C, Zhou S, Gu Z, Zhang LC. Enhanced corrosion and wear resistance properties of carbon fiber reinforced Ni-based composite coating by laser cladding. *Surface and Coatings Technology*. 2018;334:274–285. 27. Chen Y, Zhang Q, Chen Z, Wang L, Yao J, Kovalenko V. Study on the element segregation and Laves phase formation

- in the carbon nanotubes reinforced IN718 superalloy by laser cladding. *Powder Technology*. 2019;355:163–171.
- 28. He B, Ma D, Ma F, Xu K. Microstructures and wear properties of TiC coating produced by laser cladding on Ti-6Al-4V with TiC and carbon nanotube mixed powders. *Ferroelectrics*. 2019;547(1):217 225.
- 29. Sibisi PN, Popoola AP, Kanyane LR, Fatoba OS, Adesina OS, Arthur NK, Pityana SL. Microstructure and microhardness characterization of Cp-Ti/SiAlON composite coatings on Ti-6Al-4V by laser cladding. *Procedia Manufacturing*. 2019;35:272–277.
- 30. Zhao J, Gao Q, Wang H, Shu F, Zhao H, He W, Yu Z. Microstructure and mechanical properties of Cobased alloy coatings fabricated by laser cladding and plasma arc spray welding. *Journal of Alloys and Compounds*. 2019;785:846–854.
- 31. Hulka I, Utu D, Serban VA, Negrea P, Lukáč F, Chráska T. Effect of Ti addition on microstructure and corrosion properties of laser cladded WC-Co/NiCrBSi (Ti) coatings. *Applied Surface Science*. 2020;504:144349.
- 32. Spranger F, de Oliveira Lopes M, Schirdewahn S, Degner J, Merklein M, Hilgenberg K. Microstructural evolution and geometrical properties of TiB 2 metal matrix composite protrusions on hot work tool steel surfaces manufactured by laser implantation. *The International Journal of Advanced Manufacturing Technology*. 2020;106:481–501.
- 33. Wang XH, Liu SS, Zhang M, Qu KL. Effect of rare earth oxide on the microstructure and wear properties of in situ-synthesized ceramics-reinforced Fe-based laser cladding coatings. *Tribology Transactions*. 2020;63(2):345–355.
- 34. Zhu R, Zhang P, Yu Z, Yan H, Li S, Wu D, Shi H, Tian Y. Microstructure and wide temperature range self-lubricating properties of laser cladding NiCrAlY/Ag2O/Ta2O5 composite coating. *Surface and Coatings Technology*. 2020;383:125248.
- 35. Chen Z, Chen Y, Zhang Q, Yao Z, Zhang Q, Wang L, Yao J, Wang X. Study on the tensile and wear properties of laser-cladded IN718 superalloy reinforced by carbon nanoproducts transformed from carbon nanotubes. *Journal of Materials Research*. 2020;35(20):2643–2651.
- 36. Li BC, Zhu HM, Qiu CJ, Zhang DK. Development of high strength and ductile martensitic stainless steel coatings with Nb addition fabricated by laser cladding. *Journal of Alloys and Compounds*. 2020;832:154985.
- 37. Li J, Tian Y, Zhang L, Wang X, Wang X. Laser/argon-arc strengthening of titanium alloy surface with Deloro matrix composites. *Optics & Laser Technology*. 2020;123:105911.
- 38. Luo X, Cao J, Meng G, Chuan Y, Yao Z, Xie H. Systematical investigation on the microstructures and tribological properties of Fe-Al laser cladding coatings. *Applied Surface Science*. 2020;516:146121.
- 39. Ma J, Liu Z. Corrosion Behavior of C4 Coating Produced by Cladding Laser in Sulfuric Acid. *Journal of Physics: Conference Series*. 2020;1635(1): 012074.
- 40. Mohammed S, Zhang Z, Kovacevic R. Optimization of processing parameters in fiber laser cladding. *The International Journal of Advanced Manufacturing Technology*. 2020;111:2553–2568.
- 41. Savrai RA, Soboleva NN, Malygina IY, Osintseva AL. The structural characteristics and contact loading behavior of gas powder laser clad CoNiCrW coating. *Optics & Laser Technology*. 2020;126:106079.
- 42. Xiang K, Chai L, Wang Y, Wang H, Guo N, Ma Y, Murty KL. Microstructural characteristics and hardness of CoNiTi medium-entropy alloy coating on pure Ti substrate prepared by pulsed laser cladding. *Journal of Alloys and Compounds*.2020;849:156704.
- 43. Xiao Y, Liu Z. Characteristics study on in-situ NbC particles reinforced Ni-based alloy composite coating by laser cladding. *Journal of Physics: Conference Series*. 2020;1635(1): 012076.
- 44. Zhang J, Lei J, Gu Z, Tantai F, Tian H, Han J, Fang Y. Effect of WC-12Co content on wear and electrochemical corrosion properties of Ni-Cu/WC-12Co composite coatings deposited by laser cladding. *Surface and Coatings Technology*. 2020;393:125807.
- 45. Zhang L, Zhao Z, Bai P, Du W, Li Y, Yang X, Wang Q. In-situ synthesis of TiC/graphene/Ti6Al4V composite coating by laser cladding. *Materials Letters*. 2020;270:127711.
- 46. Zhao Y, Yu T, Sun J, Jiang S. Microstructure and properties of laser cladded B4C/TiC/Ni-based composite coating. *International Journal of Refractory Metals and Hard Materials*.2020;86:105112.
- 47. Zhou J, Kong D. Microstructure, Tribological performance, and wear mechanism of Cr-and Mo-reinforced FeSiB coatings by laser cladding. *Journal of Materials Engineering and Performance*. 2020;29:7428–7444.

- 48. Hu D, Liu Y, Chen H, Wang M, Liu J. Microstructure and properties of in-situ synthesized Ni3Ta-TaC reinforced Ni-based coatings by laser cladding. *Surface and Coatings Technology*. 2021;405:126599.
- 49. Li Z, Yan H, Zhang P, Guo J, Yu Z, Ringsberg JW. Improving surface resistance to wear and corrosion of nickel-aluminum bronze by laser-clad TaC/Co-based alloy composite coatings. *Surface and Coatings Technology*. 2021;405:126592.
- 50. Liu H, Sun S, Zhang T, Zhang G, Yang H, Hao J. Effect of Si addition on microstructure and wear behavior of AlCoCrFeNi high-entropy alloy coatings prepared by laser cladding. *Surface and Coatings Technology*. 2021;405:126522.
- 51. Tian ZH, Zhao YT, Jiang YJ, Ren HP. Microstructure and properties of Inconel 625+ WC composite coatings prepared by laser cladding. *Rare Metals*. 2021;40:2281–2291.
- 52. Yuan W, Li R, Chen Z, Gu J, Tian Y. A comparative study on microstructure and properties of traditional laser cladding and high-speed laser cladding of Ni45 alloy coatings. *Surface and Coatings Technology*. 2021;405:126582. 53. Li Y, Shi Y. Microhardness, wear resistance, and corrosion resistance of AlxCrFeCoNiCu high-entropy alloy coatings on aluminum by laser cladding. *Optics & Laser Technology*. 2021;134:106632.
- 54. Bartkowski D, Bartkowska A, Jurči P. Laser cladding process of Fe/WC metal matrix composite coatings on low carbon steel using Yb: YAG disk laser. *Optics & Laser Technology*. 2021;136:106784.
- 55. Liu H, Li X, Liu J, Gao W, Du X, Hao J. Microstructural evolution and properties of dual-layer CoCrFeMnTiO. 2 high-entropy alloy coating fabricated by laser cladding. *Optics & Laser Technology*. 2021;134:106646.
- 56. Riquelme A, Rodrigo P, Escalera-Rodriguez MD, Rams J. Evaluation of the wear resistance and corrosion behavior of laser cladding al/sic metal matrix composite coatings on ze41 magnesium alloy. *Coatings*. 2021;11(6): 639.
- 57. Li Y, Wang K, Fu H, Guo X, Lin J. Microstructure and wear resistance of in-situ TiC reinforced AlCoCrFeNibased coatings by laser cladding. *Applied Surface Science*. 2022;585:152703.
- 58. Ding H, Yang T, Wang W, Zhu Y, Lin Q, Guo J, Xiao Q, Gan L, Liu Q. Optimization and wear behaviors of 316L stainless steel laser cladding on rail material. *Wear*. 2023;523:204830.
- 59. Zhang HF, Zhang S, Wu H, Wang R, Zhang CH, Wu CL, Chen J, Chen HT. Mechanical properties and corrosion resistance of laser cladding iron-based coatings with two types of NbC reinforcement. *Surface and Coatings Technology*.2024;479:130558.
- 60. Zhang Z, Hua K, Cao Y, Song Y, Li X, Zhou Q, Wang H. Microstructures and properties of FeCrAlMoSix high entropy alloy coatings prepared by laser cladding on a titanium alloy substrate. *Surface and Coatings Technology*. 2024;478:130437.

About Authors

Ranjan Rajeev ©SC

Asst. Professor (Dr. B.C. Roy Engineering College, Durgapur, India), Research Scholar (National Institute of Technology, Patna, India)

Das Anil Kumar OSC

PhD, Associate Professor (National Institute of Technology, Patna, India)

Submitted: July 12, 2024 Revised: July 30, 2024 Accepted: August 27, 2024

Ultrasonic layer-by-layer treatment of PN85Y15 coating as a way to increase wear resistance of friction pair with bronze

I.S. Syundyukov [™] (10), M.A. Skotnikova (10), A.Yu. Ryabikin (10)

Peter the Great St. Petersburg Polytechnic University, St. Petersburg, Russia

[™] ilnursyundyukov@gmail.com

ABSTRACT

Tribotechnical tests on wear resistance of friction pairs "coating PN85Y15 - bronze BrB2", at loads of 100 and 300 N, sample rotation speed of 300 rpm, with lubricant Lukoil Luxe 5W40 have been carried out. It is shown that the plasma coating applied to steel 45 together with layer-by-layer ultrasonic treatment (UST) with the power of 200 W, in comparison with the coating with UST with the power of 400 W and without UST, had a higher adhesion to the base metal and sufficient porosity, which working with lubricant provided the crankshaft with increased lubricity, formation of favourable compressive residual stresses, formation in the coating of a two-component structure of large (~40 μ m) granules and small (~1–7 μ m) superhard intermetallic particles of phases Fe₂Al₅, which filled surface imperfections and reduced the coating roughness by 2 times, reduced the friction coefficient by 2 times, weight wear by 12 times and contact temperature by an average of 5 °C.

KEYWORDS

plasma spraying • tribotechnical tests • ultrasonic treatment • surface roughness • friction coefficient contact temperature

Acknowledgements. The research was carried out at the expense of a grant from the Russian Science Foundation, No. 22-19-00178, https://rscf.ru/en/project/22-19-00178.

Citation: Syundyukov IS, Skotnikova MA, Ryabikin AYu. Ultrasonic layer-by-layer treatment of PN85Y15 coating as a way to increase wear resistance of friction pair with bronze. *Materials Physics and Mechanics*. 2024;52(4): 52–62.

http://dx.doi.org/10.18149/MPM.5242024_6

Introduction

The main operational characteristic of internal combustion engines (ICE) is the wear resistance of crankshafts, because as a result of changes in the size, shape and mutual arrangement of parts due to shaft wear, the initial clearance between friction pairs is broken, which leads to the rupture of the lubricating layer, pressure drop in the system, as well as the appearance of knocking, overheating and de-strengthening of the material of parts in the engine [1-5].

At present, the most widespread application for manufacturing and restoration of crankshafts are wear-resistant iron-based coatings applied by plasma spraying. Such coatings have increased hardness, brittleness and reduced thermal conductivity due to oxide inclusions and pores. Plasma spraying units Plasma coatings are characterised by a flaky, layered structure with high heterogeneity of physical and mechanical properties due to the developed surface of joints between particles and the increased content of oxide inclusions [6-10]. Plasma spraying units do not require significant initial

investments, and easily converted to the production of powders from a variety of materials [11].

To eliminate the mentioned drawbacks the authors in the previous work in the friction pair "coating - cast iron" [12-14] applied simultaneously with plasma spraying of PN85Y15 powder particles, layer-by-layer ultrasonic treatment (UST) with 200 and 400 W power.

During the operation of crankshafts, the main defect leading to the loss of their serviceability is the wear of main and connecting rod journals paired with a piston bronze ring (liner) working with lubricant [15–31].

Therefore, the purpose of this work was to increase the wear resistance of friction pair "plasma coating - bronze", due to layer-by-layer ultrasonic treatment combined with plasma spraying of ferromagnetic powder PN85Y15.

Materials and Methods

Tribotechnical tests with synthetic grease Lukoil Luxe 5W40 were carried out on the friction machine SMTS-2 (Fig. 1), according to the scheme "Roller - Roller" with the rotation frequency of the lower roller 300 rpm, with the load on the fixed upper roller 100 and 300 N, test time 2 hours.



Fig. 1. External view of friction machine SMC-2

The following characteristics of the "coating - bronze" tribocouple were determined: torque and a friction coefficient, weight wear, contact temperature and surface roughness of the specimens before and after the test. In order to achieve measurement accuracy, each test was carried out three times.

The lower rotating roller (Fig. 2(a)) was made of antifriction beryllium bronze of BrB₂ grade (97-98 % Cu and 2 % Be, up to 0.5 % Ni). The upper, fixed rollers were fitted with inserts (Fig. 2(b)) cut from blanks (Fig. 2(c)) of 45 steel and coated with plasma sprayed PN85Y15 (84%Ni, 15%Al, 0.2%Fe) nickel-based powder (84%Ni, 15%Al, 0.2%Fe) (Fig. 2d)) without UST and with simultaneous 200 and 400 W layer-by-layer UST.

A portable profilometer - Mahr Surf PS-1 profilograph was used to assess surface roughness. Metallographic studies were carried out using a μ Vizo-MET reflected light

microimager. The phase composition of the coatings was studied with the help of X-ray structure analyser, and residual stresses were measured with the help of resistive electrocontact method of non-destructive testing on the SITON-TEST device. Micro-X-ray spectral analysis (study of the concentration distribution of elements in the coating) was performed on a Camebax micro analyser equipped with an INCA ENERGY 350 energy dispersive spectrometer at a probe electron energy of 15 keV.

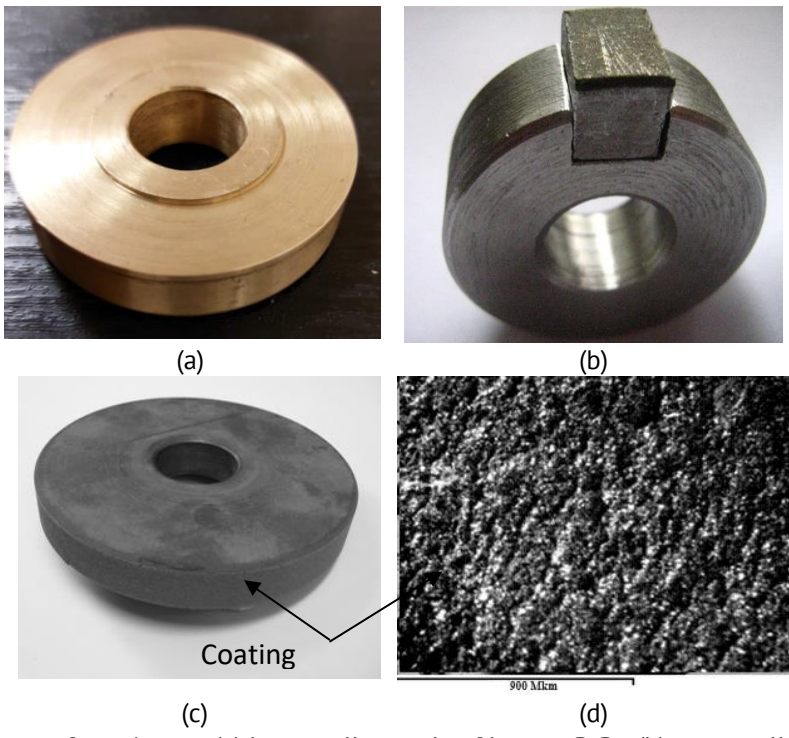


Fig. 2. The images of specimens: (a) lower roller made of bronze BrB₂; (b) upper roller with coated steel 45 insert; coated billet (c,d) for cutting out inserts and testing on the SMC-2 friction machine

Results and Discussion

Metallographic and micro-X-ray spectral studies of the coating structure

As can be seen from Fig. 3(a,b), a loose and adhesion-unstable coating without UST with a thickness of $\sim 116~\mu m$ made of large molten particles of $28-100~\mu m$ was formed. The plasma PN85Y15 powder coating applied together with a 200 W layer-by-layer UST (Fig. 3(c,d)) with a thickness of $\sim 82~\mu m$ had good adhesion to the base metal (steel 45) and was formed from two types of particles, probably with different temperature interval of their formation: large particles of 25–70 μm and small particles of 1–7 μm , which filled uneven areas.

With increasing the power of layer-by-layer UST up to 400 W, only large molten particles of $18-40~\mu m$ size were observed, which formed a coating of different thicknesses on average $\sim 46~\mu m$ (Fig. 3(e,f), having good adhesion to the base metal.

Figure 4 shows the results of micro-X-ray spectral study of the distribution of chemical elements (Ni, Al, Fe) before and after ultrasonic treatment (UST) with 200 W power in coatings deposited on steel 45 samples by plasma spraying of PN85Y15 powder. As can be seen from Fig. 4(a), if PN85Y15 powder particles are sputtered without UST a loose and adhesionally unstable coating with a thickness of \sim 120 μ m is formed. Iron from

steel 45 and nickel and aluminium from the coating mutually diffuse towards each other to form a transition layer (Fig. 4(b)), which could be responsible for the adhesion strength of the coating. As can be seen from Fig. 4(b), at a distance from the surface of $\sim 100~\mu m$, there is a sharp decrease in the content of all elements in the coating, which could lead to a drop in strength and the formation of a boundary crack.

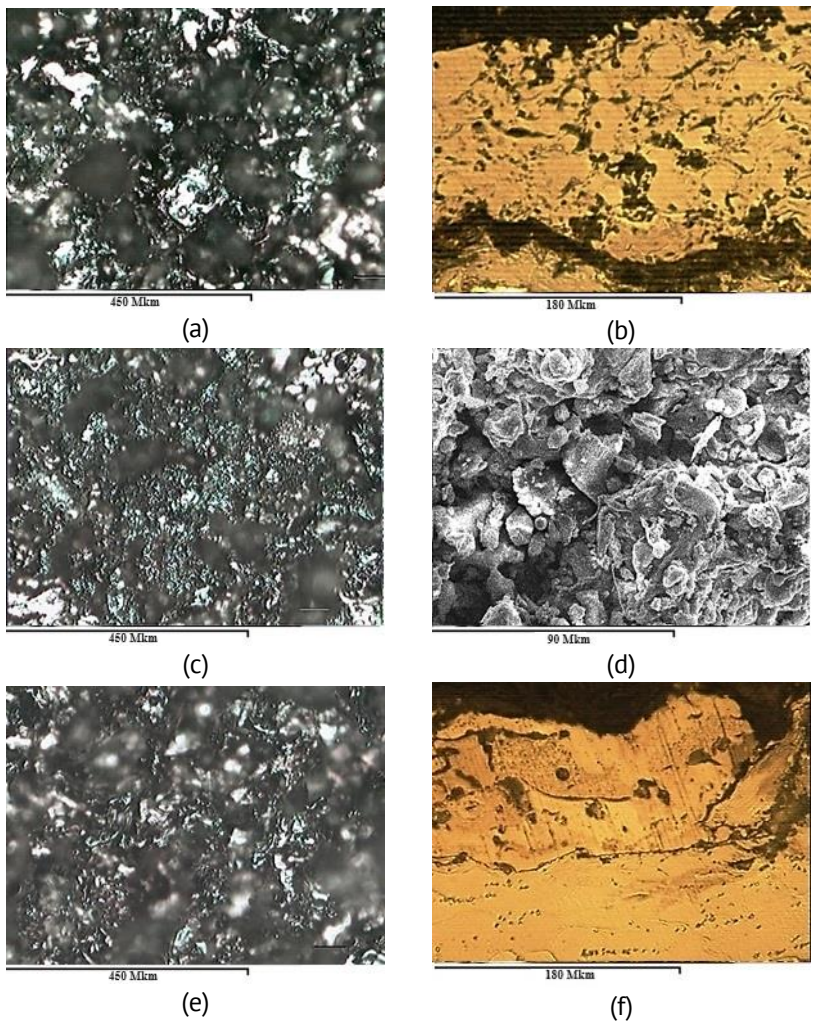


Fig. 3. Metallographic images of the surface of PN85Y15 coatings of samples from steel 45 (a,c,d,e) and their cross sections (b,f) (without UST (a,b) and with UST power 400 W (e,f), 200 W (c,d))

Figure 4(c) shows a ferromagnetic powder coating obtained using a 200 W UST. In the border zone, at a distance from the surface \sim 60 μ m (Fig. 4(d)), in the coating there was a sharp decrease in the content of Ni, Al and simultaneous transition from steel 45 elements Fe and Cr, which provided the coating with good adhesion to the base metal.

A characteristic feature of ultrasound is that, unlike thermal energy, acoustic energy affects plasma chemical reactions of liquid chemical elements, activates physical and chemical processes and is absorbed by the boundaries of grains, particles and the boundaries of the transition layer between the coating and the substrate.

It can be assumed that during magnetisation of coatings made of ferromagnetic materials (e.g., nickel, iron) magnetic moments of domains acquire preferential orientation in the direction of the external magnetic field and the coating material

deforms (expands or contracts) even before solidification (crystallisation). Probably, magnetostrictive deformation of liquid phase particles reduces the crystallisation temperature and promotes the formation of ultrafine and superhard particles of Fe₂Al₅ phases with the size of $1-7~\mu m$ after layer-by-layer UST with 200 W power.

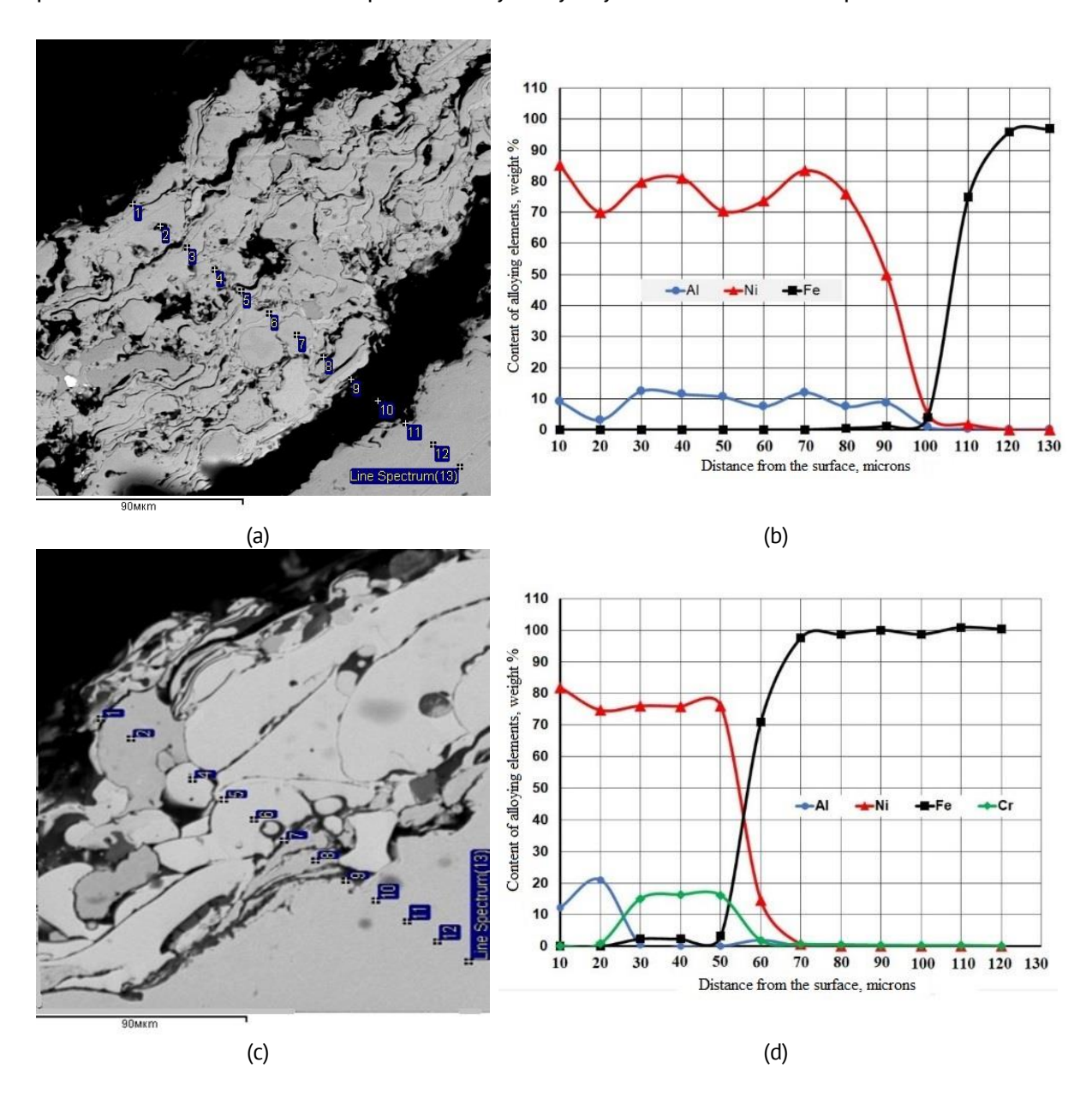


Fig. 4. Metallographic images of the surface of PN85Y15 coatings of steel 45 samples (a,c) and concentration distribution of elements (b,d) in the coating without UST (a,b) and with 200 W UST (c,d)

According to the Fe-Al equilibrium diagram [32], at the eutectic temperature of 654 °C, the solubility of iron in aluminium is negligible (0.03 at. %), while the solubility of aluminum in iron is 600 times higher and amounts to about 32 %.

As shown in Fig. 4(d), after layer-by-layer UST with 200 W, unlike the coating without UST, iron from steel 45 and aluminium from the coating mutually diffuse towards each other to form a transition layer in which aluminium dissolves into iron to form ultrafine particles Fe_2Al_5 (71 at. % Al).

At room temperature, the particles of intermetallic phase Fe_2Al_5 have a high hardness of 11.5 GPa. The appearance of such particles in the surface layer may explain the high wear resistance of the coating after layer-by-layer UST with 200 W power.

It should be noted that after layer-by-layer UST with 200 W power, in the transition layer of the coating, in which aluminium dissolves in iron and particles Fe_2Al_5 are formed, chromium with a maximum concentration of 16.35 % diffuses there from steel 45 (Fig. 4(d)), which should potentially increase the corrosion resistance of such a coating.

X-ray diffraction studies of phases and internal stresses of coatings

The results of the X-ray diffraction study of the phase composition of the coatings deposited on steel 45 samples by plasma spraying of PN85Y15 powder, without UST and with 200 W UST, are substituted in Table 1.

In the coating treated with UST power of 200 W, in comparison with the coating without UST treatment, in addition to large particles of nickel-based compounds Ni_3Al [11,33], small particles of the second phase Fe_2 Al_5 were detected (Fig. 3(c,d), Table 1). At the same time, diffraction lines of Ni_3 Al compounds on the basis of nickel were significantly broadened, which indicated the appearance of significant internal stresses in the coating.

Table 1. X-ray o	diffraction studies	of phases	and interna	l stresses of	coatings
	·			•	•

	Spray coating mode with UST	Phase	At a distance from the surface <i>h</i> , μm					
Coating grade		composition of	20	120	220	320	420	520
		the coating	Residual stress values, MPa					
PN85Y15	Without UST	Ni ₃ Al	- 18	+ 13	+ 14	+ 18	+ 20	+ 22
PN85Y15	UST 200 W	Ni ₃ Al, Fe ₂ Al ₅	- 118	- 72	- 70	- 62	- 50	- 48

As shown by the results of residual stress measurement using the SITON-TEST device, favourable compressive stresses appeared in the coating treated with a 200 W UST (Table 1). This could contribute not only to the surface hardening but also to the adhesion strength and wear resistance of the coating.

Tribotechnical studies of coatings

Figures 5 and 6 show the results of time variation of the coefficient of friction (K_{tr}) during a wear test of friction pair "coating PN85Y15 - bronze BrB₂" at the 100 and 300 N loads: before and after layer-by-layer UST of 200 and 400 W. It can be seen that the coefficient of friction of the friction pair "coating with UST-200 - bronze" decreased by 2 times (from 0.6 to 0.3) at a 100 N load in comparison with the coating without UST.

Figures 7 and 8 show the results of temperature variation in time during testing of friction pair "PN85Y15 coating - BrB2 bronze": before and after layer-by-layer UST with 200 and 400 W power at 100 and 300 N loads.

During the 100 and 300 N load tests, the coatings obtained by a 200 W layer-by-layer UST had a lower mean operating temperature in comparison with coatings without UST: 7 °C (67.7 and 60.7) and 6.3 °C (77.3 and 71.0), respectively.

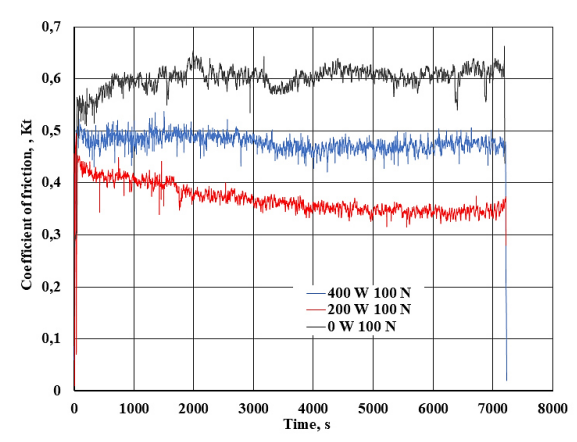


Fig. 5. Variation of friction coefficient during 2-hour test "PN85Y15 coating - BrB2 bronze" at a load of 100 N

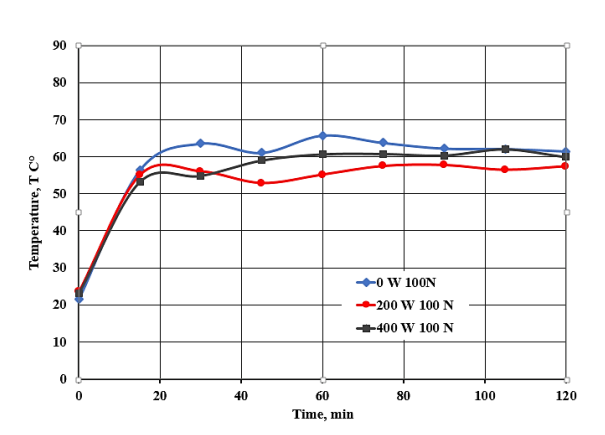


Fig. 7. Temperature change during a 2-hour test of the friction pair "PN85Y15 coating - BrB₂ bronze" at a load of 100 N

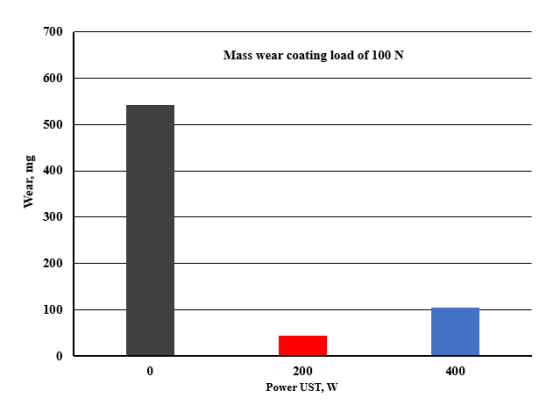


Fig. 9. Mass wear of the PN85Y15 coating after testing at a load of 100 N: before and after 200 W and 400 W layer-by-layer USTs

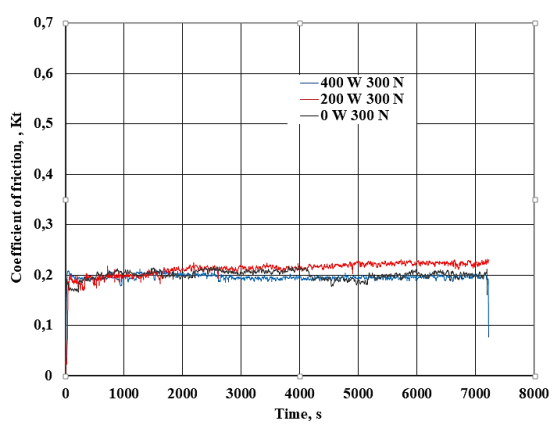


Fig. 6. Variation of friction coefficient during 2-hour test of friction pair "PN85Y15 coating -bronze BrB2" at a load of 300 N

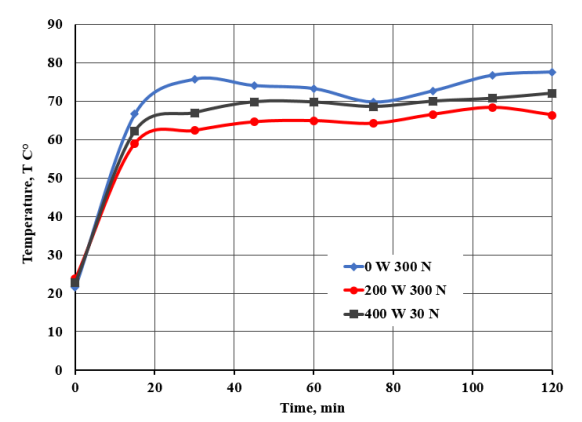


Fig. 8: Temperature change during a 2-hour test of the friction pair "PN85Y15 coating - BrB₂ bronze" at a load of 300 N

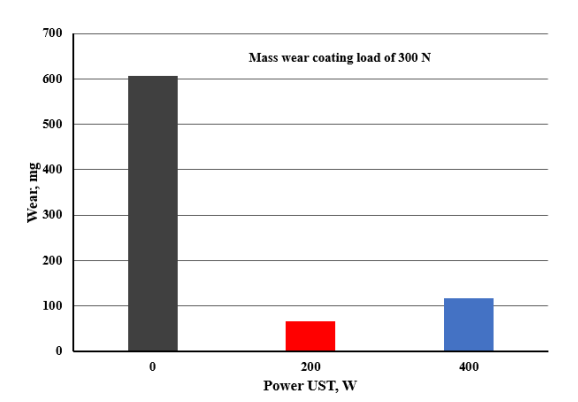


Fig. 10. Mass wear of PN85Y15 coating after tests at 300 N load: before and after layer-by-layer UST of 200 W and 400 W power

Table 2 shows the mass wear results of the PN85Y15 coating after a 2-hour 100 and 300 N load tests before and after 200 and 400 W layer-by-layer UST.

Table 2. Mass wear	of the coat	ing after	testing a	at 100 a	and 300 N load

Coating grade	Spray coating mode with	Load 100 N	Load 300 N
Coating grade	UST	Wear, mg	Wear, mg
PN85Y15	Without UST	542.67	605.67
PN85Y15	UST 200 W	44.67	66.5
PN85Y15	UST 400 W	104.67	116.67

At the 100 and 300 N load tests, the coatings obtained by plasma spraying of PN85Y15 powder combined with 200 W layer-by-layer UST had less wear in comparison with the coating without UST by more than 12 times (542.67 and 44.67 and more than 9 times (605.67 and 66.67), respectively.

Profilometric studies of the coating structure

The optical microscopy results completely coincides with the profilometric studies of the structure of the coating surfaces (see Table 3).

Table 3. Roughness parameters of PN85Y15 coatings paired with bronze after the 100 and 300 N load tests: before and after layer-by-layer UST with 200 and 400 W power

Spray coating mode with	Load 100 N			Load 300 N		
UST	Ra	Rz	<i>R</i> q	Ra	Rz	<i>R</i> q
Without UST	7.402	37.423	9.214	7.078	32.828	8.695
UST 200 W	3.182	18.331	4.082	4.203	22.260	5.231
UST 400 W	3.931	29.375	4.960	4.119	21.435	5.200

Table 4. Roughness parameters of coatings characterising wear resistance and sprayed before and after USTs of 200 W and 400 W (R_{PK} is a parameter characterising the height of protrusions that wear quickly during the first run-in period; R_K is the depth of surface profile irregularities defining the profile base, bearing area as the outer layers wear; R_{VK} is the average depth of profile depressions that determine the lubricity of the surface; $R_{PK}+R_K$ are the sum of parameters characterising wearability of working surfaces of the product, e.g. crankshaft journals)

Coating grade	Spray coating mode with UST	R_{pk}	R_k	<u>R</u> vk	$R_{\rm pk}$ + $R_{\rm k}$
PN85Y15	Without UST	48	35	17	83
PN85Y15	UST 200 W	40	55	5	95
PN85Y15	UST 400 W	46	46	8	92

Roughness parameters of powder coating sprayed with layer-by-layer UST of 200 W power are an arithmetic mean profile deviation R_a , height of profile irregularities at ten points R_z , mean square deviation of profile R_q decreased by 2 times in comparison with coating without UST. The roughness parameters characterising the wear resistance of the powder coating sprayed with layer-by-layer UST of 200 W power (R_{pk} , R_k , R_{vk}) were also improved. These parameters were obtained from the construction of the surface reference curve (Abbott curve), which characterises the percentage of material content by roughness layer height within the maximum (R_{max}) and minimum height (R_{min}) of

microroughnesses. Four parameters characterising the wear process were determined from the Abbott curve (Table 4).

As can be seen Fig. 11, the coatings obtained by plasma spraying of PN85Y15 powder combined with layer-by-layer UST with a power of 200 W, had a better complex of parameters characterising the wear process in comparison with the coating without UST (Table 4).

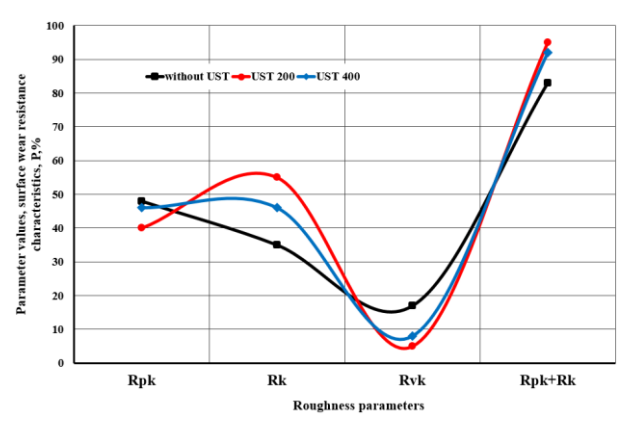


Fig. 11. Values of surface roughness parameters R_{pk} , R_k , R_{vk} characterising wear resistance of PN85Y15 coatings in the surface layer

Based on the obtained results, it can be concluded that the coatings obtained by plasma spraying of ferromagnetic powder combined with layer-by-layer UST had higher adhesion to the base metal in comparison with the coating without UST, and sufficient porosity, which provided the crankshaft with increased lubricity if working with lubricant.

In addition, the coatings obtained by layer-by-layer UST with 200 W power formed a two-component structure of large (\sim 40 µm) and small (\sim 1–7 µm)of granules, which filled the surface imperfections and provided the crankshaft not only with increased lubricity, but also with adhesive strength.

Conclusions

Based on the results obtained, it can be concluded that the coatings obtained by plasma spraying of PN85Y15 ferromagnetic powder combined with layer-by-layer UST of 200 W, compared to the coating without UST, possessed:

- 1. higher adhesion to the base metal and sufficient porosity which, when working with the lubricant, will provide the crankshaft with increased lubricity;
- 2. two-component structure of granules large (\sim 40 µm) and small (\sim 1–7 µm), which filled surface imperfections and reduced coating roughness by 2 times;
- 3. structural-phase transformations with the formation of ultrafine superhard intermetallic particles of Fe_2Al_5 ;
- 4. formation of favourable compressive residual stresses;
- 5. improvement of tribotechnical properties of friction pair "coating bronze": reduction of wear in 12 and 9 times, at load 100 and 300 N, respectively; reduction of friction coefficient in 2 times and contact temperature on average by 5 °C.

Thus, based on the results obtained, it can be concluded that plasma spraying of PN85Y15 powder with layer-by-layer UST with a power of 200 W leads to an increase in

the wear resistance of surfaces in comparison with coating without UST. Such coating is recommended for spraying on worn main and connecting rod journals of crankshafts of internal combustion engines of automobiles.

References

- 1. Melnik VD, Ukhin VI, Ivanovskaya AV. History of gas internal combustion engine Lenoir engine. *Education, Science and Youth 2023: Scientific and Practical Conference of Students and Cadets, Simferopol, 18-22 September 2023.* Simferopol: Limited Liability Company "Publishing House Typography "Arial"; 2023. p.84–86. (In Russian)
- 2. Sanzhapov RR, Sidorova TL. *Automobile in our life. Terms and definitions in the field of automobile transport.* Volgograd: Volgograd State Technical University; 2020. (In Russian)
- 3. Aleksanyan IM, Khachkinaian AE. Research of wear of crankshafts and connecting rods of engines of transport-technological machines. *Transport constructions*. *Ecology*. 2021;2: 47–55. (In Russian)
- 4. Slobodchikov VA. Restoration of crankshafts of internal combustion engines. Youth and Science. 2018;6: 75.
- 5. Marchenko EV. Methods of surface hardening of crankshaft journals. Modern research: theory, practice, results. In: *Collection of materials of the International Scientific and Practical Conference, Moscow, 29 December 2023.* Moscow: LLC "ALEF Publishing House"; 2023. p.410–414.
- 6. Drelikh IV, Ibragimov EA. Ion-plasma spraying installation of ion-plasma spraying. Actual problems of modern mechanical engineering. In: *Proceedings of the international scientific-practical conference*. 2014. p.48–50.
- 7. Sergachev DV, Kuzmin VI, Kartaev EV, Nalivaiko VI. Application of lase-optic diagnostic of the parameters of the alumina particles in the additive technology of surface modification of materials by highly concentrated source of energy. *Izvestiya Vuzuv. Fizika.* 2014;57(10): 254–258. (In Russian)
- 8. Marakhtanov MK, Klimenko GK, Chjo VN. Investigation of roughness characteristics of the coating applied by plasma spraying. *BMSTU Journal of Mechanical Engineering*. 2014;2(647): 72–76. (In Russian)
- 9. Makarov AV, Malygina IY, Burov SV, Savrai RA. *Method of ultrasonic hardening treatment of parts*. Patent RU 2643289. 2018.
- 10. Kalita VI, Radyuk AA, Kovalevskaya JG, Sharkeyev YP, Komlev DI, Tolmachev AI, Ivannikov AY, Zakharov IN, Bagmutov VP. Hardening of plasma coating from high speed steel at electromechanical and ultrasonic treatment. *Technology of Mechanical Engineering*. 2019;11: 30–37. (In Russian)
- 11. Ermakov S, Shvecov O. Features of obtaining powders for additive machines by plasma spraying. *Materials Physics and Mechanics*. 2021;47(6): 843–855.
- 12. Syundyukov IS, Skotnikova MA, Padgurskas J, Tsvetkova GV, Tarasenko EB. Wearproof structural and phase status of the surface of preparation of steel 45 after plasma spraying of powder PN85Y15. *Material Today: Proceedings*. 2020;30: 650–655.
- 13. Skotnikova MA, Syundyukov IS, Ryabikin AYu, Ivanova GV. Increasing the Wear Resistance of Crankshafts by the Plasma Spraying Method. In: *Lecture Notes in Mechanical Engineering*. Cham; Springer; 2023. p.142–152.
- 14. Khmelevskaya VB, Moseiko ES. Covering research by a plasma dusting with ultrasonic processing for hardening of ship rowing shaft. *Metalworking*. 2012;1: 40–43. (In Russian)
- 15. Gots AN. Increase of wear resistance of crankshaft necks. *Modern Problems of Science and Education*. 2011;6: 110. (In Russian)
- 16. Suminov IV, Belkin PN, Epelfeld AV, Ludin VB, Krit BL, Borisov AM. *Plasma-electrolytic surface modification of metals and alloys. Volume I.* Moscow: Technosphere; 2011. (In Russian)
- 17. Denisov AS, Tugushev BF, Gorshenina EY. Stress analysis of the second kind in a crankshaft restored by cladding metal coatings. In: *Bulletin of Saratov State Technical University*. 2011. p.38–43. (In Russian)
- 18. Denisov AS, Tugushev BF, Vidineev AA, Gorshenina EY, Kulakov OA, Zakharov VP. Analysis of the significance of processes that determine the resource of the engine crankshaft. *Motor Transport Enterprise*. 2010;5: 53–56. (In Russian)
- 19. Kadyrmetov AM, Pustovalov AS, Menyailov KA. Ways to improve electric arc plasmatrons of linear scheme and prospects for their use in plasma spraying processes. *Science, Technology and Education*. 2015;1(7):10-12. (In Russian)

- 20. Kadyrmetov AM, Drapalyuk MV, Nikonov VO, Maltsev AF. Features of the process of plasma spraying with electromechanical processing of coatings. *Polythematic Network Electronic Scientific Journal of Kuban State Agrarian University*. 2013;89: 760–771. (In Russian)
- 21. Chyosov YS, Zverev EA, Vakhrushev NV, Partz KA, Khakholin AV, Kiryushkin VD. Optimisation of modes of plasma spraying of coatings. Problems of increasing the efficiency of metalworking in industry at the present stage. In: *Materials of the 11th All-Russian Scientific-Practical Conference*. 2013. p.70–72. (In Russian) 22. Nikonov VO. Development of the automated process of hardening and restoration of machine parts by
- plasma spraying with simultaneous electromechanical processing. *Actual directions of scientific research of the XXI century: theory and practice*. 2014;2(4–3): 228–230. (In Russian)
- 23. Posmetyev VI, Kadyrmetov AM, Nikonov VO. Perspective methods of plasma spraying of coatings with simultaneous electromechanical processing. *Voronezh Scientific and Technical Bulletin*. 2013;2(2): 88–91. (In Russian)
- 24. Kornienko EE, Mul DO, Rubtsova OO, Rubtsova OA, Vaschenko SP, Kuzmin VI, Gulyaev IP, Sergachev DV. Effect of plasma spraying regimes on structure and properties of Ni3Al coatings. *Thermophysics and Aeromechanics*. 2016;23(6): 919–927.
- 25. Kornienko EE, Rubtsova OA, Gulyaev IA, Gulyaev IP, Kuzmin VI. Structural features of the coatings of the Ni-Al system obtained by air-plasma spraying. *IOP Conference Series: Materials Science and Engineering*. 2017;286: 012028.
- 26. Ivancivsky VV, Skeeba VYu, Zverev EA, Vakhrushev NV, Parts KA. Increase in wear resistance of nickel plasma coatings under traditional and combined treatment conditions. *IOP Conf. Series: Earth and Environmental Science*. 2018;194: 042006.
- 27. Kengesbekov A, Rakhadilov B, Sagdoldina Z, Buitkenov D, Dosymov Y, Kylyshkanov M. Improving the Efficiency of Air Plasma Spraying of Titanium Nitride Powder. *Coatings*. 2022;12(11): 1644.
- 28. Kengesbekov AB, Rakhadilov BK, Zhurerova LG, Uazyrkhanova GK, Kambarov YeYe. Formation of TiN coatings by air plasma spraying. *Bulletin of the Karaganda University Physics Series*. 2022;108(4): 22–31.
- 29. Zverev EA, Skeeba VYu, Skeeba PYu, Khlebova IV. Defining efficient modes range for plasma spraying coatings. *IOP Conf. Series: Earth and Environmental Science*. 2017;87(8): 082061.
- 30. Kravchenko IN, Kolomeichenko AV, Sharifullin SN, Kuznetsov YuA, Baranov YuN, Glinsky MA, Kolomeichenko AA. Application of nanostructured coatings by plasma spraying. *IOP Conf. Series: Journal of Physics: Conf. Series.* 2018;1058: 012046.
- 31. Kuzmin VI, Gulyaev IP, Sergachev DV, Palagushkin BV, Lebedev OY. Application of functional coatings by supersonic thermal plasma flows. *Journal of Physics: Conference Series*. 2021;2131: 052053.
- 32. Sampath S, Jiang XY, Matejicek J, Prchlik L, Kulkarni A, Vaidya A. Role of thermal spray processing method on the microstructure, residual stress and properties of coatings: an integrated study for Ni-5 W. % Al bond coats. *Materials Sci. and Engng A.* 2004;364(1–2): 216–231.
- 33. Hashemi SM, Enayati MH, Fathi MH. Plasma Spray Coatings of Ni-Al-SiC Composite. *J. of Thermal Spray Technology*. 2009;18: 284–291.

About Authors

Ilnur S. Syundyukov DSC

Research Engineer (Peter the Great St. Petersburg Polytechnic University, St. Petersburg, Russia)

Margarita A. Skotnikova 🗓 Sc

Doctor of Technical Sciences

Professor (Peter the Great St. Petersburg Polytechnic University, St. Petersburg, Russia)

Alexey Yu. Ryabikin 🗓 Sc

PhD Student (Peter the Great St. Petersburg Polytechnic University, St. Petersburg, Russia)

Accepted: September 23, 2024

Submitted: July 3, 2024 Revised: September 11, 2024

Thermal analysis of wear of polymer-polymer friction pairs in vacuum and atmosphere conditions

A.O. Pozdnyakov 1,2 10, E.B. Sedakova 2 10

ABSTRACT

A study of friction and wear of polyoxymethylene-polyoxymethylene and polytetrafluoroethylene-polytetrafluoroethylene pairs with simultaneous registration of the level of heating caused by friction has been carried out. The data obtained were analyzed both by using the energetic wear versus friction power plots and by using the solutions of finite element simulations of the thermal problem in the realistic friction geometry of the thrust bearing type used in the experiments. The solutions provide estimates of heating in vacuum and atmosphere. The calculated heating levels in vacuum suggest that triboinduced scissions of polyoxymethylene macromolecules registered by means of mass-spectrometry in polyoxymethylene-polyoxymethylene pair are initiated at temperatures below the temperatures of the onset of pure thermal decomposition of this polymer and its melting. Correlation between the presence of triboinduced scissions of macromolecules upon friction force transition, the registered exponential growth of wear upon increase of friction power in polyoxymethylene-polyoxymethylene pair and the absence of these phenomena in other pairs studied suggests that triboinduced scissions of macromolecules is governing mechanism controlling overall wear of the polymers studied. The approach was also shown to be informative in comparison of the wear of these polymers against steel and of the wear of pure polyoxymethylene and its composite with C₆₀ fullerene.

KEYWORDS

polymer • polymer composite • sliding surface temperature • friction pair • friction force • friction work wear resistance • vacuum • convection • mass-spectrometry • plastic deformations • polyoxymethylene polytetrafluoroethylene • glass transition temperature

Citation: Pozdnyakov AO, Sedakova EB. Thermal analysis of wear of polymer-polymer friction pairs in vacuum and atmosphere conditions. *Materials Physics and Mechanics*. 2024;52(4): 63–80. http://dx.doi.org/10.18149/MPM.5242024_7

Introduction

The wear process of polymers and their composites is an important practical problem [1–3]. Its experimental study consists of measurements of the main interrelated parameters: friction force (F_{fr}) , normal load (F_n) or nominal pressure $(P = F_n/S)$, where S is a nominal contact area), relative sliding speed of rubbing bodies (V) and the value of sample mass loss (Δm) . Important parameter in wear studies is a proportionality coefficient, usually called "energetic wear", between Δm and the total work spent by friction forces during the experiment $I = \Delta m/A$ ($A = \int_0^L F_{fr} \cdot dx$, where x is the current path length, L is the total friction path length). In the case of polymer materials, the role of heating is significant, due to the strong dependence of their properties on temperature. Therefore, the account of the triboinduced heating of the samples (ΔT) is needed in relation to the above parameters. Our previous works [4,5] have shown that I measured in polyoxymethylene (POM)-POM symmetric pair exponentially increases with increasing parameter $P \cdot V$. This

¹ loffe Institute, Saint-Petersburg, Russia

² Institute for Problems in Mechanical Engineering of RAS, Saint-Petersburg, Russia

[™] ao.pozd@mail.ioffe.ru

64

parameter is found in the analytical solution of diffusion equations describing heating level at the interface between two semi-infinite bodies in perfect contact (see, e.g. [6]):

$$\Delta T = \frac{2 \cdot J}{\lambda} \cdot \sqrt{\frac{k \cdot t}{\pi}},\tag{1}$$

where J is the energy flow into one of the contacting bodies, $k = \frac{\lambda}{\rho \cdot C_v}$ is the thermal diffusivity coefficient, λ is the thermal conductivity coefficient, ρ is the density, C_v is the specific heat capacity, t is time.

In [4,5] we used this equation to qualitatively judge on the trends in heating level at the interface. However, the conditions necessary to obtain the analytical solution (1) are the time-independent magnitude of the heat source during friction (specific friction power): $W = F_{fr} \cdot V/S = \mu \cdot F_{rr} \cdot V/S = \mu \cdot P \cdot V = \text{const}$ (μ is the coefficient of proportionality of the one-term Amonton-Coulomb law: $F_f = \mu \cdot F_n$, usually called the friction coefficient) and the constancy of the thermal properties of the bodies (k = const). Note, the value of W is thus equal to $P \cdot V$ parameter with an accuracy to multiplier μ . The distribution of friction power in counter body (1) and (2) is described by: $J_1 = W \cdot k_d$, $J_2 = W \cdot (1 - k_d)$, where J_1 and J_2 are flows into the bodies (1) and (2), respectively [6], k_d is the heat distribution coefficient. In real dynamic friction experiments, F_{fr} and k (see e.g. [7]) depend on sliding time at a constant F_n . Equation (1) also does not take into account heat removal by convection and radiation and thus cannot be used for long-term friction. Convection heat loss is obviously significant during friction under atmospheric conditions and is negligible in vacuum conditions. Note also that the measurements of the temperature directly at the interface is a complex experimental problem. In this regard, for real experimental conditions where the bodies of specific finite sizes and material properties are used, it is necessary to develop computational approaches that take into account the factors discussed above. Recently, the analysis of thermal problems in friction were actively carried out by using numerical methods [8–16], including the finite element method (FEM). Many studies address the solution of the inverse thermal problems in friction with at least partial account of experimental parameters (see [11] and references therein), however the relation of tribogenerated heating to polymer wear has not been sufficiently explored in recent works, though the problem was formulated in earlier studies [17].

Our studies suggest [4,5] that the scissions of macromolecules are a reason of friction force transitions from low to high level in POM-POM pair and determine the wear of the polymer. Quantitative analysis of the interrelations between transformations of macromolecules and macroscopic wear as well as understanding of the nature of these interrelations require quantitative estimates of triboinduced heating of the friction interface in the real experimental geometry. The purpose of our work is, therefore, to adapt FEM analysis to the real experimental friction geometry we are using (thrust bearing) in order to account for heat generation at friction interface and its removal by convection in the analysis of wear of model polymer-polymer friction pairs in atmosphere and vacuum conditions. The attempt is done to apply the results of simulations to the interpretation of experimental data on wear of symmetrical friction pairs polytetrafluoroethylene (PTFE)-PTFE and POM-POM. A qualitative comparison of these data with the data obtained in the case of friction of these polymers against steel was also carried out. An analysis of these issues for such friction pairs has not been found in the

literature, despite the ongoing theoretical and practical interest in this problem [18-23]. The study is important, among other things, because the friction of polymer against polymer is also realized in the case of friction of polymers against inorganic surfaces, e.g. metals, due to the formation of polymer transfer layers on their surface.

Materials and Methods

To determine F_{fr} and Δm under atmospheric conditions, a friction machine of our own design was used. The machine realizes friction in thrust sliding bearing geometry [4]. Figure 1 is a drawing of the unit that implements friction. It consists of a steel rod (1), located in the motor gearbox, driven by three-phase motor. A hollow cylinder-counterbody made of polymer (2) is tightly installed into the top face of the rod. A flat polymer or steel plate counterbody (3) fixed at steel table holder surface (4) is loaded onto the top of the hollow cylinder by normal load. The table with the plate is fixed on the top of the gyroscopically adjusted rod (5), which rotates freely in zirconium oxide rolling bearings (6). The rotation of the table (4) and rod (5) caused by the friction of the hollow cylinder, loaded onto flat plate-counterbody and rotating around its axis, is restrained by a rigid thin steel rod (not shown). One end of this thin rod is fixed at the outer radius of the table (7), and the other on a strain gauge beam (not shown).

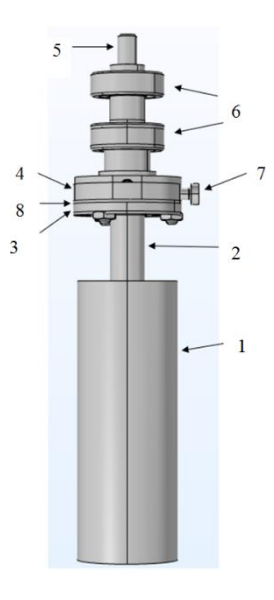


Fig. 1. General view of the friction unit implementing friction. Rotating steel rod (1), hollow cylinder counterbody (2), plate counterbody (3), steel table holder (4), rotating steel rod (5), zirconium oxide bearings (6), screw-holder (7) of the thin rod (see text) connecting the table-holder and the strain gauge beam thus constraining rod (5) from rotation, electrical and heat-insulating paper layer (8)

The force measured by the strain gauge beam is proportional to the torque created by friction [4]. This enables calculation of the friction force F_{fr} from the given radius of the outer side of the table-holder, inner and outer radii of the friction generated ring at the plate counterbody (with an accuracy of 0.1 mm the latter radii corresponded to the radii r_1 and r_2 of the hollow cylinder [4]). The table holder is covered with an electrical and thermal insulating layer of paper of around 0.5 mm thickness (8), located between

the plate (3) and the table (4). Due to its low thermal conductivity, the presence of this insulating layer increases sensitivity of the measurements of small absolute values of temperature. The flat plate is fixed to the holder table by using screws. The compression force of the tightening screws was not quantitatively measured in different experiments (this is typical for majority of the works in tribological practice). This may lead to deviations of, e.g., the thermal diffusivity of the paper layer from the value used in the calculations (Table 1).

Table 1. Material properties used in calculations

	POM	PTFE	Steel 20	Paper
ρ, kg/m³	1410.00	2200.00	7900.00	500.00
C _v , J/kgK	1470.00	1500.00	420.00	1340.00
λ, W/(m·K)	0.31	0.167÷0.300	45.00	0.04
$k = \frac{\lambda}{\rho \cdot C_{\nu}}, \text{m}^2/\text{sec}$	1.49·10 ⁻⁷	9.95·10 ⁻⁷	1.35·10 ⁻⁵	6.00 (± 2.00) 10 ⁻⁸ (see text)
T _g *, K	182.00 [24]	160.00 [24] 140.00 ÷ 400.00 [25]		
T _m **, K	442.00	600.00	1790.00	
σ_o^{***} , MPa	140.00	50.00	1000.00	

^{*} glass transition temperature

The counterbodies are hollow cylinders with a height of 18 mm, external (r_2) and internal (r_2) radii of 4.5 and 3 mm and plates with a thickness of $\sim 1-2$ mm and lateral dimensions of $\sim 15 \times 20$ mm. They were cut from industrial PTFE (PKP, PolimerkhimpromTM), POM (POM-H TiconaTM) and grade 20 steel (GOST 1050-88) material. POM-fullerene C_{60} composites were prepared by introducing a saturated solution of C_{60} in toluene into the polymer melt with constant mechanical stirring of the mixture for several minutes at a temperature of ~ 200 °C. Fullerene C_{60} powder with a concentration of $C_{60} > 99$ wt. % was used (Fullerene Technologies company). After mechanical mixing of the components, the melt was cast onto glass substrate, subjected to compression between two glass plates under a pressure of ~ 5 MPa and non-isothermally cooled to room temperature. The degree of dispersion of fullerene in the composite was not controlled at this stage of research. It can be noted that the resulting composites had a darker, light ochre color compared to the white color of the original POM. The fullerene concentration in the composite was ~ 0.5 mass. %.

The contact surfaces of the samples were grinded to a roughness of $R_a \sim 0.5 \, \mu m$, determined with a TR-200 profilometer. Before rubbing, the samples were washed with warm distilled water and dried. Friction started at room temperatures (T_{amb}) at atmospheric humidity ~ 50 %. The mass loss Δm of the samples as a result of friction was determined using Kern 770 analytical balances as the difference in the mass of the sample (both the hollow cylinder and the plate were weighed) before and after friction. Before weighing, the samples were carefully wiped with a clean, dry calico cloth to remove wear particles. The presence of the particles was controlled by using an optical microscope. The accuracy of determining the mass of samples is 0.1 mg. Experiments

^{**} melting temperature

^{***} Brinell hardness

were carried out in the range of loads F_n up to 150 N (contact pressure up to ~ 4 MPa, for the nominal contact area $S = \pi \cdot (r_1^2 - r_2^2)$ and sliding speeds up to 0.11 m/s. The temperature during friction was measured with a chromel-alumel thermocouple. The tip of the thermocouple is tightly clamped between a flat, stationary plate counterbody and an insulating paper layer located at the surface of sample holder table. The distance between the friction interface and the measuring point used in the calculations is thus estimated as the thickness of the plate counterbody in the given experiment. The accuracy of lateral position of the thermocouple tip is estimated at the level of ~ 1 mm. The values of material properties [23,24] used in FEM simulations are given in Table 1. Experiments in vacuum conditions of mass-spectrometer were earlier performed by using the friction unit of the same geometry and properties. Experiments in mass-spectrometer are discussed elsewhere [4] in more detail.

Results and Discussion

Statistics of Δm values was collected in experiments carried out in atmosphere for sliding speed V range of $0.021 \div 0.1$ m/sec (calculation based on the average radius of a hollow cylinder $0.5 \cdot (r_1 + r_2)$) and P values in the range of $0.39 \div 3.6$ MPa. Comparable statistics of around 20 measurements was collected for all pairs. Figure 2(a) shows the experimental points corresponding to all experiments performed, presented in double logarithmic coordinates $\Delta m + A$ (A is the total work of friction in the given experiment). Hollow circles show the results obtained for the PTFE-PTFE pair, gray circles - for the POM-POM pair. Data for steel-PTFE and steel-POM pairs are shown as solid and hollow squares, respectively. It can be seen that when the experimental parameters change in the same range of P and V values, the data for the POM-POM pair have an order of magnitude greater scatter compared to the PTFE-PTFE, steel-PTFE and steel-POM pairs. For PTFE-PTFE, steel-PTFE and steel-POM pairs, the dependences of Δm on A are quite satisfactorily fit by linear functions (straight lines 1,2,3). In the case of the POM-POM pair, the scatter of data does not allow us to identify a general linear dependence for all combinations of P and V. Note, however, that for fixed P and V, the dependences of Δm on A in the POM-POM pair has much smaller scatter, similar to that recorded in the PTFE-PTFE pair, and can also be described by similar linear relationships which are not shown in the figure for view convenience of the data. They shift upwards upon growth of W. These observations make it reasonable to plot the value of the proportionality coefficient between these values $(I = \Delta m/A)$ versus the value of the friction power W. These plots (Fig. 2(b)) show that for the POM-POM pair the value of I increases exponentially upon the growth of the value of W. For POM-POM pair friction coefficient is ~ 0.35 for the data shown in Fig. 2. This level of μ is detected after friction force transition $F^{min}_{fr} \rightarrow F^{max}_{fr}$ in POM-POM pair (see below in Fig. 4(a) and other examples in [4,5]). Before $F^{min}_{fr} \rightarrow F^{max}_{fr}$ transition in POM-POM pair the value of μ is ~ 0.1, close to that for other pairs studied. In these pairs no transition of friction force was detected in our dynamical friction force measurements. The mass loss of the samples at the level of friction force corresponding to $\mu \sim 0.1$ in POM-POM pair is below sensitivity level of analytical balances (± 0.1 mg). The increase in the value of I with increasing W for the pairs PTFE-PTFE, steel-PTFE and steel-POM is not obvious.

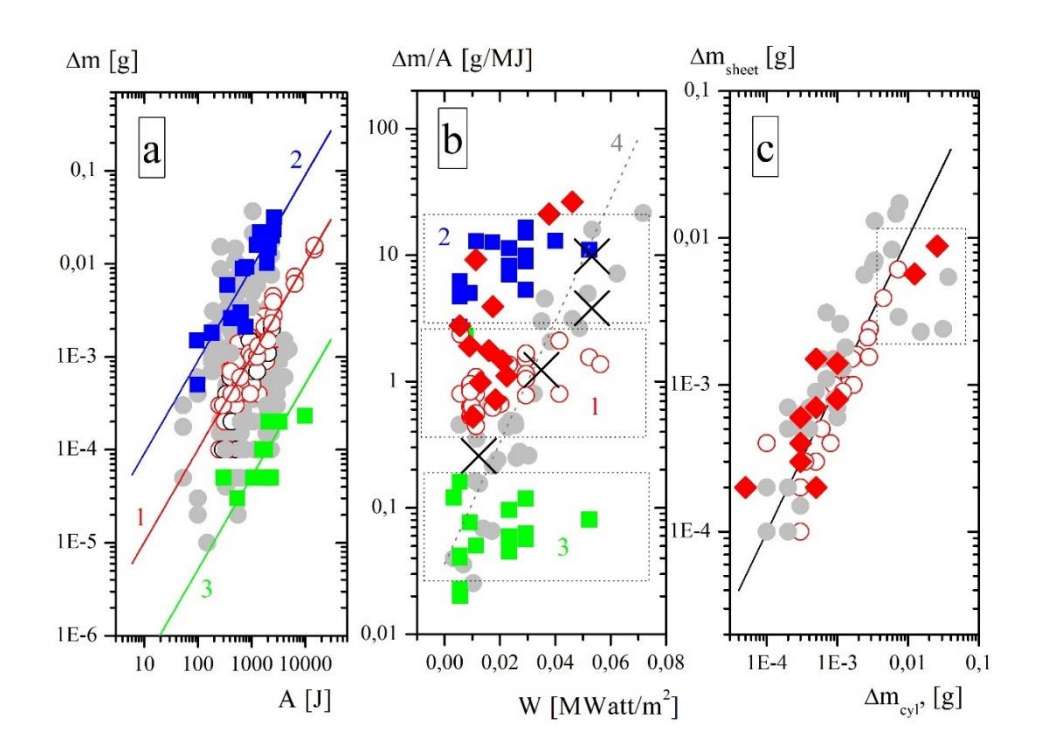


Fig. 2. (a) Dependences of Δm on the friction work (A) for experiments carried out for all combinations of P and V. Gray solid circles: POM-POM friction pair. Open red circles: PTFE-PTFE pair (line 1), solid blue squares: steel-PTFE pair (line 2), solid green squares – steel-POM pair (line 3). Double logarithmic coordinates are used; (b) dependences of the magnitude of coefficient $\Delta m/A$ on the magnitude of W for friction pairs PTFE-PTFE (box 1, open red circles), steel-PTFE (box 2, solid blue squares), steel-POM (box 3, solid green squares), POM-POM (gray solid circles around line 4). Crosses: data from experiments with the POM-POM- C_{60} pair. Solid red rhombs: POM-POM friction pairs in a vacuum. The ordinate axis is logarithmic. For symmetric POM-POM and POM-POM- C_{60} pairs the mean values of Δm of cylinder and plate counter bodies are plotted; (c) dependences of the mass loss of the stationary plate (Δm_{plate}) versus the mass loss of the cylinder (Δm_{cyl}). Gray solid circles: POM-POM pair. Open red circles: PTFE-PTFE pair. Solid red rhombs – friction experiments with POM-POM pairs in a vacuum. Double logarithmic coordinates are used

The average / values for these pairs were, respectively, 0.99 ± 0.02 g/MJ (PTFE-PTFE), 9 ± 0.7 g/MJ (steel-PTFE), and 0.03 ± 0.005 g/MJ (steel-POM).

Crosses in Fig. 2(b) show the measurements carried out at different W for the POM-C₆₀ composite upon friction against POM. It can be seen that, within the range of experimental scatter, the difference between the values of I of pure POM and POM-C₆₀ composite is difficult to distinguish. It can be assumed that the similar wear values of the composite and pure POM are due to the strong aggregation of fullerene in the matrix as a consequence of the method of mixing the components we used. Further efforts are underway to deal with the problem.

Figure 2(c) shows the dependences of the mass loss of the stationary plate (Δm_{plate}) versus mass loss of the cylinder (Δm_{cyl}) for the described experiments. The straight line in Fig. 2 shows the dependence for equal values of mass loss of the counterbodies: $\Delta m_{\text{plate}} = \Delta m_{\text{cyl}}$. It is seen that for the PTFE-PTFE pair, the experimental points (hollow circles) are located near this dependence. This implies even wear of plate and cylinder in

this pair. In the case of POM-POM pair, the experimental points obtained for W < 0.03 MW/m² are also located around this dependence, thus indicating even wear of the plate and the cylinder at low friction powers. However, for W > 0.03 MW/m² (points highlighted by the box in Fig 2(c)), the measurements show strong increase in wear of the POM cylinder compared to wear of POM plate. Similar results were obtained in the case of POM-POM friction in vacuum (solid red rhombs highlighted by the box in Fig. 2(c)). Note here that for these vacuum experiments with POM-POM pair (solid red rhombs in Fig. 2(b)), the values of I are located above the characteristic exponential dependence of I versus W for the POM-POM friction pair under atmospheric conditions (line 4). This suggests higher heating at friction interface due to the absence of heat removal by convection in vacuum. For other pairs the $I \div W$ dependences in $P \cdot V$ range accessible in our vacuum friction machine ($P \cdot V$ up to ~ 0.15 MPa·m·sec⁻¹) were comparable in vacuum and in atmosphere. Recall, the value of W is equal to more widely used in practice $P \cdot V$ parameter with an accuracy to multiplier equal to friction coefficient μ .

The experimental data described above qualitatively suggest that growth of W and hereto related increase in heating in the POM-POM pair result in transition from even wear of the cylinder and the plate to increased wear of the cylinder compared to the plate. This effect is not observed in the PTFE-PTFE pair in the range of W studied. This suggests that tribogenerated heating does not result in uneven wear in this pair and does in POM-POM pair. The small and comparable scatter of the $\Delta m \div A$ dependences for the steel-POM and steel-PTFE pairs may also indicate a negligible effect of heating on wear in these friction pairs.

As shown in [4,5], the mechanism of POM wear in the thermodynamically compatible POM-POM pair is reasonably interpreted by triboinduced scissions of POM macromolecules in a shear field. By using mass-spectrometry it was shown [4] that the scissions initiate $F^{min}_{fr} \to F^{max}_{fr}$ transition in POM-POM pair. For PTFE-PTFE, steel-PTFE and steel-POM and other POM-polymer pairs studied in [4], neither friction force transitions nor macromolecular volatile products of scission are recorded at comparable initial W levels. This is in good accord with the absence of changes in I upon growth of W level in PTFE-PTFE pairs, steel-PTFE and steel-POM pairs (see above discussion of Fig. 2(b)). The exponential dependence of I on W in the POM-POM pair measured after $F^{min}_{fr} \to F^{max}_{fr}$ transition covers the range of I in all three other pairs studied (highlighted by boxes in Fig. 2(b)). The effects described above make a more detailed quantitative analysis of tribogenerated temperatures at the friction interface important and is considered below.

Simulation method and Discussion

To calculate tribo-induced heating (ΔT), preliminary modeling of the friction geometry of the friction unit (Fig. 1) used in the work has been carried out. The main part of the unit, which realizes friction *per se* in the geometry of the thrust bearing, is shown in Fig. 3(a). Simplifications made to construct the model shown in Fig. 3(a) were justified by the following factors. In real friction geometry, zirconium oxide ball bearings (6 in Fig. 1), located in a lining of the same material, do not move when friction experiments are performed and have very low thermal conductivity. The area of their contact with the bearing lining is also vanishingly small compared to the contact areas of other objects in

the model. In this regard, they were not used in the calculation geometry used. Calculations also show that the increase of the size of steel rods (1,5 in Fig. 1) above that used in simulations described below led to negligible (at the level of 1 K) changes in the resulting temperature dependencies. Account of small machine parts of the real drawing (Fig. 1) resulted in negligible changes to these dependencies and were not modeled.

Mathematically, heating processes can be described by solutions of non-stationary diffusion equation of the form [26]:

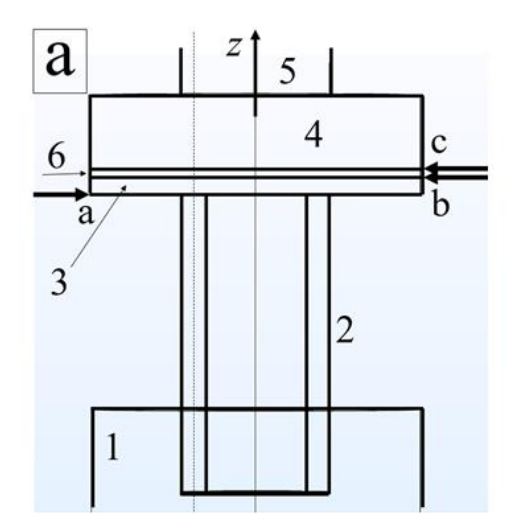
$$\frac{\partial T}{\partial t} - k \cdot \nabla^2 T = 0, \tag{2}$$

with given boundary and initial conditions. The equation assumes infinite heat propagation velocity and serves as first approximation for more realistic models [27]. To analyze the thermal problem, we developed calculation programs in the Comsol Multiphysics6.2™ software package for numerical calculations using FEM [28,29] based on Galerkin type methods [30]. Its use greatly simplifies the analysis of three-dimensional temperature distributions in contacting bodies and the time dependences of ΔT . To analyze the thermal problem in the geometry discussed above, the *Heat Transfer in Solids* simulation block was used, which implements the solution of Eq. (2) using FEM, in combination with the non-stationary simulation block Time Dependent Study. Geometric regions were meshed into a grid of tetrahedrons with their size decreasing near the interface by using the procedure of creating boundary layers. The boundary conditions associated with heat transfer by convection were specified at all surfaces of the objects constituting the geometry except their ends. Note, heat fluxes by radiation constituted a small fraction of the total flux, therefore this heat removal channel was not directly taken into account in the calculations. However, it is implicitly included in the total heat removal, taken into account by the effective convective heat removal coefficient (see below).

FEM calculations using realistic experimental geometry were preliminary compared to analytical solutions of model thermal problems. For a one-dimensional diffusion equation for two semi-infinite bodies in perfect planar contact, with a time-independent energy flow J at the interface $(J = -\lambda \cdot \frac{\partial T(0,t)}{\partial z})$, the analytical solution for the temperature distribution in the direction perpendicular to the interface has the form [6]:

$$\Delta T = \frac{2 \cdot J}{\lambda} \cdot f(q) \cdot \sqrt{\frac{k \cdot t}{\pi}},\tag{3}$$

where $f(q) = e^{-q^2} - 2 \cdot q^2 \cdot \int_1^{\infty} d\eta \cdot e^{-\eta^2 \cdot q^2}$, $q = \frac{z}{\sqrt{4 \cdot k \cdot t}}$, z is the coordinate in the direction perpendicular to the interface, J is the heat flow into one of the contacting bodies. This ideal geometry obviously does not account for convective and radiative fluxes. In Fig. 3(b), curve 1 shows the calculation obtained by using FEM for the case of contact between the flat top ends of two identical solid cylinders (their full length is the same as the length of the full realistic geometry, radius 10 mm, that is maximum radius in real geometry) made of POM without account for heat removal by convection. Calculation parameters used are mean value of F_{fr} from friction force dependence in Fig. 4(a) (27 N), heat distribution coefficient $k_d = 0.5$ and time of friction 900 sec. This simplifies comparison with experimental data analysis of symmetric pairs. This profile reflects



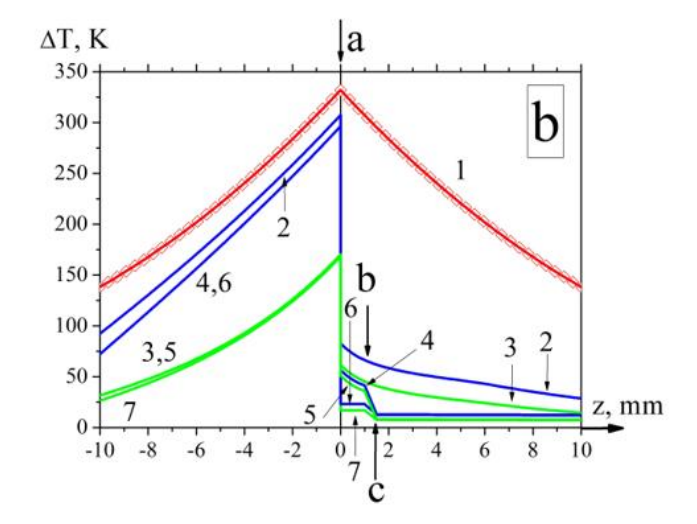


Fig. 3. (a) Side view of the geometry of the friction unit used in FEM simulations. Steel rod (1), hollow cylinder made of PTFE or POM (2), plate counterbody made of POM, PTFE or steel (3), steel table-holder (4), located on a freely rotating steel rod (5), paper insulating layer (6). Radii of cylinder rod (1) and table table holder (4) used in calculations are: $r_0 = 10$ mm. Size of the hollow cylinder (2): height 18 mm, outer (r_1) and inner (r_2) radii: 4.5 and 3 mm, thickness of the counterbody plate 1 mm, thickness of the insulating layer 0.5 mm. The depth of insertion of the hollow cylinder into the rod is 5 mm. The length of the rod (1) and cylinder (5) used in the calculations was chosen to be equal to 70 mm; (b) temperature distribution profiles along the z axis shown in fragment (a). 1 is the profile obtained by using FEM without a heat removal for a model of two identical solid POM cylinders with a radius $r_0 = 10$ mm in contact of their flat top ends. The open rhombs around curve 1 show the analytical solution obtained using Eq. (3) (F_{fr} = 27 N, t = 900 sec in both calculations, see text). Profiles 2-7 were obtained for real geometry given by the fragment (a) along dashed curve located at the center of the edge of the hollow cylinder (see text). Profiles 2 (blue), 3 (green) – all machine parts have POM material properties, h = 0 Watt/($m^2 \cdot K$)), $3 - h = 8 \text{ Watt/(m}^2 \cdot \text{K)}$, respectively. Profiles 4 (blue), 5 (green) – machine parts have material properties of real friction unit, friction pair POM-POM, h = 0 Watt/(m^2 ·K) and h = 8 Watt/(m^2 ·K), respectively. Profiles 6, 7 the same for friction pair POM (cylinder)-steel (plate), h = 0 Watt/(m²·K), h = 8 Watt/(m²·K), respectively. Arrows a, b, c show the interfaces between the cylinder and the plate, between the plate and the insulating layer, between the insulating layer and the steel table-holder, respectively

the temperature distribution in the center of the solid cylinders along z axis (Fig. 3(a)). Points in Fig. 3(b) show the solutions obtained by using Eq. (3). It can be seen that the analytical solutions agree with the results of FEM simulations with high accuracy. Near the ends of the cylinders, that is, at a considerable distance from the friction interface, slight deviations from analytical solutions are observed (not shown).

The temperature distributions along the radius of a solid cylinder obtained in FEM simulations were also analyzed. Boundary conditions at the surfaces of objects caused by heat removal by convection are described by relation: $\lambda (dT/dn)_{n=0} = -h \cdot (T_{n=0} - T_{amb})_{n=0}$, where n is the value of the corresponding coordinate, and the origin of coordinates is associated with the boundary, h is the heat removal coefficient [27]. They were compared to the analytical solution for the temperature profile along the radius of the cylinder of infinite length cooled by convective heat removal from external surfaces characterized by heat removal coefficient h (the solution of the diffusion equation by the method of separation of variables is described, e.g., in [27]):

$$\theta = \theta_o \cdot \sum_{n=1}^{\infty} \frac{2 \cdot J_1(\mu_n)}{[J_o(\mu_n)^2 + J_1(\mu_n)^2]} \cdot J_o(\mu_n \cdot \frac{r}{r_o}) \cdot exp(-\mu_n^2 \cdot \frac{k \cdot t}{r_o^2}), \tag{4}$$

72 A.O. Pozdnyakov, E.B. Sedakova

where t is time, $\theta = T(t,r) - T_{amb}$ and $\theta_o = T_{init} - T_{amb}$ are the current and initial temperatures relative to the ambient temperature T_{amb} , respectively, $T(t=0,r) = T_{init}$ is the condition of the same temperature over the entire cylinder prior to cooling, J_o and J_1 are Bessel functions of the zero and first order, respectively, μ_n are parameters determined graphically by solutions of the equation $\frac{J_o(\mu)}{J_1(\mu)} = \frac{\mu}{Bi}$, $Bi = \frac{h \cdot ro}{\lambda}$ (Biot number), r_o is the radius of the cylinder, r is the distance from its center along the radius. In this case, the dome-shaped profiles (not shown) of the ΔT distribution along the radius of the cylinder with the maximum ΔT in its center calculated by using FEM coincided with the analytical solutions (Eq. (4) with four series number was used) with the same high accuracy as in the example of ΔT profiles along the cylinder axis discussed above. The mesh parameters of the geometry used in the above model FEM calculations were applied in the calculations of the real geometry (Fig. 3(a)) used for fitting the experimental ΔT dependences reported below.

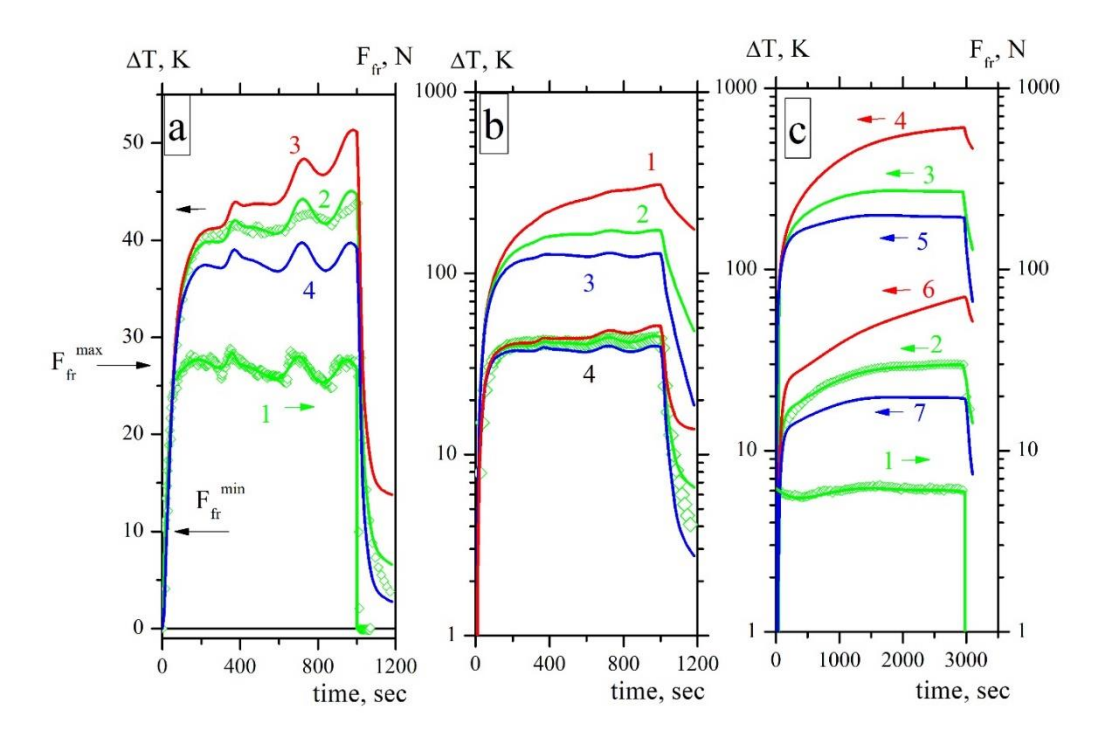


Fig. 4. (a) Example of synchronous measurements of friction force (open green rhombs 1 with an arrow in the direction of the right axis) and temperature (open green rhombs 2) for a POM-POM friction pair. Curve 1 shows the approximation of the experimentally measured dependence $F_{fr}(t)$ used in FEM calculations. Curve 2 shows the FEM calculation of heating at the measurement point for h = 8, red curve 3 for h = 0 Watt/(m²-K), blue curve 4 for h = 16 Watt/(m²-K). Friction conditions: V = 0.021 m/sec, $F_n = 72$ N. The signal recording step used is ~ 0.5 sec. The thickness of the counterbody plate is ~ 0.5 mm; (b) FEM prediction of the level of heating at the friction interface on the side of hollow cylinder (Fig. 3(b)) for the same experiment as that used in the fragment (a). Red curve 1: h = 0 Watt/(m²-K), green curve 2: h = 8 Watt/(m²-K) (curve 2), blue curve 3: h = 16 Watt/(m²-K). Curves in area 4 are curves 2,3,4 from the fragment (a); (c) example of synchronous measurements of friction force (open green rhombs 1) and temperature (open green rhombs 2) for a PTFE-PTFE friction pair. Green curve 3: FEM prediction of heating level at the friction interface on the hollow cylinder side (Fig. 3(b)) for h = 8 Watt/(m²-K), red curve 4: h = 0 Watt/(m²-K), blue curve 5: h = 16 Watt/(m²-K). Curves 6 and 7: simulated heating level at the measurement point for h = 8 Watt/(m²-K) and h = 16 Watt/(m²-K), respectively. Friction conditions: V = 0.11 m/sec, $F_n = 72$ N. Counterbody plate thickness ~ 1.5 mm

Curves 2–7 in Fig. 3(b) show the calculated ΔT profiles along the cylinder axis for a real friction unit. In this case, shown are profiles along a line located at the center of the edge of the hollow cylinder at radius $r = (r_1 + r_2)/2$ parallel to the axis z. The calculation for $F_{fr}(t)$ dependence for POM-POM pair presented in Fig. 4(a,b) for time of friction of 900 sec is used for illustration. Arrows a, b, c in Fig. 3(b) indicate locations of friction interface, the interface between the plate-counter body and the insulating layer, the interface between the layer and the surface of steel sample holder, respectively. The initial condition in the calculations was chosen to be constant temperature of all objects in the model, equal to the ambient temperature (T_{amb} , in the calculations it is set as the initial temperature prior to onset of friction). The boundary conditions in the calculations were the function of the power of the plane heat source at the friction interface ($W(t) = F_{fr}(t) \cdot V/S$) determined from the experimentally measured dependence $F_{fr}(t)$ and the heat removal by convection from the outer surfaces of contacting bodies except the ends of the steel rods. The characteristic features of the profiles are typical for all other calculations. In general terms, they reveal lower level of heating for the real geometry even for h=0 Watt/ $(m^2 \cdot K)$ (curves 2,4,6) compared to ideal geometry consisting of 2 solid POM cylinders (curve 1). This is due to the presence of steel mechanical parts with high thermal conductivity (rods and plate holder, Fig. 1) in real geometry. This shows that the use of Eq. (1) strongly overestimates calculated temperatures of our real geometry at large friction times and can be used only for qualitative estimates even in the case of absence of convection. As a reference, profiles 2 and 3 present the calculation of real geometry where all parts of the friction unit have material properties of POM. In real geometry containing steel machine parts in the friction unit (rotating and fixed steel rods, Fig. 1) the profiles have the shape of curves 4,5 for h = 0 Watt/($m^2 \cdot K$) and h = 8 Watt/($m^2 \cdot K$). In the case of the same real geometry where plate counterbody has material properties of steel, the profile is more uniform across the thickness of the steel plate counterbody (curves 6,7). The calculations discussed below were carried out for measurement point located at a distance equal to the thickness of the plate, that is at the location of chromel-alumel thermocouple tip firmly clamped between the plate and the surface of the steel table holder covered with insulating layer. Note, in the context of thermal problem considered, the role of insulating layer is to increase the ΔT level within the plate, thus increasing the magnitude of the measured level of absolute temperature. In the calculations of symmetric friction pairs, we used the equal distribution of W in upper (1) and lower (2) counterbodies, that is for heat distribution coefficient $k_d = 0.5$ ($J_1 = J_2 = W/2$) consistent with Sharron formula valid for semi-infinite bodies [31]. This is a reasonable approximation for our calculations of symmetrical friction pair, e.g. POM-POM characterized by nonlinear dependence of I on W (Fig. 2(b)).

In the context of this study another important observation from Fig. 3(b) is the higher temperature level on the side of polymer cylinder compared to that on plate side in our geometry. This difference appears and increases with increasing time of friction. This effect is mainly determined by the difference in the lengths of the polymer cylinder and plate (~ 20 times) in contact with steel rods-holders (Fig. 1). It can also be seen that account of heat removal by convection (h = 8 Watt/($m^2 \cdot K$)) leads to a decrease in heating levels. They are easily visually discerned Fig. 3(b)) in profiles for different pairs in the area of the plate and less visually discerned in the area of cylinder. The higher level of heating

near the interface on the side of hollow cylinder is in good agreement with the increase of its wear discussed in previous section for high W levels in the POM-POM pair (Fig. 2(c)). The similarity in cylinder and plate wear at low W in POM-POM pair seems to indicate that in this range of W in the POM-POM pair, wear is weakly dependent on the level of heating at the interface. Recall that the absence of the wear growth of the cylinder in the PTFE-PTFE pair (Fig. 2(c)) also indicates negligible effect of heating on PTFE wear in the entire range of W used in this study.

Figure 4 shows examples of heating calculations of two typical temperature measurements in real thrust bearing geometry for the POM-POM (Fig. 4(a,b)) and PTFE-PTFE (Fig. 4(c)) pairs. In these experiments the normal load was the same, the sliding speed velocity V is 5 times higher in the case of PTFE-PTFE pair. Many additional examples of the behavior of friction force exhibiting typical $F^{min}_{fr} \rightarrow F^{max}_{fr}$ transitions (horizontal arrows in Fig. 4(a)) in POM-POM pair [4,5]. At lower W compared to the one shown in Fig 4(a) the $F^{min}_{fr} \rightarrow F^{max}_{fr}$ the path length for transition in POM-POM required to occur increases. For the pairs PTFE-PTFE (Fig. 4(c)), PTFE-steel and POM-steel, no transition is observed in the range of W studied. In these pairs the experimentally measured temperature dependences for these pairs were similar at given W. Note here that it would also be a case in POM-POM pair if this pair would not exhibit $F^{min}_{fr} \rightarrow F^{max}_{fr}$ transitions. The simulations of the experimental dependences for asymmetric PTFE-steel and POM-steel pairs meet the complexities of formulation of the thermal model e.g. discussed below in the text in terms of heat distribution coefficient and are not considered in this paper.

In Fig. 4(a), curve 1 shows a nonlinear approximation (polynomials with an order close to 7 were used) of the experimentally determined $F_{fr}(t)$ (open rhombs) time dependence at constant V. In calculation of $W(t)=F_{f}(t)\cdot V/S$ required for FEM simulations as a boundary condition, we used average sliding speed at the center of the contact edge $V = \pi \cdot (r_1 + r_2) \cdot \upsilon$ (υ [Hz] is a rotation frequency of the hollow cylinder). S was put equal to nominal contact area $S = \pi \cdot (r_1^2 - r_2^2)$. It can be seen that the shape of the experimentally measured temperature dependence $\Delta T(t)$ (open rhombs around curve 2) is best fit by simulated temperature dependence (curve 2) obtained for the measurement point (~ 0.5 mm from the friction zone) using a heat removal coefficient value of 8 Watt/(m²·K) for all objects of the experimental geometry (Fig. 3(a)). This value is close to mean value $(h = 8.48 \text{ Watt/(m}^2 \cdot \text{K}))$ obtained in [23] by calculations of convection problem under assumption of laminar air flow for PTFE samples of the similar shapes and dimensions used in our work as well as in the same friction geometry. It can be also noted that the calculation of cooling after the friction is ceased (the case of cooling the friction joint as a whole unperturbed by friction) best fits the experimental curves also for $h = 8 \text{ Watt/(m}^2 \cdot \text{K)}$. The dependence of the calculated temperature at the measurement point for h = 0 Watt/(m²·K) and h = 16 Watt/(m²·K) are shown by curves 3 and 4 (Fig. 4(a)), respectively. The value h = 0 Watt/($m^2 \cdot K$) describes the vacuum conditions with an accuracy to heat removal by radiation. More smooth fitting curves, characterized by reduction in absolute temperature values not exceeding 1 K, can be obtained by twice increase in the lengths of the steel rods 1, 5 (Fig. 3(a)) in the geometry simulated. However, in this work we did not set the task to fully optimize the experimental parameters. This requires complicated study of inverse thermal problem (see, e.g. [11] and references therein). Note here that Fig. 4(a) shows that the temperature increment at the measurement point during friction in vacuum (h = 0 Watt/($m^2 \cdot K$), curve 3) compared to the case of friction in atmospheric conditions (h = 8 and 16 Watt/($m^2 \cdot K$), curves 2,4) is ~ 5–10 K.

The calculations help in quantifying the possible reasons of changes in the experimentally measured heating level at the measurement point for given h. Reference test calculations have shown that the change in the absolute value of ΔT , calculated at the measurement point (located at a distance from the friction interface equal to the thickness of the plate), can reach ~ 10 K when its coordinate changes along the plane of the plate from the center of the hollow cylinder to its edge. Changes in this value related to a possible change in the thermal diffusivity of the insulating paper layer under the plate counterbody upon its mechanical tightening to the table holder by using screws (see discussion in the previous section and Table 1), can also reach ~ 10 K. Increase in the accuracy of measurements would increase the accuracy of calculations of temperature at the measurement point. This can obviously be achieved also by using a more accurate approximations of the experimental dependences $F_{f}(t)$, more advanced methods of positioning of the thermocouple, account of its inertia [11,14] and, probably, precision in the size of the samples. However, certain differences in the thermal diffusivity of paper insulating layer as a consequence of not yet measured degree of tightening of the screws required for firm fixation of the plate counterbody in each experiment alter the calculated value of maximum ΔT at the friction interface by a value not exceeding one Kelvin.

An additional increase in the accuracy of calculations and fitting procedure can be further achieved by taking into account the dependence of the sliding speed on the radius of the cylinder and the edge effects in contact pressure. The use of smaller time steps in recording temporal evolution of the measured F_{fr} and ΔT is also promising. For example, in a more realistic case of plastic contact of the asperities of rough surfaces, the area of real contact (A_0) can be estimated from the relation: $A_0/S \approx P/\sigma_0$ [6] (plasticity limit in compression or Brinell hardness, σ_o , see Table 1). In our experiments P reaches \sim 4 MPa, i.e. the actual contact area can be a few percent of the nominal one. The friction time of roughness tips of size $D \sim 1$ µm before leaving the contact is $D/V \sim 10^{-4}$ s. Using relation $J = 0.5 \cdot \mu \cdot \sigma_o \cdot V$ ([6] and references therein), the sufficiently precisive at this short time range, from Eq. (1) we obtain upper estimate of the calculated ΔT of a single flash on a roughness in vacuum at the level strongly below 1 K. The small magnitude of temperature flashes and small heat penetration depths of these flashes into the subsurface layers of around several micrometers [6,32] suggest that they would introduce small high-frequency contribution to our calculation of heating performed by taking into account the nominal contact area. Oscillatory heating behavior (Fig. 4(a)) observed for the POM-POM pair with a characteristic oscillation time around tens of seconds accords well with the behavior of F_{fr} and reflects more smooth processes of tribo-induced structural changes at the interface. Analysis of the complete pattern and accuracy of temperature measurements, including account of wear debris particles, is out of range of this paper. These questions are the subject of ongoing research, in particular with acoustic emission methods since in POM-POM pair the clearly detected noise in acoustic region is detected. It is absent in other pairs studied. This study requires analysis of elastic waves generation which are expected to be in complicated relation to heat flow in the case of mutual sliding of wavy surfaces [33,34].

Curves 1–3 in Fig. 4(b) show the predictive calculation of the temperature versus time dependences at the friction interface on the side of the cylinder (see explanation to profiles in Fig. 3) for h = 0 Watt/(m²·K), h = 8 Watt/(m²·K) and h = 16 Watt/(m²·K). For convenience of comparison, the curves located around experimental points in Fig. 4(b) are the curves 2-4 from Fig. 4(a). From Fig. 4(b) it is seen that the temperature at the interface in vacuum becomes approximately 120 K higher than that in air conditions $(h = 8 \text{ Watt/(m}^2 \cdot \text{K}))$ upon friction. This reasonably explains the increase in energetic wear during friction in vacuum (red solid rhombs, Fig. 2(b)) compared to friction in atmospheric conditions (gray circles, Fig. 2(b)) at the similar levels of W. Sharp increase in ΔT occurs upon friction force transition $F^{min}_{fr} \rightarrow F^{max}_{fr}$ (horizontal arrows in Fig. 4(a)). As is shown in our works [4,5] the transition is accompanied by formation of the tribodecomposition products of POM macromolecules. Note that the amount of tribodecomposition products formed grows with initial level of W [4]. Our suggested mechanism of the formation of tribodecomposition products at these low temperatures is interpenetration of the POM macromolecules across friction interface [4,5], their orientation and scission. Calculations of ΔT in real geometry for various $F_{t}(t)$ measurements performed at various W (e.g. from data obtained in the vacuum of mass-spectrometer given in [4,5]) show that all the transitions of the friction force $F^{min}_{fr} \rightarrow F^{max}_{fr}$ in the POM-POM pair are initiated at temperatures at the interface not exceeding ~ 50 °C both in atmosphere and vacuum conditions. The formation of decomposition products and the simultaneous increase in the friction force in the POM-POM pair at these temperatures excludes both melting of polyoxymethylene ($T_m \sim 170 \, ^{\circ}\text{C}$ [25]) and the lowest, the less intense, pure thermal decomposition stage of this polymer observed in the thermal decomposition spectra of friction transferred submicron layers of POM at temperatures above 110 °C [4]. Note here that this stage is not yet firmly attributed to the decomposition of intact POM since, due to difficulty of dissolution of POM, thin layers of this polymer could be formed [4] at the substrate only by rubbing POM sample against it. The main stages of thermal decomposition undoubtedly related to decomposition of intact POM start to appear above 200 °C.

The P and V conditions of the experiment in Fig. 4(b) provide estimate of the W value of ~ 0.015 MWatt/m² after $F^{min}_{fr} \rightarrow F^{max}_{fr}$ transition (μ ~ 0.35) in POM-POM pair (initial W before transition ~ 0.005 MWatt/m²), at which the temperature at the interface in air conditions can reach around 170°C, that is the melting temperature of POM. Note that $F^{min}_{fr} \rightarrow F^{max}_{fr}$ transition is also observed for much lower levels of initial W [5]. In the imaginary experiment in vacuum (h = 0 Watt/($m^2 \cdot K$)) for the same $F_{fr}(t)$ dependence (Fig. 4(b)), the temperature at interface would attain ~ 300 °C (curve 1). Heating calculations for various experimental $F_{tr}(t)$ dependences obtained in vacuum of ~ 10⁻⁶ Torr for the POM-POM pair (see, e.g., [4,5]) predict heating strongly above 300 °C after the transitions $F^{min}_{fr} \rightarrow F^{max}_{fr}$. These temperatures correspond to the temperatures of almost complete thermal decomposition of thin submicron layers of POM (see the thermal decomposition spectra of friction generated submicron thickness POM layers in [4]). This implies very strong growth of the mass-spectral lines of the thermal decomposition products of POM. However, the simultaneously recorded [4,5] intensity of the formation of POM decomposition products (oxymethylene and trioxane), expected to increase sharply at these high temperatures, on the contrary, reaches saturation and practically does not change with increasing friction time at these high predicted temperatures. The ratio of oxymethylene and trioxane in the spectra also does not change, though in the case of pure thermal mechanism of POM decomposition, increase in the contribution of the intensity of oxymethylene would be expected, since oxymethylene is the only product of POM mass-spectrum upon pure thermal decomposition [4] at the same sensitivity of the registration channel of mass-spectrometer. It can be assumed that the absence of strong increase in the intensity of decomposition products in POM-POM pair in vacuum upon long friction time after $F^{min}_{fr} \rightarrow F^{max}_{fr}$ transition might indicate specific and not yet understood behavior of the friction interface at melting point which can alter its thermal characteristics. This might be accounted for in further development of the simplified thermal model we use by considering heat effects associated, e.g., with formation of active macroradicals in air and vacuum as well as other concomitant phenomena.

In asymmetric friction pairs (e.g. polymer-steel) described above in the previous section in terms of *I-W* plots, the distribution of tribogenerated energy into contacting bodies can be described by a heat distribution coefficient k_d not equal to 0.5 used in our calculations of symmetric pairs POM-POM and PTFE-PTFE. The calculation shows that change in the value of k_d by ~ 5 % can lead to a change in the heating level at the interface by ~ 10 K. This issue can become important in the study of heterogeneous friction pairs where the macromolecular scissions and the related change in wear observed in POM-POM pair would be found. Note additionally, in the case of asymmetric pairs the polymer transfer layer may continuously change the heat transfer coefficient (e.g. for steel-PTFE pair the qualitative estimate of Sharron formula gives high k_d value of ~ 0.9 [23]) towards the $k_d \sim 0.5$ value for symmetric pair. This requires additional modifications of the model not yet considered in the current work. In this regard note, that in the work [5] we presented the data on friction and wear of POM against polyetheretherketone (PEEK). PEEK has thermal properties close to those of POM. Thus, k_d in this pair is expected to be close to 0.5. Nonetheless, the effects we observed in [5] for POM-PEEK pair are similar to those we observe in this work in the case of polymers sliding against steel, i.e. stable behaviour of friction force, absence of the $F^{min}_{fr} \rightarrow F^{max}_{fr}$ transitions characteristic for POM-POM pair, absence of the dependence of I on W and absence of the decomposition products of both POM and PEEK. This additionally implies that friction force transitions and the related wear behavior are rather dependent on the molecular mechanisms initiating scission of macromolecules and are dependent on the nature of the polymers in contact.

The calculated maximum heating temperatures in PTFE-PTFE pair in air conditions for typical value of $\mu \sim 0.1$ are strongly lower than in POM-POM pair at the same initial (before $F^{min}_{fr} \rightarrow F^{max}_{fr}$ transition in POM-POM pair) level of W. This is due to around three times higher μ in POM-POM pair after $F^{min}_{fr} \rightarrow F^{max}_{fr}$ transition. E.g., for initial levels of W of ~ 0.03 MW/m², calculated heating temperatures at the interface during friction under atmospheric conditions exceed values of $\Delta T \sim 400$ K for POM-POM pair (not shown) compared to $\sim 200-300$ K in PTFE-PTFE pair (Fig. 4(c)). Heating at the level of $\Delta T \sim 400$ K already corresponds to temperatures of intense thermal decomposition of POM macromolecules [4], but are somewhat lower than similar temperatures for PTFE (see analysis of the thermal decomposition spectra of a number of depolymerizing polymers in [35]). The absence of friction force transitions in PTFE-PTFE, steel-POM, and steel-PTFE pairs and the absence of thermal decomposition products of these polymers

during friction of these pairs in vacuum measured in [4,5] may indicate that wear of these pairs in vacuum at the levels of W used in these works (up to $\sim 0.005 \text{ MW/m}^2$) is not a consequence of tribo-induced ruptures of macromolecules or of their pure thermal decomposition and have, thus, pronounced mechanical nature.

The use of higher initial W values requires more advanced technical means of friction realization in vacuum. It is to note, with this regard, that the example of friction force measurements with PTFE-PTFE pair ($W \sim 0.02 \text{ MW/m}^2$) in atmosphere conditions shown in Fig. 4(c) corresponds to V value five times higher than those used up to now in our vacuum measurements [4,5]. It is seen from the figure, that, similar to the case of POM-POM pair discussed above, the experimentally measured temperature dependence at measurement point is best fit by using simulated curve for experimentally measured $F_{fr}(t)$ and for $h = 8 \text{ Watt/(m}^2 \cdot \text{K)}$ (Fig. 4(c), curve 2). The simulations with other values of h are described in figure captions. As is seen, at this high sliding velocity, FEM calculations for $h = 0 \text{ Watt/(m}^2 \cdot \text{K)}$ predict that heating of PTFE-PTFE interface in vacuum would attain $\sim 600 \, ^{\circ}\text{C}$ (curve 4, Fig. 4(c)), that is, the temperatures of intense thermal decomposition of PTFE [35]. This would imply the formation of large quantities of PTFE monomer: tetrafluoroethylene. Experimental verification of this prediction awaits further experimental research.

Conclusions

- 1. In order to quantify experimentally measured friction generated temperatures and predict the temperatures at the friction interface from the measured friction force dependences, finite elements simulations in realistic thrust bearing geometry used in the study have been developed with account for atmospheric and vacuum conditions via heat convection coefficients.
- 2. The simulation approach is shown to give significant improvements in the accuracy of the temperature calculations compared to analytical solutions. The approach provides the estimate of the heating level required to initiate triboinduced scissions of POM macromolecules observed *via* the mass-spectrometric registration of the triboinduced volatile products, differing from those registered upon pure thermal decomposition of POM. This level is estimated to be below the temperatures of melting and intense thermal decomposition of POM, thus supporting triboinduced nature of bond scissions. The absence of the increase of the decomposition products formation in the friction regimes at simulated heating level corresponding to the intense thermal decomposition of POM above melting point of this polymer suggests that the mechanism of pure thermal decomposition of macromolecules cannot explain the wear behavior in POM-POM pair and requires the presence of triboinduced scissions of macromolecules formed at the early stages of friction upon friction force transition from low to high level.
- 3. The simulations are in good accord with the exponential dependence of energetic wear on the level of friction force power observed in the case of friction of POM-POM and absence of changes of energetic wear with friction power in other pairs studied. The energetic wear of polymer-polymer and polymer-steel pairs not accompanied by scissions of macromolecules and friction force transitions (PTFE-PTFE, POM-steel, PTFE-steel) is shown to be independent on the level friction power and on the triboinduced heating. The

energetic wear in these pairs was obtained to be: $I \sim 1$ g/MJ (PTFE-PTFE), ~ 10 g/MJ (steel-PTFE) and $I \sim 0.03$ g/MJ (steel-POM). In the POM-POM pair before friction force transition, associated with macromolecular bond scissions, the wear of POM was below sensitivity of the balances used. It might be thus suggested that I before friction force transition in POM-POM pair also does not depend on friction power and might be estimated to not exceed the level of the lowest value registered in the study of ~ 0.03 g/MJ.

4. The approach developed provides new strategies and instruments for the research of practically important problem of friction and wear of polymers and their composites. For example, the approach has been shown to be informative in comparing wear of POM and its composite with fullerene.

References

- 1. Friedrich K, Schlarb AK. (eds.) Tribology of Polymeric Nanocomposites. Butterworth-Heinemann; 2008.
- 2. Yumashev A, Mikhaylov A. Development of polymer film coatings with high adhesion to steel alloys and high wear resistance. *Polymer Composites*. 2020;41(7); 2875–2880.
- 3. Chichinadze AV. (ed.) Osnovi Tribologii (trenie, iznos, smazka). Moscow: Mashinostroenie; 2001. (In Russian)
- 4. Pozdnyakov AO. Formation of Decomposition Products of Macromolecules Upon Friction of Polymer Against Polymer. *Tech. Phys. Lett.* 2023;49: 108–111.
- 5. Pozdnyakov AO, Syanshun L, Sedakova EB. Molecular Mechanisms of Polyoxymethylene Wear. *Journal of Friction and Wear*. 2024;45(1): 24–31.
- 6. Persson BNJ. Sliding Friction. Verlag: Springer; 2000.
- 7. Conte M, Pinedo B, Igartua A. Frictional heating calculation based on tailored experimental measurements. *Tribol. Int.* 2014;74: 1–6.
- 8. Grzes P. Determination of the maximum temperature at single braking from the FE solution of heat dynamics of friction and wear system of equations. *Numerical Heat Transfer, Part A: Applications*. 2017;71(7): 737–753.
- 9. Grigoriadis K, Mavros G, Knowles J, Pezouvanis A. Experimental investigation of tyre–road friction considering topographical roughness variation and flash temperature. *Tribology International*. 2023;181: 108294.
- 10. Belhocine A, Abdullah OI. Finite element analysis (FEA) of frictional contact phenomenon on vehicle braking system. *Mechanics Based Design of Structures and Machines*. 2020;50(9): 2961–2996.
- 11. Nosko O, Tsybrii Yu. Inverse determination of sliding surface temperature based on measurements by thermocouples with account of their thermal inertia. *Tribology International*. 2021;164: 107200.
- 12. Frankel JI, Chen H. Analytical developments and experimental validation of a thermocouple model through an experimentally acquired impulse response function. *International Journal of Heat and Mass Transfer.* 2019;141: 1301–1314.
- 13. Roda-Casanova V, Fernandes CMCG. A comparison of analytical methods to predict the bulk temperature in polymer spur gears. *Mechanism and Machine Theory*. 2022;173: 104849.
- 14. Nosko O, Tsybrii Y, Torrelio Arias TPG, Senatore A. Temperature Measurements at Tyre Tread Rubber on Sandpaper Oscillatory Sliding Contacts Using Acicular Grindable Thermocouples. *Tribol. Lett.* 2024;72:75.
- 15. Roda-Casanova V, Sanchez-Marin F, Martinez-Cuenca R. Convective heat transfer modelling in dry-running polymer spur gears. *International Journal of Mechanical Sciences*. 2023;241: 107927.
- 16. Vettergen VI, Bashkarev AY, Suslov MA. Kinetics of friction and wear of polymer composite materials. *Phys. Solid State*. 2005;47: 1681–1686.
- 17. Ratner SB, Lur'ie YG. The relation between wear and the thermochemical stability of polymers. *Polymer Science U.S.S.R.* 1966;8(1): 93–99.
- 18. Sivebaek IM, Samoilov VN, Persson BNJ. Frictional Properties of Confined Polymers. *Eur. Phys. J.* 2008;27: 37 46.
- 19. Mergler YJ, Schaake RP, Huis in't Veld AJ. Material transfer of POM in sliding contact. *Wear*. 2004;256(3–4): 294–301.
- 20. Jia BB, Liu XJ, Cong PH, Li TSh. An investigation on the relationships between cohesive energy density and tribological properties for polymer–polymer sliding combinations. *Wear*. 2008;264(7-8): 685–692.
- 21. Laux KA, Schwartz CJ. Effects of contact pressure, molecular weight, and supplier on the wear behavior and transfer film of polyetheretherketone (PEEK). *Wear*. 2013;297(1–2): 919–925.

- 22. Samyn P, Baets PD. Friction and wear of acetal: A matter of scale. Wear. 2005;259(1-6): 697-702.
- 23. Sedakova EB, Kozyrev YuP, Thermal distribution in the PTFE-steel frictional pair. Russ. Engin. Res. 2016; 36:727-730.
- 24. Privalko VP. The glass temperature of polytetrafluoroethylene and polyoxymethylene. *Polym. Sci. U.S.S.R.* 1976;18(6): 1392–1397.
- 25. Brandrup J, Immergut EH, Grulke EA. Polymer Handbook. Two Volumes Set 4th ed. Wiley; 1989.
- 26. Fourier JB. *The Analytical Theory of Heat*. The University Press; 1882.
- 27. Lykov AV. Theory of Thermal Conductivity. Moscow: Higher School; 1967. (In Russian)
- 28. Gallager R. Metod Konechnih Elementov: Osnovi. Moscow: Mir; 1984. (In Russian)
- 29. Desai YM, Eldho TI, Shah AH. Finite Element Method with Applications in Engineering. Pearson Education India; 2011.
- 30. Galerkin BG. Beams and plates. Series in some questions of elastic equilibrium of beams and plates. Vestnik Ingenerov; 1915. (In Russian)
- 31. Stephen W. Fundamental Principles of Heat Transfer. New York: Pergamon Press; 1977.
- 32. Janahmadov AK. *Analysis of the Fractal Structure of Rough Friction Surfaces to Establish Transient Regimes of Frictional Contact. J. Frict. Wear.* 2023;44: 391–396.
- 33. Kiselev AP, Lazarev VA. Bouncing of the load and radiation of sound in dry friction. *Tech. Phys.* 1997;42: 581–583.
- 34. Babici LM, Tudor A, Romeu J. Stick-Slip Phenomena and Acoustic Emission in the Hertzian Linear Contact. *Appl. Sci.* 2022;12: 9527.
- 35. Pozdnyakov AO, Ginzburg BM, Ivanov MA, Stepanov SV, Pozdnyakov OF. Studying polymer-on-metal friction by thermodesorption mass spectrometry. *Tech. Phys. Lett.* 2007;33: 462–465.

About Authors

Aleksei O. Pozdnyakov 🗓 Sc

80

Candidate of Physical and Mathematical Sciences Senior Researcher (loffe Institute, Saint-Petersburg, Russia) Senior Researcher (Institute for Problems in Mechanical Engineering of RAS, Saint-Petersburg, Russia)

Elena B. Sedakova 🗓 Sc

Doctor of Technical Sciences

Leading Researcher (Institute for Problems in Mechanical Engineering of RAS, Saint-Petersburg, Russia)

Submitted: April 4, 2024 Revised: May 20, 2024 Accepted: June 18, 2024

Structure and strength of Mg-Zn-Zr alloy subjected to high pressure torsion

D.A. Aksenov ^{1 ⊠}, ¹⁰ M.A. Shishkunova ^{1,2}, ¹⁰ R.N. Asfandiyarov ^{1,2}, ¹⁰ Y.R. Sementeeva ^{1,2}

ABSTRACT

Magnesium alloys are considered a promising material for the production of biodegradable implants. However, their widespread adoption is hindered by their low strength and high corrosion rate. Deformation can enhance the strength characteristics; however, due to the limited number of slip planes in magnesium alloys, choosing the deformation processing regime for them is a non-trivial task. This study presents the results of research aimed at determining the influence of processing modes by high-pressure torsion on the transformation mechanisms of the structure and mechanical characteristics of the Mg-8.6Zn-1.2Zr alloy. It is shown that at room temperature, predominantly a twinning structure is formed, with microhardness values reaching 1200 MPa. However, it is demonstrated that such a structure leads to significant embrittlement of the Mg-8.6Zn-1.2Zr alloy. Deformation at a temperature of 250 °C leads to the formation of recrystallized grains with a size of 3–4 μ m. After 5 revolutions of high-pressure torsion, the microhardness is 820 MPa, and the tensile strength is 335 MPa, with an elongation of 13 %.

KEYWORDS

magnesium alloys • biomedical applications • severe plastic deformation • bioresorbable materials • nanomaterials

Acknowledgements. The work was supported by the Russian Science Foundation (project No. 22-79-10325).

Citation: Aksenov DA, Shishkunova MA, Asfandiyarov RN, Sementeeva YR. Structure and strength of Mg-Zn-Zr alloy subjected to high pressure torsion. *Materials Physics and Mechanics*. 2024;52(4): 81–91. http://dx.doi.org/10.18149/MPM.5242024_8

Introduction

Magnesium is characterized by low density while exhibiting outstanding mechanical properties such as high ductility and specific strength. Therefore, magnesium alloys have received significant attention as lightweight structural materials. However, some magnesium alloys possess properties such as biocompatibility and an elastic modulus close to that of human bone tissue, making them suitable for medical implant materials [1–3]. Magnesium and its alloys are biodegradable, allowing for the production of temporary implants and thus reducing the number of surgical interventions, avoiding the need for repeat surgery procedures, and reducing the traumatic effect [4,5]. It is worth noting that magnesium is non-toxic and hypoallergenic, being essential for human metabolism and naturally present in bone tissues [4,6]. The Young's modulus of magnesium alloys, being close to the modulus of bone under loading, helps to reduce the effect of stress differences occurring in the "bone-implant" system [7]. To ensure adequate bone tissue restoration, a magnesium alloy implant must possess a certain corrosion rate and high levels of mechanical properties. This requirement is formulated

¹ Institute of Molecule and Crystal Physics of the Ufa Federal Research Center of the Russian Academy of Sciences, Ufa, Russia

² Ufa University of Science and Technology, Ufa, Russia

[™] aksyonovda@mail.ru

based on the fact that a certain amount of time is needed for the complete fusion of bone fragments, during which the implant dissolves, leading to a corresponding decrease in the overall strength of the structure. Naturally, there is a gradual "transfer" of load from the implant to the bone. This aspect underscores the necessity of obtaining an implant with a specified dissolution rate and certain strength characteristics [5,6].

One of the effective methods for improving the comprehensive mechanical properties of metallic materials is deformation processing with the refinement of structural components down to an ultrafine-grained (UFG) state, enhancing their size uniformity. However, magnesium and its alloys poorly undergo deformation processing at room temperature due to their hexagonal close-packed (HCP) lattice, which limits the number of active slip systems [8]. Thus, the application of approaches to enhance the mechanical properties of magnesium alloys based on plastic deformation requires careful selection of processing regimes and the use of combined treatments, including heat treatment and pre-deformation [9,10].

Of particular interest is the application of thermo-mechanical processing based on severe plastic deformation (SPD), which is one of the most effective methods used to form UFG structures in metals today. Among the possible SPD methods, some of the main ones are equal-channel angular pressing (ECAP) and high-pressure torsion (HPT) [11–13]. Magnesium and its alloy processing by ECAP are carried out at relatively high temperatures, which helps avoid segmentation and cracking caused by low ductility at room temperature. However, during processing at high temperatures, one of the main structure transformation processes is recrystallization [14,15]. HPT processing has its advantages and disadvantages; however, from a scientific point of view, it allows processing under "critical" conditions for the material, thereby determining the real range of thermo-mechanical processing regimes available for the investigated material. For example, HPT for magnesium alloys allows avoiding undesirable cracking even at room temperature, due to high hydrostatic pressure [16]. Also, compared to ECAP, HPT has the advantage of forming a structure with smaller grain size and makes it possible to analyze structural and phase transformations under extreme conditions for the material [16–18]. The structure transformation processes of pure magnesium during HPT are discussed in the literature [19,20], however, regarding the Mg-Zn-Zr alloy system, there are not many studies [21– 24], and this work is aimed at expanding the knowledge about changes in the structure and properties of the Mg-Zn-Zr alloy under high pressures. The Mg-Zn-Zr system is interesting because already in the annealed state, the samples have a tensile strength close to 300 MPa [25]. The alloying elements Zn and Zr are non-toxic and can lead to additional strengthening and refinement of the structure [26,27]. Based on the above, the aim of this study is to establish the influence of the high-pressure torsion (HPT) process on the structure and properties of the biodegradable magnesium alloy in the Mq-Zn-Zr system.

Materials and Methods

The research material selected for the study is the biodegradable magnesium alloy Mg-8.6Zn-1.2Zr (grade MA14). Based on preliminary studies and literature data [28,29], the initial structural condition obtained through prolonged annealing process at a temperature of $430 \pm 10^{\circ}$ C for 24 hours in a Snol 8.2/1000 furnace has been adopted.

As stated above, high-pressure torsion (HPT) was chosen as the investigated method. The specimens were in the form of disks with a thickness of 2 mm and a diameter of 10 mm. HPT was conducted at a pressure of 6 GPa on flat anvils, at temperatures of 20 and 250 °C. Samples were obtained after 1 and 5 rotations of torsion, at a constant angular velocity of 1 rpm.

Structural analysis was performed using a Carl Zeiss Axio Observer A1m optical microscope. The linear density of twins was calculated using the equation [30]: $\rho=N/L$, (1)

where N is the number of twins occurring within the segment, and L is the length of the segment.

X-ray structural analysis was conducted using a Bruker D8 Advance diffractometer with $CuK\alpha$ radiation, with continuous sample rotation (20 degrees/min) and step scanning (step size 0.02°, exposure time 1 s) in the angular range of $2\Theta = 30^{\circ} - 90^{\circ}$. To evaluate dislocations, an approach based on modified Williamson-Hall and Warren-Averbach methods as described in references [31,32] was implemented.

Microhardness was measured using a Micromet 5101 microhardness tester. A diamond indenter in the form of a tetrahedral pyramid with a square base under a load of 100 g was lowered onto the ground and held for 10 seconds. The measurements were carried out along the diagonal of the sample.

Tensile mechanical tests were conducted on "miniature" specimens (see Fig. 1), cut using an electroerosion machine ARTA 120 in such a way that the working part fell within the middle radius region of the sample (see Fig. 1). The length of the working part was 4 mm, thickness was 0.8 mm, and width was 0.6 mm. The tests were performed at a deformation rate of 0.24 mm/min at room temperature.

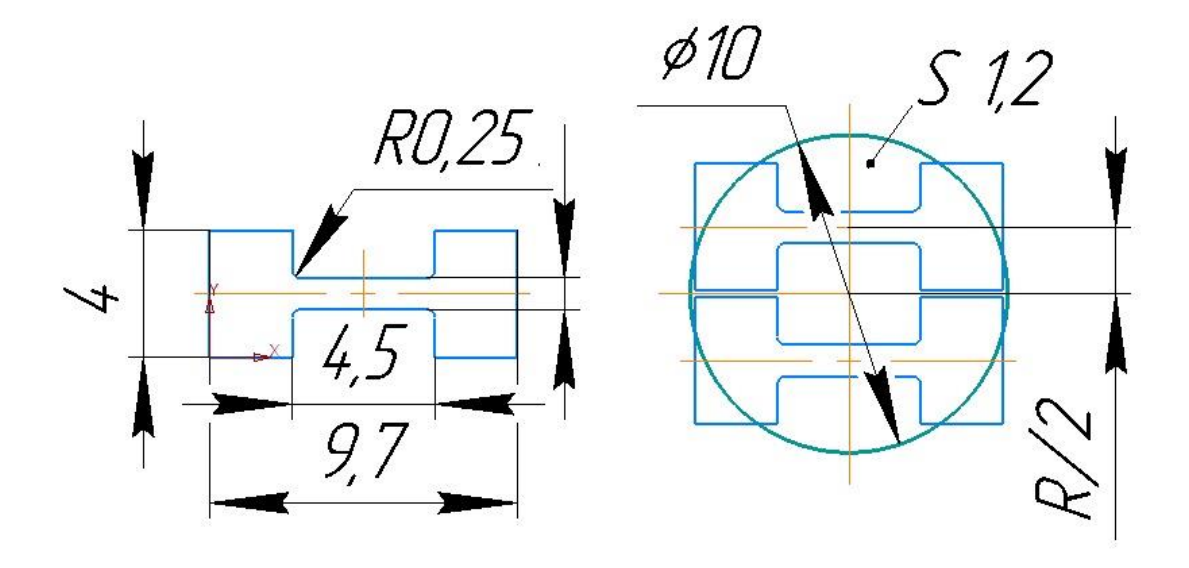


Fig. 1. Drawing of a "small" tension specimen and scheme of cutting a "small" tension specimen

Results and Discussion

The initial state is characterized by a structure of a mixed nature (see Fig. 2). Large grains of $30 \pm 10 \, \mu m$ and clusters of recrystallized grains along the boundaries of the strips with an average size of $4 \pm 2 \, \mu m$ are observed.

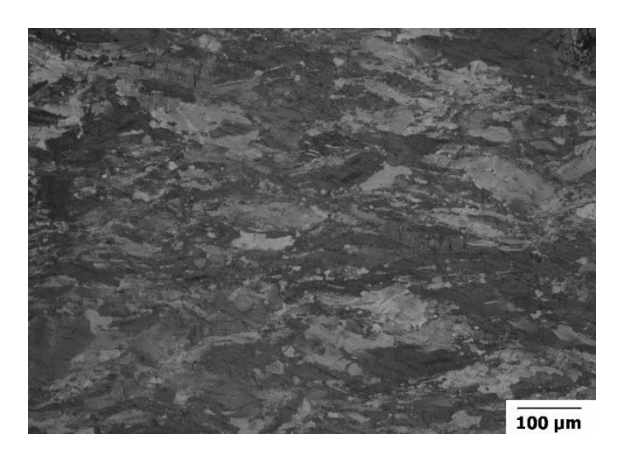


Fig. 2. The structure of the initial state of the Mg-8.6Zn-1.2Zr alloy

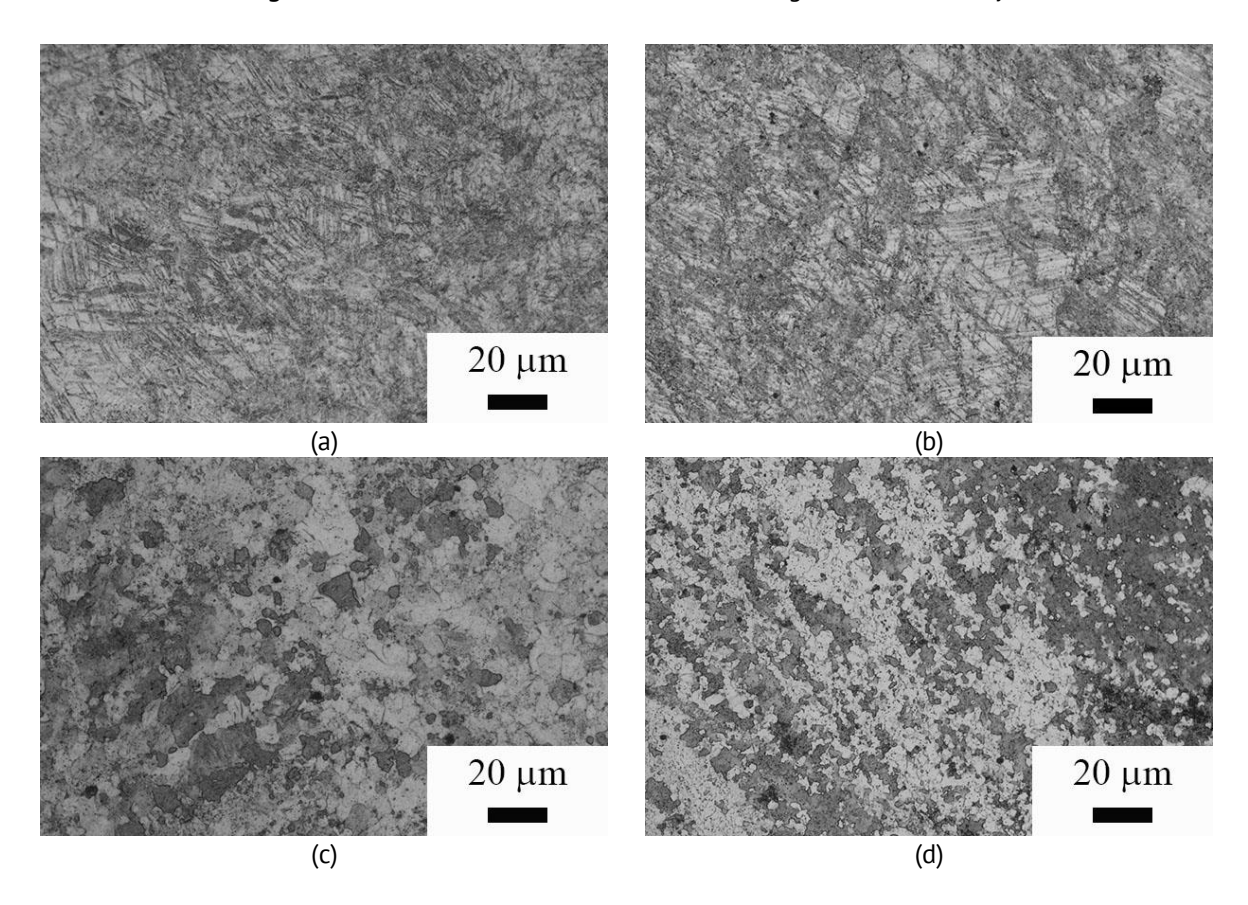


Fig. 3. The structure of Mg-8.6Zn-1.2Zr alloy specimens after high-pressure torsion (HPT) deformation: 1 rotation at 20 °C (a), 5 rotations at 20 °C (b), 1 rotation at 250 °C (c), and 5 rotations at 250 °C (d)

The analysis of the structure after HPT deformation indicates that at room temperature, one of the main mechanisms of structure transformation is twinning (see Fig. 3(a,b)). The calculation of twin linear density shows that after 1 rotation, the twin

density is 0.14 μ m⁻¹, and after 5 rotations, the twin density decreases by 3 times to 0.05 μ m⁻¹. The average twin thickness after 1 rotation is 2.6 ± 1.3 μ m, and after 5 rotations, it is 2.1 ± 1.1 μ m. The structure is highly twinned, and grain boundaries are poorly distinguishable; however, in the work [21], the formation of recrystallized grains with a size of ~1 μ m and larger grains containing twins in their body is noted. It is worth noting that in the mentioned work, the applied pressure was only 2 GPa, which is three times less than in this study.

A temperature of 250 °C is considered high for magnesium alloys, so a large number of recrystallized grains are observed in the samples after HPT at this temperature (see Fig. 3(c,d)). After 1 rotation, the average size of recrystallized grains is 4.0 \pm 1.3 μ m, and larger grains containing twins in their body are also observed. After 5 rotations, twins are hardly observed, and the average size of recrystallized grains remains almost unchanged at 3.0 \pm 1.4 μ m.

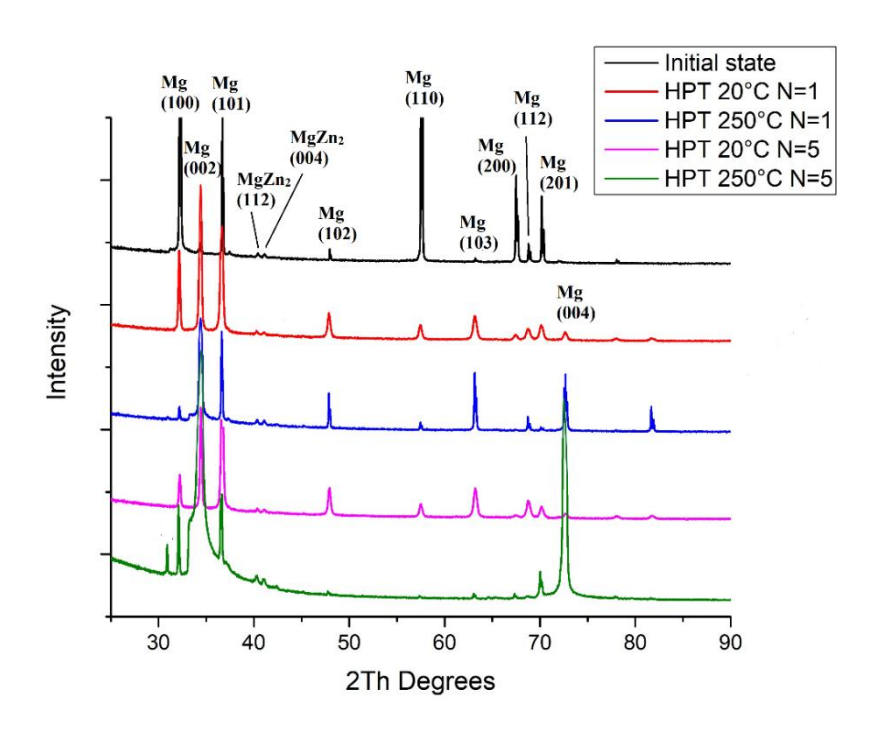


Fig. 4. X-ray diffraction patterns of the Mg-8.6Zn-1.2Zr alloy in the initial state and after high-pressure torsion

The conducted phase X-ray structural analysis indicates the presence of 0.3~% by weight of the MgZn₂ phase in the initial state (Fig. 4). Deformation by high-pressure torsion (HPT), regardless of the regime, leads to an increase in the content of this phase to 1.2-1.3~% by weight, indicating the decomposition of the solid solution during deformation. Analysis of the diffraction patterns allowed to establish a substantial refinement of the structure, as evidenced by the data on the coherent scattering region (CSR) (Table 1). The main refinement occurs during the first rotation, and no significant changes are observed with an increase in the number of rotations up to 5. Moreover, deformation at room temperature results in more substantial refinement compared to deformation at 250~%C. CSR reduces approximately 7 times to $38~\pm~4~\text{nm}$ after 1 rotation and reaches $32~\pm~3~\text{nm}$ after 5 rotations. Deformation at a higher temperature leads to a

3-fold reduction in CSR to 81 ± 6 nm after 1 rotation, and this value remains unchanged after 5 rotations. The magnitude of microstrains in the samples subjected to HPT at $250 \, ^{\circ}$ C is three times smaller than in the samples after HPT at room temperature.

Analysis of dislocation density allowed establishing that during high-pressure torsion (HPT) at room temperature, the density increases by ~ 2 times, reaching values of 6.7×10^{14} m⁻² after 5 rotations. This density value is 1.5 times lower than at 250 °C. The main increase in the number of dislocations for both conditions occurs after 1 rotation. HPT for 5 rotations at 250 °C leads to an increase in defect density to 9.9×10^{14} m⁻².

Table 1	. X-rav	diffraction	anal	vsis	results

State	Lattice parameter, nm		CSR*, nm	Microstrain	Dislocation density, 10 ¹⁴ m ⁻²
	а	С	CSK , IIIII	MICIOSCIAIII	Distocation density, 10-1 in -
Initial	0.3202	0.5200	257±14	0.1271±0.0014	3.5
HPT 20 °C 1 rev.	0.3200	0.5197	38±4	0.5394±0.0079	6.1
HPT 20 °C 5 rev.	0.3203	0.5200	32±3	0.5472±0.0066	6.7
HPT 250 °C 1 rev.	0.3203	0.5200	81±6	0.1703±0.0054	9.7
HPT 250 °C 1 rev.	0.3203	0.5200	78±5	0.1781±0.0060	9.9

The investigation of microhardness (Fig. 5) revealed that the main strengthening occurs after 1 rotation of high-pressure torsion (HPT) both at room temperature and at an elevated temperature of 250 °C. At room temperature, the microhardness reaches approximately 1220 ± 60 MPa, and its distribution across the sample diameter is shown in Fig. 4. After 5 rotations, no changes in microhardness are observed. HPT at 250 °C leads to an increase in microhardness after 1 rotation to the level of 780 ± 50 MPa, and after 5 rotations, no significant change in microhardness (820 ± 50 MPa) is observed. It should be noted that for the magnesium alloy, there is no heterogeneity in the distribution of microhardness across the sample diameter, as also noted in the study [21].

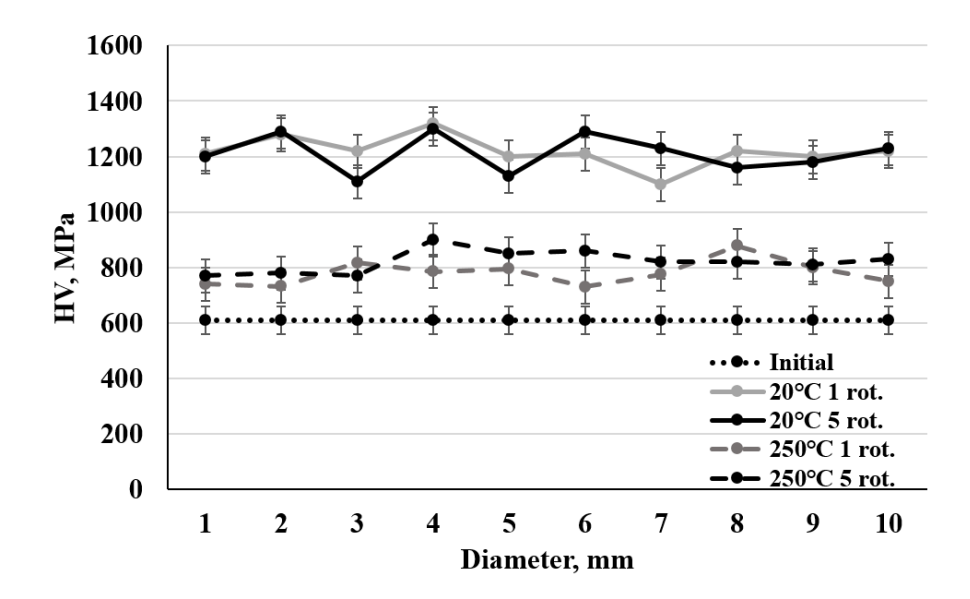


Fig. 5. The microhardness of the Mg-8.6Zn-1.2Zr alloy in the initial state and after high-pressure torsion

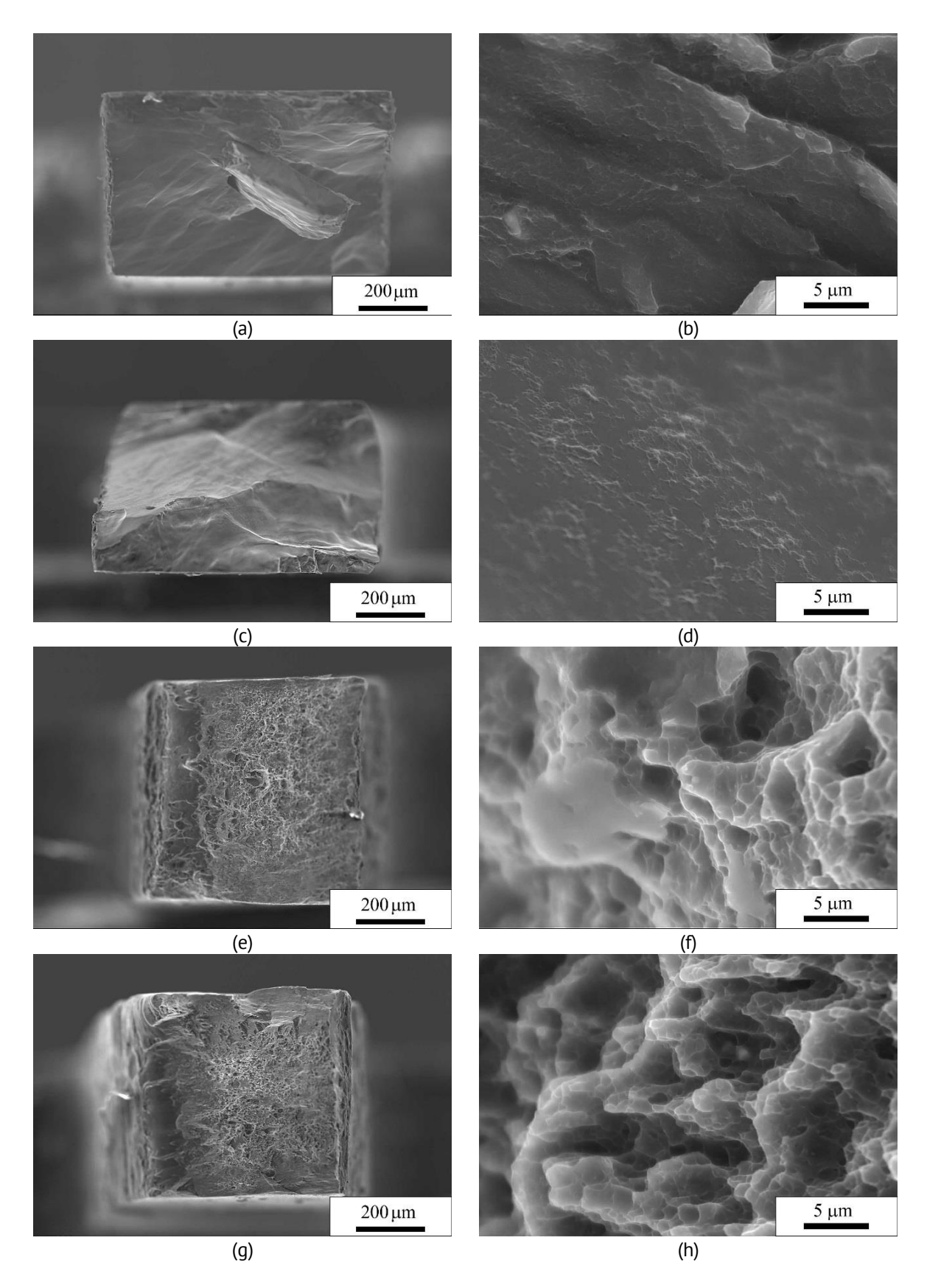


Fig. 6. The images of the fractures at magnifications of $\times 100$ and $\times 4000$ of the Mg-8.6Zn-1.2Zr alloy after high-pressure torsion (HPT) at temperatures of 20 °C for 1 (a,b) and 5 (c,d) rotations, and 250 °C for 1 (e,f) and 5 (g,h) rotations

Tensile tests indicate that effective strengthening occurs during hot deformation. The high-pressure torsion (HPT) regime at 250 °C for 5 rotations substantially increases both the tensile strength (335 \pm 8 MPa) and the yield strength (275 \pm 5 MPa) in the Mg-8.6Zn-1.2Zr alloy (Table 2). One rotation of HPT at 250 °C leads to an increase in tensile strength to 305 \pm 7 MPa, however, the yield strength remains at the initial level of 185 \pm 5 MPa. Deformation with 1 and 5 rotations of HPT at room temperature does not result in strengthening of the Mg-8.6Zn-1.2Zr magnesium alloy. The plasticity of the samples after HPT at 250 °C is explained by the presence of recrystallized grains.

Table 2. Mechanical properties

State	UTS, MPa	YTS, MPa	Elongation, %
Initial	270±5	180±5	15±1
HPT 20 °C N=1	285±5	-	<2%
HPT 20 °C N=5	290±5	-	<2%
HPT 250 °C N=1	305±7	185±5	15±1
HPT 250 °C N=5	335±8	275±5	13±1

To further understand the reasons behind such mechanical behavior, a fractographic analysis of the fractures was conducted (Fig. 6). At high magnification, it is observed that the fractures of the samples after room temperature high-pressure torsion (HPT) have a cellular relief. The fracture occurs by shear, which is typical for cast magnesium materials [33]. Fracture usually initiates from the surface. Twins act as barriers to dislocation propagation, leading to deformation localization and crack propagation in a shear-limited mode. Therefore, the obtained data on the ultimate tensile strength cannot be considered as final values.

In the case of the condition after hot HPT with recrystallized grains, a ductile fracture appearance is observed. Despite fracture initiation from the surface, deformation localization does not occur. In the central part of the samples after 1 and 5 rotations, elongated pits aligned with the fracture direction are observed. The average size of the pits is $1.3 \pm 0.5 \, \mu m$ and $1.1 \pm 0.4 \, \mu m$ for 1 and 5 rotations, respectively, indicating a similar fracture behavior for both conditions. A dimple region is observed on the opposite side of the fracture initiation. Such a characteristic fracture appearance has been observed multiple times in magnesium samples after deformation processing [34].

Conclusions

1. Deformation of the Mg-8.6Zn-1.2Zr alloy by High-Pressure Torsion at room temperature results predominantly in a twin structure. The main strengthening occurs after 1 rotation. In this state, the average twin thickness is $2.6 \pm 1.3 \, \mu m$, and the linear density is $0.15 \, \mu m^{-1}$. The state exhibits high microhardness at the level of 1200 MPa, and the specimens demonstrate brittleness, as evidenced by mechanical tests and fractographic studies. After 5 rotations, there is a decrease in the twin linear density to $0.05 \, \mu m^{-1}$, while the twin thickness is $2.1 \pm 1.1 \, \mu m$. Significant changes in mechanical properties and fracture characteristics during tensile testing relative to specimens after 1 rotation are not observed for this state.

2. High-Pressure Torsion at 250 °C leads to the formation of predominantly recrystallized structure. After 1 rotation, the average grain size is $4.0 \pm 1.3 \, \mu m$. This state is characterized by an average microhardness across the diameter of 780 MPa, increased strength of 305 ± 7 MPa, and ductility of 15 %. For this state, a ductile fracture mode is observed during tensile testing. After 5 rotations at 250 °C, recrystallized grains with a size of $3.0 \pm 1.4 \, \mu m$ are observed in the structure. The state is characterized by an average microhardness of 820 MPa, high strength of 335 ± 8 MPa, yield strength of 275 ± 5 MPa, and ductility of $13 \, \%$. 3. During high-pressure torsion of the Mg-8.6Zn-1.2Zr alloy, an active process of deformation-induced decomposition of the supersaturated solid solution occurs. Regardless of the deformation temperature and the number of rotations, there is an increase in the proportion of the MgZn₂ phase from 0.3 to $1.2-1.3 \, \text{wt}$. %.

References

- 1. He M, Chen L, Yin M, Xu S. Review on magnesium and magnesium-based alloys as biomaterials for bone immobilization. *Journal of Materials Research and Technology*. 2023;23: 4396–4419.
- 2. Zhang T, Wang W, Liu J, Wang L, Tang Y, Wang K. A review on magnesium alloys for biomedical applications. *Frontiers in Bioengineering and Biotechnology*. 2022;10: 953344.
- 3. Tan J, Ramakrishna S. Applications of Magnesium and Its Alloys: A Review. *Applied Sciences*. 2021;11(15): 6861.
- 4. Tsakiris V, Tardei C, Clicinschi FM. Biodegradable Mg alloys for orthopedic implants A review. *Journal of Magnesium and Alloys*. 2021;9(6): 1884–1905.
- 5. Claes L, Recknagel S, Ignatius A. Fracture healing under healthy and inflammatory conditions. *Nature Reviews Rheumatology*. 2012;8(3): 133–143.
- 6. Wolf FI, Cittadini A. Chemistry and biochemistry of magnesium. *Molecular Aspects of Medicine*. 2003;24(1–3): 3–9.
- 7. Shi H, Xu C, Hu X, Gan W, Wu K, Wang X. Improving the Young's modulus of Mg via alloying and compositing A short review. *Journal of Magnesium and Alloys*. 2022; 10(8): 2009–2024.
- 8. Lapovok R, Thomson PF, Cottam R. The effect of grain refinement by warm equal channel angular extrusion on room temperature twinning in magnesium alloy ZK60. *Journal of Materials Science*. 2005;40: 1699–1708.
- 9. Ying T, Huang JP, Zheng M, Wu K. Influence of secondary extrusion on microstructures and mechanical properties of ZK60 Mg alloy processed by extrusion and ECAP. *Transactions of Nonferrous Metals Society of China*. 2012;22(8): 1896–1901.
- 10. Bragov AM, Konstantinov AY, Lomunov AK, Petrovtsev AV. The dynamic properties of zirconium-containing magnesium alloy MA14-T1. *Materials Physics and Mechanics*. 2016;28(1/2): 101–105.
- 11. Valiev RZ, Langdon TG. Principles of equal-channel angular pressing as a processing tool for grain refinement. *Progress in Materials Science*. 2006;51(7): 881–981.
- 12. Zhilyaev AP, Langdon TG. Using High-Pressure Torsion for Metal Processing: Fundamentals and Applications. *Progress in Materials Science*. 2008;53(6): 893–979.
- 13. Medvedev AYe, Murashkin MYu, Enikeev NA, Ovid'ko IA, Valiev RZ. Strength and electrical conductivity of ultrafine-grained aluminum alloy Al-2Fe subjected to annealing and straining. *Materials Physics and Mechanics*. 2015;24(3): 297–307.
- 14. Figueiredo RB, Langdon TG. Principles of grain refinement and superplastic flow in magnesium alloys processed by ECAP. *Materials Science and Engineering: A.* 2009;501(1–2): 105–114.
- 15. Figueiredo RB, Langdon TG. Grain refinement and mechanical behavior of a magnesium alloy processed by ECAP. *Journal of Materials Science*. 2010;45(17): 4827–4836.
- 16. Zhilyaev AP, Kim BK, Nurislamova GV, Baró MD, Szpunar JA, Langdon TG. Orientation imaging microscopy of ultrafine-grained nickel. *Scripta Materialia*. 2002;46(8): 575–580.
- 17. Zhilyaev AP, Kim BK, Szpunar JA, Baró MD, Langdon TG. The microstructural characteristics of ultrafine-grained nickel. *Materials Science Engineering: A.* 2005;391(1–2): 377–389.
- 18. Valiev RZ, Ivanisenko YuV, Rauch EF, Baudelet BF. Structure and deformation behaviour of Armco iron subjected to severe plastic deformation. *Acta Materialia*. 1996;44(12): 4705–4712.
- 19. Edalati K, Yamamoto A, Horita Z, Ishihara T. High-pressure torsion of pure magnesium: Evolution of mechanical properties, microstructures and hydrogen storage capacity with equivalent strain. *Scripta Materialia*. 2011;64(1): 880–883.

- 20. Ahmadkhaniha D, Huang Y, Jaskari M, Järvenpää A, Sohi MH, Zanella C, Karjalainen LP, Langdon TG. Effect of high-pressure torsion on microstructure, mechanical properties and corrosion resistance of cast pure Mg. *Journal of Materials Science*. 2018;53: 16585–16597.
- 21. Torbati-Sarraf SA, Langdon TG. Properties of a ZK60 magnesium alloy processed by high-pressure torsion. *Journal of Alloys and Compounds*. 2014;613: 357–363.
- 22. Lee HJ, Ahn B, Kawasaki M, Langdon TG. Evolution in hardness and microstructure of ZK60A magnesium alloy processed by high-pressure torsion. *Journal of Materials Research and Technology*. 2015;4(1): 18–25.
- 23. Torbati-Sarraf SA, Sabbaghianrad S, Langdon TG. Microstructural properties, thermal stability and superplasticity of a ZK60 Mg alloy processed by high-pressure torsion. *Letters on Materials*. 2015;5(3): 287–293.
- 24. Castro MM, Montoro LA, Isaac A, Kawasaki M, Figueiredo RB. Mechanical mixing of Mg and Zn using high-pressure torsion. *Journal of Alloys and Compounds*. 2021;869: 159302.
- 25. Zhang WS, Liu XT, MA JF, Wang WK, Chen WZ, Liu YX, Yang JL. Evolution of microstructure and mechanical properties of ZK60 magnesium alloy processed by asymmetric lowered-temperature rolling. *Transactions of Nonferrous Metals Society of China*. 2022;32(9): 2877–2888.
- 26. Cai S, Lei T, Li N, Feng F. Effects of Zn on microstructure, mechanical properties and corrosion behavior of Mg–Zn alloys. *Materials Science and Engineering C*. 2012;32(9): 2570–2577.
- 27. Qian M, St. John DH, Frost MT. In: *Magnesium Alloys and Their Applications*. Wiley-VCH: Wolfsburg; 2003. 28. Chen M, Ma C, Liu Q, Cheng M, Wang H, Hu X. Plastic Deformation Mechanism of High Strength and Toughness ZK61 Magnesium Alloy Plate by Multipass Horizontal Continuous Rolling. *Materials*. 2023;16(3):1320. 29. Alawad MO, Alateyah AI, El-Garaihy WH, BaQais A, Elkatatny S, Kouta H, Kamel M, El-Sanabary S. Optimizing the ECAP Parameters of Biodegradable Mg-Zn-Zr Alloy Based on Experimental, Mathematical
- 30. Ostrikov OM. Features of evolution of wedge-shaped twins in bismuth single crystals subjected to polysynthetic twinning. *Journal of Applied Mechanics and Technical Physics*. 2008;49(3): 519–525.

Empirical, and Response Surface Methodology. *Materials*. 2022;15(21): 7719.

- 31. Ungar T, Borbely A. The Effect of Dislocation Contrast on X-Ray Line Broadening: A New Approach to Line Profile Analysis. *Applied Physics Letters*. 1996;69(21): 3173–3175.
- 32. Muiruri A, Maringa M, du Preez W. Evaluation of Dislocation Densities in Various Microstructures of Additively Manufactured Ti6Al4V (Eli) by the Method of X-ray Diraction. *Materials*. 2020;13(23): 5355.
- 33. Fridman YB. *Mechanical properties of metals. Part 1: Deformation and Destruction.* Moscow: Mashinostroenie. 1974. (In Russian)
- 34. Karparvarfard SMH, Shaha SK, Behravesh SB, Jahed H, Williams BW. Microstructure, texture and mechanical behavior characterization of hot forged cast ZK60 magnesium alloy. *Journal of Materials Science* & *Technology*. 2017;33(9): 907–918.

About Authors

Denis A. Aksenov Denis A. Aksenov

Junior Researcher (Institute of Molecule and Crystal Physics of the Ufa Federal Research Center of the Russian Academy of Sciences, Ufa, Russia)

Maria A. Shishkunova D Sc

Junior Researcher (Institute of Molecule and Crystal Physics of the Ufa Federal Research Center of the Russian Academy of Sciences, Ufa, Russia)

Rashid N. Asfandiyarov D SC

Candidate of Technical Sciences

Researcher (Institute of Molecule and Crystal Physics of the Ufa Federal Research Center of the Russian Academy of Sciences, Ufa, Russia)

Yulia R. Sementeeva Sc

Junior Researcher (Institute of Molecule and Crystal Physics of the Ufa Federal Research Center of the Russian Academy of Sciences, Ufa, Russia)

Submitted: July 19, 2024 Revised: August 6, 2024 Accepted: August 27, 2024

The effect of martensite stabilization in titanium nickelide after various methods of pre-deformation: simulation with a single set of constants

A.E. Volkov ^{1 \to \bar{\pi}}, F.S. Belyaev ^{2 \bar{\pi}}, N.A. Volkova ^{1 \bar{\pi}}, E.A. Vukolov ¹,

M.E. Evard ¹ , T.V. Rebrov ¹

ABSTRACT

Design of shape memory alloy sensors and actuators requires taking into account the martensite stabilization effect, which consists in a shift upward of the reverse martensitic transformation temperatures after preliminary deformation. In this work it is assumed that this effect is due to damage in martensite domain boundaries during pre-straining. This idea is accounted for in a microstructural model by introducing a variable for boundaries damage and formulating evolution equations. The reverse transformation temperature shift is described with one set of constants for three pre-straining modes: deformation of a specimen in the martensitic state, cooling under a constant stress, and deformation in the austenitic state inducing martensite by stress. For Ti50Ni50 and Ti49Ni51 (at. %), the model matches experimental data well for the first two modes and qualitatively for the third.

KEYWORDS

shape memory alloys • titanium-nickel • martensite stabilization • modeling • microstructural model

Acknowledgements. This work has been supported by the grants the Russian Science Foundation, RSF 23-29-01006.

Citation: Volkov AE, Belyaev FS, Volkova NA, Vukolov EA, Evard ME, Rebrov TV. The effect of martensite stabilization in titanium nickelide after various methods of pre-deformation: simulation with a single set of constants. Materials Physics and Mechanics. 2024;52(4): 91-99.

http://dx.doi.org/10.18149/MPM.5242024 9

Introduction

Shape memory alloys (SMA) are widely used in industry and medicine due to their ability to recover the initial shape during the reverse martensitic transformation (MT) at heating after deformation in the low-temperature phase (martensite). For such applications as thermomechanical actuators or thermal sensors it is in many cases important to know at what temperatures will the shape recovery occur.

The characteristic temperatures A_s and A_f , at which the reverse MT in the undeformed material begins and ends, are material constants. However, experiments show that if the material acquired a deformation in the martensitic phase it can retain structure of martensite when heated to temperatures above A_s in the undeformed material. This phenomenon is known as the martensite stabilization effect (MSE). It can be either beneficial or undesirable depending on the application of the SMA. The magnitude of the shift of A_s depends on the degree of prior deformation.

¹ St. Petersburg State University, St. Petersburg, Russia

² Institute for Problems of Mechanical Engineering RAS, St. Petersburg, Russia

[□] a.volkov@spbu.ru

The effect of martensite stabilization in titanium nickelide has been studied since 1991 [1]. It was observed after various pre-deformation treatment (cold rolling, stretching, and shear in the martensitic state, stress-induced MT, cooling under stress from austenite) for mono- and polycrystals of SMA [2-16]. Different hypotheses about the causes of MSE were proposed in [2-16]. S.A. Kustov et al. [11,12] proposed two mechanisms of MSE: one - mechanical stabilization due to pinning martensite boundaries and the second – chemical stabilization due to atomic reordering. In these works mechanical stabilization is related to aging. Thus, time independent MSE is due only to the chemical stabilization. S.P. Belyaev et al. [16] put forward a hypothesis that the main cause of MSE is the damage to intermartensitic boundaries, which hinders the reverse transition and therefore shifts its temperatures upward. This hypothesis was used in [17] for modeling MSE after pre-deformation by stretching in the martensitic state. A new variable ζ , responsible for the degree of intermartensitic boundary damage, was introduced. It was assumed that ζ increases with the degree of martensite orientation. The evolution equations proposed in that work for ζ were used to model MSE caused by pre-deformation of Ti₅₀Ni₅₀ alloy specimens in the martensitic state up to various values of strain. The obtained dependences for the shift in the onset temperatures of the reverse MT were in good agreement with the experiment. In the present work, the formulae for calculating the evolution of boundaries damage parameter ζ were adjusted and supplemented to model the MSE caused by other methods of pre-straining.

Microstructural model of SMA

Modeling the functional-mechanical properties is an essential and convenient tool for studying phase transformations, phase stability, and thermomechanical behavior of SMAs. The microstructural model described in [17–20] accounts for reversible phase deformation, microplastic deformation (plastic accommodation of martensite), and the evolution of deformation defects. The internal variables of this model are (1) volume fractions of martensite orientation variants obtained by equivalent but differently oriented Bain's deformations; (2) microplastic deformations associated with these variants; (3) densities of oriented and scattered deformation defects. For describing the material structure, a hierarchy of regions is established: a representative volume consists of grains differing in the orientation of crystallographic axes, and each grain contains austenite and martensite variants. Reuss' hypothesis is accepted: the macroscopic strain described by the small strain tensor ε is calculated as the average value of the grain strains ε^{gr} . For crystals, this strain can be divided into the sum of elastic ε^{e} , thermal ε^{T} , phase ε^{Ph} , microplastic ε^{mp} , and plastic ε^{p} components:

phase
$$\varepsilon^{\rm Ph}$$
, microplastic $\varepsilon^{\rm mp}$, and plastic ε^p components:
$$\varepsilon = \sum_i f_i \varepsilon^{\rm gr}(\omega_i), \qquad \varepsilon^{\rm gr} = \varepsilon^{\rm e} + \varepsilon^{\rm T} + \varepsilon^{\rm Ph} + \varepsilon^{\rm mp} + \varepsilon^p, \tag{1}$$

where ω_i are the crystallographic orientation axes, f_i are the volume fractions of grains with orientation ω_i , and the sum is taken over all grain orientations (argument ω_i is further omitted). According to the Reuss' hypothesis, the mixture rule is also applied to the phase deformations within each grain:

$$\varepsilon^{\text{gr}} = (1 - \Phi_{\text{M}})\varepsilon^{\text{A}} + \frac{1}{N} \sum_{n=1}^{N} \Phi_{n} \varepsilon^{\text{M}n}, \qquad \Phi_{\text{M}} = \frac{1}{N} \sum_{n=1}^{N} \Phi_{n}, \tag{2}$$

where ε^A and ε^{Mn} are the strains of the austenite and the n-th martensite variant, N is the number of Bain deformation orientation variants, Φ_M is the total volume fraction of martensite in the grain, and Φ_n is the normalized fraction of the n-th martensite variant (so that its volume fraction relative to the grain volume is Φ_n/N). The phase strain of an individual martensite variant is the Bain's deformation D_n that implements the lattice transformation. Since the fraction of the n-th variant is Φ_n/N ,

$$\varepsilon^{\rm Ph} = \frac{1}{N} \sum_{n=1}^{N} \Phi_n D_n. \tag{3}$$

Microplastic deformations are plastic deformations caused by phase deformation incompatibility. They accommodate martensite and reduce the elastic energy of interphase stresses. A simplified calculation of microplastic deformations is based on the idea that the growth of each Bain martensite variant initiates a combination of shears creating a deformation proportional to the deviator of phase deformation. Thus, we can apply an equation similar to Eq. (3):

$$\varepsilon^{\rm mp} = \frac{1}{N} \sum_{n=1}^{N} \kappa \varepsilon_n^{\rm p} dev D_n, \tag{4}$$

where internal variables $\varepsilon_n^{\rm p}$ serve as "measures" of microplastic deformations, $dev D_n$ is the deviator of the tensor D_n , and κ is a material constant. The equations for Φ_n and $\varepsilon_n^{\rm p}$ are formulated in terms of generalized thermodynamic forces – derivatives of the Gibbs potential G with respect to these variables. For a grain,

$$G = (1 - \Phi_{\rm M})G^{\rm A} + \frac{1}{N} \sum_{n=1}^{N} \Phi_n G^{\rm M}n + G^{\rm mix}, \tag{5}$$

where G^A and G^{Mn} are eigen potentials of austenite and the n-th martensite variant, without accounting for their interaction, and G^{mix} is the "mixing potential", equal to the elastic energy of interphase stresses. In Eq. (5), the eigen potentials are:

$$G^{a} = G_{0}^{a} - S_{0}^{a}(T - T_{0}) - \frac{c_{\sigma}^{a}(T - T_{0})^{2}}{2T_{0}} - \varepsilon_{ij}^{0Ta}(T)\sigma_{ij} - \frac{1}{2}D_{ijkl}^{a}\sigma_{ij}\sigma_{kl} \ (a = A, Mn), \tag{6}$$

where the upper index a=A denotes austenite and a=Mn-n-th martensite variant; G_0^a and S_0^a are Gibbs potential and entropy at the reference stress $\sigma=0$ and temperature $T=T_0$ (at which $G_0^A=G_0^{Mn}$); $\varepsilon_{ij}^{0Ta}(T)$ are strains of the phases at $\sigma=0$; c_σ^a are specific heat capacities at $\sigma=0$ and D_{ijkl}^a are elastic compliances. For T_0 , the estimate from [21] is accepted: $T_0=\frac{Ms+Af}{2}$ (hereinafter M_s , M_f , A_s , A_f are the characteristic transformation temperatures). Calculation of the $G^{\rm mix}$ potential is a very difficult task. As a simplest estimate, a quadratic form is used similar to that in the model developed by E. Patoor et al. [22,23]. It takes into account that this energy increases with an increase in the volume fractions of martensite Φ_n and decreases due to oriented deformation defects b_n , the appearance and movement of which provides plastic accommodation of martensite – plastic deformations ε_n^p :

$$G_n^{mix} = \frac{\mu}{2} \sum_{m,n=1}^{N} A_{mn} (\Phi_m - b_m) (\Phi_n - b_n), \tag{7}$$

where the matrix (A_{mn}) describes the self-action and interaction of martensite variants. In the TiNi alloy, the primary self-accommodation of martensite is achieved by grouping variants into correspondent variants pairs (CVP) [24–26]. A decrease of G^{mix} energy due to

the formation of CVP is accounted by the proper negative components in the matrix (A_{mn}) . The form of this matrix is taken from [17]. From Eqs. (6) and (7) we find the force causing the growth of the *n*-th variant of martensite:

$$F_n(T, \sigma, \Phi) = -N \frac{\partial G}{\partial \Phi_n} \approx \frac{q_0}{T_0} (T - T_0) + \sigma_{ij} : D_{ij}^n - \mu \sum_{m=1}^N A_{mn} (\Phi_m - b_m).$$
 (8)

The existence of the hysteresis of the martensite volume fraction dependences on temperature is accounted by introducing a dissipative force F^{fr} , which counteracts the movement of the interface, so that the transformation condition has the form:

$$F_n = \pm F^{\rm fr} \,, \tag{9}$$

where the force F_n is determined by Eq. (8), the plus sign corresponds to the direct transformation, and the minus sign – to the reverse. The value of $F^{\rm fr}$ is expressed in terms of the transformation characteristics: $F^{\rm fr}=q_0(M_s-T_0)/T_0$. The variations laws for the variables b_n and $\varepsilon_n^{\rm p}$ are derived from the condition of microplastic flow:

$$|F_n^p - F_n^\rho| = F^y$$
, $(F_n^p - F_n^\rho) dF_n > 0$, where F_n^p is the generalized force conjugate to the variables b_n :

$$F_n^p = -N\frac{\partial G}{\partial b_n} = \mu \sum_{m=1}^N A_{mn}(\Phi_m - b_m),\tag{11}$$

 F^{y} and F_{n}^{ρ} are forces describing isotropic and kinematic hardening. The microplastic flow condition (10) is similar to the classical plastic flow condition for a uniaxial stress state: generalized forces F_n^p , F^y and F_n^ρ play the role of stress, flow stress and internal (eigen) stress (or back stress), respectively. Microplastic flow generates deformation defects, which in this model are divided into two groups: scattered defects f and oriented defects b_n . The evolution equations for them are proposed in the form:

$$\dot{b}_n = k_b \left(\dot{\varepsilon}_n^{\text{mp}} - \frac{|b_n|}{\beta^*} \dot{\varepsilon}_n^{\text{mp}} H \left(b_n \dot{\varepsilon}_n^{\text{mp}} \right) \right), \quad \dot{f} = \sum_{m=1}^N \left| \dot{\varepsilon}_m^{\text{mp}} \right|, \tag{12}$$

where k_b , β^* are material constants, H is the Heaviside function. Further we assume that scattered defects create isotropic hardening, and reversible ones – kinematic hardening. This is accounted for by the so-called closing equations – relations between the defect density f and force F^{y} , as well as between b_{n} and force F_{n}^{ρ} . In this model, they are selected in the simplest form:

$$F^{y} = a_{y}f, \qquad F_{n}^{\rho} = a_{\rho}b_{n}, \tag{13}$$

where a_v and a_ρ are material constants. From conditions (9) and (10) and Eqs. (8) and (11)-(13) the evolutionary equations follow, allowing to calculate the increments of the internal variables Φ_n , $\varepsilon_n^{\rm mp}$, b_n , f_n for given increments of stress and temperature and then using Eqs. (1)–(4) to find the reversible and irreversible macroscopic strains.

Calculation of damage to intermartensitic boundaries

In this paper, the description of the MSE, as well as in [17], is based on the idea of calculating the damage of the intermartensitic boundaries and its effect on the dissipative force F^{fr}. Observations of the structure of the boundaries [16] show that they are damaged during growth of martensitic plates on the late stages of MT, as well as by the growth of some plates at the expense of others during the reorientation of martensite occurring at

the deformation of samples in the martensitic state. Accordingly, in this model, the equations for the evolution of the damaged boundaries are proposed:

$$d\zeta = k_1 \frac{(\Phi_M - \Phi_{crit})H(\Phi_M - \Phi_{crit})}{(1 - \Phi_{crit})(1 + k_3\zeta^2)} d\tilde{r}H(d\tilde{r}), \tag{14}$$

$$d\zeta = \frac{\zeta_1 - \zeta}{\Phi_M(1 + k_3 \zeta^2)} d\Phi_M H(d\Phi_M), \tag{15}$$

$$d\zeta = 0, (16)$$

$$d\zeta = 0,$$

$$\zeta_1 = k_2 \frac{(\Phi_M - \Phi_{crit})H(\Phi_M - \Phi_{crit})}{(1 - \Phi_{crit})}\tilde{r}.$$
(16)

Equation (14) is responsible for the change in damage during reorientation of martensite, (15) and (17) – during forward MT, (16) – during reverse MT; k_1 , k_2 , k_3 , Φ_{crit} are the constants of the material, of which k_1 is responsible for the rate of damage growth during reorientation, k_2 – during forward MT, k_3 is responsible for the rate of saturation of the damage; Φ_{crit} is the martensite volume fraction, at which damage growth begins during the direct MT.

The variable $\tilde{r} = r/\Phi_M$, where $r = \frac{1}{2(N-1)}\sum_{n=1}^N |\Phi_n - \Phi_M|$, characterizes the degree of orientation of martensite: $\tilde{r} = 0$ for completely chaotic martensite and $\tilde{r} = 1$ for completely monodomenized martensite. The main hypothesis is that the dissipative force of resistance to the movement of damaged boundaries increases with the increase in their damage. Thus, the dissipative force F^{fr} in the MT condition (9) must be replaced by F^{fr}_{MSE} , which depends on the boundaries damage. In this work, the equation for the force F_{MSE}^{fr} is proposed in the form: $F_{MSE}^{fr} = F^{fr}(1+\zeta^k)$, where F^{fr} is the force of resistance to the movement of undamaged boundaries, k is the constant of the material, taking into account the nonlinearity of the effect of damage on the friction force and, accordingly, on the shift of the characteristic temperatures of the reverse MT.

Simulation of experiments studying the martensite stabilization effect

For comparison with experimental data, the following calculations were carried out, in which the preliminary strain is produced in three different ways: (1) deformation in the martensitic state due to the reorientation of martensite; (2) cooling under constant stress with accumulation of the strain due to direct MT; (3) deformation in the austenitic state at a temperature, at which martensite is induced by stresses.

The calculated dependences of strain on temperature are shown in Fig. 1. Comparison with the observed shift of the reverse MT start temperature A_s was carried out for Ti₅₀Ni₅₀ and Ti₄₉Ni₅₁ alloys experimentally studied in [16]. The following values of constants were used. For $Ti_{50}Ni_{50}$ alloy: characteristic temperatures are $M_s = 57$ °C, $M_f = 64$ °C, $A_s = 82$ °C, $A_f = 89$ °C, the latent heat of transformation is $q_0 = -110$ MJ/ m^3 , constants for MSE are $k_1 = 5.6$, $k_2 = 6.0$, $k_3 = 0.75$, $\Phi_{crit} = 0.5$, $k_1 = 1.8$. For Ti₄₉Ni₅₁ alloy: characteristic temperatures are $M_s = -20$ °C,, $M_f = -33$ °C, $A_s = -7$ °C, $A_f = 3$ °C, the latent heat of transformation is $q_0 = -150 \, MJ/m^3$, constants for MSE are $k_1 = 6.0$, $k_2 = 14.5$, $k_3 = 12.0$, $\Phi_{crit} = 0.5$, k = 10.

The temperatures of phase transformations were taken from the study [16], and the other constants were determined on the basis of the data presented in the same work.

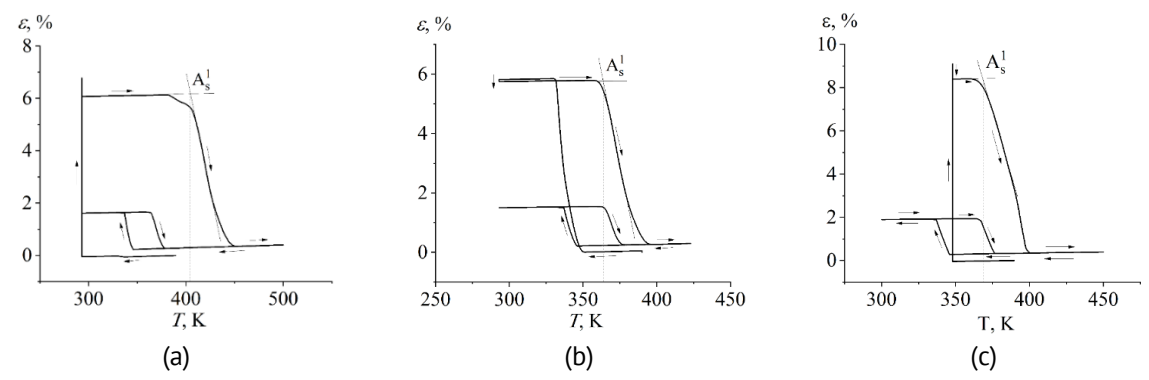


Fig. 1. Dependences of strain on temperature at: preliminary deformation, heating to a completely austenitic state and a subsequent thermal cycle (cooling – heating) showing the effect of the reversible (two-way) shape memory. The preliminary strain is produced by: (a) deformation in the martensitic state; (b) cooling under stress; (c) deformation in the austenitic state producing stress-induced martensite

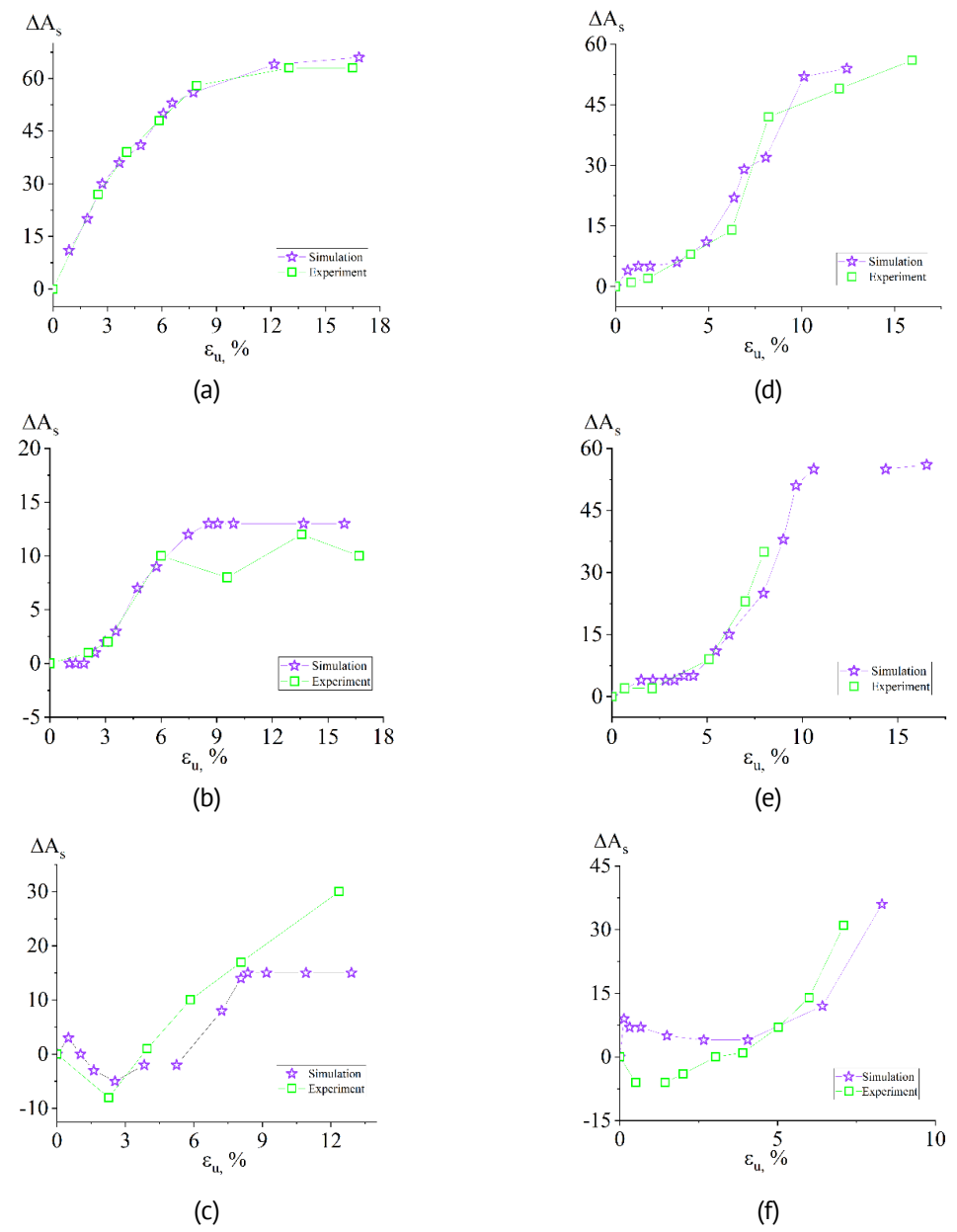


Fig. 2. Dependences of the shift of the reverse MT start temperature $\Delta A_s = A_s^1 - A_s^0$ on the magnitude of the pre-strain for alloys $Ti_{50}Ni_{50}$ ((a) I method, (b) II method, (c) III method) and $Ti_{49}Ni_{51}$ ((d) I method, (e) II method, (f) III method)

Figure 2(a-c) shows the dependences of the shift of the reverse MT start temperature A_s for $Ti_{50}Ni_{50}$ alloy on the residual deformation ε_u , produced respectively by the first, second and third methods. The experimental values are taken from [16]. From Fig. 2(a,b) one can see that for the first and second methods of pre-straining, for which the constants were calibrated, the simulation gives results that are in good agreement with the experiment. For the third method of pre-straining (Fig. 2(c)) the calculation also shows good agreement with the experiment, except for large degrees of pre-strain (above 8 %). The results of similar calculations for $Ti_{49}Ni_{51}$ alloy are shown in Fig. 2(d-f). It should be noted that the simulation satisfactorily describes the increase in A_s for all three methods of pre-straining, despite the significant difference between the $A_s(\varepsilon_u)$ dependences for Ti₄₉Ni₅₁ and Ti₅₀Ni₅₀ alloys. In particular, in the first method of prestraining for both alloys A_s increases monotonously with ε_u tending to saturation, however, for $Ti_{50}Ni_{50}$ alloy the $A_s(\varepsilon_u)$ dependence is convex (Fig. 2(a)), and for $Ti_{49}Ni_{51}$ alloy it has a point of inflexion (Fig. 2(d)). The selection of constant values makes it possible to describe the MSE in both of these alloys. A significant discrepancy between the calculated and experimental values of A_s is observed only for Ti₄₉Ni₅₁ alloy with the third method of pre-straining for low values of ε_u , less than 3 % (Fig. 2(f)).

Conclusion

A hypothesis that the damage of the intermartensitic boundaries during preliminary deformation influences the dissipative force opposing the reverse martensitic transformation can explain the martensite stabilization effect – shift upward of the reverse transformation start temperature $A_{\rm s}$. Equations proposed in this paper for calculating the evolution of the boundaries damage make it possible to achieve a satisfactory, and are good description of the martensite stabilization effect appearing after three different methods of pre-straining. Microstructural modeling of the functional and mechanical properties of shape memory alloys $Ti_{50}Ni_{50}$ and $Ti_{49}Ni_{51}$, performed with an account of the martensite stabilization effect, allow obtaining dependences of the $A_{\rm s}$ temperature on the magnitude of the preliminary strain. These dependences are in a good quantitative agreement with experimental data in the cases if the pre-strain is produced by deformation of a specimen in the martensitic state or cooling it under a load, and in a good qualitative correspondence in the case of inducing martensite by stress.

References

- 1. Lin HC, Wu SK, Chou TS, Kao HP. The effects of cold rolling on the martensitic transformation of an equiatomic Ti Ni alloy. *Acta Metallurgica et Materialia*. 1991;39(9): 2069–2080.
- 2. Piao M, Otsuka K, Miyazaki S, Horikawa H. Mechanisms of the As temperature increase by predeformation in thermoelastic alloys. *Materials Transactions*, *JIM*. 1993;34(10): 919–929.
- 3. Liu Y, Favier D. Stabilisation of martensite due to shear deformation via variant reorientation in polycrystalline NiTi. *Acta Materialia*. 2000;48(13): 3489–3499.
- 4. Liu Y, McCormick PG. Thermodynamic analysis of the martensitic transformation in NiTi-I. Effect of heat treatment on transformation behaviour. *Acta Metallurgica et Materialia*. 1994;42(7): 2401 2406.
- 5. Liu Y, Tan GS. Effect of deformation by stress-induced martensitic transformation on the transformation behaviour of NiTi. *Intermetallics*. 2000;8(1): 67-75.

- 6. Tan GS, Liu Y. Comparative study of deformation-induced martensite stabilization via martensite reorientation and stress-induced martensitic transformation in NiTi. *Intermetallics*. 2004;12(4):373–381.
- 7. Liu Y. Mechanistic simulation of deformation-induced martensite stabilization. *Materials Science and Engineering*: A. 2004;378(1–2): 459–464.
- 8. Liu Y, Tan G, Miyazaki S. Deformation-induced martensite stabilisation in [100] single-crystalline Ni–Ti. *Materials Science and Engineering: A.* 2006;438–440: 612–616.
- 9. Ortin J, Planes A. Thermodynamics of thermoelastic martensitic. *Acta Metallurgica*. 1989;37(5): 1433–1441. 10. Wollants P, Roos JR, Delaey L. Thermally- and stress-induced thermoelastic martensitic transformations in the reference frame of the equilibrium thermodynamics. *Progr Mater Sci.* 1993;37: 227–288.
- 11. Kustov S, Pons J, Cesari E, Morin M, Van Humbeeck J. Athermal stabilization of Cu–Al–Be β 1' martensite due to plastic deformation and heat treatment. *Materials Science and Engineering: A.* 2004;373(1–2): 328–338.
- 12. Kustov S, Pons J, Cesari E, Van Humbeeck J. Chemical and mechanical stabilization of martensite. *Acta Materialia*. 2004;52(15): 4547–4559.
- 13. Belyaev S, Resnina N, Iaparova E, Ivanova A, Rakhimov T, Andreev V. Influence of chemical composition of NiTi alloy on the martensite stabilization effect. *Journal of Alloys and Compounds*. 2019;787: 1365–1371.
- 14. Belyaev S, Resnina N, Rakhimov T, Andreev V. Martensite stabilisation effect in Ni-rich NiTi shape memory alloy with different structure and martensitic transformations. *Sensors and Actuators A: Physical.* 2020;305: 111911.
- 15. Belyaev S, Resnina N, Ivanova A, et al. Martensite Stabilization Effect in the Ni50Ti50 Alloy After Preliminary Deformation by Cooling Under Constant Stress. *Shape Memory and Superelasticity*. 2020;6: 223–231.
- 16. Belyaev S, Resnina N, Ponikarova I, Iaparova E, Rakhimov T, Ivanova A. Damage of the martensite interfaces as the mechanism of the martensite stabilization effect in the NiTi shape memory alloys. *Journal of Alloys and Compounds*. 2022;921:166189.
- 17. Belyaev FS, Volkov AE, Volkova NA, Vukolov EA, Evard ME, Rebrov TV. Simulation of the effect of martensite stabilization in titanium nickelide after deformation in the martensitic state. *Mechanics of Composite Materials and Structures*. 2023;29(4): 470–482. (In Russian)
- 18. Belyaev F, Evard M, Volkov A, Volkova N. A microstructural model of SMA with microplastic deformation and defects accumulation: Application to thermocyclic loading. *Materials Today: Proceedings*. 2015;2: S583—S587.
- 19. Volkov AE, Evard ME, Volkova NA, Vukolov EA. Microstructural modeling of a TiNi beam bending. *Materials Physics Mechanics*. 2023;51(2): 177–186.
- 20. Beliaev FS, Evard ME, Ostropiko ES, Razov AI, Volkov AE. Aging Effect on the One-Way and Two-Way Shape Memory in TiNi-Based Alloys. *Shape Memory and Superelasticity*. 2019;5(3): 218–229.
- 21. Salzbrenner RJ, Cohen M. On the thermodynamics of thermoelastic martensitic transformations. *Acta Metallurgica*. 1979;27(5): 739–748.
- 22. Patoor E, Eberhardt A, Berveiller M. Micromechanical modelling of superelasticity in shape memory alloys. *Le Journal de Physique IV*. 1996;6: C1-277—C1-292.
- 23. Patoor E, El Amrani M, Eberhardt A, Berveiller M. Determination of the origin for the dissymmetry observed between tensile and compression tests on shape memory alloys. *Le Journal de Physique IV*. 1995;5: C2-495—C2-500.
- 24. Nishida M, Nishiura T, Kawano H, Imamura T. Self-accommodation of B19' martensite in Ti-Ni shape memory alloys Part I. Morphological and crystallographic studies of variant selection rule. *Philosophical Magazine*. 2012;92(17): 2215–2233.
- 25. Madangopal K, Singh J, Banerjee S. Self-accommodation in Ni-Ti shape memory alloys. *Scripta Metallurgica et Materialia*. 1991;25(9): 2153–2158.

About Authors

Aleksandr E. Volkov (10) Sc

Doctor of Physical and Mathematical Sciences Professor (St. Petersburg State University, St. Petersburg, Russia)

Fedor S. Belyaev D Sc

Candidate of Physical and Mathematical Sciences Senior Researcher (Institute for Problems of Mechanical Engineering RAS, St. Petersburg, Russia)

Natalia A. Volkova 🗓 Sc

Candidate of Physical and Mathematical Sciences Associate Professor (St. Petersburg State University, St. Petersburg, Russia)

Egor A. Vukolov D Sc

Student (St. Petersburg State University, St. Petersburg, Russia)

Margarita E. Evard D Sc

Candidate of Physical and Mathematical Sciences Associate Professor (St. Petersburg State University, St. Petersburg, Russia)

Timofey V. Rebrov

PhD Student (St. Petersburg State University, St. Petersburg, Russia)

Submitted: January 24, 2024 Revised:

Revised: February 12, 2024 Accepted: August 7, 2024

Interface shear damage of novel biocomposite materials based on polyhydroxyalkanoates biopolymer matrix

A. Mokaddem ¹ D, M. Belkheir D, M. Rouissat D, B. Doumi J, D, A. Boutaous D

ABSTRACT

Bioplastics reinforced with natural fibers are gaining attention for their potential in various emerging ecofriendly applications, resulting in new materials with exceptional mechanical and thermal properties. This study examines PHA biopolymer plastic as a polymer matrix for natural fibers, specifically date palm, coconut, and sisal. It focuses on calculating shear damage at the fiber-matrix interface for the biocomposites date palm/PHAs, coconut/PHAs, and sisal/PHAs. The results show that under mechanical stresses (σ = 40, 45, 50, and 55 MPa), damage levels increase due to the accumulation of stresses, with sisal/PHAs exhibiting more severe degradation at the interface compared to date palm/PHAs and coconut/PHAs. These findings highlight the significant role of natural fibers in enhancing the mechanical properties of composite materials.

KEYWORDS

bioploymers • PHA • natural fibers • date palm • coconut • sisal

Acknowledgements. This work was supported by the General Direction of Scientific Research and Technological Development of the Ministry of Higher Education and Scientific Research of Algeria. (PRFU:A25N01CU320120230001).

The authors wish to convey heartfelt appreciation to everyone who played a role in the successful culmination of this research endeavor. Foremost, the authors extend their gratitude for the financial support generously provided by the General Direction of Scientific Research and Technological Development of the Ministry of Higher Education and Scientific Research of Algeria.

Citation: Mokaddem A, Belkheir M, Rouissat M, Doumi B, Boutaous A. Interface shear damage of novel biocomposite materials based on polyhydroxyalkanoates biopolymer matrix. *Materials Physics and Mechanics*. 2024;52(4): 100–113.

http://dx.doi.org/10.18149/MPM.5242024_10

Introduction

Nowadays, the exploration of composite and biocomposite polymers has captivated researchers and manufacturers alike, motivating an in-depth investigation into this dynamic field [1–4]. The focal point of this pursuit extends beyond the enhancement of existing properties, aiming to innovate and introduce novel materials tailored for a diverse range of contemporary applications [5,6]. Composite materials, constructed by arranging various components such as fibers (synthetic or natural), matrices (thermoset or thermoplastic), and fillers, undergo a transformative process, resulting in the creation of materials with enhanced mechanical, thermal, and physicochemical properties [7,8].

¹Centre Universitaire Nour Bachir El-Bayadh, El Bayadh, Algeria

² Université de Tlemcen, Tlemcen, Algeria

³ Dr. Tahar Moulay University of Saïda, Saïda, Algeria

⁴ Université des Sciences et de la Technologie d'Oran Mohamed-Boudiaf, Oran, Algeria

[™] mokaddem.allel@gmail.com

These materials often exhibit superior strength [9], durability [10], and resistance to environmental factors compared to their individual constituents [11]. The emergence of biocomposite polymers, where natural fibers or fillers are incorporated into a polymer matrix, underscores a deliberate move towards sustainability and eco-friendliness in material design [12,13]. These materials find widespread application in diverse sectors, including biomedical, telecommunications, construction, aeronautics, and beyond [14–16]. In the biomedical field, the biocompatible nature of these polymers makes them invaluable for the development of implants, drug delivery systems, and other medical devices [17,18]. In telecommunications, their lightweight and durable properties make them ideal for components in electronic devices and sensing components [19,20]. Moreover, these materials play a pivotal role in eco-conscious building practices, offering sustainable alternatives for construction materials [21-23]. In aeronautics, where lightweight yet robust materials are essential, composite and biocomposite polymers have become integral to aircraft design, contributing to fuel efficiency and environmental sustainability [24-26]. In the pivotal area of food packaging, these materials are increasingly recognized for their eco-friendly nature and tailored properties, presenting a sustainable choice that aligns with environmental consciousness [27,28]. This expansive influence underscores the pivotal role of these materials in shaping a greener and more technologically advanced future across diverse industries. In the scope of this study, our attention is directed towards a meticulous investigation into the polyhydroxyalkanoates (PHA) biopolymer plastic as polymer matrix for natural fiber namely date palm, coconut, and sisal. The principal objective is to attain a thorough understanding of how the distinct reinforcing fibers impact the behavior of the PHA biopolymer matrix. In recent literature, several works have been dedicated to investigating the properties of PHA, positioning it as a leading candidate for emerging applications. The authors in [29] have conducted an extensive examination of the latest progress in PHA bioproduction, covering a spectrum from native to diversified cell factories. The exploration encompasses discussions on recovery and purification techniques, and the evaluation of the current status of industrial applications is positioned as a crucial milestone for startups. The culmination of the overview involves addressing contemporary challenges and outlining future prospects, providing valuable insights into a trajectory geared towards diminished carbon emissions and the realization of sustainable development goals. In [30], authors have presented an overview of the natural weathering behavior exhibited by representative completely biodegradable composites. The impacts of natural weathering on these composites closely align with those observed in natural fiber composites featuring conventional non-degradable matrices. Interestingly, no discernible influence of biodegradation from the biopolymer matrices manifested under natural weathering conditions for a minimum of 2 years. However, physical and mechanical deteriorations of the composites became evident after a few months of exposure, with the severity primarily dependent on the fiber content. In essence, the accessibility of the natural fibers and the rate of moisture ingress into the bulk matrix emerge as crucial factors governing the stability of biodegradable composites during natural weathering. Furthermore, a multitude of recent studies has underscored the profound impact of polyhydroxyalkanoates (PHA) biopolymers, shedding light on their fabrication processes and elucidating their influence across various contemporary industrial trends [31–34].

The present work delves into a comprehensive exploration of the mechanical properties of the polyhydroxyalkanoates (PHA) biopolymer, particularly when reinforced with natural fibers such as date palm, coconut, and sisal. The overarching goal is to develop novel materials boasting enhanced mechanical strength. By scrutinizing the distinctive characteristics of each fiber type, the study seeks to unveil their individual impacts and collective contributions to the overall attributes of the biocomposite. The investigation entails the calculation of shear damage at the fiber-matrix interface for three specific biocomposite materials date palm/PHAs, coconut/PHAs, and sisal/PHAs employing a genetic operator crossing approach based on the length of each fiber. This analysis is conducted under the influence of various applied mechanical stresses. The focused examination is intricately designed to provide valuable insights into the dynamic interplay between Date Palm, Coconut, Sisal, and the Polyhydroxyalkanoates (PHA) biopolymer matrix, thereby enriching our comprehension of the interface behavior in biocomposite materials such as bioplastic polymers.

Materials and Methods

Polyhydroxyalkanoates biopolymer matrix

Polyhydroxyalkanoates (PHAs) have very varied physicochemical properties depending on their chemical composition [35–38]. For example, the mechanical properties and crystallinity of the material vary depending on the presence of co-monomers. They can be implemented using techniques comparable to phase inversion and are resistant to most organic solvents. The PHA is non-toxic, biocompatible, biodegradable thermoplastics that can be produced from renewable resources. They have a high degree of polymerization, are highly crystalline, optically active and isotactic (stereochemical regularity in repeating units), piezoelectric and insoluble in water. These features make them highly competitive with polypropylene, the petrochemical derived plastic [39].

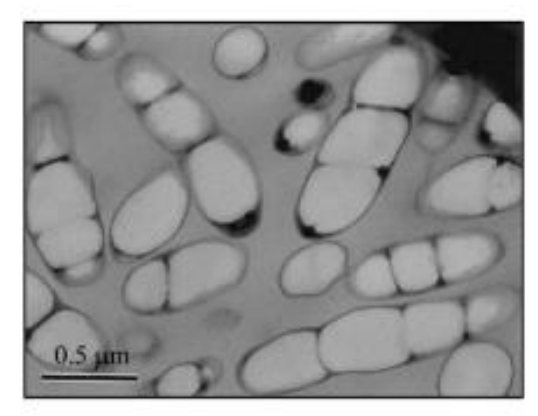


Fig. 1. Electron microscopy image of bacteria (Ralstoniaeutropha) containing polyhydroxyalkanoate granules

PHAs are a family of linear, biosourced and biodegradable polyesters, with varied structures and properties. PHAs are made of hydroxyalkanoate (HA) monomer units with different lengths and functionalities. The nomenclature of a monomer unit refers to the total number of carbons present and the location of the side chain if there is one. They have the particularity of being produced by bacteria. The first bacterial polyhydroxyalkanoates (PHAs) were discovered in 1925 by the French scientist Maurice Lemoigne [37,39,40]. Indeed, in the presence of a source of carbon, nitrogen and oxygen, certain Bacteria have the ability to generate PHA granules to use as an energy reserve. Figure 1 highlights in particular by transmission electron microscopy the presence of these PHA granules in bacteria of the Ralstoniaeutropha type [37,41]. The properties of PHA depend largely on the nature and content of the monomers which it contains [35–38]. In Table 1, the physical properties of the PHA biopolymer have been illustrated [42–45].

Table 1. Physical properties of the PHA biopolymer [42-45]

Matrix	Young's modulus, GPa	Tensile strength, MPa	Elongation at break, %
PHA	3.0	43.0	5.0

Fibers

Date palm fibers (DPFs) have very interesting properties that allow them to be exploited in different applications such as the production of biochar [46] and the manufacture of ropes and baskets [47]. In addition, they are biodegradable and they have a very low environmental impact and above all their technical-economic advantages, DPFs are widely used in industrial sectors and currently in automation, automobiles, aeronautics and construction in order to improve thermal insulation [48,49], The literature showed that date palm fibers can have high cellulose purity up to 70 %. The density of date palm is between 1.18 and 1.45 gm/cm³ which are comparable to other widely used natural fibers. Date palm fibers can be used in automotive applications, in particleboard manufacturing and as reinforcement to panels to be used as thermal or sound insulation [50]. The major problem is that PDFs are hydrophilic in nature, which generates compatibility and interfacial bonding problems due to the hydrophobic nature of their matrix. To solve this problem, several physical and chemical treatment methods have been considered by many researchers and scientists [51,52]. One of the most effective is chemical treatment using the sodium hydroxide process. The principle of this treatment is to eliminate the existing amorphous polymers on the surface and to obtain celluloserich fibers which improve the mechanical properties of the pure matrix when used as reinforcement [53,54].

Coconut fibers. Coconut is the fruit of the coconut palm (Cocosnucifera), one of the representatives of the palm family or Arecaceae. The exterior of the fruit is smooth and light green or orange in color when the flower is not ripe (young coconut); brown in color and covered with a thick layer of brown woody fiber surrounding the mature nut (ripe coconut), and composed of a solid spherical shell which protects an edible whitish kernel. The coconut palm is found in tropical countries. The coir surrounds and protects the coconut, the fruit of the coconut tree. It is extracted manually or mechanically, then washed and dried. The fibers measure up to 35 cm in length with a diameter ranging from 12 to 25 µm. They have a high lignin content which makes them stronger than cotton.

They also have good resistance to microbial action and salt water. Traditionally, coconut fiber is used to make rope, fishing nets, canvas, carpets, brushes, brooms or mattress padding. More recently, geotextiles, made entirely from coir, are used to combat soil erosion. We also find insulation in the form of flexible panels and plywood (fibers and resins). Coconut fibers are classified as seed or fruit fibers. Coconut fiber is entirely biodegradable and transformed into substrate. It is suitable for mulching poor and sandy lands, hydroculture, massifs, annuals, flowering plants, trees, shrubs and rose bushes as well than the ground cover. These fibers are short and fine. In fact, plant fibers are classified into three categories: 1 - Seed or fruit fibers (e.g. cotton, coconut), 2 - Leaf fibers (e.g. sisal, abaca, esparto), 3 - Bast fibers or stem fibers (Ex: flax, jute, hemp, ramie) [55].

Sisal fibers. Sisal is a resistant plant in hot and arid climates, often unsuitable for other cultures. It only flowers once times, just before dying. Like all agaves, sisal forms a rosette of thick leaves that ends in a sharp point and has spiny edges. These leaves, although full of water, are very rigid thanks to the numerous fibers they contain. Fibers located inside the leaves lengthwise, are more abundant towards the surface. Defibration is carried out just after harvest. The pulp is scraped by hand or mechanically, releasing the fibers. They are several long tens of centimeters, thick and solid. A drying step is necessary before gathering the fibers ready for braiding of the plant. Sisal fiber is traditionally used to make ropes like that used, before plastic replaced it, to tighten straw bales. Traditional sisal clothing is found in China and Laos. These fibers also serve as flexible reinforcements to reinforce plaster or for composite materials. Sisal is increasingly used in high value-added finished products and for various other uses; it is the constant and superior quality of this sisal which allows its use in more profitable finished products. These product categories particularly plaster reinforcement in the construction sector and pulp production; have experienced constant growth for several years. The long fibers which are part of the hard fibers are generally used for the manufacture of baling twines, tying twines, ropes, maritime twines and polishing fabrics. Short fibers are used for the production of carpets and construction panels. Sisal fibers are also used in the paper industry to improve the performance of filter paper made from wood cellulose pulp. [55–58].

The different physical properties of fibers used in genetic modeling have been illustrated in Table 2.

Table 2. Physical properties of different fibers used in genetic modeling

Fiber	Density, g/cm ³	Deformation, %	Tensile strength, MPa	Young's modulus, GPa		
Sisal [59-62]	1.50	5.12	228.00	9.40		
Coconut [63,64]	1.17	13.70	107.00	5.00		
Date palm [64]	1.08	17.40	290.00	5.25		

Weibull formalism

The findings in our investigation were obtained using a genetic simulation primarily rooted in the Weibull formalism. This approach was adopted to assess the damage at the interface of the three materials, incorporating genetic operators like selection, crossing, and mutation. The Weibull formula (Eq. (1)), as outlined in [64-68], is employed to characterize the damage to the matrix under uniform stress conditions.

$$D_m = 1 - exp \left\{ -\frac{V_{eff}}{V_0} \left(\frac{\sigma_f}{\sigma_0} \right)^m \right\}, \tag{1}$$

where σ_f represents an applied stress, V_{eff} denotes the matrix volume, m and σ_0 are the Weibull parameters, V_0 signifies the initial volume of the matrix.

The fiber is regarded as an element within an assembly of links, each having its distinct breaking strength. Fracture frequency arises when the weakest link in the assembly experiences a break. The failure of a fiber along its entire length is primarily influenced by repetitions. This rupture can be characterized by a law analogous to that of the matrix, as described in [65,69,70].

$$D_f = 1 - exp \left\{ -A_f * L_{equi} * \left(\frac{\sigma_{max}^f}{\sigma_{of}} \right)^{m_f} \right\}, \tag{2}$$

where σ_{max}^f represents the maximum stress applied to the fiber, σ_{0f} is an initial stress applied to the fiber, m_f are Weibull parameters, $A_f = \pi^* a^2$, L_{equi} is the length of the fiber at equilibrium.

Fiber-matrix interface damage

The interface or interphase exhibits distinct properties compared to the constituents, specifically concerning mechanical properties. Despite these differences, it holds a crucial role in facilitating the transfer of forces between the matrix and the fiber. The quality of the interface is, therefore, a determining factor in shaping the ultimate performance of composites, as emphasized in references [71,72]. For this reason, the mechanical characterization of this pivotal area is imperative. The characterization of the interface involves determining its mechanical properties based on the materials used for the fiber and matrix. Additionally, it may be contingent on any modifications such as treatments that the materials undergo, including chemical formulations of the matrix, surface treatments of fibers, aging, etc. [71]. The composite test pieces undergo various types of testing, exemplified by the tensile test conducted at a specified angle relative to the fiber direction, the interlaminar shear test on a short further, and the three or four-point bending test. Additionally, monofilament test pieces are subjected to a range of tests, including the release test pull-out or micro-drop, the fragmentation test, and the indentation test, among others [71]. In our numerical simulation, we employed Eq. (3) derived from the pull-out heaving test. This test involves raising a fiber, either partially or entirely immersed in a micro test tube, by applying a pulling force [71,73]. The average shear stress τ_{app} at the interface is determined by:

$$\tau_{app} = \frac{F_{max}}{2\pi r l_e},\tag{3}$$

where F_{max} is the maximum force measured; r : average radius of the fiber; l_e is the length of the fiber inserted into the matrix (length of the interface).

Results and Discussion

The composite materials with fiber reinforcements have optimized mechanical and physical properties, which depend not only on those of their constituents, their architecture but also on the bond between fiber and matrix. The quality of this fiber/matrix interface, which plays a primordial role in the mechanical resistance of composite materials, depends on several factors that can be identified using different

tests carried out at the microscopic scale. Most of the experimental techniques described the fiber-matrix interface are often expensive and require significant preparation and implementation time, and that the geometry of plant fibers is highly variable. There are often surface defects [71]. For this reason, we have proposed and developed a simple numerical method based on genetic algorithms to characterize the mechanical properties of the fiber-matrix interface shear damage. The current study involved the computation of shear damage at the fiber-matrix interface for three distinct biocomposite materials: date palm/PHAs, coconut/PHAs, and sisal/PHAs, employing the genetic operator crossing approach. The damage to the fiber and matrix was calculated using Eqs. (1) and (2), respectively. The material-specific values presented in Tables 1 and 2 were applied in the computation of the objective function. Subsequently, the interface shear damage was determined based on the length of each fiber for the studied materials, subjected to various applied mechanical stresses (σ = 40, 45, 50, 55 MPa).

As per Cox's model [74], the transfer of load leads to the generation of interfacial shear stresses, reaching maximum amplitude at the ends of the fiber and exhibiting very small values in the middle. Cox observed that these stresses display symmetry at the midpoint of the fiber. To aid in this analysis, he presented the two tensile and shear stresses, as illustrated in Fig. 2. This figure served to rationalize our selection of specific points utilized in our genetic modeling, namely (-L, -L/2, 0, L/2, L).

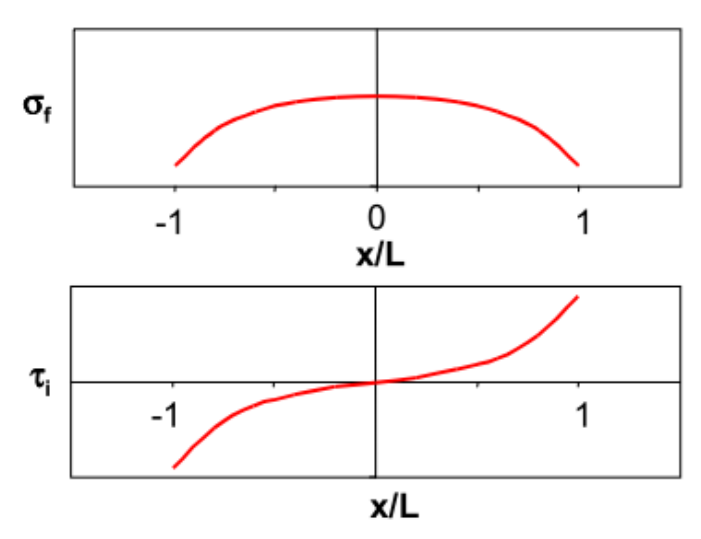


Fig. 2. Cox model; stress profiles in the fiber (σf) and at the interface (τi) [74]

Figures 3–5 visually represent the damage at the interface for the three distinct biocomposite materials. In particular, Fig. 3 depicts the initiation of shear damage at the interface (denoted as "D") for the date palm/PHAs biocomposite material. The damage initiates at a threshold of 0.089 when σ = 45 MPa and progressively increases to a maximum value of 0.165 at σ = 55 MPa. Furthermore, Fig. 2 illustrates the symmetry of weak damage in the middle of the fiber and strong damage at the ends of the fiber, as depicted by the black and green colors in Fig. 3. From the results, it can be inferred that an elevation in mechanical stress corresponds to an increase in the degree of damage. In the case of this material, the degradation of the interface is relatively modest.

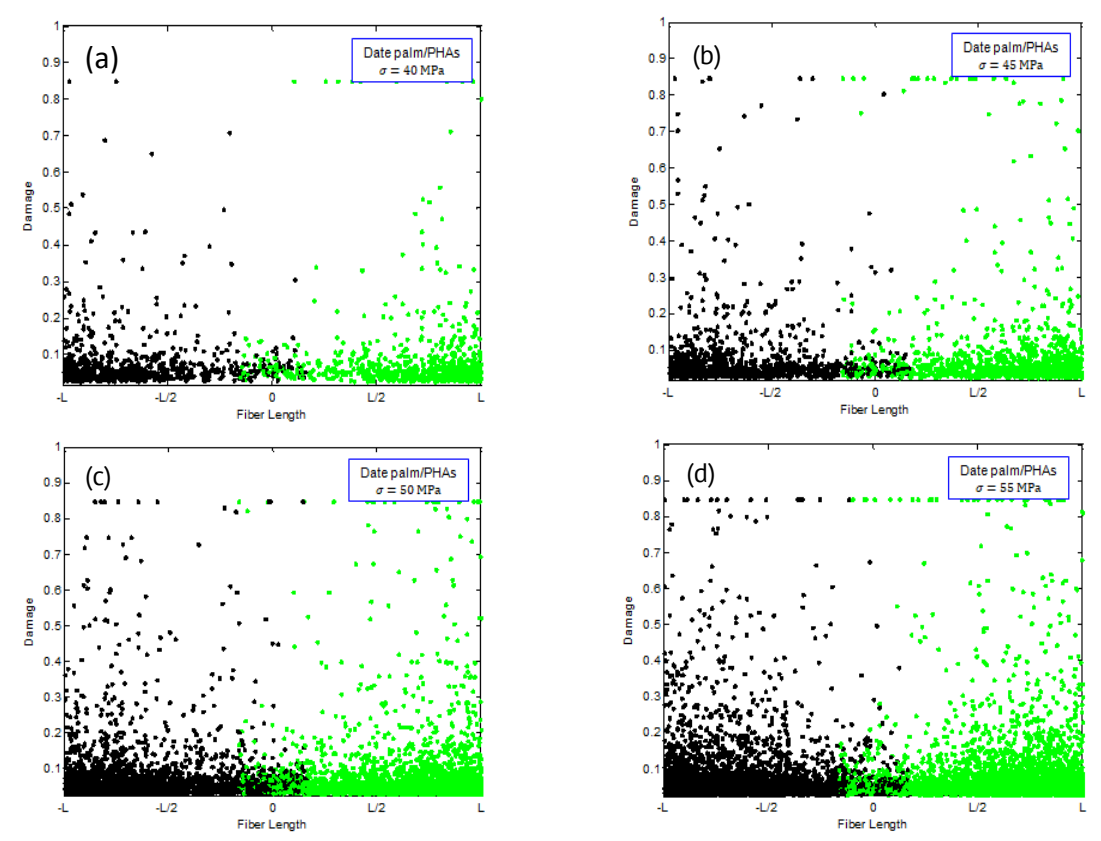


Fig. 3. Interface shear damage of date palm/PHAs biocomposite material: (a) σ = 40 MPa, (b) σ = 45 MPa, (c) σ = 50 MPa, (d) σ = 55 MPa

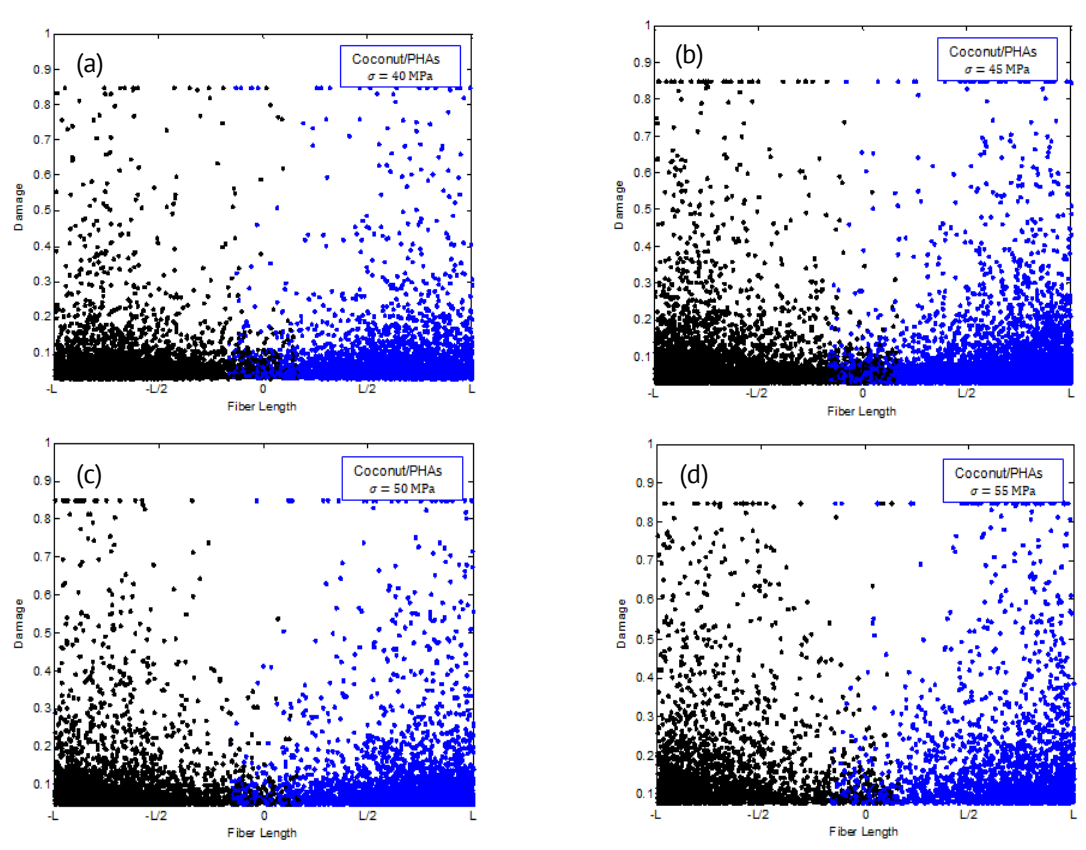


Fig. 4. Interface shear damage of coconut/PHAs biocomposite material: (a) σ = 40 MPa, (b) σ = 45 MPa, (c) σ = 50 MPa, (d) σ = 55 MPa

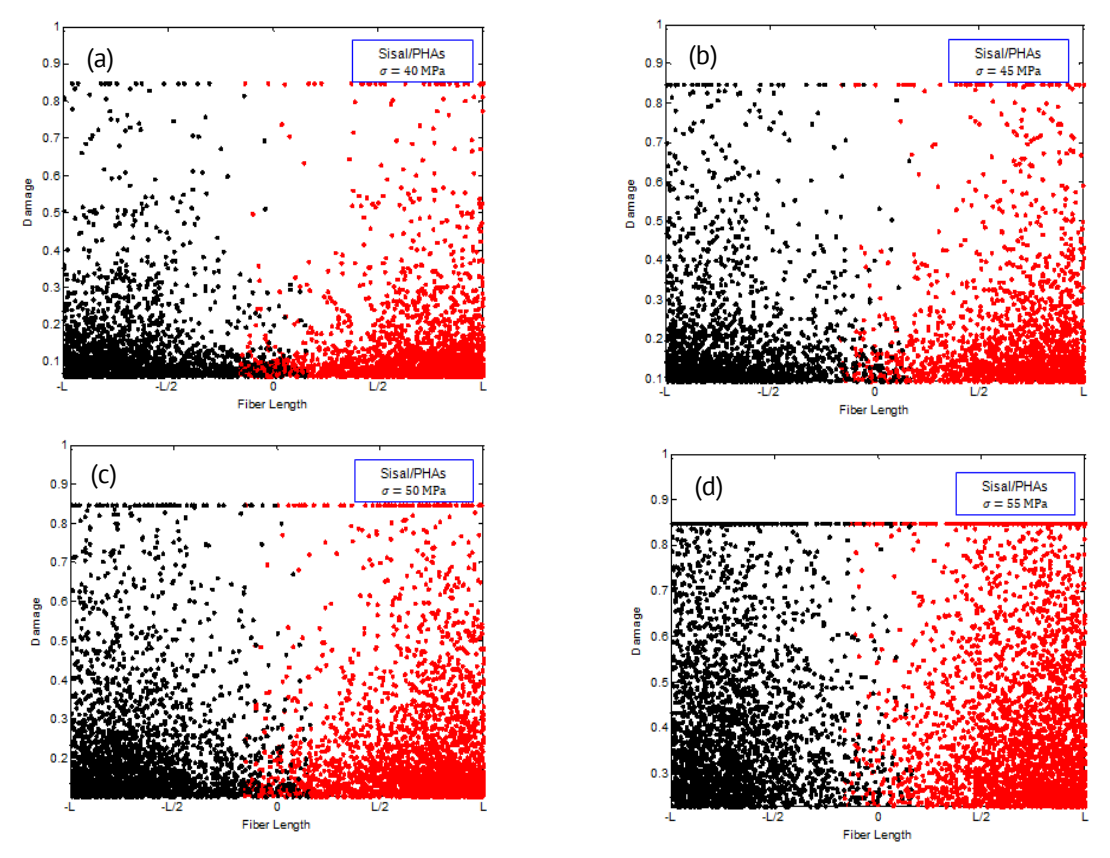


Fig. 5. Interface shear damage of sisal/PHAs biocomposite material: (a) σ = 40 MPa, (b) σ = 45 MPa, (c) σ = 50 MPa, (d) σ = 55 MPa

Figure 4 illustrates the extent of damage at the interface of the coconut/PHAs biocomposite material. The graph shows the initiation of shear damage at the interface, denoted as "D," at a value of 0.112 for a mechanical stress of σ = 45 MPa, escalating to a peak value of 0.2 at σ = 55 MPa. Similar to the preceding material, a symmetric pattern of weak damage in the middle and strong damage at the ends of the fiber is discernible for the coconut/PHAs biocomposite material. This is represented by distinct colors, black and blue, in Fig. 4. The elevation in damage level in the coconut/PHAs biocomposite material suggests that mechanical stresses concentrate at the interface, leading to a more pronounced degradation of the interface compared to the date palm/PHAs biocomposite material.

Figure 5 illustrates that the damage at the interface, labeled as "D," in the Sisal/PHAs biocomposite material commences at a value of 0.181 under a stress of 45 MPa and rises to a peak value of 0.389 when subjected to a stress of 55 MPa. Furthermore, the symmetry of the damage level is relatively low in the central region and significantly higher towards the ends of the fiber, as indicated by the contrasting colors of black and red in Fig. 5. The results suggest that the escalation in damage level is attributed to the accumulation of mechanical stresses, resulting in more severe degradation at the interface of the sisal/PHAs biocomposite material compared to the date palm/PHAs and coconut/PHAs biocomposite materials.

The aforementioned findings align with recent studies conducted by [50,75–78], which consistently affirm that the inclusion of natural fibers, especially date palm fiber, significantly enhances interfacial adhesion in composite materials. These studies highlight that natural fibers contribute substantially to the improved mechanical properties of composite materials, gradually supplanting synthetic fibers due to their specific strength, rigidity, lightness, and cost-effectiveness. Natural fiber-reinforced composites emerge as green, biodegradable, and sustainable materials, finding applications across various industries such as automotive, marine, aerospace, construction, wind energy, and consumer goods.

Conclusions

This study places a focused lens on the realm of bioplastics, particularly polyhydroxyalkanoates (PHA) reinforced with natural fibers (date palm, coconut, and sisal). The evaluation of shear damage at the fiber-matrix interface, facilitated through a genetic operator crossing approach based on the length of each fiber, sheds light on the pivotal role of mechanical stresses in influencing interface degradation. Findings indicate that varying mechanical stresses (σ = 40, 45, 50, and 55 MPa) correlate with an escalation in damage levels, underscoring the cumulative impact of these stresses. Noteworthy is the distinct behavior observed in the Sisal/PHAs biocomposite material, revealing more pronounced degradation compared to its counterparts. This observation accentuates the intricate interplay between natural fibers and the PHA biopolymer matrix. Importantly, these outcomes align with recent studies conducted by the authors in [50,75–78] highlighting the broader transition toward eco-friendly materials, emphasizing the substantial contribution of bioplastics reinforced with natural fibers in elevating mechanical properties.

In practical terms, the enhanced mechanical properties of these biocomposites make them suitable for a variety of eco-friendly applications. For example, packaging solutions, in lightweight automotive components, in durable construction materials. The specific degradation behavior of sisal/PHAs could also be advantageous in applications requiring controlled material breakdown, such as in agricultural or disposable products.

Future research should aim to optimize the fiber-matrix interface to reduce the degradation observed, especially in sisal/PHAs composites. Additionally, exploring other natural fibers or hybrid fiber combinations could enhance the performance of these bioplastics. Additionally, a key direction for future work involves incorporating advanced learning techniques, such as machine learning algorithms, to accurately model and predict the behavior of these biocomposites under various environmental conditions.

References

- 1. Anwer AH, Ahtesham A, Shoeb M, Mashkoor F, Ansari MZ, Zhu S, Jeong C. State-of-the-art advances in nanocomposite and bio-nanocomposite polymeric materials: A comprehensive review. *Advances in Colloid and Interface Science*. 2023;318: 102955.
- 2. Kumar RS, Sasikumar R, Dhilipkumar T. Exploiting agro-waste for cleaner production: A review focusing on biofuel generation, bio-composite production, and environmental considerations. *Journal of Cleaner Production*. 2024;435: 140536.

- 3. Kangishwar S, Radhika N, Sheik AA, Chavali A, Hariharan S. A comprehensive review on polymer matrix composites: Material selection, fabrication, and application. *Polymer Bulletin*. 2023;80(1): 47–87.
- 4. Anerao P, Kulkarni A, Munde Y. A review on exploration of the mechanical characteristics of 3D-printed biocomposites fabricated by fused deposition modelling (FDM). *Rapid Prototyping Journal*. 2024;30(3): 430–440. 5. Gupta M, Jain A, Kamineni JN, Burela RG. Advances and applications of biofiber-based polymer composites. In: *Advances in Bio-Based Fiber*. Elsevier; 2022. p.575–602.
- 6. Nazrun T, Hassan MK, Hossain MD, Ahmed B, Hasnat MR, Saha S. Application of Biopolymers as Sustainable Cladding Materials: A Review. *Sustainability*. 2023;16(1): 27.
- 7. Joshi AG, Bharath KN, Basavarajappa S. Recent progress in the research on natural composite brake pads: A comprehensive review. *Tribology-Materials, Surfaces & Interfaces*. 2023;17(3): 237 259.
- 8. Benallel A, Tilioua A, Garoum M. Development of thermal insulation panels bio-composite containing cardboard and date palm fibers. *Journal of Cleaner Production*. 2024;434: 139995.
- 9. Dhanola A. A comprehensive overview on tribo-mechanical characteristics of hybrid plant fiber-based biocomposites. *Emergent Materials*. 2023;6: 1707–1726.
- 10. Aher PD, Patil YD, Waysal SM, Bhoi AM. Critical review on biopolymer composites used in concrete. To be published in *Materials Today: Proceedings*. [Preprint] 2023. Available from: https://doi.org/10.1016/j.matpr.2023.07.212
- 11. Ryłko-Polak I, Komala W, Białowiec A. The Reuse of Biomass and Industrial Waste in Biocomposite Construction Materials for Decreasing Natural Resource Use and Mitigating the Environmental Impact of the Construction Industry: A Review. *Materials*. 2022;15(12): 4078.
- 12. Bekmezci M, Ay H, Sen F. Green composite materials and their applications. In: *Green Sustainable Process for Chemical and Environmental Engineering and Science*. Elsevier; 2023. p.159–182.
- 13. Santulli C, Fragassa C, Pavlovic A, Nikolic D. Use of Sea Waste to Enhance Sustainability in Composite Materials: A Review. *Journal of Marine Science and Engineering*. 2023;11(4): 855.
- 14. Mokaddem A, Belkheir M, Rouissat M, Boutaous A. Temperature Effect on Interface Damage of Thermoplastic Polymers Composites Materials: CF/PEEK, CF/PMMA, and CF/PPS. *Strength of Materials*. 2023;55: 1089–1099.
- 15. Mahalingam S, Manap A, Lau KS, Floresyona D, Rachman RM, Pradanawati SA, Rabeya R, Chia CH, Afandi N, Nugroho A. Review of bioresource-based conductive composites for portable flexible electronic devices. *Renewable and Sustainable Energy Reviews*. 2024;189: 113999.
- 16. El Messiry M. Biodegradable Fibers, Polymers, Composites and Its Biodegradability, Processing and Testing Methods. In: *Bio-Fiber Reinforced Composite Materials: Mechanical, Thermal and Tribological Properties.* Singapore: Springer; 2022. p.75-104.
- 17. Faheed NK. Advantages of natural fiber composites for biomedical applications: a review of recent advances. *Emergent Materials*. 2024;7: 63–75.
- 18. Prasad A, Datta S, Kumar A, Gupta M. Introduction to Next-Generation Materials for Biomedical Applications. In: *Advanced Materials and Manufacturing Techniques for Biomedical Applications*. 2023. p.1–24. 19. Agarwal R, Singh S, Shalan AE. Sustainable energy storage devices and device design for sensors and actuators applications. In: *Sustainable Energy Storage in the Scope of Circular Economy: Advanced Materials and Device Design*. 2023. p.225–290.
- 20. Vazquez-Nunez E, Avecilla-Ramirez AM, Vergara-Porras B, López-Cuellar MDR. Green composites and their contribution toward sustainability: a review. *Polymers and Polymer Composites*. 2021;29(9_suppl): S1588–S1608. 21. Bendahane K, Belkheir M, Mokaddem A, Doumi B, Boutaous A. Date and doum palm natural fibers as renewable resource for improving interface damage of cement composites materials. *Beni-Suef University Journal of Basic and Applied Sciences*. 2023;12(1): 37.
- 22. Greco PF, Pepi C, Gioffré M. A novel biocomposite material for sustainable constructions: Metakaolin lime mortar and Spanish broom fibers. *Journal of Building Engineering*. 2024;83: 108425.
- 23. Saini K, Matsagar VA, Kodur VR. Recent advances in the use of natural fibers in civil engineering structures. *Construction and Building Materials*. 2024;411: 134364.
- 24. Oyewo AT, Oluwole OO, Ajide OO, Omoniyi TE, Hussain M.A summary of current advancements in hybrid composites based on aluminium matrix in aerospace applications. *Hybrid Advances*. 2023;5: 100117
- 25. Ng LF, Subramaniam K, Mohdlshak N. An overview of the natural/synthetic fibre-reinforced metal-composite sandwich structures for potential applications in aerospace sectors. In: *Advanced Composites in Aerospace Engineering Applications*. Cham: Springer; 2022. p.177–194.
- 26. Kumari S, Soni S, Sharma A, Kumar S, Sharma V, Jaswal VS, Bhatia SK, Sharma AK. Layered double hydroxides based composite materials and their applications in food packaging. *Applied Clay Science*. 2024;247: 107216.

- 27. RoohiBano N, Gupta A, Siddiqui MH, Zaheer MR. Potential of PHA (Polyhydroxyalkanoates) Polymers as Packaging Materials: From Concept to Commercialization. In: *Biobased Packaging Materials: Sustainable Alternative to Conventional Packaging Materials.* Singapore: Springer; 2024. p.67–100.
- 28. Olusanya JO, Mohan TP, Kanny K. Processing of Biobased Packaging Materials. In: *Biobased Packaging Materials: Sustainable Alternative to Conventional Packaging Materials.* Singapore: Springer; 2024. p.37–66.
- 29. Diankristanti PA, Lin YC, Yi YC, Ng IS. Polyhydroxyalkanoatesbioproduction from bench to industry: Thirty years of development towards sustainability. *Bioresource Technology*. 2024;393: 130149.
- 30. Chan CM, Pratt S, Laycock B. Effects of Natural Weathering on Aesthetics, Thermal and Mechanical Properties of Completely Biodegradable Composites. In: *Aging Effects on Natural Fiber-Reinforced Polymer Composites: Durability and Life Prediction.* Singapore: Springer; 2022. p.173–188.
- 31. Mello de AFM, de Souza Vandenberghe LP, Machado CMB, Brehmer MS, de Oliveira PZ, Binod P, Sindhu R, Soccol CR. Polyhydroxyalkanoates production in biorefineries: A review on current status, challenges and opportunities. *Bioresource Technology*. 2024;393: 130078.
- 32. Ladhari S, Vu NN, Boisvert C, Saidi A, Nguyen-Tri P. Recent Development of Polyhydroxyalkanoates (PHA)-based Materials for Antibacterial Applications: A Review. *ACS Applied Bio Materials*. 2023;6(4): 1398–1430.
- 33. Gómez-Gast N, López Cuellar MDR, Vergara-Porras B, Vieyra H. Biopackaging potential alternatives: Bioplastic composites of polyhydroxyalkanoates and vegetal fibers. *Polymers*. 2022;14(6): 1114.
- 34. Awasthi SK, Kumar M, Kumar V, Sarsaiya S, Anerao P, Ghosh P, Singh L, Liu H, Zhang Z, Awasthi MK. A comprehensive review on recent advancements in biodegradation and sustainable management of biopolymers. *Environmental Pollution*. 2022;307: 119600.
- 35. Anjum A, Zuber M, Zia KM, Noreen A, Anjum MN, Tabasum S. Microbial production of polyhydroxyalkanoates (PHAs) and its copolymers: A review of recent advancements. *International Journal of Biological Macromolecules*. 2016;89: 161–174.
- 36. Loeb S. The Loeb-Sourirajan membrane: How it came about. In: *Synthetic Membranes*. American Chemical Society; 1981. p.1–9.
- 37. Tomietto P. Contribution des polyhydroxyalcanoates (PHA) dans l'élaboration de matériaux membranaires pour des séparations en phase liquide (Doctoral dissertation, Rennes 1). 2020.
- 38. Reddy CSK, Ghai R, Kalia V. Polyhydroxyalkanoates: an overview. *Bioresource Technology*. 2003;87(2): 137 146.
- 39. Chee JY, Yoga SS, Lau NS, Ling SC, Abed RM, Sudesh K. Bacterially produced polyhydroxyalkanoate (PHA): converting renewable resources into bioplastics. *Current Research, Technology and Education Topics in Applied Microbiology and Microbial Biotechnology.* 2010;2: 1395–1404.
- 40. Dawes EA, Senior PJ. The role and regulation of energy reserve polymers in micro-organisms. *Advances in Microbial Physiology*. 1973;10: 135–266.
- 41. Sudesh K, Abe H, Doi Y. Synthesis, structure and properties of polyhydroxyalkanoates: biological polyesters. *Progress in Polymer Science*. 2000;25(10): 1503–1555.
- 42. Pérez-Rivero C, Hernandez-Raquet G. Polyhydroxyalcanoates: une alternative 'bio' aux plastiques traditionnels. *Innovations Agronomiques*. 2017;58: 99–112.
- 43. Liu F, Hashim NA, Liu Y, Abed MM, Li K. Progress in the production and modification of PVDF membranes. *Journal of Membrane Science*. 2011;375(1-2): 1–27.
- 44. Tsuge T. Metabolic improvements and use of inexpensive carbon sources in microbial production of polyhydroxyalkanoates. *Journal of Bioscience and Bioengineering*. 2002;94(6): 579–584.
- 45. Sastri V. High-Temperature Engineering Thermoplastics: Liquid Crystalline Polymers, and Fluoropolymers. In: *Plastics in Medical Devices. Properties, Requirements, and Applications.* Elsevier; 2010. p.175–215.
- 46. Usman AR, Abduljabbar A, Vithanage M, Ok YS, Ahmad M, Ahmad M, Al-Wabel MI. Biochar production from date palm waste: Charring temperature induced changes in composition and surface chemistry. *Journal of Analytical and Applied Pyrolysis*. 2015;115: 392–400.
- 47. Alawar A, Hamed AM, Al-Kaabi K. Characterization of treated date palm tree fiber as composite reinforcement. *Composites Part B: Engineering*. 2009;40(7): 601–606.
- 48. Al-Oqla FM, Sapuan SM, Ishak MR, Nuraini AA. Predicting the potential of agro waste fibers for sustainable automotive industry using a decision making model. *Computers and Electronics in Agriculture*. 2015;113: 116–127.
- 49. Oushabi A, Sair S, Abboud Y, Tanane O, Bouari AE-L. Natural thermal-insulation materials composed of renewable resources: characterization of local date palm fibers (LDPF). *Journal of Materials and Environmental Science*. 2015;6(12): 3395–3402.

- 50. Elseify LA, Midani M. Characterization of Date Palm Fiber. In: Midani M, Saba N, Alothman OY. (eds.) *Date Palm Fiber Composites. Composites Science and Technology.* Singapore: Springer; 2020. p.227–255.
- 51. Cao Y, Sakamoto S, Goda K. Effects of heat and alkali treatments on mechanical properties of kenaf fibers. In: 16th International Conference on Composite Materials, Kyoto, Japan, 8–13 July 2007. 2007. p.8–13.
- 52. Ibrahim ID, Jamiru T, Sadiku ER, Kupolati WK, Agwuncha SC, Ekundayo G. Mechanical properties of sisal fibre-reinforced polymer composites: a review. *Composite Interfaces*. 2016;23(1): 15–36.
- 53. Liu M, Silva DAS, Fernando D, Meyer AS, Madsen B, Daniel G, Thygesen A. Controlled retting of hemp fibres: effect of hydrothermal pre-treatment and enzymatic retting on the mechanical properties of unidirectional hemp/epoxy composites. *Composites Part A: Applied Science and Manufacturing*. 2016;88: 253–262.
- 54. Khlif M, Chaari R, Bradai C. Physico-mechanical characterization of poly (butylene succinate) and date palm fiber-based biodegradable composites. *Polymers and Polymer Composites*. 2022;30: 09673911221080157.
- 55. Vissac A. Matière en fibres. *Sciences de l'Homme et Société*. 2014. dumas-03035822. Available from: https://dumas.ccsd.cnrs.fr/dumas-03035822 [Accessed 19th December 2023].
- 56. Alvarez VA, Fraga AN, Vazquez A. Effects of the moisture and fiber content on the mechanical properties of biodegradable polymer–sisal fiber biocomposites. *Journal of Applied Polymer Science*. 2004;91(6): 4007–4016.
- 57. Alvarez VA, Vázquez A. Influence of fiber chemical modification procedure on the mechanical properties and water absorption of MaterBi-Y/sisal fiber composites. *Composites Part A: Applied Science and Manufacturing*. 2006;37(10): 1672–1680.
- 58. Samouh Z. *Textiles à base de fibres naturelles d'origine marocaine pour application matériaux composites (Doctoral dissertation*). Centrale Lille Institut; 2021.
- 59. Sridhar MK, Basavarajappa G, Kasturi SG, Balasubramanian N. Evaluation of jute as a reinforcement in composites. *Ind J of Textile Res.* 1982;7: 87–92.
- 60. Khazanchi AC, Saxena M, Rao TC. Textile composites in building constructions. Paris; 1990.
- 61. Bisanda ETN, Ansell MP. Properties of sisal-CNSL composites. *Journal of Materials Science*. 1992;27: 1690–1700.
- 62. SavastanoJr H, Agopyan V, Nolasco AM, Pimentel L. Plant fibre reinforced cement components for roofing. *Construction and Building Materials*. 1999;13(8): 433–438.
- 63. Christine DA, Séraphin DA, Olivier BM, Edjikémé E. Effet de l'addition de fibres de coco traitées à la potasse sur les propriétés mécaniques des matériaux de construction à base d'argile-ciment. European Scientific Journal. 2018;14(36): 104-116.
- 64. Daher S. Optimisation de la formulation d'un béton de chanvre: effet des interactions physico-chimiques entre les particules végétales et le liant (Doctoral dissertation). Université de Picardie Jules Verne; 2022.
- 65. Weibull W. A statistical theory of the strength of materials. *Royal Swedish Academy of Engineering Sciences Proceedings*. 1939;151:1–45.
- 66. Mokaddem A, Alami M, Boutaous A. A study by a genetic algorithm for optimizing the arrangement of the fibers on the damage to the fiber-matrix interface of a composite material. *The Journal of The Textile Institute*. 2012;103(12): 1376–1382.
- 67. Alami O, Belkheir M, Rouissat M, Mokaddem A, Doumi B, Boutaous A. Improving hybrid nanocomposite performances using genetic approach. *Applied Sciences and Convergence Technologies*. 2023;32(3): 63-68.
- 68. Mokaddem A, Alami M, Doumi B, Boutaous A. Prediction by a genetic algorithm of the fiber matrix interface damage for composite material. Part 1: Study of shear damage to two composites T300/914 and Peek/APC2. *Strength of Materials*. 2014;46(4): 543-547.
- 69. Mokaddem A, Alami M, Temimi L, Boutaous A. Study of the effect of heat stress on the damage of the fibre matrix interface of a composite material (T300/914) by means of a genetic algorithm. *Fibres & Textiles in Eastern Europe*. 2012;6A(95): 108-111.
- 70. Mokaddem A, Alami M, Ziani N, Beldjoudi N, Boutaous. A Prediction by a genetic algorithm of the fiber matrix interface damage for composite material. Part 2: study of shear damage to Graphite / Epoxy nanocomposite. *Strength of Materials*. 2014;46(4): 548–552.
- 71. Nguyen DC. *Caractérisation de l'interface fibre/matrice: application aux composites polypropylène/chanvre* (Doctoral dissertation). Troyes; 2016. [Accessed on 20th 2023]
- 72. Favre JP. Interface dans les composites fibreux. *Techniques de l'ingénieur*. 1992; Plastiques et composites, (A7765).
- 73. Li Y, Pickering KL, Farrell RL. Determination of interfacial shear strength of white rot fungi treated hemp fibre reinforced polypropylene. *Composites Science and Technology*. 2009;69(7-8): 1165-1171.
- 74. Cox HL. The elasticity and strength of paper and other fibrous materials. *British Journal of Applied Physics*. 1952;3(3): 72.

75. Mulla MH, Norizan MN, Abdullah CK, Rawi NFM, Kassim MHM, Salleh KM, Abdullah N, Norrrahim MNF. Dynamic mechanical properties of sugar palm fiber-reinforced polymer composites: a review. *Polymer Bulletin*. 2024;81: 7737–7789.

76. Kaouche N, Mebrek M, Mokaddem A, Doumi B, Belkheir M, Boutaous A. Theoretical study of the effect of the plant and synthetic fibers on the fiber-matrix interface damage of biocomposite materials based on PHAs (polyhydroxyalkanoates) biodegradable matrix. *Polymer Bulletin*. 2022;79(9): 7281-7301.

77. Khakpour H, Ayatollahi MR, Akhavan-Safar A, Da Silva LFM. Mechanical properties of structural adhesives enhanced with natural date palm tree fibers: Effects of length, density and fiber type. *Composite Structures*. 2020;237: 111950.

78. Ahmed MM, Dhakal HN, Zhang ZY, Barouni A, Zahari R. Enhancement of impact toughness and damage behaviour of natural fibre reinforced composites and their hybrids through novel improvement techniques: A critical review. *Composite Structures*. 2021;259: 113496.

About Authors

Allel Mokaddem (1) Sc

PhD, Professor (Centre Universitaire Nour Bachir El-Bayadh, El Bayadh, Algeria)

Mohammed Belkheir D Sc

PhD, Professor (Centre Universitaire Nour Bachir El-Bayadh, El Bayadh, Algeria)

Mehdi Rouissat D Sc

PhD, Professor (Centre Universitaire Nour Bachir El-Bayadh, El Bayadh, Algeria), Professor (Université de Tlemcen, Tlemcen, Algeria)

Bendouma Doumi D Sc

PhD, Professor (Dr. Tahar Moulay University of Saïda, Saïda, Algeria)

Ahmed Boutaous D Sc

PhD, Professor (Université des Sciences et de la Technologie d'Oran Mohamed-Boudiaf, Oran, Algeria)

Accepted: March 10, 2024

Submitted: December 27, 2023 Revised: February 25, 2024

Hybrid of a nonlinear Maxwell-type viscoelastoplastic model with the linear viscoelasticity constitutive constitutive equation and properties of crossbred creep and stress-strain curves

A.V. Khokhlov 🖾 1,2 📵

- ¹ Lomonosov Moscow State University, Moscow, Russia
- ² North-Eastern Federal University, Yakutsk, Russia
- [™] andrey-khokhlov@ya.ru

ABSTRACT

A generalization for the physically nonlinear Maxwell-type constitutive equation is proposed with two material functions for non-aging rheonomic materials, which have been studied analytically in previous articles to elucidate its properties and application. To extend the set of basic rheological phenomena that it simulates, we propose to add the third strain component expressed as the Boltzmann-Volterra linear integral operator governed by an arbitrary creep function. To generalize and conveniently tune the constitutive relation, to fit it to various materials and various lists of phenomena (test data), we introduce a weighting factor (i.e. nonlinearity factor) into the equation. This allows us to crossbreed primary physically nonlinear Maxwell-type model with the linear viscoelasticity equation in an arbitrary proportion, to construct a hybrid model and to regulate prominence of different phenomena described by the two constitutive equations we crossbred. General expression for stress-strain curves at constant stress rate and for the creep and recovery curves families obtained using the proposed hybrid constitutive equation are derived and analyzed. The basic properties of the stress-strain curves and the creep-recovery curves are studied assuming three material functions are arbitrary. They are also compared to the properties obtained using primary Maxwell-type model and linear viscoelasticity theory. New properties are found that allow the hybrid model to tune the form of the stress-strain curves and the creep-recovery curves and to simulate additional effects observed in constant stress rate tests and creep-recovery tests of various materials at different stress rates and stress levels.

KEYWORDS

viscoplasticity • viscoelasticity • creep • physical non-linearity • material functions • stress-strain curves family stress rate sensitivity • equilibrium stress-strain curve • creep-recovery curves • applicability indicators

Acknowledgements. The research was supported by the Russian Science Foundation grant No. 22-13-20056 "Development of resource-saving solid-phase technology for molding products and composite materials for the Arctic on the basis of polytetrafluoroethylene". Available online: https://rscf.ru/project/22-13-20056/.

Citation: Khokhlov AV. Hybrid of a nonlinear Maxwell-type viscoelastoplastic model with the linear viscoelasticity constitutive constitutive equation and properties of crossbred creep and stress-strain curves *Materials Physics and Mechanics*. 2024; 52(4): 114–140.

http://dx.doi.org/10.18149/MPM.5242024_11

Introduction

The problem of reliable modeling of thermomechanical behavior and fracture of materials and structures, the issues of construction or selection of adequate constitutive equations (CEs) for viscoelastoplastic materials (out of dozens and hundreds proposed in the literature), analysis of their properties and the scope of application, sphere of influence of material functions (MFs) and phenomenological limitations on them, development of identification and certification techniques, still remain relevant in mechanics, materials

science and the practice of engineering calculations. For a reasonable choice of the CE, determination of its possibilities and the scope of application, for competent processing of experimental data and identification of MFs and parameters of the chosen CE it is necessary to study *analytically* general properties of loading and unloading curves, relaxation curves, creep curves under stepwise loading programs generated by the CE with *arbitrary* MFs [1-10]. It is also necessary to investigate the influence of loading parameters and characteristics of MFs, to identify the necessary conditions (indicators) of applicability of the CE to the modeled material.

In the series of papers [4-10] (and others) such an analysis was performed for a physically nonlinear CE:

 $\varepsilon(t)=E^{-1}F(\sigma(t))+\eta^{-1}\int_0^tV(\sigma(\tau))d\tau$, or $\dot{\varepsilon}=E^{-1}[F'(\sigma)\dot{\sigma}+\tau_r^{-1}V(\sigma)],\, t>0$, (1) connecting (in one-dimensional case) the strain $\varepsilon(t)$ with the history of stress changes $\sigma(\tau), \tau \in [0;t]$, in isothermal deformation processes of stable rheonomic materials (stress and time are assume to be dimensionless). The CE (1) includes two increasing MFs F(x), $V(x), x \in (\omega_-, \omega_+)$ (their constraints are given in the next section) and two constants: $E, \eta > 0$. The elastic modulus E and the viscosity coefficient η are explicitly extracted from the MF to account for the effect of temperature in the form $E=E(T), \eta=\eta(T)$ [5]. The CE (1) is based on the decomposition of the total strain into the sum of elastic and viscoplastic components: $\varepsilon=\varepsilon_e+\varepsilon_v, \varepsilon_e=F(\sigma)/E, \dot{\varepsilon}_v=V(\sigma)/\eta$.

It is aimed at describing a set of effects typical of non-aging materials with heredity and plasticity, high rate sensitivity and, possibly, tension-compression asymmetry. The CE (1) combines relative simplicity and wide scope of applicability: it generalizes a number of classical models (due to the arbitrariness of MFs F(x) and V(x)) and describes a very wide range of rheological effects typical of many rheonomic materials exhibiting viscoelastic and plastic properties [4–10].

The CE (1) generalizes (includes) the classical power-law models of viscous flow and creep (see the surveys and the references on these topics in works [4,5,8]), the Herschel-Bulkley and Shvedov-Bingham rheological models, and the special case of the Sokolovsky-Malvern model. In the case of $F(x) \equiv 0$, $V(x) = x|x|^{n-1}$, n > 1, the CE (1) gives the power law of flow (Norton-Bailey model), the most popular (due to its simplicity) in the theory of creep, viscoplasticity, hydrodynamics of non-Newtonian fluids and the rheology of polymers [11-41]. It has been used to model the dependence of steady-state creep rate on stress [11–19,24,25,29], power-law fluid flows (in particular, those associated with oil production) [20-24], superplastic flow of materials [32-40], and the motion of avalanches and mudflows [41]. Setting F(x) = x and $V(x) = x|x|^{n-1}$, we obtain a model with linear elasticity and power-law viscosity, which has been used in a number of works to describe the creep curves, to model superplasticity and to solve specific problems [8–10,13,34,42–45]. In [46,47], the CE, related to the CE (1), was used as the basis for a nonlinear model for describing the shear strain of thixotropic viscoelastic fluids, which takes into account the influence of the kinetics of formation and destruction of intermolecular bonds and associates of macromolecules on viscosity and shear modulus and the influence of the deformation process to this kinetics. The general tensor formulation of nonlinear Maxwell-type CEs for (severe strain of) viscoelastic media, related to the CE (1), the description of kinematics, thermodynamic aspects and

methods of specifying the CRs were studied in [48–53]. Those papers focused on describing the behavior of fluids and discussed experiments and effects inherent in fluids (polymer melts and solutions, etc.). However, they did not consider creep, relaxation and stress-strain curves generated by the CE, did not ask many questions specific to mechanics of deformable solids, and did not analyze the corresponding phenomenological constraints on the MFs and parameters of the CE (1) and methods for their identification. The CE (1) with arbitrary MFs F(x) and V(x) has not been systematically investigated and validated before the works [4–10].

Thus, the CE (1) generalizes several commonly used models and describes a wide range of rheological effects (see the next section and [4-10] for more details). However, along with many advantages, it has some features that limit its scope of applicability. Thus, the CE (1) is not capable of describing some effects observed during the deformation of many materials. For example, in [7,8] the following was proved:

- 1. the CE (1) models only creep at a constant rate (steady-state creep, characteristic of many ductile metals, polymers in a viscous-flow state and materials in a state of superplasticity) and is not capable of describing the stages of transient and accelerated creep, as well as limited creep, characteristic, for example, of many polymers;
- 2. the CE (1) does not describe recovery after complete unloading ("reverse creep", "elastic aftereffect"), i.e. the process of *gradual* relaxation of the accumulated strain reaching a certain constant level at large values of time, as it is observed in tests of many materials (for example, for cross-linked polymers and for bone tissue, reverse creep curves tend to the asymptote $\varepsilon = 0$). The CE (1) describes only the *instantaneous* recovery of the elastic part of strain. The "highly elastic" component of strain, which ensures gradual decrease, is completely absent in model (1);
- 3. under cyclic loading beyond the elastic limit, the CE (1) always gives ratcheting at a constant rate: "unlimited" increase in plastic strain without stabilization and adaptability, cyclic weakening.

Due to the abundance of advantages and possibilities of the CE (1), as well as the presence of several disadvantages, it is advisable to generalize the CE in such a way as to preserve the advantages, but eliminate the noted disadvantages and expand the range of rheological effects described by it and its scope of applicability. This is precisely the main purpose of this article (see the next sections).

The most important types of uniaxial tests, which make it possible to capture and examine various aspects of material behavior, to detect signs of nonlinearity in its behavior and to gather sufficiently rich information for the selection and identification of the CE, are the tests on loading (shear, tension, compression) at a constant rate $\sigma(t)=bt$ and on creep at a constant stress and recovery after unloading (reverse creep) [4,7,11–17,54–56] for different stress levels and durations of the loading stage $\bar{\sigma},T>0$, i.e. study of the response $\varepsilon(t;\bar{\sigma},T)$ of a material (specimen) to a rectangular stress pulse: $\sigma(t;\bar{\sigma},T)=\bar{\sigma}[h(t)-h(t-T)],t>0$, (2) where h(t) is the Heaviside function, instantaneous unloading and endurance at the $\sigma(t)=0,t>T$.

Another objective of this article is to derive equations for the curves family and creep-recovery curves generated by the new CE (4) with three *arbitrary MFs* under loadings in the form (2). We also aim to study the influence of loading parameters and

characteristics of all MFs, in particular, to identify new qualitative properties (effects), which make it possible to describe a more general CE (4) in comparison with the CE (1). In the future, the properties found will be used to develop methods for identifying the CE (4) and searching for its applicability indicators using experimental creep and recovery curves of materials, as was done for the CE (1) in [4-10,56].

On restrictions on MFs of the CE (1) and its scope of applicability

The MF F defines in the CE (1) the elastic strain $\varepsilon_e(\sigma)$. The minimum primary constraints on it are: F(x), $x \in (\omega_-, \omega_+)$ is a continuous (strictly) increasing function with a piecewise continuous derivative, such that F(0) = 0. These conditions ensure that the signs of stress and elastic strain $\varepsilon_e(\sigma)$ coincide and that the condition $\varepsilon_e(0)=0$ is met. From the strictly increasing F(x) it follows that $\varepsilon_{e}(|\sigma|)$ and the energy of elastic strain increase with increasing $|\sigma|$ and the existence of the inverse to F function f. The viscosity function $V(x)/\eta$ in the CE (1) controls the viscoplastic properties: it governs the material memory, the rate of dissipation, relaxation rate, creep and plastic strain accumulation rate, the sensitivity of stress (in particular, the instantaneous modulus and flow stress) to the strain rate, and the long-term strength [4–10]. The minimum constraints on it are: V(x)is a continuous (non-strictly) increasing function on the interval (ω_-, ω_+) , such that V(0) = 0. These constraints on the MF provide, in particular, an increase in strain-stress curves and creep curves, a decrease in relaxation and long-term strength curves, a description of the complex of rheological effects typical of viscoelastoplastic materials (see below), and the thermodynamic consistency of the CR, i.e., the positivity of the stress work $\sigma(\tau)$ in an arbitrary deformation process and the non-negativity and increasing of dissipation $W[t, \sigma(\tau)]$: $\dot{W}(t) = \sigma(t)V(\sigma(t))/\eta > 0$. If ω_+ and ω_- are finite, they can be interpreted as tensile strength at tension and compression (as material parameters). Mathematical properties of the operator (1), literature reviews and related to (1) models used in the theory of creep, superplasticity and polymer mechanics, taking into account the effect of temperature and generalization of the CE (1) to the triaxial stress state are given in [4-10].

In [4-10] and others, were analytically studied the equations of the basic quasistatic curves families generated by the CE (1) with arbitrary MFs F(x) and V(x): relaxation and creep curves with arbitrary initial loading to a given level stage, creep under stepwise loading, long-term strength, stress-strain curves at constant and piecewise constant strain or loading rates, under cyclic loading. The general properties of these curves were studied depending on the characteristics of MFs and parameters of loading programs: intervals of monotonicity and convexity, inflection points, responses to discontinuities in the input process (jumps and breaks), asymptotics and two-sided estimates of theoretical curves, the nature of the convergence of their families to limit curves at the tendency of the parameters of loading programs (strain or loading rate, duration of the initial stage of loading, etc.) to zero and infinity, conditions for memory decay, the effect of permutation of loading stages on asymptotics and residual strain, etc. As a result of comparing the discovered properties of the theoretical curves with typical qualitative properties of test curves for a wide class of viscoelastoplastic materials (with a target list of mechanical effects), the necessary additional constraints on MFs were derived to

ensure adequate modeling of the main rheological effects, and theoretical and experimental applicability indicators of the CE (1) were identified, as well as those effects that it fundamentally cannot describe at any MFs.

A systematic study of the CE (1), carried out in a series of works [4–10] and others, showed that it can be used to describe a set of basic rheological effects typical of viscoelastoplastic materials with memory, high sensitivity to loading rate, and, possibly, tension-compression asymmetry. They are characterized by the following features of mechanical behavior:

- 1. increasing loading curves at a constant rate, which can be either convex upward or may have an inflection point;
- 2. positive rate sensitivity;
- 3. monotonous decrease and convexity of the unloading curve or the presence of a maximum point or inflection point on it (depending on the rate and level of loading),
- 4. lack of recovery (strain relaxation) after a stress pulse exceeding the elastic limit and complete unloading;
- 5. significant influence of the duration and rate of loading on the magnitude of plastic strain;
- 6. pronounced stage of flow at constant stress in stress-strain curves with constant rate and (increasing) dependence of the flow stress on rate;
- 7. "unlimited" increase in plastic strain under cyclic loading beyond the elastic limit (ratcheting without stabilization and adaptability, cyclic weakening);
- 8. creep at a constant rate;
- 9. stress relaxation to zero or non-zero value;
- 10. increase in compliance and rate sensitivity, an increase in the dissipation rate, relaxation rate, creep and ratcheting rates with increasing temperature.

Such materials (in certain deformation modes) include, for example, many polymers, their melts and solutions, solid fuels, asphalt concrete, high-modulus polyethylene yarns, geofabrics and geogrids, ice and frozen soils, titanium and aluminum alloys, carbon and ceramic materials at high temperatures, etc.

The analysis of the properties of theoretical curves generated by the CE (1) [4–10] showed that two main cases should be distinguish, in which the CE (1) (or the modeled material) behaves differently. In the first case, |V(x)| > 0 for all $x \neq 0$, 2) $V(x) \equiv 0$ at a certain interval $Z:=[\sigma_-,\sigma_+] \subset (\omega_-,\omega_+)$, $\sigma_- \leq 0$, $\sigma_+ \geq 0$, $\sigma_+ \neq \sigma_-$ (by definition, σ_- and σ_+ are the lower and upper bounds of the set of zeros of the MF V(x)). In the second case, as long as $\sigma(t) \in Z$, the CE models the elastic behavior of the material: the dissipation is small and there is no hysteresis loop on the loading-unloading curve, the relaxation and creep are absent, the stress-strain curve does not depend on the loading (or strain) rate at $\varepsilon \in [\varepsilon_-, \varepsilon_+]$, where $\varepsilon_\pm := F(\sigma_\pm)/E$). Thus, σ_- and σ_+ play the role of elastic limits (and creep thresholds) of the material under compression and tension. At $\sigma > \sigma_+$ (or $\sigma < \sigma_-$) the dissipation is significant and viscoplastic properties also begin to appear. For example, in [10], the elastic limit equal to one tenth of the tensile strength was found from the testing data of a complex polyester yarn and the methods of identification of the CE (1), developed in [8], were tested.

The use of a MF of the second kind, i.e. with $\sigma_+ > 0$, is very convenient for taking

into account the features of the manifestation of nonlinear viscoelastoplastic properties in testing data of a particular material, namely, for connecting the nonlinear viscoplasticity model (1) to the linear viscoplasticity CE (3) and surgical adjustment of this connection. Due to the material parameters σ_+ and w it is possible to add to the CE (3) the nonlinear viscoplasticity, starting from any stress $\sigma \geq \sigma_+ > 0$ and in any proportion.

Generalization of the CE (1) by crossbreeding with the linear viscoelasticity CE

A natural way to generalize the CE (1) in such a way as to preserve its advantages, but eliminate the noted disadvantages and expand the range of rheological effects described by it and its scope of applicability, is to add to the CE (1) a third strain component – viscoelastic, highly elastic strain, i.e, to sequentially attach to the nonlinear Maxwell-type model a linear viscoelastic element (a parallel connection is also promising, but will entail a distortion of the good properties already presented in the CE (1)): $\varepsilon = \varepsilon_e + \varepsilon_v + \varepsilon_{ve}$. This viscoelastic element can be chosen differently: a Scott-Blair fractal element can be added, Voigt or Kelvin models, etc. But it seems most reasonable to maximize the communication in this direction, i.e., to add a term governed not by two or three parameters, but expressed in general form by the linear Boltzmann-Volterra integral operator with an arbitrary creep function (CF):

$$\varepsilon(t) = \int_0^t \Pi(t - \tau) \, d\sigma(\tau), \, \sigma(t) = \int_0^t R(t - \tau) \, d\varepsilon(\tau), \, t \ge 0.$$
 (3)

If, of course, it is possible to analyze in sufficient depth the properties of such a complex CE, depending on three arbitrary MFs, and to learn how to adjust these properties in order to describe typical material testing data. For generality and convenience of model control, its adjustment to different materials and lists of modeled effects, we introduce a weighting factor $w \in [0;1]$ (nonlinearity factor), which allows us to "mix" the CE (1) and the linear viscoelasticity operator (3) (and the effects modeled by them) in any proportions:

$$\varepsilon(t) = wE^{-1}F(\sigma(t)) + w\eta^{-1} \int_0^t V(\sigma(\tau))d\tau + (1-w) \int_0^t \Pi(t-\tau) d\sigma(\tau), t > 0.$$
 (4)

Thus, the new CE (4) is a hybrid (and simultaneous generalization) of the nonlinear CE (1) and the linear viscoelasticity CE (3) (at w=0, the nonlinearity is switched off and the linear viscoelasticity CE is obtained, and at w=1 the CE (1) is obtained). It is the parameter w that allows us to adjust the contributions of the CE (1) and the CE (3) and thus to adjust the severity of the effects they model.

Further, we assume minimal constraints on the CF $\Pi(t)$, t > 0, in the CE (4), inherited from the viscoelasticity CE (3) [1]: it is positive, differentiable, increasing and convex upward by $(0; \infty)$. For example, the following CF:

$$\Pi = At^u, u \in (0; 1), A > 0,$$
 (5)

defines the so-called "fractal" element of "fractional" models with the fractional differentiation operator. It has the property $\Pi(0) = 0$, which characterizes irregular viscoelastic models (the corresponding relaxation function has a singularity at t = 0: $R(t) = Bt^{-u}$) [54]. The following CFs family:

$$\Pi(t) = \alpha t + \beta - \gamma e^{-\lambda t}, \lambda > 0, \alpha, \beta \ge 0, \gamma \in [0, \beta], \tag{6}$$

generates at $\gamma \in (0; \beta)$, $\alpha, \beta > 0$ all four regular structural models of four elements (they are equivalent), and at $\alpha = 0$ it generates two regular models of three elements (Kelvin and Poynting-Thomson models). Since $\Pi(0) = \beta - \gamma$, then the CF (6) generates irregular

models when $\gamma=\beta$: at $\lambda\beta=0$ it is the Newtonian fluid, at $\alpha=0$ it is the Voigt model, at $\alpha>0$ it generates both singular models of three elements. At $\gamma=0$ (6) it gives the linear Maxwell-type model. These CFs will be used to illustrate the properties of the creep and recovery curves generated by the CE (4). The case $\gamma<0$ in (6) violates the constraint $\ddot{\Pi}(t)\leq 0$, which entails an increase in the recovery curve (15) (a contradiction with experimental data).

The generalization of the CE (4) to the triaxial stress state in the case of isotropic media can be carried out according to the same standard scheme as the generalization of the CE (1), based on the postulate about the absence of cross-influence of the spherical and deviatoric parts of the stress and strain tensors $\sigma(t)$ and $\varepsilon(t)$ to each other (i.e., independence of volumetric strain from tangential stresses, and shear strains from average stress) and the postulate about the proportionality of deviators $s = \sigma - \sigma_0 I$, $e = \varepsilon - \varepsilon_0 I$ [9]:

$$\varepsilon_{ij}(t) = \frac{3}{2}\varepsilon(t)\sigma(t)^{-1}s_{ij}(t) + \frac{1}{3}\theta(t)\delta_{ij},
\varepsilon(t) = \mathbf{M}\sigma = E^{-1}F(\sigma(t)) + \eta^{-1}\int_{0}^{t}V(\sigma(\tau))d\tau,
\theta(t) = \mathbf{M}_{0}\sigma_{0} = E_{0}^{-1}F_{0}(\sigma_{0}(t)) + \eta_{0}^{-1}\int_{0}^{t}V_{0}(\sigma_{0}(\tau))d\tau,$$
(7)

where $\sigma_0(t) = \sigma_{ii}(t)/3$, $3\varepsilon_0 = \theta(t) = \varepsilon_{ii}(t)$, $\sigma(t) = (\frac{3}{2}s_{ij}s_{ij})^{0.5}$, $\varepsilon(t) = (\frac{2}{3}e_{ij}e_{ij})^{0.5}$ are the average stress, volumetric strain and the intensity of stresses and strains. This CE expresses $\varepsilon(t)$ through the history of $\sigma(t)$ and is governed by two pairs of MFs F(x), V(x) and $F_0(x)$, $V_0(x)$, whose constraints are described in the previous section, and the parameters E, η , E_0 , $\eta_0 > 0$. The CE (7) can be crossbred according to the described scheme with the general linear viscoelasticity CE for isotropic media:

$$\varepsilon_{ij}(t) = e_{ij} + \varepsilon_0 \delta_{ij}, e_{ij}(t) = \frac{3}{2} \mathbf{\Pi} s_{ij}(t), \theta = \mathbf{\Pi_0} \sigma_0, \tag{8}$$

$$\mathbf{\Pi}y = \int_0^t \Pi(t - \tau) \, dy(\tau), \, \mathbf{\Pi}_0 y = \int_0^t \Pi_0(t - \tau) \, dy(\tau), \, t > 0, \tag{9}$$

with two arbitrary MFs $\Pi(t)$ and $\Pi_0(t)$ (functions of shear and volumetric creep), i.e., consider the CE expressing $\varepsilon(t)$ through the history of $\sigma(t)$ as follows:

$$\varepsilon_{ij}(t) = e_{ij}(t) + \frac{1}{3}\theta(t)\delta_{ij},
e_{ij} = \frac{3}{2}w\frac{M\sigma}{\sigma(t)}s_{ij}(t) + \frac{3}{2}(1-w)\Pi s_{ij}(t),
\theta = wM_{0}\sigma_{0} + (1-w)\Pi_{0}\sigma_{0}$$
(10)

The CE (10), like the CEs (7) and (8), describes the processes of isothermal deformation of non-aging isotropic viscoelastic media by connecting the histories of changes in the components of the deviators s, e and the first invariants $\sigma_0(t)$ and $\varepsilon_0(t)$ of the stress tensors $\sigma(t)$ and small strains $\varepsilon(t)$ at an arbitrary point of the body. The CE (10) contains six MFs: three governing the change in shape (F, V, Π) and three governing the volumetric strain (or only one or two in the case of simplifications associated, for example, with the postulation of an elastic or linearly viscoelastic relation between the volumetric strain and the average stress).

A systematic study of the three-dimensional CE (10) and the study of the possibilities for modeling triaxial effects (in particular, the scenarios for changes in time of the transverse strain coefficient under creep and other types of loading, the influence of volumetric strain and hydrostatic pressure on the tension-compression curve [9,56]) – these are the topics of subsequent articles. The analysis should begin with the one-

dimensional operator (4). In the case of uniaxial ("pure") shear, when only the components $\sigma_{12}=\sigma_{21}$ of the stress tensor are nonzero, there will be $\sigma_0(t)\equiv 0$, $s(t)=\sigma(t)$, and from the CE (10) it follows, that $\theta(t)\equiv 0$, $e(t)=\varepsilon(t)$, only the components $\varepsilon_{12}=\varepsilon_{21}$ are nonzero and they are connected to $\sigma_{12}(t)$ by an operator in the form (4). Therefore, all statements proved below about the creep and strain curves generated by the uniaxial CE (4) are automatically transferred to the CE (10) in the case of shear, as well as in the case of hydrostatic loading without shape change: for the volumetric creep curves $\theta(t,\bar{\sigma}_0)$ and loading curves $\sigma_0(\theta,b)$ families all properties are preserved when the triple of MFs F, V, Π are replaced by the MFs F_0,V_0,Π_0 .

Creep curves generated by the CE (1) and the CE (4)

At the stress $\sigma(t) = \bar{\sigma} h(t)$, t > 0, the CE (1) generates the creep curves family: $\varepsilon(t,\bar{\sigma}) = r(\bar{\sigma})t + cF(\bar{\sigma})$, or $\varepsilon(t,\bar{\sigma}) = c[V(\bar{\sigma})\tau_r^{-1}t + F(\bar{\sigma})]$ (11) where $c = E^{-1}$, $r(\bar{\sigma}) = \eta^{-1}V(\bar{\sigma}) = c\tau_r^{-1}V(\bar{\sigma})$, $\tau_r := \eta/E$ is the relaxation time of the linear Maxwell-type model with V(x) = F(x) = x (τ_r is convenient to use for dimensionless time).

If $V(x) \equiv 0$ on a certain segment $[\sigma_-, \sigma_+]$, $\sigma_- < 0$, $\sigma_+ > 0$, then at $\sigma \in [\sigma_-, \sigma_+]$ the CE (1) models (nonlinearly) the elastic behavior of the material and at $\bar{\sigma} \in [\sigma_-, \sigma_+]$ the creep is absent (the elastic limits for compression and tension coincide with the creep thresholds).

If $V(\bar{\sigma}) \neq 0$, then all creep curves are linear in time at t>0, i.e., for any MFs, the CE (1) models only creep at a constant rate (as does the linear Maxwell-type model), the rate $|r(\bar{\sigma})|$ increases with the increase of $|\bar{\sigma}|$. Since $V(\bar{\sigma})>0$ at $\bar{\sigma}>0$ and increases, the creep curve (11) increases along t (at $\bar{\sigma}>0$) and along $\bar{\sigma}$, which is observed in tests of stable materials.

A pronounced stage of creep at a constant rate is characteristic of many plastic metals, polymers in a viscous-flow state, and materials in a state of superplasticity. The creep curves of polymers have a stage of steady-state creep only at sufficiently high temperatures, when the polymer is in a viscous-flow state. The CE (1) is not capable of describing the stages of transient and accelerated creep, as well as limited creep, characteristic, for example, of many polymers.

For example, Fig. 1(a) shows the creep and recovery curves of 110×2250 complex polyester yarn under tension according to program (2), carried out in 2019 by O.N. Stolyarov and A.V. Khokhlov at the Peter the Great St. Petersburg Polytechnic University (on the Instron 5965 universal measuring complex). The basic characteristics of the yarn were measured beforehand. Linear density of the yarn $\theta = 220$ tex, specific density of the yarn material $\gamma = 1360$ kg/m³, elastic modulus 15.3 ± 1.1 GPa, breaking force $N_* = 150 \pm 5$ N (tensile strength $\sigma_* = 960 \pm 35$ MPa, relative strength of the yarn is 0.7 N/tex), relative elongation at break is 11 ± 0.75 % (based on the results of ten tests to break with a crosshead rate of 50 mm/min). Figure 1(a) shows creep and recovery curves of yarn specimens (the length of the working part of the specimen is 100 mm) for different stress levels: the curve i corresponds to the stress $\bar{\sigma} = \bar{\sigma}_i = i\sigma_*/10$ (from 10 to 50 % of the tensile strength). The ideal program (2) was implemented as follows: "instantaneous" loading (more precisely, very fast: within 1-3 sec, at a rate of

1500 N/min) of the specimen to a given stress level $\bar{\sigma}$, holding for a time $t_* = 4\tilde{t}$, $\tilde{t} = 3600$ sec (1 hour), "instantaneous" unloading and subsequent holding at (almost) zero stress (2 N) for a time of $2\tilde{t}$ to analyze the recovery process.

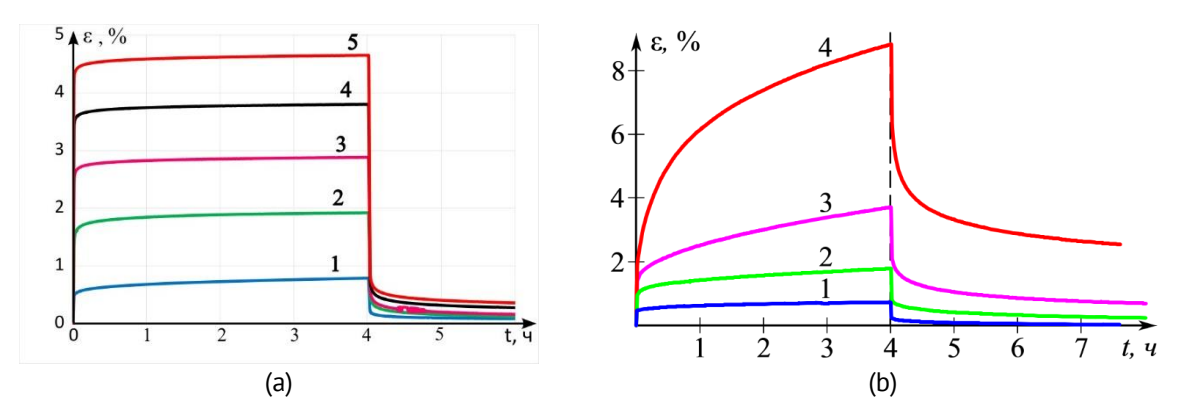


Fig. 1. Test creep and recovery curves at different tensile loads for a polyester yarn (a) and polyamide-6 (b)

The data of these tests the CE (1) approximates well except for the initial segments of the creep curve and the recovery stage. However, the data from tests of polyamide-6 under tension (Fig. 1(b)) the CE (1) cannot describe for the reasons mentioned above (creep at an unstable rate, pronounced reverse creep). S.B. Sapozhnikov at the South Ural State University (in August 2022) carried out these (preliminary) tests according to the following program. Rapid loading up to $\bar{\sigma} = \bar{\sigma}_i = 10$; 20; 25; 30 MPa, observation of creep at constant stress for 4 hours (curves 1–4), "instant" unloading and observation of recovery at (almost) zero stress for 4 hours. To select the stress levels, preliminary tests to failure were carried out at different loading rates and the conditional tensile strength of polyamide-6 was found in the range of loading rates from 0.5 to 50 MPa/min and $\sigma_* = 60 \pm 5$ MPa (true stress at the break $\sigma_* = 80 \pm 10$ MPa, relative elongation at break is from 20 to 50%). For polyamides and similar materials, the proposed CE (4) is useful.

Since the response of the linear CE (3) to the loading program $\sigma(t) = \bar{\sigma} h(t)$, has the form $\varepsilon(t, \bar{\sigma}) = \bar{\sigma} \Pi(t)$, then the CE (4) generates the creep curves family: $\varepsilon(t, \bar{\sigma}) = wr(\bar{\sigma})t + wcF(\bar{\sigma}) + (1 - w)\bar{\sigma}\Pi(t)$. (12)

Since $w \in [0;1]$, then the creep curves family (12) increases along $\bar{\sigma}$, which coincides with the typical properties of creep curves of structurally stable materials. At $\bar{\sigma} > 0$ the additional term $(1-w)\bar{\sigma}\Pi(t)$ increases along t and is convex upward (since $\Pi(t)$ is increasing and convex upward). Therefore, the creep curve (12) increases along t and is convex upward at t > 0, as in linear viscoelasticity, but no longer depends linearly on the stress level $\bar{\sigma}$ (since the first two terms do not have this property). At w > 0.5 the influence of the first term on the creep rate and the accumulation of irreversible (residual) strain is significant, and it is possible to make the creep curve as close as desired to the straight-line creep curve (11) by increasing w. On the contrary, at $w \to 0$ it is possible to make the relative contribution of terms nonlinear along σ as small as desired and give the creep curves family any shapes characteristic of linear viscoelasticity. The convexity of the creep curve (12) means that the CE (4), like the linear viscoelasticity CR, is not capable of describing accelerated creep (the third stage of creep).

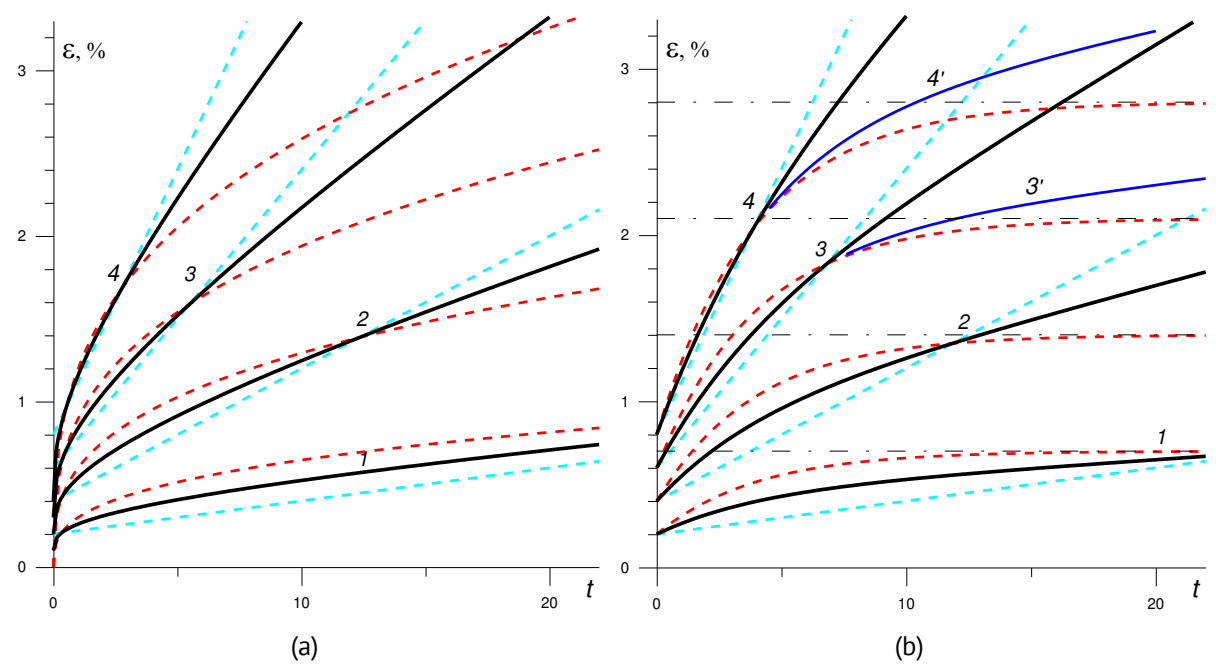


Fig. 2. Creep curves for four stress levels $\bar{\sigma}=0.1;0.2;0.3;0.4$ (curves 1-4), generated by several models of the form (4) with F(x)=x, V(x)=x|x|, E=50, $\eta=50$ and three different weighting factors w=0;0.5;1 (red, black, and light blue curves): (a) three models with the creep function (5) with u=1/3, A=0.03; (b) three models with the creep function (6), $\alpha=0$, $\beta=0.07$, $\gamma=0.05$, $\lambda=0.25$

Figure 2(a) shows the creep curves of the three CE (4) with F(x) = x, V(x) = x|x|, E = 50, $\eta = 50$ (then $\tau_r = 1$), $\Pi = At^u$, u = 1/3, A = 0.03 with three different weighting factors w = 0; 0.5; 1 (red, black, and light blue curves) for four stress levels $\bar{\sigma} = 0.1; 0.2; 0.3; 0.4$ (curves 1-4). Dimensionless time is plotted along the abscissa axis: the considered qualitative properties of the curves do not depend on its scaling, $\bar{\sigma}$ and E are dimensionless by dividing by one tenth the quasi-static tensile strength at a standard rate. Since $\Pi(0) = 0$, the initial value of the creep curve $\varepsilon(0) = wcF(\bar{\sigma})$.

Figure 2(b) shows the creep curves of the three CE (4) with the same MFs F(x)=x, $V(x)=x|x|, E=50, \eta=50$ ($\tau_r=1$) and three weighting factors w=0; 0.5; 1 (red, black, and light blue curves) for the same $\bar{\sigma}=0.1$; 0.2; 0.3; 0.4 (curves 1-4), but with a different CF: in the form (6) with $\alpha=0$, $\beta=0.07$, $\gamma=0.05$, $\lambda=0.25$. That is, to modify the CE (1) with the same MFs, the Kelvin model with retardation time $1/\lambda=4=4\tau_r$ and relaxation time $(\beta-\gamma)/(\beta\lambda)=8/7$ was used. Its CF is limited, $\Pi(\infty)=\beta$, the creep curves of this model (red lines) tend at $t\to\infty$ to asymptotes $\varepsilon=\bar{\sigma}\beta$. This example clearly shows how significantly the creep curves of the CE (4) differ from the creep curves of the CE (1) due to the introduction of an additional strain component (and the MF Π , that governs it). Obviously, changing the "hybridization" parameter $w\in[0;1]$ provides a wide range of possibilities to adjust the shape of the creep curves of the CE (4) (Fig. 2(b) shows in blue the creep curves 3',4', generated by the CR (4) with the same MFs, but with w=0.1).

Creep and recovery curves

The creep and recovery curves, generated by the CE (1), are its responses to a rectangular stress pulse (2) with parameters T > 0, $\bar{\sigma} > \sigma_+ \ge 0$. Substituting Eq. (2) into Eq. (1) gives the equation for the creep and recovery curves family:

$$\varepsilon(t; \bar{\sigma}, T) = r(\bar{\sigma})t + cF(\bar{\sigma}) \text{ at } t < T, \varepsilon(t; \bar{\sigma}, T) = p(\bar{\sigma}, T) \text{ at } t > T, \tag{13}$$

$$r(\bar{\sigma}) = \eta^{-1}V(\bar{\sigma}), \, p(\bar{\sigma}, T) = \eta^{-1}V(\bar{\sigma})T = c\tau_r^{-1}V(\bar{\sigma})T. \tag{14}$$

The strain jump at the point t=T is equal to $-cF(\bar{\sigma})$, $c=E^{-1}$, at t>T the strain becomes constant and equal to the creep strain $p(\bar{\sigma},T)$ accumulated over time T. At complete unloading, only the elastic strain $\varepsilon(+0)=cF(\bar{\sigma})$ disappears, and the entire accumulated creep strain turns out to be irreversible, plastic. This is precisely the behavior that many metals (and other materials) exhibit at sufficiently high temperatures. Thus, the CE (1) does not describe "reverse creep", i.e., the process of gradual relaxation of the accumulated strain to some constant level at large values of time, as is observed in tests of many materials. The CE (1) describes only the instantaneous recovery (the limiting, idealized case) of elastic strain. The "highly elastic" component of strain, which ensures gradual decrease, is completely absent in model (1). The residual strain $p(\bar{\sigma},T)$ is proportional to the duration of the loading stage T, depends only on the MF V (as does the creep rate $r(\bar{\sigma})$) and increases with increasing $\bar{\sigma}$.

Due to (13), the trace left by a finite stress pulse (2) is never erased, i.e., the memory of model (1) is not fading, but is "permanent". The inability to describe materials with fading memory is a disadvantage of the CE (1), which narrows the range of modeled materials and processes.

However, this indicates that the CE (1) may be capable of describing not only viscoelasticity, but also viscoplasticity. This hypothesis is confirmed by the presence of horizontal asymptotes in the stress-strain curves generated by the CE (1) at a constant strain rate, horizontal asymptotes, i.e., flow segments at constant stress (without subsequent strengthening), as is observed in materials in a state of superplasticity [32-40] (they are characterized by creep at a constant rate and the absence of recovery after unloading).

The MF F does not affect the creep rate, its jumps and plastic strain $p(\bar{\sigma}, t_*)$, and V does not affect instant strain jumps. This allows to determine the MFs $\gamma V(x)$ and F(x)/E separately based on the material creep and recovery curves [7].

The response of the linear CE (3) to a rectangular stress pulse (2) has the form: $\varepsilon(t) = \bar{\sigma}S(t;T), S(t;T) := \Pi(t) h(t) - \Pi(t-T) h(t-T), t > 0.$

At the point t=T the creep and recovery curve $\varepsilon(t)$ has a jump $-\bar{\sigma}\Pi(0)$, and $\dot{\varepsilon}(t)$ has a jump $-\bar{\sigma}\dot{\Pi}(0)$. In the interval t>T the equation of creep and recovery curves has the following form:

$$\varepsilon(t;\bar{\sigma},T) = \bar{\sigma}S(t;T), S(t;T) = \Pi(t) - \Pi(t-T), t > T. \tag{15}$$

From the (non-strict) requirement that the recovery curve (15) decreases (with any T) it follows that $\dot{\Pi}(t)$ does not increase [54]. Therefore, a constraint should be imposed on the CF in the CE (1): $\Pi(t)$ has no downward convexity segments. Since $\dot{\Pi}(t)$ decreases on the ray t>0 and $\dot{\Pi}(t)>0$, there exists a limit $v:=\dot{\Pi}(\infty)\geq 0$. Since the function (15) is decreasing and positive (bounded from below), it has at $t\to\infty$ a limit $\varepsilon_\infty\geq 0$, and $\varepsilon_\infty=\bar{\sigma}S(\infty,T)$. It is easy to prove that $S(\infty,T)=vT$ [54], i.e., in the case of v>0 after

complete unloading (infinitely long), the residual strain $\varepsilon_{\infty} = \bar{\sigma}vT$ remains. This means that at v > 0, the memory of the integral operator Π , defining the CE (3), does not fade.

It can be proven that v>0 for all regular structural models with even number of elements and all singular models with odd number of elements. If the CF is bounded (as for all regular structural models of an even number of elements), then v=0 and $\varepsilon_{\infty}=0$. It can also be v=0 for an unbounded CF, for example, for a power-law CF $\Pi=At^u$, $u\in(0;1)$, A>0. For models (6) $v=\alpha$ and $S(t;T)=\alpha T+\mu e^{-\lambda t}$, $\mu=\gamma(e^{\lambda T}-1)$; in particular, v>0 at $\alpha>0$ (for the Maxwell-type model and its sequential connection with the Voigt model); for the Maxwell-type model and Newtonian fluid $\gamma=0$ and $\varepsilon(t)=\bar{\sigma}\alpha T\equiv {\rm const}$ at t>T, i.e. there is no recovery at all. For the Voigt (singular two-element model) and Kelvin (regular three-element model) models $\alpha=0$, and therefore the creep and recovery curve (15) has the form $\varepsilon(t)=\bar{\sigma}\mu e^{-\lambda t}$, and $\varepsilon_{\infty}=0$.

The creep and recovery curve of the CE (4) is obtained by combining the responses (13) and (15) of the CE (1) and the linear CE (3) to the stress pulse (2): at t < T $\varepsilon(t; \bar{\sigma}, T)$ is given by equation (12), and at t > T:

$$\varepsilon(t; \bar{\sigma}, T) = wp(\bar{\sigma}, T) + (1 - w)\bar{\sigma}S(t; T), S(t; T) = \Pi(t) - \Pi(t - T), t > T.$$
(16)

Obviously, both terms (16) increase in absolute value with increasing $|\bar{\sigma}|$, and $|\varepsilon(t;\bar{\sigma},T)|$ increases along $|\bar{\sigma}|$ and decreases along t at t>T (since S(t;T) decreases). These properties reflect typical qualitative properties of creep and recovery curves of structurally stable materials, i.e., the CE (4) adequately describes the recovery effect, in contrast to the CE (1). At $t\to\infty$ there is a limit (residual strain, horizontal asymptote for (16)):

$$\varepsilon_{\infty}(\bar{\sigma}, T) = wp(\bar{\sigma}, T) + (1 - w)\bar{\sigma}vT = w\eta^{-1}V(\bar{\sigma})T + (1 - w)\bar{\sigma}vT, v := \dot{\Pi}(\infty) \ge 0.$$
 (17)

It is proportional to the duration of the loading stage T (this is one of the applicability indicators of the CE (4)), does not depend on the MF F and increases with increasing $\bar{\sigma}$. If the CF is chosen so that v=0, then the residual strain (16) can be made as small as desired by decreasing the parameter w, and thus "remove" the residual strain given by the CE (1), if the CE is adjusted to the testing data of a specific material requires this.

At the point t=T the creep and recovery curve (12), (16) has a jump $-wcF(\bar{\sigma})-(1-w)\Pi(0)\bar{\sigma}$. It is equal in absolute value to the jump $\varepsilon(0+;\bar{\sigma},T)=$ $=wcF(\bar{\sigma})+(1-w)\Pi(0)\bar{\sigma}$ at the point t=0. The equality of these jumps is another applicability indicator of the CE (4): this property is not always satisfied in material tests. If $\Pi(0)=0$ (such linear models are called irregular, they have many specific properties [54]; these include, in particular, the Voigt model, the fractal element and all their successive connections), then the creep and recovery curve (15) is continuous at the point t=T, and the jump of the creep and recovery curve (12), (16) is equal to $-wcF(\bar{\sigma})$ and it can be made as small as desired by decreasing w.

Figure 3(a) shows the creep and recovery curves of three CE (4) with F(x) = x, V(x) = x|x|, E = 50, $\eta = 50$ (then $\tau_r = 1$), the CF (5) with u = 1/3, A = 0.03 and three weighting factors w = 0; 0.5; 1 (red, black and light blue curves) for loadings (2) with T = 10 and three stresses $\bar{\sigma} = 0.1$; 0.2; 0.3 (curves 1-3). Since $\Pi(0) = 0$, the creep and recovery curves of the (linear) CE with c w = 0 are continuous at the point t = T and the jump of any creep and recovery curve of the model with w = 0.5 (black curves) is half the jump of the creep and recovery curve of the model with w = 1 (i.e. model (1)) for the same $\bar{\sigma}$. Since $v = \dot{\Pi}(\infty) = 0$, for all creep and recovery curves the (linear) CE with w = 0, $\varepsilon_{\infty}(\bar{\sigma}, T) = 0$, i.e. they converge at $t \to \infty$ to a common asymptote $\varepsilon = 0$.

Therefore, the residual strain $\varepsilon_{\infty}(\bar{\sigma},T)$ of the model with w=0.5 is two times smaller than that of the model (1) (the asymptotes of curves 1-3 are shown as dash-dotted straight lines), and the recovery is slow (in comparison, for example, with Fig. 3(b)). This example clearly shows how significantly different the creep and recovery curves of the CE (4) are from the creep and recovery curves of the CE (1) due to the introduction of an additional strain component (and the MF Π , that controls it).

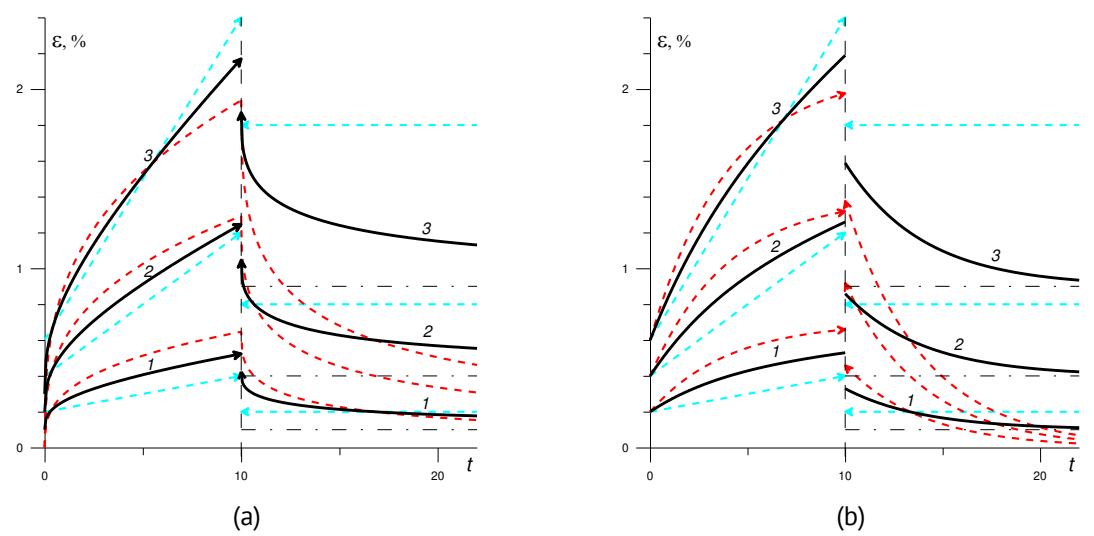


Fig. 3. Creep and recovery curves for three stress levels $\bar{\sigma}=0.1;0.2;0.3$ (curves 1-3) generated by several models of the form (4) with $F(x)=x, V(x)=x|x|, E=50, \eta=50$ and three different weighting factors w=0;0.5;1 (red, black, and light blue curves): (a) three models with the creep function (5) with u=1/3, A=0.03; (b) three models with the creep function (6) with $\alpha=0, \beta=0.07, \gamma=0.05, \lambda=0.25$

Figure 3(b) shows the creep and recovery curves of three CR (4) with the same MFs $F(x)=x,\ V(x)=x|x|,\ E=50,\ \eta=50\ (\tau_r=1)$ with three different weighting factors w=0;0.5;1 (red, black and light blue curves) for loadings (2) with T=10 and three stress levels $\bar{\sigma}=0.1;0.2;0.3$ (curves 1-3), but with a different CF: in the form (6) with $\alpha=0,\ \beta=0.07,\ \gamma=0.05,\ \lambda=0.25$. That is, to modify the CE (1) with the same MFs, the Kelvin model with retardation time $1/\lambda=4=4\tau_r$ is used; its CF is limited, $\Pi(\infty)=\beta,\ \Pi(0)=\beta-\gamma,\ S(t;T)=\gamma(e^{\lambda T}-1)e^{-\lambda t}$ and the creep and recovery curves of this model (red lines) have jumps $\Pi(0)\bar{\sigma}=(\beta-\gamma)\bar{\sigma}$ at the points t=0 and t=T, and at $t\to\infty$ they tend to common asymptote $\varepsilon=0$ (for any material parameters and any $\bar{\sigma}$, since $\varepsilon_\infty=\bar{\sigma}vT=0$) with a rate $e^{-\lambda t}$ (much faster than the model in Fig. 3(a)).

It should be noted that the results of this section allow us to derive the equation of creep curves of the CE (4) under arbitrary stepwise loading (with any number of stress stages) by analogy with those obtained in articles [4,7,54].

General properties of stress-strain curves generated by the linear viscoelasticity CE

The loading $\sigma(t)=bt$ at a constant rate b>0 (for definiteness, we consider the case b>0), the linear CE (3) maps into following strain: $\varepsilon(t,b)=bQ(t)=bt\Theta(t)$, $Q(t)=\int_0^t\Pi(\tau)\,d\tau,\,\Theta(t)=t^{-1}Q(t),\,t>0$.

Excluding the parameter t gives the loading curves generated by the CE (3) under loading $\sigma(t) = bt$:

$$\varepsilon(\sigma,b) = bQ(\sigma/b) = \Theta(\sigma/b)\sigma, \, \sigma \ge 0. \tag{18}$$

The properties of averaging $\Theta(t)$ are similar to the properties of the CF [55, 56]: $\Theta(t)$ is an increasing smooth function at t>0, $\Pi(t)/2<\Theta(t)<\Pi(t/2)<\Pi(t)$ (since $\Pi(t)$ is increasing and convex upward), $\Theta(0+)=\Pi(0)$, $\Theta(\infty)=\Pi(\infty)$, $\dot{\Theta}(0+)=\dot{\Pi}(0+)/2$, and Q has the following properties: Q(0)=0, $Q(\infty)=\infty$, $\dot{Q}(t)=\Pi(t)>0$, $\ddot{Q}(t)=\dot{\Pi}(t)>0$, $\ddot{Q}(t)=\dot{\Pi}(t)<0$, $\ddot{Q}(t)=$

To obtain the equations of loading curves (18) in the form $\sigma = \sigma(\varepsilon, b)$, it is necessary to introduce into consideration the function P(x), x > 0 inverse to the increasing function Q: $\sigma(\varepsilon, b) = bP(\varepsilon/b)$, $\varepsilon, b > 0$. (19)

From the positivity and increase of the CF, it follows that P is an increasing upward convex function, P(0)=0, $P(\infty)=\infty$, $P'(0+)=1/\Pi(0)$ (in particular, $P'(0+)=\infty$, if $\Pi(0)=0$), $P'(\infty)=1/\Pi(\infty)$, the function P(x)/x is decreasing and P(x)/x>P'(x) at x>0 [3]. From the constraints $\dot{\Pi}>0$ and $\ddot{\Pi}\leq 0$ on the CF and the properties of the functions Q and P, the following general properties of the loading curves (19) follow.

The tangent and secant moduli of the stress-strain curves (19) are: $\sigma'_{\varepsilon}(\varepsilon,b)=1/\varepsilon'_{\sigma}(\sigma,b)=1/\Pi(\sigma/b)$ and $\sigma/\varepsilon=1/\Theta(\sigma/b)$ (since the uniaxial CE (3) coincides with the linear viscoelasticity CE for the components of the deviators of the stress and strain tensors, they can be considered shear moduli, although similar properties can be derived for loading curves in tension or compression [56]). Since $\varepsilon'_{\sigma}(\sigma,b)>0$ and $\sigma'_{\varepsilon}>0$, any loading curve (18) increases along σ , and the loading curve $\sigma=\sigma(\varepsilon,b)$ increases along ε at any δ . Since the CF increases, $\varepsilon'_{\sigma}(\sigma,b)$ increases along δ and decreases along δ , and $\sigma'_{\varepsilon}(\varepsilon,b)$ decreases along δ and increases along δ . Therefore, for any $\delta>0$ the loading curves (18) are convex downward, and the loading curves in the form (19) are convex upward on the semi-axis $\varepsilon>0$. The upward convexity of the loading curve up to the beginning of fracture or to the yield point is characteristic of many polymers, asphalt concretes, metals and alloys [11,18,19,24,27,28,32-34].

The stress-strain curves family (18) decreases along b, since $\dot{\theta}(t) > 0$ and $\theta(\sigma/b)$ decreases along b, and the loading curves family in the form (19) increases along b (the higher the rate, the higher lies the loading curve $\sigma = \sigma(\varepsilon, b)$), i.e. the CE (3) models only positive rate sensitivity.

The stress-strain curve (18) depends on b, but the instantaneous modulus (shear modulus G or volumetric modulus K) does not depend on the loading rate: $G:=\sigma'_{\varepsilon}(0,b)=\Pi(0)^{-1}$ (for models with $\Pi(0)=0$ it will be $G=\infty$). At $\varepsilon\to\infty$ the tangent and secant moduli tend to the common limit $G_{\infty}=R(\infty)=1/\Pi(\infty)\geq 0$ (if the CF is limited, then $G_{\infty}>0$; if the CF is not limited, then $G_{\infty}=0$). Thus, the long-term modulus G_{∞} also does not depend on the loading rate.

Any stress-strain curve (18) lies "above" (along the ε axis) the straight line $\varepsilon = \Pi(0)\sigma$, since $\Theta(t) > \Theta(0+) = \Pi(0)$, and all the stress-strain curves in the form $\sigma(\varepsilon,b)$ lie below (along the σ axis) this straight line. More precisely, in the case of $\Pi(0) \neq 0$ (for regular models), two-sided estimates are valid for all loading curves (18) and (19): $\Pi(0)\sigma < \varepsilon(\sigma;b) < \Pi(\infty)\sigma$, $G_\infty \varepsilon < \sigma(\varepsilon,b) < G\varepsilon$. (20)

At $b \to +\infty$ the stress-strain curves family $\varepsilon(\sigma;b)$ of any regular model converges from above (and the family $\sigma(\varepsilon,b)$ from below) to the straight line $\varepsilon = \sigma/G$ uniformly on any segment of

the σ axis [55]: $\sup_{[0,\omega]} |\varepsilon - \sigma/G| = \sup_{[0,\omega]} \sigma|\Theta(\sigma/b) - \Pi(0)| = \omega|\Theta(\omega/b) - \Pi(0)| \to 0$, since $\dot{\Theta}(t) > 0$ and $\Theta(0+) = \Pi(0)$. Therefore, the straight line $\sigma = G\varepsilon$ is the instant loading curve of the CE (3) in the case of $\Pi(0) \neq 0$. The stress-strain curves family at a constant strain rate also converges to it [55]. If $\Pi(0) = 0$ (as in the CF (5)), then $G = \infty$, the tangent to any loading curve (18) at zero is horizontal, and the tangent to the loading curve in the form (19) is vertical, and the loading curves family (18) uniformly converges at $b \to +\infty$ to the straight line $\varepsilon = 0$.

At $b \to 0$ the stress-strain curves family (18) always converges (from above) to the straight line $\sigma = G_{\infty}\varepsilon$ (equilibrium loading curve) uniformly on any segment of the semi-axis $\varepsilon > 0$. This is also true in the case of unbounded or singular relaxation functions.

The stress-strain curve (18) has an asymptote at $\sigma \to \infty$ only when the CF is limited and the integral $Y:=\int_0^{+\infty}[\Pi(\infty)-\Pi(\tau)]\,d\tau$ converges (obviously, Y>0) [55], its equation: $\varepsilon=\Pi(\infty)\sigma-bY$, or $\sigma=G_\infty(\varepsilon+Yb)$. All the stress-strain curves $\sigma(\varepsilon,b)$ tend to an asymptote from below. Its angular coefficient is equal to the long-term modulus G_∞ and does not depend on b. The question of the existence of asymptotes for the stress-strain curves is not purely abstract, since reaching an asymptote (straightening of stress-strain curves, "linear hardening" mode) can occur in the operating range of strains and stresses.

For example, for models (6) $Q=0.5\alpha t^2+\beta t-\gamma\lambda^{-1}(1-e^{-\lambda t})$, and the stress-strain curves family (18) has the following form:

$$\varepsilon(\sigma, b) = 0.5\alpha b^{-1}\sigma^2 + \beta\sigma - \gamma\lambda^{-1}b(1 - e^{-\lambda\sigma/b}), \sigma > 0. \tag{21}$$

The instantaneous modulus $G=1/(\beta-\gamma)$; for models with $\gamma=\beta$ (singular) $G=\infty$. If $\alpha=0$, i.e, for Voigt (with $\gamma=\beta$) and Kelvin ($\gamma\in(0;\beta)$) models, then $\Pi(\infty)=\beta<\infty$, $Y=\gamma/\lambda$, $G_\infty=1/\beta$, and each loading curve has an asymptote $\sigma=\beta^{-1}(\varepsilon+\gamma\lambda^{-1}b)$ at $\varepsilon\to\infty$. If $\alpha>0$, then $\Pi(\infty)=\infty$ and the loading curve (21) have no asymptotes. For the Maxwell-type model (the CF (6) with $\gamma=0$, $\alpha,\beta>0$) $G=1/\beta$, $G_\infty=0$ and the loading curves family converges at $b\to0$ to the function $\sigma=0$.

Figure 4(a) shows the stress-strain curves (21) of the Kelvin model (the CF (6) with $\alpha = 0$) at $\lambda = 0.1$, $\beta = 1$, $\gamma = 0.9$ (then $\Pi(0) = \beta - \gamma$, $G = 1/(\beta - \gamma) = 10$, $G_{\infty} = 1/\beta = 1$, retardation time $\tau = 1/\lambda = 10$, relaxation time $\tau_r = (1 - \gamma/\beta)\tau = 0.1\tau$) for the rates b=0.001; 0.01; 0.1; 1 (black loading curves 1–4). Each loading curve $\sigma(\varepsilon,b)$ at $\varepsilon\to\infty$ has an asymptote $\sigma = G_{\infty}(\varepsilon + y\tau b)$. The dash-dotted red straight lines 0 and ∞ are the instantaneous and equilibrium stress-strain curves $\sigma = G\varepsilon$ and $\sigma = G_{\infty}\varepsilon$, appearing in estimate (20); the family of loading curves of Kelvin model with any value of λ converges to them at $b \to \infty$ and $b \to 0$. For comparison, the stress-strain curves (21) of the Voigt model with $\gamma = \beta = 1$, the same $\lambda = 0.1$ and retardation time $\tau = 10$ (blue dashed loading curves 1''-4'') are given. For it, $\Pi(0)=0$ (and the model is singular, since the relaxation function contains the term $\eta\delta(t)$ with the delta-function), $G=\infty$, $G_{\infty}=1/\beta=1$, the equilibrium loading curve $\sigma = G_{\infty} \varepsilon$ coincides with the straight line 0, at $b \to \infty$ the family $\varepsilon(\sigma,b)$ converges to $\varepsilon=0$, and the loading curves $\sigma(\varepsilon,b)$ converge to the vertical semiaxis (i.e. the instantaneous loading curve does not exist). Each stress-strain curve at $\varepsilon \to \infty$ has an asymptote $\sigma = G_\infty \varepsilon + \tau b$, parallel to the equilibrium loading curve 0. The light blue curves 1'-4' are the loading curves (21) of the Maxwell-type model (i.e., the model with the CF (6) with $\gamma = 0$) with $\alpha = 1$, $\beta = 1$ for the same rates. Like Voigt model

it depends on two material parameters, but is regular: $\Pi(0) = \beta$, $G = 1/\beta = 1$, $\Pi(\infty) = \infty$, $G_{\infty} = 0$, relaxation time $\tau_r = \beta/\alpha = 1$. The stress-strain curves of the Maxwell-type model have no asymptotes. At $b \to 0$ and $b \to \infty$ the loading curves family $\sigma(\varepsilon,b)$ converges to the straight lines $\sigma=0$ and $\sigma=G\varepsilon$ (the straight line 0). The light blue dashed curves 2'-4' are the stress-strain curves of Maxwell-type model with the same instantaneous modulus G=10, as the stress-strain curves 1-4 of the Kelvin model, i.e., the Maxwell-type model with $\beta=0.1$, $\alpha=1$. Therefore, its instantaneous loading curve coincides with the curve ∞ . The curve 1''' is the loading curve of the fractal model (5) with u=0.3 for b=0.1, i.e., exactly the stress-strain curve 3 from Fig. 4(b).

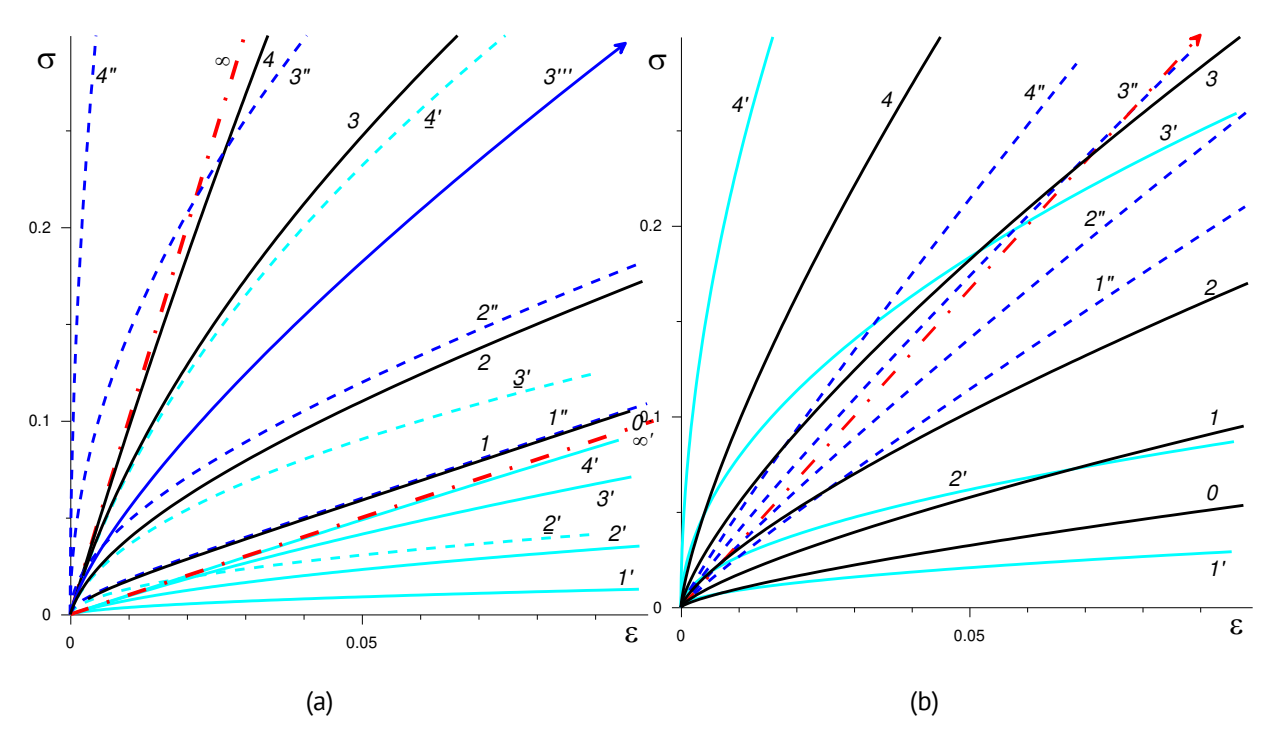


Fig. 4. (a) Stress-strain curves (21) generated by the classic Kelvin-Voigt, Maxwell and standard linear solid models (blue, light blue, and black curves) at four stress rates b = 0.001; 0.01; 0.1; 1 (curves 1-4, 1'-4'); (b) stress-strain curves (22) generated by three models of the form (5) with u = 0.3; 0.9; 0.1 (black, light blue, and blue curves) at stress rates b = 0.001; 0.01; 0.1; 1 (curves 1-4, 1'-4', 1''-4')

Let us consider the loading curves of a fractal element, i.e., the model with a power-law CF (5) (it corresponds to an unlimited unbounded relaxation function $R(t) = A^{-1}C(u)t^{-u}$, $C(u) = (u\pi)^{-1}\sin u\pi$ [55]). For the CF (5) $\Pi(0) = 0$ (the model is irregular), $\Pi(\infty) = \infty$, $\Theta = A(u+1)^{-1}t^u$, and the equation of loading curves (18) has the following form:

$$\varepsilon(\sigma,b) = A(u+1)^{-1}\sigma(\sigma/b)^{u}, \text{ or } \sigma(\varepsilon,b) = [(u+1)A^{-1}b^{-1}\varepsilon]^{1/(u+1)}b. \tag{22}$$

 $G=\infty,\ G_\infty=0$, at $\varepsilon\to\infty$ the loading curves have no asymptote. At $b\to 0$ the loading curves family $\sigma(\varepsilon,b)$ converges to the function $\sigma=0$, and at $b\to\infty$ the family $\varepsilon(\sigma,b)$ converges to $\varepsilon=0$, i.e., the loading curves $\sigma(\varepsilon,b)$ converge to the semi-axis, the segment in the estimate (20) turns into the first quadrant.

Figure 4(b) shows the curves (22) of three models of the form (5) with A=0.3 and u=0.3;0.9;0.1 (black, light blue and blue dashed curves) for loading rates

b=0.001; 0.01; 0.1; 1 (loading curves 1-4, 1'-4', 1''-4''). An additional curve 0 is for b=0.0001. As u increases, the tangent modulus in the vicinity of zero increases, and the loading curves (22) become increasingly higher. At small u, the model becomes much less sensitive to rate: the curves straighten and come closer (loading curves 1''-4''), the fan opening angle quickly decreases, and at $u\to 0$ it contracts into a straight line $\sigma=A^{-1}\varepsilon$ (red dash-dotted line).

Properties of stress-strain curves with constant rate generated by the CE (1)

The loading $\sigma(t)=bt$ at a constant rate b>0 CE (1) maps into the strain: $\varepsilon(t;b)==E^{-1}F(bt)+\eta^{-1}\int_0^tV(b\tau)\mathrm{d}\tau=E^{-1}[F(bt)+(\tau_rb)^{-1}I(bt)],\ I(s):=\int_0^sV(x)dx,$ $\tau_r:=\eta/E.$

Excluding the time $t = \sigma/b$, we obtain the stress-strain curves equation:

$$\varepsilon(\sigma, b) = E^{-1}[F(\sigma) + (\tau_r b)^{-1}I(\sigma)], b, \sigma > 0.$$
(23)

If $\sigma_+>0$ (i.e., $V(x)\equiv 0$ at $x\in [0;\sigma_+]$), then at $\sigma<\sigma_+$ $I(\sigma)\equiv 0$, and therefore the stress-strain curve (23) has the form $\varepsilon(\sigma,b)=F(\sigma)/E$, i.e., the CE describes the behavior of a nonlinearly elastic material and the stress-strain curve does not depend on the loading rate at $\sigma<\sigma_+$. If $\sigma>\sigma_+$ (in particular, in the case of $\sigma_+=0$), then V(x)>0 and $I(\sigma)>0$, and therefore the stress-strain curve depends on the rate b: the loading curves family (23) decreases along b at $\sigma>\sigma_+$, and the loading curves family in the inverse form $\sigma=\sigma(\varepsilon,b)$ increases along b at $\varepsilon\geq\varepsilon_+$, where $\varepsilon_+:=F(\sigma_+)/E$ (the higher the loading rate, the higher lies the stress-strain curve $\sigma=\sigma(\varepsilon,b)$). For the strain (23), the estimate from below $\varepsilon(\sigma,b)\geq E^{-1}F(\sigma)$ at $b,\sigma>0$ is valid (if $\sigma>\sigma_+$, then the inequality is strict), and therefore for loading curves in the form $\sigma(\varepsilon,b)$ for all $b,\varepsilon>0$ the estimate from above $\sigma(\varepsilon,b)\leq f(E\varepsilon)$ is true, where $f=F^{-1}$ is the inverse function of F. At $\varepsilon>\varepsilon_+$ this estimate can be refined:

$$\sigma_{+} < \sigma(\varepsilon, b) < f(\varepsilon), \varepsilon > \varepsilon_{+}$$
 (24) (in the case of $\sigma_{+} = 0$ it is true for all $\varepsilon > 0$, and in the case of $\sigma_{+} > 0$ $\sigma(\varepsilon, b) = f(\varepsilon)$ at $\varepsilon \le \varepsilon_{+}$).

The MF I(s) increases and is convex downward at $\sigma > \sigma_+$, since I''(s) = V'(s) > 0. Therefore, all loading curves (23) increase along σ and the loading curves $\sigma = \sigma(\varepsilon, b)$ increase along ε , and if $F''(x) \geq 0$, then $\varepsilon''(\sigma) > 0$, the loading curves (23) are convex downward, and the loading curves $\sigma = \sigma(\varepsilon)$ are convex upward for any b.

As a result of analyzing the implicit representation of the loading curves (23) under the above mentioned minimum constraints on the two MF in [8], other basic properties of the loading curves $\sigma = \sigma(\varepsilon, b)$, b > 0 were found. Many properties of the loading curves of the nonlinear CE (1) are similar to the properties of the loading curves of the linear integral viscoelasticity CE. In particular, the CE (1) is also unable to describe the negative rate sensitivity [57–60] and the behavior of materials for which the dependence of the instantaneous modulus on the loading rate or strain has been reliably established: polymers at sufficiently high temperatures, copper, tin, aluminum, titanium alloys in the superplasticity regime, etc. [8,32–40,61–64]. Polymers in the glassy state and many other materials do not exhibit rate sensitivity at sufficiently small strains. This effect can be described only by replacing the instantaneous modulus with a secant modulus or one averaged in the vicinity of zero. These properties are the inapplicability indicators of the

CE (1), along with its inability to model creep at a variable rate, fading memory, recovery after unloading, the Mullins effect, and adaptability under soft asymmetrical cyclic loading [4–10]. But, in contrast to the loading curves of the linear CE, which are always convex upward, the loading curves of the CE (1) can (if F''(x) < 0) have inflection points and convexity downward on a certain interval $\varepsilon < \tilde{\varepsilon}(b)$, (at sufficiently small strain, as in many elastomers, foams, and biological tissues: ligaments, tendons, vessels [18,65–69]).

There are several other features of the loading curves of the CE (1) in comparison with the loading curves of the linear CE:

- 1. the dependence of the loading curve of the CE (1) on the loading rate *b* is monotonic, but nonlinear and can be different under tension and compression;
- 2. the tangent modulus of the loading curves $\partial \sigma/\partial \varepsilon = E[F'(\sigma) + (\tau_r b)^{-1}V(\sigma)]^{-1}$ depends on the rate (increases along b), but instantaneous moduli in tension and compression $E_{\pm} = E/F'(0\pm)$ (limit values of the tangent modulus of the loading curves at $\varepsilon \to 0 \pm 0$) do not depend on the rate b and the MF V, and can be different;
- 3. the instantaneous and equilibrium loading curves of the CE (1) (the limits of the loading curves family $\sigma(\varepsilon,b)$ at $b\to 0+$ and at $b\to \infty$) are no longer necessarily rectilinear: at $b\to \infty$ the loading curves family $\sigma(\varepsilon,b)$ converges on the ray $\varepsilon\geq 0$ to the curve $\sigma=f(E\varepsilon), f=F^{-1}$ (curve ∞ in Fig. 5) uniformly on any segment of the axis ε . And at $b\to 0+$ the loading curves family $\sigma(\varepsilon,b)$ converges to the constant $\sigma=\sigma_+$ on the ray $\varepsilon\geq \varepsilon_+$ (curve 0 in Fig. 5), where $\varepsilon_+:=F(\sigma_+)/E$. And at $\varepsilon\in[0;\varepsilon_+]$ it converges to the function $\sigma=f(E\varepsilon)$. The equilibrium loading curve of the CE (1) has a different form in the cases of $\sigma_+=0$ or $\sigma_+>0$: if $\sigma_+=0$, the loading curves family $\sigma(\varepsilon,b)$ converges at $b\to 0+$ to the straight line $\sigma\equiv 0$ on the entire ray $\varepsilon\geq 0$, and if $\sigma_+>0$, it converges to the diagram of an ideal elastoplastic material with a yield stress $\sigma_y=\sigma_+$ and an initial segment of elastic strain $\sigma=f(E\varepsilon),\ \varepsilon\in[0;\varepsilon_+]$ [8]. Setting $\sigma_+>0$ and $V(x)\equiv 0$ at $x\in[0,\sigma_+]$ ensures that the initial segments of all loading curves $\sigma(\varepsilon,b)$ at $\varepsilon\in[0;\varepsilon_+]$ (i.e., at $\sigma\leq\sigma_+$) coincide with the curve $\sigma=f(E\varepsilon)$ (Fig. 5).

All discovered general properties of tensile loading curves are also inherent in compression loading curves, i.e., at b<0 (and $\sigma<0$): you just need to replace the signs of all inequalities with their inverses and upward convexity with downward convexity, $b\to 0+$ with $b\to 0-$, $\sigma_+\geq 0$ with $\sigma_-\leq 0$, $\varepsilon_+\geq 0$ with $\varepsilon_-=E^{-1}F(\sigma_-)\leq 0$, the segment $[0;\varepsilon_+]$ with $[\varepsilon_-;0]$, $[0,\sigma_+]$ with $[\sigma_-;0]$. The parameter $\sigma_-\leq 0$ (the lower bound of the set of zeros, the MF V(x)) has the same physical meaning in compression as σ_+ in tension.

Figure 5 shows the loading curves $\sigma(\varepsilon, b)$ of the model with $\sigma_+ > 0$ and the MF $V(x) \equiv 0$ at $x \in [\sigma_-, \sigma_+]$:

$$V = A_{+}(x - \sigma_{+})^{n} \text{ at } x > \sigma_{+},$$

$$V = -A_{-}|x - \sigma_{-}|^{m} \text{ at } x < \sigma_{-};$$

$$F(x) = x + qV(x), x > 0,$$
(25)

 $A_+,A_->0$, $m,n\ge 1$, $q\ge 0$ (for any $q\ge 0$ the constraints F'(x)>0 and F(0)=0 are satisfied, since they are satisfied for V). At $\sigma\in [\sigma_-,\sigma_+]$ this model describes a linearly elastic material, and at $\sigma\notin [\sigma_-,\sigma_+]$ rheonic properties and tension-compression asymmetry appear (if $\sigma_-\neq -\sigma_+$ or $A_-\neq A_+$ or $m\ne n$). The loading curve (23) has the following form: $\varepsilon=E^{-1}\sigma$ at $\sigma\in [0,\sigma_+]$, $\varepsilon=E^{-1}[\sigma+qA_+(\sigma-\sigma_+)^n+A_+(n+1)^{-1}(\sigma-\sigma_+)^{n+1}(\tau_r b)^{-1}]$, $\sigma>\sigma_+$.

Figure 5 shows the loading curves of this model with q=5, $\sigma_+=0.1$, n=2, $A_+=1$, $\eta=10$, E=10, $\tau_r=1$ for $b=10^{i-7}$, $i=1,\ldots,6$ (curves 1-6). All loading curves have a common straight segment $\sigma=E\varepsilon$, $\varepsilon\leq\varepsilon_+$, $\varepsilon_+=\sigma_+/E$, independent of rate. At $\sigma>\sigma_+$ the loading curves depend on the rate and shift upward as b increases. At $b\to 0$ $\sigma(\varepsilon,b)\to \sigma_+$ for any $\varepsilon\geq\varepsilon_+$, i.e., the loading curves family $\sigma(\varepsilon,b)$ converges to the loading curves of an ideal elastoplastic material with a yield stress $\sigma_y=\sigma_+$ ($\sigma=\sigma_+$ is the straight line O). The dashed curve ∞ is the limited loading curve at $b\to \infty$ (since q>0, the instantaneous loading curve is not rectilinear at $\sigma>\sigma_+$). For comparison, the dash-dotted line shows the limiting loading curves at $b\to \infty$ and $b\to 0$ for $\sigma_+=0.05$ (see the estimate (24)).

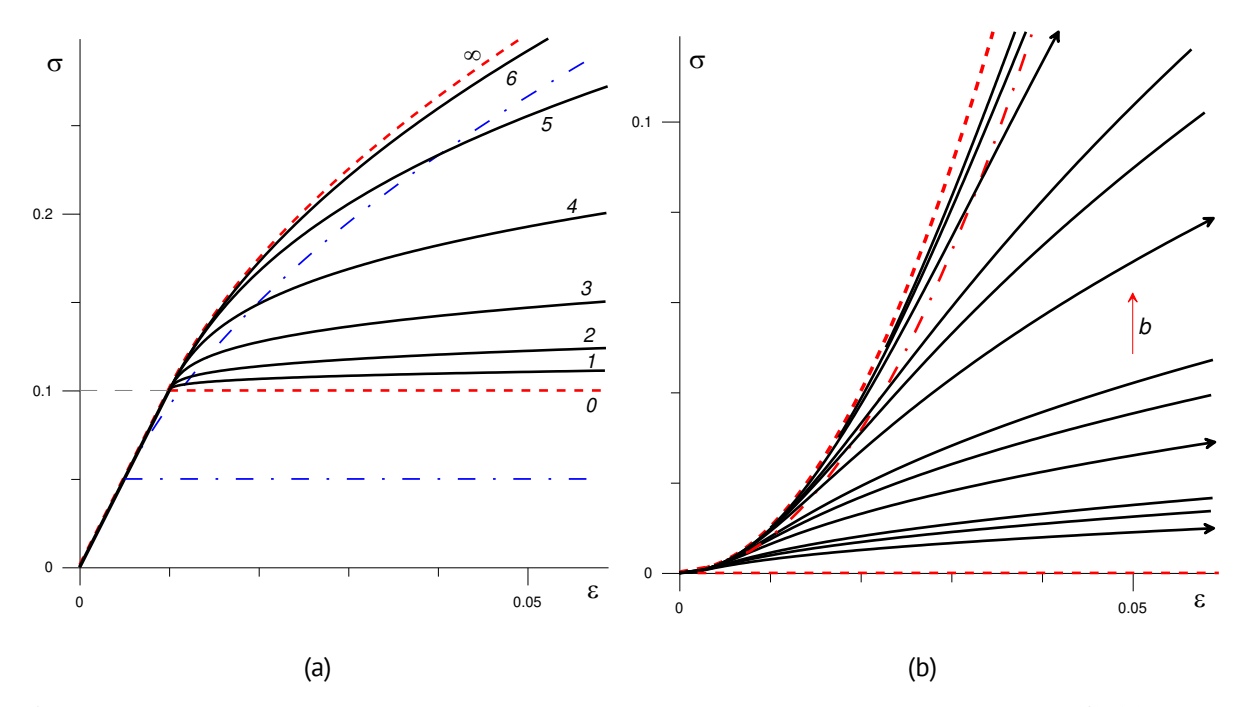


Fig. 5. Different forms of stress-strain curves $\sigma(\varepsilon, b)$, generated by the constitutive equation (1): (a) curves $\sigma(\varepsilon, b)$ generated by the model (25) with $\sigma_+ > 0$ at stress rates $b = 10^{i-7}$, i = 1, ..., 6 (curves 1-6) and limit curves at $b \to 0+$ or $b \to \infty$; (dashed lines); (b) stress-strain curves generated by the model (1) with $\sigma_+ = 0$, $\tau_r = 1$, $F = x^{1/2}$ and V = x at stress rates $b = 1 \cdot 10^{-i}$; $2 \cdot 10^{-i}$; $3 \cdot 10^{-i}$, i = 4; 3; 2; 1

For the power-law MFs $F = x^m$, $V = x^n$ we have $I(s) = (n+1)^{-1}s^{n+1}$, and the loading curve (23) takes the form: $\varepsilon(\sigma, b) = E^{-1}\sigma^m + (\gamma b)^{-1}(n+1)^{-1}\sigma^{n+1}$.

In the case of $n>m-1\geq 0$, $F''(x)\geq 0$ and V(x) increases, therefore all loading curves $\sigma(\varepsilon,b)$ with b>0 are convex upward on the semi-axis $\varepsilon>0$. At m<1 this is not the case: the loading curves have an inflection point and a segment of convexity downwards in the vicinity of zero (see [8] and Fig. 5(b)). Figure 5(b) shows the loading curves $\sigma(\varepsilon,b)$ of the model with $F=x^m, V=x^n, m=0.5, n=1, \eta=E=10, \tau_r=1$ for different rates: $b=1\cdot 10^{-i}$; $2\cdot 10^{-i}$; $3\cdot 10^{-i}$, i=4; 3; 2; 1 (the loading curves $b=1\cdot 10^{-i}$ are marked with arrows). The dashed loading curves are the limit curves $\sigma=f(E\varepsilon)$, $f=y^{1/m}$, at $b\to\infty$ (instantaneous loading curves) and $\sigma=0$ at $b\to0$ (equilibrium loading curve). The dash-dotted curve is the geometric locus of inflection points $(\tilde{\varepsilon}(b), \tilde{\sigma}(b))$ of the loading curves with different b>0; the set $\{(\tilde{\varepsilon}(b), \tilde{\sigma}(b))|b>0\}$ does

not depend on η and τ_r , since $\tilde{\sigma}$ and $\tilde{\varepsilon}$ 3 depend only on the parameter $\tau_r b$ [8], and η s included only in it.

Properties of the loading curves with constant rates generated by the CE (4)

The stress-strain curve of the CE (4) is obtained by combining the responses of the CE (1) and the linear CE (3) to the loading $\sigma = bt$, b > 0:

$$\varepsilon(\sigma,b)=wE^{-1}[F(\sigma)+(\tau_rb)^{-1}I(\sigma)]+(1-w)\Theta(\sigma/b)\sigma, b,\sigma>0,$$
 (26) where $I(s)$ and $\Theta(t)$ are defined in (23) and (18). The equation (26) specifies the stress-strain curves family $\sigma=\sigma(\varepsilon,b)$ of the CE (4) in implicit (inverse) form. The strain (26) increases along σ and decreases along b at b 0, and the stress-strain curves family b 0 increases along b 1 and b 2. The derivative b 1 b 2 b 3 b 4 and b 5 b 6 (since the CF increases), and at b 6 does not depend on b 7 and the MF b 7 b 8 b 9 b 9 or b 9 (since the CF increases), and at b 9 does not depend on b 9 and the MF b 9 b 9 b 9. It is obvious that b 9 b 9 and adding the previously proven estimates from below for terms (27) (in particular, b 9 b 9 b 9 b 9 (155), we obtain at any b 7 b 9 the following estimate:

 $\varepsilon(\sigma,b) > E^{-1}\Phi(\sigma)$, $b,\sigma > 0$, $\Phi(\sigma) = wF(\sigma) + E(1-w)\Pi(0)\sigma$. (27) (the inequality is strict even at $\sigma < \sigma_+$ in contrast to the inequality for the loading curves of the CE (1)). Since $\Phi(\sigma)$ is an increasing function (and $\Phi(0) = 0$), then there is an inverse function φ , $\varphi(0) = 0$, and for all loading curves in the form $\sigma(\varepsilon,b)$ the estimate from above is valid: $\sigma(\varepsilon,b) < \varphi(E\varepsilon)$ at $b,\varepsilon > 0$ (it does not depend on the MF V). In the case of the model with F(x) = x it has the form $\sigma(\varepsilon,b) \leq [w + E(1-w)\Pi(0)]^{-1}E\varepsilon$, and in the case of the model with $\Pi(0) = 0$ (as does the CF (5), for example) it has the form $\sigma(\varepsilon,b) \leq f(Ew^{-1}\varepsilon)$, where $f=F^{-1}$.

The stress-strain curves (26) inherit the general properties of the stress-strain curves $\varepsilon(\sigma,b)$, generated by the CE (1) or the CE (3), but they lose some (because the properties of the stress-strain curves of the crossbred CEs are different) and acquire new ones. For arbitrary MFs F, V, Π , subject only to the minimal constraints of one of previous section, and any $w \in (0;1)$, the following statements are true.

- 1. The stress-strain curves family (26) increases along σ and decreases along b at $\sigma, b > 0$, and the loading curves family in the form $\sigma = \sigma(\varepsilon, b)$ increases along ε and b, and the estimate $\sigma(\varepsilon, b) < \varphi(\varepsilon)$ is true at $b, \varepsilon > 0$.
- 2. If $F''(x) \ge 0$, then $\varepsilon''(\sigma) > 0$, the stress-strain curves (26) are convex downward, and the loading curves $\sigma = \sigma(\varepsilon)$ are convex upward for any b, and if F''(x) < 0, then the loading curves $\sigma(\varepsilon,b)$ of the CE (4) can have points of inflection and convexity downward on a certain interval $\varepsilon < \tilde{\varepsilon}(b)$, as well as the stress-strain curves of the CE (1) (in contrast from the CE (3)).
- 3. The tangent modulus of stress-strain curves $\sigma(\varepsilon, b)$ $\partial \sigma / \partial \varepsilon = [wE^{-1}(F'(\sigma) + (\tau_r b)^{-1}V(\sigma)) + (1-w)\Pi(\sigma/b)]^{-1}$ increases along b at any $\varepsilon > 0$ (i.e., $\sigma > 0$).
- 4. Instantaneous modulus of stress-strain curves $\sigma(\varepsilon, b)$ (limit of the tangent modulus at $\varepsilon \to 0$ +) $G = [wE^{-1}F'(0) + (1-w)\Pi(0)]^{-1}$ does not depend on the rate b and MF V (and can be equal to 0 or ∞).
- 5. At $b \to \infty$ $\Theta(\sigma/b) \to \Theta(0+) = \Pi(0)$ the stress-strain curves family (26) also converges

to the function $E^{-1}\Phi(\sigma)$ on the ray $\sigma \geq 0$ (see (27)). Therefore the loading curves family in the form $\sigma(\varepsilon,b)$ converges at $b\to\infty$ to the inverse function $\varphi(E\varepsilon)$ on the semi-axes $\varepsilon\geq 0$, i.e., the curve $\sigma=\varphi(E\varepsilon)$ is the instantaneous loading curve of the CE (4) (it does not depend on the MF V, in particular, on the material parameter σ_+ , and on the CF $\Pi(t)$, because in the definition of $\Phi(\sigma)$ only the initial value $\Pi(0)$ is included). It is easy to check that the convergence is uniform on any segment of the ε axis.

6. If $\Pi(0)=0$, then $\Phi(\sigma)=wF(\sigma)$, $\varphi(\varepsilon)=f(\varepsilon/w)$ and the instantaneous stress-strain curve has the form $\sigma=f(Ew^{-1}\varepsilon)$, i.e., is obtained from the loading curves of the CE (1) by tension along the ε axis with a coefficient w. In contrast to the linear CE (3), it does not degenerate into a vertical straight line $\varepsilon=0$, if $\Pi(0)=0$. That is adding the CE (1) with any weighting factor w>0 (arbitrarily small) to the singular linear model produces its regularization. This can also be seen from the formula for the instantaneous modulus G, which no longer goes to infinity in the case of $\Pi(0)=0$ (provided that $F'(0)\neq 0$).

7. If $\sigma_+=0$, then for any $\sigma>0$ from (26) follows $\varepsilon(\sigma,b)\to\infty$ at $b\to 0+$, and the stress-strain curves family $\sigma=\sigma(\varepsilon,b)$ converges at $b\to 0+$ (and $\varepsilon=$ const) to the function $\sigma\equiv 0$ on the entire ray $\varepsilon\geq 0$. The first is obvious (since $I(\sigma)>0$ at $\sigma>0$, and $b^{-1}\to\infty$), and to prove the second we need to fix $\varepsilon=\bar\varepsilon=$ const in (26) and go to the limit $b\to 0+$: assuming that $\sigma(\varepsilon,b)\to\sigma_*$, $\sigma_*>0$, we obtain that the first term in (26) has a finite limit $wE^{-1}F(\sigma_*)$, the third term has a limit $(1-w)\Theta(\infty)\sigma_*=(1-w)\Pi(\infty)\sigma_*$, which can be finite at $\Pi(\infty)<\infty$, and the second term is $wE^{-1}(\tau_rb)^{-1}I(\sigma_*)\to\infty$, and therefore the entire sum tends to infinity, which contradicts the finiteness of the left side of (26). Therefore, the assumption $\sigma_*>0$ is untrue and $\sigma_*=0$ for any $\varepsilon\geq 0$. For models with $\sigma_+>0$ the equilibrium diagram may differ from $\sigma\equiv 0$.

8. If $\sigma_+ > 0$ in the MF of the CE (4), then $I(\sigma) \equiv 0$ at $\sigma \leq \sigma_+$, and therefore the stress-strain curve (26) has the following form:

 $\varepsilon(\sigma, b) = wE^{-1}F(\sigma) + (1 - w)\Theta(\sigma/b)\sigma, \ \sigma \le \sigma_+, \ b > 0,$ that is, in contrast with the CE (1) (case w = 1) the stress-strain curve depends on the rate

at $\sigma \leq \sigma_+$ (Fig. 6(a)) also. Since $\Pi(0) < \Theta(t) < \Pi(\infty)$ [55], then at $\Pi(\infty) < \infty$ (T.e. $G_\infty > 0$) the two-sided estimate is true: $E^{-1}\Phi(\sigma) < \varepsilon(\sigma,b) < E^{-1}\Phi_\infty(\sigma)$, $\sigma \leq \sigma_+$, b > 0, $\Phi_\infty(\sigma) = wF(\sigma) + E(1-w)\Pi(\infty)\sigma$. Since $\Phi(\sigma)$ and $\Phi_\infty(\sigma)$ are the increasing functions, then applying to the inequalities the inverse functions $\varphi = \Phi^{-1}$ and $\varphi_\infty = \Phi^{-1}_\infty$ ($\varphi(0) = 0$) and $\varphi_\infty(0) = 0$, because $\varphi(0) = 0$, $\varphi_\infty(0) = 0$, we obtain an estimate for the loading curves (29) in the form $\sigma = \sigma(\varepsilon,b)$: $\varphi_\infty(E\varepsilon) < \sigma(\varepsilon,b) < \varphi(E\varepsilon)$ at $\varepsilon \leq \bar{\varepsilon}_+(b)$, b > 0, where $\bar{\varepsilon}_+(b) = \varepsilon(\sigma_+,b) = wE^{-1}F(\sigma_+) + (1-w)\Theta(\sigma_+/b)\sigma_+$ (the strain value corresponding to the stress $\sigma = \sigma_+$ now depends on the loading rate in contrast to the value $\varepsilon_+ = F(\sigma_+)/E$ in the CE (1)). The function $\bar{\varepsilon}_+(b)$ decreases monotonically (since $\Theta(t)$ increases) and

 $\bar{\varepsilon}_{+}(b) \to \hat{\varepsilon}$ at $b \to 0$ + (fig. 6a), where: $\hat{\varepsilon} = \varepsilon(\sigma_{+}, \infty) = wE^{-1}F(\sigma_{+}) + (1 - w)\Pi(\infty)\sigma_{+} = E^{-1}\Phi_{\infty}(\sigma_{+}).$ (29)

9. For models with $\sigma_+ > 0$ and $\Pi(\infty) < \infty$ (Fig. 6(a)) the loading curves family (28) at $b \to 0$ + has a limit $E^{-1}\Phi_{\infty}(\sigma)$ at all $\sigma \le \sigma_+$ (since $\Theta(\infty) = \Pi(\infty)$ [55]), $\hat{\varepsilon} < \infty$ and the stress-strain curves family $\sigma(\varepsilon,b)$, $\varepsilon \le \bar{\varepsilon}_+(b)$, converges to the function $\sigma = \varphi_{\infty}(E\varepsilon)$, $\varepsilon \in [0;\hat{\varepsilon}]$, i.e., the equilibrium stress-strain curve increases.

10. For models with $\sigma_+ > 0$ and $\Pi(\infty) = \infty$ (Fig. 6(b)) $\varepsilon(\sigma, b) \to \infty$, $\hat{\varepsilon} = \infty$ and the stress-strain curves family $\sigma(\varepsilon, b)$ converges to the function $\sigma \equiv 0$ at all $\varepsilon \geq 0$, i.e. the equilibrium stress-strain curve is the same as in the case of $\sigma_+ = 0$.

11. For models with $\sigma_+ > 0$ and $\Pi(\infty) < \infty$ the equilibrium curve at $\sigma > \sigma_+$, i.e., at $\varepsilon > \hat{\varepsilon}$, coincide with the straight line $\sigma = \sigma_+$ (and at $\varepsilon \in [0; \hat{\varepsilon}]$ has a form $\sigma = \varphi_\infty(E\varepsilon)$, as proven above). The proof is similar to the proof of property 7: the assumption $\sigma_* > \sigma_+$ leads to a contradiction, and therefore $\sigma_* = \sigma_+$ (only then $I(\sigma_*) = 0$, the second term in the limit of the right side of (26) vanishes, and it has a finite limit, since this is true for the third term due to the condition $\Pi(\infty) < \infty$).

Figure 6(a) shows the stress-strain curves of three CE (4) with the same material parameters and MFs (25) as in Fig. 5(a) ($\sigma_+ = 0.1$, E = 10, $\tau_r = 1$), and the CFs in the form (6) with the same parameters as in Fig. 4(a) ($\lambda = 0.1$, $\beta = 1$, $\gamma = 0.9$, $\beta = 1$, $\gamma = 0.9$, $\gamma =$ retardation time $\tau = 1/\lambda = 10$, relaxation time $\tilde{\tau}_r = 1$), with three different weighting factors w = 1; 0.5; 0 (light blue, black and blue curves) for six rates $b = 10^{i-6}$, i = 1, ..., 6(curves 1-6). The light blue stress-strain curves 1'-5' (for w=1) coincide with the stressstrain curves of the CE (1) in Fig. 5(a) (they have a common straight segment OA, independent of the rate: $\sigma = E\varepsilon$, $\varepsilon \leq \varepsilon_+$, $\varepsilon_+ = \sigma_+/E$), the blue stress-strain curves 3"-6" (for w = 0 and b = 0.001; 0.01; 0.1; 1) coincide with the loading curves of the linear Kelvin model in Fig. 4(a) (stress-strain curves $1^{"}$, $2^{"}$ at lower rates merge with the equilibrium loading curve $0^{"}$), dash-dotted blue straight lines $0^{"}$ and $\infty^{"}$ are the limit stress-strain curves at $b \to 0$ and $b \to \infty$ from the estimate (20), the dashed red curves 0' and ∞' – are the limit stress-strain curves for CE (1) (the same as in fig. 5a), the dash-dotted red curve ∞ is the limit stress-strain curve $\sigma = \varphi(E\varepsilon)$, $\varepsilon \ge 0$, of the CE (4) at $b \to \infty$. At $b \to 0$ $\sigma(\varepsilon,b) \to \sigma_+$ for any $\varepsilon \ge \hat{\varepsilon}$, in our example $\Pi(\infty) < \infty$, $0 < G_\infty < E$ and $\hat{\varepsilon} = 0.055$; for models with $G_{\infty} > \sigma_+/\varepsilon_+ = E\sigma_+/F(\sigma_+)$ it will be $\hat{\varepsilon} < \varepsilon_+$). On the segment [0; $\hat{\varepsilon}$] the stressstrain curves family of the CE (4) $\sigma(\varepsilon, b)$ converges at $b \to 0$ to the linear function (since the MF F is linear and $\Pi(\infty) < \infty$), the graph of which is the segment OB, $B(\hat{\varepsilon}, \sigma_+)$.

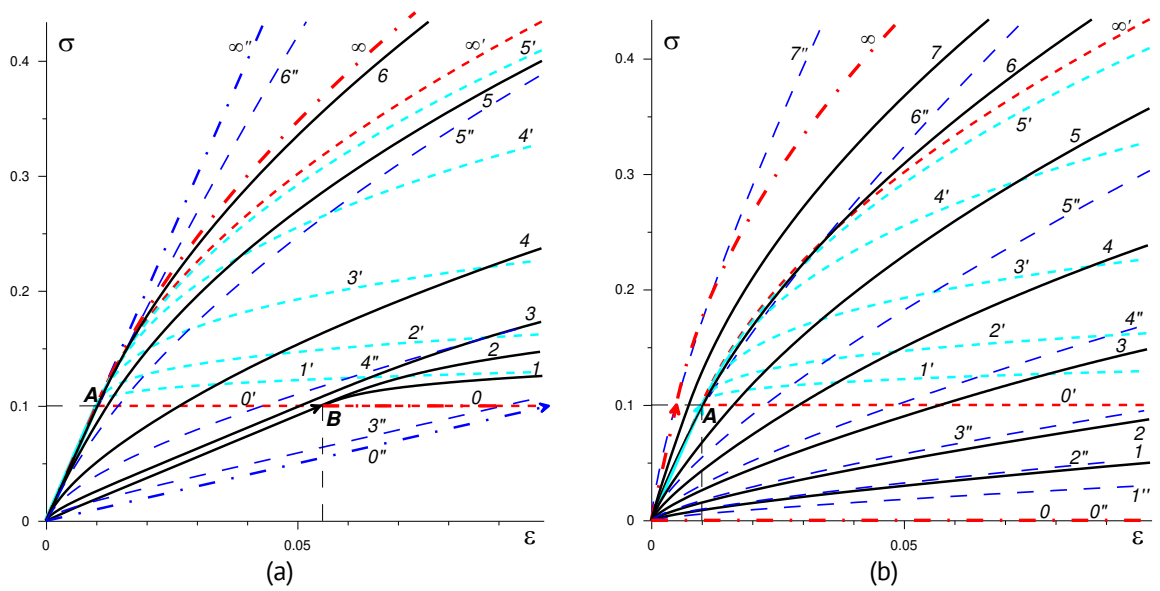


Fig. 6. Stress-strain curves $\sigma(\varepsilon, b)$ generated by the constitutive equation (4) with the same material functions (25) as in the Fig. 5(a) for three different weighting factors w=0;0.5;1 (light blue, black, and blue curves) at stress rates $b=10^{i-6}, i=1,\ldots,7$ (curves 1-7): (a) crossbreed of the model (1) and the standard linear solid model (6) (with the same material parameters as in the Fig. 4(a)); (b) crossbreed of the model (1) and the fractional model (5) with u=0.3, A=0.3

Figure 6(b) shows the stress-strain curves of three CE (4) with the same material parameters and MFs (25) as in Fig. 5(a) ($\sigma_+ = 0.1$, E = 10, $\tau_r = 1$), but with power-law CFs (5) with u = 0.3, A = 0.3, with three different weighting factors w = 1; 0.5; 0 (light blue, black and blue curves) for seven rates $b = 10^{i-6}$, i = 1,...,7 (curves 1'-5', 1-7, 1"-7"). The light blue stress-strain curves 1'-5' (for w=1) coincide with the stress-strain curves of the CE (1) in Figs. 5(a) and 6(a) (they have a common straight segment OA, independent of the rate: $\sigma = E\varepsilon$), the dashed red curves 0' and ∞ ' are the limit loading curves at $b \to 0$ and $b \to \infty$ (the same as in Fig. 6(a)). The blue stress-strain curves 2'' - 6''(for w = 0 and b = 0.0001; 0.001; 0.01; 0.1; 1) coincide with stress-strain curves 0-4 of the linear fractal model (5) in Fig. 4(b); it is irregular, $\Pi(0) = 0$, $G = \infty$, $\Pi(\infty) = \infty$, $G_{\infty} = 0$, at $b \to 0$ its stress-strain curves family (22) $\sigma(\varepsilon,b)$ converges to the function $\sigma \equiv 0$, as at $b \to \infty$ the family $\varepsilon(\sigma,b)$ converges to $\varepsilon = 0$, i.e., the stress-strain curves $\sigma(\varepsilon,b)$ converge to the vertical semi-axis. For this reason, at $b\to 0$ the stress-strain curves family of the CE (4) with $w \in (0,1)$ (see the black loading curves 1-7) converges to the function $\sigma = 0$ on the entire semi-axis $\varepsilon \ge 0$ (property 10), and at $b \to \infty$ converges to the function $\sigma = \varphi(E\varepsilon) = f(Ew^{-1}\varepsilon), \varepsilon \ge 0, f = F^{-1}$ (the dash-dotted red curve ∞), since according to (27) $\Phi(\sigma) = wF(\sigma)$.

If the value of w-1 is sufficiently small, then the contribution of the last term to the strain (26) is negligible, the properties of the loading curves (26) coincide with the properties of the stress-strain curves (23) of the CE (1) with the exception of two qualitative differences:

1. for models with $\sigma_+ > 0$ at any $w \neq 1$ the stress-strain curve (26) depends on the loading rate even in the range $\sigma \in [0; \sigma_+]$ (see (28)), in which $V(x) \equiv 0$ and $I(\sigma) \equiv 0$, although this dependence is weakly expressed if the material parameter w is close to one; 2. the equilibrium stress-strain curve for $w \neq 1$ can differ qualitatively from the limiting case w = 1 (Fig. 6(b)) and has a different form in the cases $\sigma_+ = 0$ or $\sigma_+ > 0$, and in the latter case the key role is played by the limited or unbounded nature of the CF $\Pi(t)$ (see properties of loading curves 7-11): for the models with $\sigma_+ = 0$ or with $\sigma_+ > 0$ and $\Pi(\infty) = \infty$ (Fig. 6(b)), the equilibrium curve has a form $\sigma \equiv 0$ on the entire ray $\varepsilon \geq 0$, and for the models with $\sigma_+ > 0$ and $\Pi(\infty) < \infty$ (Fig. 6(a)) the value (29) is finite and the equilibrium curve is non-zero: $\sigma = \varphi_\infty(E\varepsilon)$ at $\varepsilon \in [0; \hat{\varepsilon}]$ and $\sigma = \sigma_+$ at $\varepsilon > \hat{\varepsilon}$.

Conclusion

The paper formulates a generalization (4), (10) of the physically nonlinear CE of Maxwell-type viscoelastoplasticity (1), (7) with four MFs (two MFs in the uniaxial case (4)), the general properties, the arsenal of possibilities, and the scope of applicability of which have been studied earlier in a series of articles by the author [4–10]. In order to generalize the CE (1), (7), preserving its advantages, but eliminating the detected disadvantages that reduce its applicability, and to expand the range of rheological effects it describes, it is proposed to add a third (viscoelastic) strain component to the CE (1), (7), a term expressed by the linear integral Boltzmann–Volterra operator (3), (8) with arbitrary CF. For generality and convenience of model control, for its adjustment for different materials and lists of simulated effects, in addition to the three MFs, a weighting factor $w \in [0;1]$ (degree of nonlinearity) is introduced into the CE (4), which allows "mixing" the nonlinear

CE (1), (7) and the linear viscoelasticity operator (3), (8) in arbitrary proportions and regulate the severity of different sets of effects modeled by them. Thus, the CE (4), (10) is a hybrid (and simultaneous generalization) of the CE (1), (7) and the linear viscoelasticity CE (3), (8) (at w=0 nonlinearity is switched off, and the linear viscoelasticity CE is obtained, and at w=1 the nonlinear CE (1) is obtained). The proposed CE allows not only to expand the scope of applicability of the CE (1), (7), but also to connect the nonlinear viscoplasticity model (1), (7) to the linear viscoelasticity CE (3), (8), and to surgically adjust this connection depending on the characteristics of the testing data of a particular material: thanks to the choice of two material parameters σ_+ and w, nonlinear viscoplasticity can be added, starting from any stress $\sigma \ge \sigma_+ > 0$ and in any proportion.

The equations for the creep and recovery curves families and constant-rate loading curves generated by the proposed CE (4) with three arbitrary MFs are derived, their general properties and the influence of loading parameters and characteristics of all MFs on them are analytically studied and compared with the properties of the creep and stress-strain curves of crossbred CEs (1) and (3). In particular, new qualitative properties (effects) are identified that make it possible to describe the more general CE (4) in comparison with the original CE (1). It is verified that the generalization eliminates a number of disadvantages of the CE (1), but retains its valuable qualities (4–8). For example:

- 1. the CE (4) makes it possible to describe not only creep at a constant rate, as the CE (1), but also creep at a variable rate, as well as limited creep, characteristic, for example, of many polymers;
- 2. the CE (4) describes the recovery after complete unloading ("reverse creep") with a gradual yielding of strain to a certain constant level at large values of times;
- 3. the possibilities for describing the various properties of the stress-strain curves families, in particular the forms of equilibrium and instantaneous loading curves, are significantly expanded;
- 4. adding the CE (1) with any weighting factor w > 0 (arbitrarily small) to any singular linear model of the form (3), (8) produces its regularization (in particular, the instantaneous modulus no longer goes to infinity in the case of $\Pi(0) = 0$, and such a model appears with an instantaneous loading curve instead of a limiting vertical straight line at $b \to \infty$ [55,56]).

Thus, the performed primary analysis showed that the proposed more general CE (4), (7) provides many opportunities for describing the various properties of stress-strain curves and creep and recovery curves of materials (for adjusting their shape and tuning them to testing data). It also allows expanding significantly the range of described rheological effects and the range of applicability of the Maxwell-type viscoelastoplasticity relation and deserves further research and application in modeling. In the following papers, the properties found will be used to develop methods for identifying the CE (4), (7) from the loading and creep curves and recovery curve of materials, as was done for the CE (1), (7) in [5,7–10,56].

References

- 1. Khokhlov AV. Two-sided estimates for the relaxation function of the linear theory of heredity via the relaxation curves during the ramp-deformation and the methodology of identification. *Mechanics of Solids*. 2018; 53(3): 307–328.
- 2. Khokhlov AV. Analysis of properties of ramp stress relaxation curves produced by the Rabotnov non-linear hereditary theory. *Mechanics of Composite Materials*. 2018;54(4): 473–486.
- 3. Khokhlov AV. Properties of the Set of Strain Diagrams Produced by Rabotnov Nonlinear Equation for Rheonomous Materials. *Mechanics of Solids*. 2019;54(3): 384–399.
- 4. Khokhlov AV. Long-term strength curves generated by the nonlinear Maxwell-type model for viscoelastoplastic materials and the linear damage rule under step loading. *Journal of Samara State Technical University, Ser. Physical and Mathematical Sciences.* 2016;20(3): 524–543.
- 5. Khokhlov AV. The nonlinear Maxwell-type model for viscoelastoplastic materials: Simulation of temperature influence on creep, relaxation and strain-stress curves. *The Journal of Samara State Technical University, Ser. Physical and Mathematical Sciences*. 2017;21(1): 160–179. [In Russian]
- 6. Khokhlov AV. A Nonlinear Maxwell-Type Model for Rheonomic Materials: Stability under Symmetric Cyclic Loadings. *Moscow University Mechanics Bulletin*. 2018;73(2): 39–42.
- 7. Khokhlov AV. Applicability Indicators and Identification Techniques for a Nonlinear Maxwell-Type Elasto-Viscoplastic Model using Multi-Step Creep Curves. *Herald of the Bauman Moscow State Technical University. Series Natural Sciences*. 2018(6): 92–112. [In Russian]
- 8. Khokhlov AV. Applicability indicators and identification techniques for a nonlinear Maxwell–type elastoviscoplastic model using loading–unloading curves. *Mechanics of Composite Materials*. 2019;55(2): 195–210.
- 9. Khokhlov AV. Possibility to Describe the Alternating and Non-monotonic Time Dependence of Poisson's Ratio during Creep Using a Nonlinear Maxwell-Type Viscoelastoplasticity Model. *Russian Metallurgy (Metally)*. 2019;10: 956–963.
- 10. Khokhlov AV, Shaporev AV, Stolyarov ON. Loading-unloading-recovery curves for polyester yarns and identification of the nonlinear Maxwell-type viscoelastoplastic model. *Mechanics of Composite Materials*. 2023;59(1): 129–146.
- 11. Rabotnov YuN. Creep Problems in Structural Members. Moscow: Nauka; 1966. [In Russian]
- 12. Bugakov II. Creep of polymer materials. Moscow: Nauka; 1973. [In Russian]
- 13. Malinin NN. Creep design of engineering structures. Moscow: Mashinostroenie Publ.; 1981. [In Russian]
- 14. Gokhfel'd DA, Sadakov OS. *Plasticity and creep in structural elements under repeated loading*. Moscow: Mashinostroenie Publ.; 1984. [In Russian]
- 15. Nikitenko AF. Creep and long-term strength of metallic materials. Novosibirsk: NGASU; 1997. [In Russian]
- 16. Betten J. Creep Mechanics. Berlin: Springer; 2008.
- 17. Lokoshchenko AM. Creep and long-term strength of metals. Moscow: Fizmatlit Publ.; 2016. [In Russian]
- 18. Lakes RS. Viscoelastic Materials. Cambridge: Cambridge Univ. Press; 2009.
- 19. Bergstrom JS. Mechanics of Solid Polymers. Theory and Computational Modeling. Elsevier; 2015.
- 20. Vinogradov GV, Malkin AYa. Polymer rheology. Moscow: Khimiya Publ.; 1977. [In Russian]
- 21. Larson RG. Constitutive Equations for Polymer Melts and Solutions. Butterworth: Boston; 1988.
- 22. Gupta RK. Polymer and composite rheology. NY: Marcel Dekker; 2000.
- 23. Malkin AY, Isayev AI. Rheology: Conceptions, methods, applications. 2-nd Ed. Toronto: ChemTec Publishing; 2012.
- 24. Brinson HF, Brinson LC. Polymer Engineering Science and Viscoelasticity. Springer; 2008.
- 25. Kalinnikov AE, Vakhrushev AV. Creep of materials of different tensile and compressive strengths under variable loads. *Mechanics of Composite Materials*. 1982;18(3): 267–272.
- 26. Fatemi A, Yang L. Cumulative fatigue damage and life prediction theories: A survey of the state of the art for homogeneous materials. *International Journal of Fatigue*. 1998;20(1): 9–34.
- 27. Launay A, Maitournam MH, Marco Y, Raoult I, Szmytka F. Cyclic behaviour of short glass fibre reinforced polyamide: Experimental study and constitutive equations. *International Journal of Plasticity*. 2011;27(8): 1267–1293.
- 28. Darabi MK, Al-Rub RKA, Masad EA, Huang CW, Little DN. A modified viscoplastic model to predict the permanent deformation of asphaltic materials under cyclic-compression loading at high temperatures. *International Journal of Plasticity*. 2012;35: 100–134.
- 29. Takagi H, Dao M, Fujiwara M. Prediction of the Constitutive Equation for Uniaxial Creep of a Power-Law Material through Instrumented Microindentation. *Testing and Modeling. Materials Transactions.* 2014;55(2): 275–284.
- 30. Chinh NQ, Szommer P. Mathematical description of indentation creep and its application for the determination of strain rate sensitivity. *Materials Science & Engineering A.* 2014;611: 333–336.

139 A.V. Khokhlov

31. Petukhov DS, Keller IE. Dual plane problems for creeping flows of power-low incompressible medium. *The Journal of Samara State Technical University, Ser. Physical and Mathematical Sciences.* 2016;20(3): 496–507. [In Russian]

- 32. Kaibishev OA. Superplasticity of industrial alloys. Moscow: Metallurgiya Publ.; 1984. [In Russian]
- 33. Nieh TG, Wadsworth J, Sherby OD. Superplasticity in metals and ceramics. Cambridge Univ. Press; 1997.
- 34. Padmanabhan KA, Vasin RA, Enikeev FU. Superplastic Flow: Phenomenology and Mechanics. Berlin: Springer; 2001.
- 35. Segal VM, Beyerlein IJ, Tome CN, Chuvil'deev VN, Kopylov VI. *Fundamentals and Engineering of Severe Plastic Deformation*. NY: Nova Science Pub. Inc.; 2010.
- 36. Zhilayev AP, Pshenichnyuk AI. *Superplasticity and grain boundaries in ultrafine-grained materials*. Cambridge: Cambridge Intern. Sci. Publ.; 2010.
- 37. Cao Y. Determination of the creep exponent of a power-law creep solid using indentation tests. *Mechanics of Time-Dependent Materials.* 2007;11:159–172.
- 38. Megahed M, Ponter ARS, Morrison CJ. An experimental and theoretical investigation into the creep properties of a simple structure of 316 stainless steel. *International Journal of Mechanical Sciences*. 1984;26(3): 149–164.
- 39. Enikeev FU. Experimental evaluation of speed sensitivity of superplastic material in strongly non-uniform deflected mode. *Industrial Laboratory. Diagnostics of Materials*. 2007;73(10): 44–50. [In Russian]
- 40. Mochugovskiy AG, Mosleh AO, Kotov AD, Khokhlov AV, Kaplanskaya LY, Mikhaylovskaya AV. Microstructure Evolution, Constitutive Modelling, and Superplastic Forming of Experimental 6XXX-Type Alloys Processed with Different Thermomechanical Treatments. *Materials*. 2023;16(1): 445.
- 41. Eglit ME, Yakubenko AE, Zayko JS. Mathematical Modeling of Slope Flows of Non-Newtonian Media. *Proceedings of the Steklov Institute of Mathematics*. 2018;300: 219–229.
- 42. Radchenko VP, Shapievskii DV. Mathematical creep model for micro-nonhomogeneous non-linear elastic material. *Prikladnaya mekhanica I tekhnicheskaya fizika*. 2008;49(3): 157–163. [In Russian]
- 43. Naumenko K, Altenbach H, Gorash Y. Creep Analysis with a Stress Range Dependent Constitutive Model. *Archive of Applied Mechanics*. 2009;79: 619–630.
- 44. Lu LY, Lin GL, Shih MH. An experimental study on a generalized Maxwell model for nonlinear viscoelastic dampers used in seismic isolation. *Engineering Structures*. 2012;34(1): 111–123.
- 45. Monsia MD. A Simplified Nonlinear Generalized Maxwell Model for Predicting the Time Dependent Behavior of Viscoelastic Materials. *World Journal of Mechanics*. 2011;1:158–167.
- 46. Stolin AM, Khokhlov AV. Nonlinear model of shear flow of thixotropic viscoelastoplastic continua taking into account the evolution of the structure and its analysis. *Moscow University Mechanics Bulletin*. 2022;77(5): 127–135.
- 47. Khokhlov AV, Gulin W. Analysis of the nonlinear Maxwell-type constitutive equation for shear flow of tixotropic viscoelastic media accounting for interaction of deformation process and structure evolution. *Phisical Mesomechanics*. 2023;26(6): 621–642.
- 48. Gorodtsov VA, Leonov AI. On the kinematics, nonequilibrium thermodynamics, and rheological relationships in the nonlinear theory of viscoelasticity. *Journal of Applied Mathematics and Mechanics*. 1968;32(1): 62–84.
- 49. Leonov AI, Lipkina ECh, Paskhin ED, Prokunin AN. Theoretical and experimental investigations of shearing in elastic polymer liquids. *Rheologica Acta*. 1976;15(7/8): 411–426.
- 50. Pal'mov VA. Rheological models in the nonlinear mechanics of deformable bodies. *Uspekhi mekhaniki*. 1980;3(3): 75–115. [In Russian]
- 51. Prokunin AN. On the non-linear Maxwell-type defining equations for describing the motions of polymer liquids. *Journal of Applied Mathematics and Mechanics*. 1984;48(6): 699–706.
- 52. Leonov AI, Prokunin AN. Non-linear Phenomena in Flows of Viscoelastic Polymer Fluids. London: Chapman and Hall; 1994.
- 53. Leonov AI. Constitutive equations for viscoelastic liquids: Formulation, analysis and comparison with data. *Rheology Series*. 1999;8: 519–575.
- 54. Khokhlov AV. Analysis of creep curves produced by the linear viscoelasticity theory under cyclic stepwise loadings. *The Journal of Samara State Technical University, Ser. Physical and Mathematical Sciences.* 2017;21(2): 326–361. [In Russian]
- 55. Khokhlov AV. Specific features of stress-strain curves at constant stress rate or strain rate yielding from linear viscoelasticity. *Problems of Strength and Plasticity*. 2015;77(2): 139–154. [In Russian]
- 56. Khokhlov AV. Analysis of the bulk creep influence on stress-strain curves under tensile loadings at constant rates and on Poisson's ratio evolution based on the linear viscoelasticity theory. *The Journal of Samara State Technical University, Ser. Physical and Mathematical Sciences*. 2019;23(4): 671–704. [In Russian] 57. Krishtal MM. Instability and mesoscopic inhomogeneity of plastic deformation (analytical review). Part
- I. Phenomenology of the sharp yield point and jerky flow. *Phisical Mesomechanics*. 2004;7(5–6): 5–26.
- 58. Rudskoi AM, Rudaev Yal. Mechanics of dynamic superplasticity of aluminum alloys. St. Petersburg: Nauka; 2009. [In Russian]

- 59. Yu D, Chen X, Yu W, Chen G. Thermo-viscoplastic modeling incorporating dynamic strain aging effect on the uniaxial behavior of Z2CND18.12N stainless steel. *International Journal of Plasticity*. 2012;37: 119–139.
- 60. Trusov PV, Chechulina EA. Serrated yielding: physical mechanisms, experimental dates, macrophenomenological models. *PNRPU Mechanics Bulletin*. 2014;(3): 186–232. [In Russian]
- 61. Lin YC, Chen XM. A critical review of experimental results and constitutive descriptions for metals and alloys in hot working. *Materials and Design*. 2011;32(4): 1733–1759.
- 62. McClung AJW, Ruggles-Wrenn MB. The rate (time)-dependent mechanical behavior of the PMR-15 thermoset polymer at elevated temperature. *Polymer Testing*. 2008;27(7): 908–914.
- 63. Kastner M, Obst M, Brummund J, Thielsch K, Ulbricht V. Inelastic material behavior of polymers Experimental characterization, formulation and implementation of a material model. *Mechanics of Materials*. 2012;52: 40–57.
- 64. Yun KS, Park JB, Jung GD, Youn SK. Viscoelastic constitutive modelling of solid propellant with damage. *International Journal of Solids and Structures*. 2016;80: 118–127.
- 65. Fung YC. Biomechanics. Mechanical Properties of Living Tissues. New York: Springer; 1993.
- 66. Diani J, Fayolle B, Gilormini P. A review on the Mullins effect. *European Polymer Journal*. 2009;45(3): 601–612.
- 67. Zhu Y, Kang G, Yu C, Poh LH. Logarithmic rate based elasto-viscoplastic cyclic constitutive model for soft biological tissues. *Journal of Mechanical Behavior of Biomedical Materials*. 2016;61: 397 409.
- 68. Qi H, Boyce M. Stress-strain behavior of thermoplastic polyurethanes. *Mechanics of Materials*. 2005;37(8): 817–839.
- 69. Drozdov AD, Dusunceli N. Unusual mechanical response of carbon black-filled thermoplastic elastomers. *Mechanics of Materials*. 2014;69(1): 116–131.

About the Author

Andrew V. Khokhlov (1) Sc

Ph. D. in Technical Sciences

Senior Researcher (Institute of Mechanics, Lomonosov Moscow State University, Moscow, Russia)

Associate Professor (Department of Composites Mechanics, Faculty of Mechanics and Mathematics, Lomonosov Moscow State University, Moscow, Russia)

Leading Researcher (Laboratory "Polymer composites for the North", North-Eastern Federal University, Yakutsk, Russia)

Submitted: November 24, 2023 Revised: May 21, 2024 Accepted: August 28, 2024

Synthesis of WO_{2,72}:Fe thin films via ammonium tungstate precursor by spray pyrolysis technique and annealing

E. Ouadah, [®] N. Hamdadou [™], [®]

Laboratoire de Micro et de Nanophysique, Ecole Nationale Polytechnique d'Oran, Oran, Algérie

[™] nasreddine.hamdadou@enp-oran.dz

ABSTRACT

In this study, $WO_{2.72}$:Fe thin films have been prepared on glass substrates heated to a fixed temperature of 350 °C by the spray pyrolysis technique, from an aqueous ammonium tungstate solution (NH_4)₁₀ H_2 (W_2O_7)₆ with a concentration of 0.005 M. The dopant concentrations were 1, 3 and 5 %. After deposition, the thin films were annealed at 550 °C for 4 h. The characterization results revealed that Fe doping has a significant effect on the morphology of thin films depending on its concentration. In addition, it promotes crystallites growth and improves the surface quality. GIXRD analysis has shown that the thin films obtained after the annealing are polycrystalline in nature, the structure of the $WO_{2.72}$ films was monoclinic, with space groups P2/m (10). The growth direction was variable depending on the doping concentration. It was noticed that the peaks positions, the preferential grain orientation and the structural parameters are affected by the doping concentrations, which had no effect on the phase type of the obtained films. The $WO_{2.72}$ films have interesting optical properties; high transmittance in the visible range of 75 % as well as high absorption in the ultra-violet range from 1.4 to 0.2 a.u. Moreover, the films exhibit both direct and indirect electronic transitions, which are red-shifted due to Fe-doping.

KEYWORDS

WO_{2.72} thin film • spray pyrolysis • Fe-doping • roughness • GIXRD • spectrophotometry

Citation: Ouadah E, Hamdadou N. Synthesis of WO_{2.72}:Fe thin films via ammonium tungstate precursor by spray pyrolysis technique and annealing. *Materials Physics and Mechanics*. 2024;52(4): 141–151. http://dx.doi.org/10.18149/MPM.5242024 12

Introduction

WO_x tungsten oxides are n-type wide band gap semiconductor (2.5 – 3.6 eV), and can easily be produced as thin films with high optical transparency in the visible range. These materials allow us to use its in many applications such as: solar energy conversion, semiconductor gas sensors, photocatalysis, electrochemical screens and field emission devices FED [1,2]. Among the different phases of tungsten oxides, non-stoichiometric tungsten oxides WO_{3-x} , x < 3 are important due to oxygen vacancy defects [3,4]. Particularly in recent years, the nanomaterials of WO_{2.72} have attracted the attention of several works because they have excellent properties for nanotechnology applications [5]. In addition, WO_{2,72} with monoclinic structure is the poorest in oxygen among non-stoichiometric tungsten oxide materials [6]. They have presented various morphologies like nanospheres, nanowires, nanofibers and sea urchin-shaped nanostructures [6]. Several preparation techniques have been used to prepare WO_{2.72} thin films, including thermal evaporation of tungsten oxide [7], solvothermal techniques [8], physical vapor deposition PVD, sol-gel process, the electrochemical technique and chemical vapor deposition CVD [9], spray pyrolysis technique [10]. Several works have been carried out on the nanorods and the nanowires of WO_{2.72} [11,12].

© E. Ouadah, N. Hamdadou, 2024.

142 E. Ouadah, N. Hamdadou

In this work, we have used the reactive chemical spraying technique in liquid phase (spray pyrolysis) for the preparation of $WO_{2.72}$ thin films, because it's simple, economical with a high growth rate and even the injection of dopants is without any difficulty. The obtained thin films have been annealed at 550 °C for 4 hours. To improve the physical and chemical properties of the $WO_{2.72}$ thin films, several dopants have been used such as Ti, Fe [13,14], Al [15], Mo [16], Ce and La [17,18]. We have chosen the Fe element as a dopant with doping concentrations 1, 3 and 5 %, because it has an important role in reducing the band gap of $WO_{2.72}$.

Experimental details

Thin films preparation

 $WO_{2.72}$ thin films were deposited on glass substrates of dimensions $26 \times 10 \times 1$ mm at constant temperature of 350 °C by spray-pyrolysis using a HOLMARC brand. The glass substrates were cleaned previously in an ultrasonic bath with acetone and ethanol three times for 5 min; then, with deionized water to remove traces of microscopic impurities.

The precursor solution of 0.005 M was prepared from ammonium tungstate $(NH_4)_{10}H_2(W_2O_7)_6$ dissolved in 100 ml of deionized water. After that, the solution was sprayed using a syringe-attached sprayer. The air-directed spray stream has been used as a carrier gas. The substrate-nozzle distance and the spraying rate were 12 cm and 200 μ l/min, respectively, with an air pressure of 1.5 bar. The deposition time was 8 min.

The Fe dopant concentration was 1, 3 and 5 at. %. After cooling to room temperature, the films were annealed at 550 °C for 4 hours using a MAGMA THERM programmable tubular oven, with a heating rate of 10 °C/min. The purpose of this annealing is to improve the densification and crystallization. Table 1 depicts the deposition parameters of the films.

Table 1. Deposition parameters of WO _{2.72} :Fe thin film	Table 1. [Deposition	parameters	of WO _{2.72}	:Fe thin films
---	------------	------------	------------	-----------------------	----------------

Parameter	Value
Substrate	Glass
Substrate temperature, °C	350
Precursor volume, ml	20
Solvent	Deionized water
Dopant	Fe
Spray rate, μl/min	200
Nozzle-substrate distance, cm	12
Spray duration, min	8
Annealing temperature, °C	550
Annealing duration, h	4

Thin films characterization

The films thickness was measured using a Bruker Dektak XT profilometer, which also gives the roughness parameters of the surface. The data processing was carried-out by Vision 64 software. The structural properties were obtained by grazing incidence X-ray diffraction (GIXRD) using an INEL Equinox 3000 diffractometer operating in the range of $0-120^{\circ}$ with a filtered Cu-K α radiation ($\lambda = 1.54056$ Å). The data processing was

performed by Match 3 software. The optical transmittance and absorbance spectra were carried out at room temperature by a dual beam UV-Visible spectrophotometer Specord 210 Plus in the wavelength range of 300–1100 nm.

Results and Discussion

Film thickness and profile analysis

The surface profilometry is a non-destructive technique and allows studying the film profile. Several parameters are reliable to the surface roughness. Table 2 shows the primary profile Pp, the total profile Pt and the thickness e of WO_{2.72}:Fe films annealed at 550 °C for 4 h. It is observed that the surface primary and total profiles decrease with Fe-doping.

Table 2. Thickness, primary profile and total profile of WO_{2.72}:Fe thin films after annealing at 550 °C for 4 h

71 71					
Parameter	Doping concentration, %				
raiailletei	1	3	5		
e, nm	352	396	245		
P _P , Å	28108	12403	5624		
P _t , Å	31275	13866	6214		

Table 3. Surface profile parameters of WO_{2.72}:Fe films after annealing at 550 °C for 4 h

Parameter	Doping concentration, %					
Parameter	1	3	5			
P _q , Å	2710.87	2747.67	759.65			
P_{sk}	5.074	2.29	4.856			
P_{ku}	40.52	7.397	27.362			
P _z , Å	31275.04	13866.13	6214.45			
P _v , Å	3166.71	1462.19	589.65			

Furthermore, the other parameters such as the root mean square deviation of the assessed profile $P_{\rm q}$, the skewness of the assessed profile $P_{\rm sk}$, the kurtosis of the assessed profile $P_{\rm ku}$, are gathered in Table 3. These parameters are often used to get insights on the surface quality. The assessed profile is characterized by three parameters, its maximum height $P_{\rm z}$, its maximum profile peak height $P_{\rm p}$, and its maximum profile valley depth $P_{\rm v}$:

height
$$P_z$$
, its maximum profile peak height P_p , and its maximum profile valley depth P_v :

$$\begin{cases}
P_q = \left[\frac{1}{l} \int_0^l Z^2(x) dx\right]^{1/2} \\
P_{\text{sk}} = \frac{1}{(P_{q_l})^3} \left[\frac{1}{l} \int_0^l Z^3(x) dx\right] \\
P_{\text{ku}} = \frac{1}{(P_{q_l})^4} \left[\frac{1}{l} \int_0^l Z^4(x) dx\right] \\
P_Z = P_P + P_V \\
P_v = \frac{1}{\text{CN}} \sum_{i=1}^{CN} P v_i
\end{cases}$$
(1)

Figure 1 shows the variation of the surface profile parameters with Fe-doping concentration. It is observed that the parameters P_q , P_z , P_p and P_v decrease with increasing of the dopant concentration. Hence, Fe-doping improves the surface quality. It is evident that thermal treatment at higher temperatures promotes the growth of the crystallites and enhances the roughness of the surface.

144 E. Ouadah, N. Hamdadou

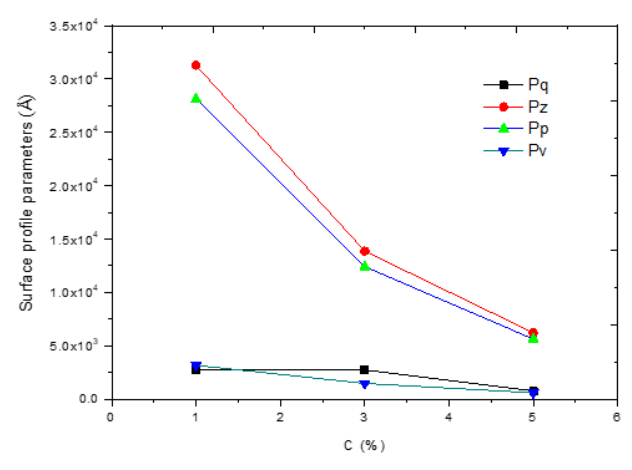


Fig. 1. Same surface profile parameters of $WO_{2,72}$: Fe thin films as a function of doping concentration

GIXRD analysis

Grazing incidence X-ray diffraction (GIXRD) technique was used to determine the structure, crystallographic growth directions, lattice parameters, and average grains size. Before annealing, the thin films are amorphous (Fig. 2(a)). Figure 2(b) shows the GIXRD patterns of $WO_{2.72}$:Fe films after annealing at 550 °C for 4 hours.

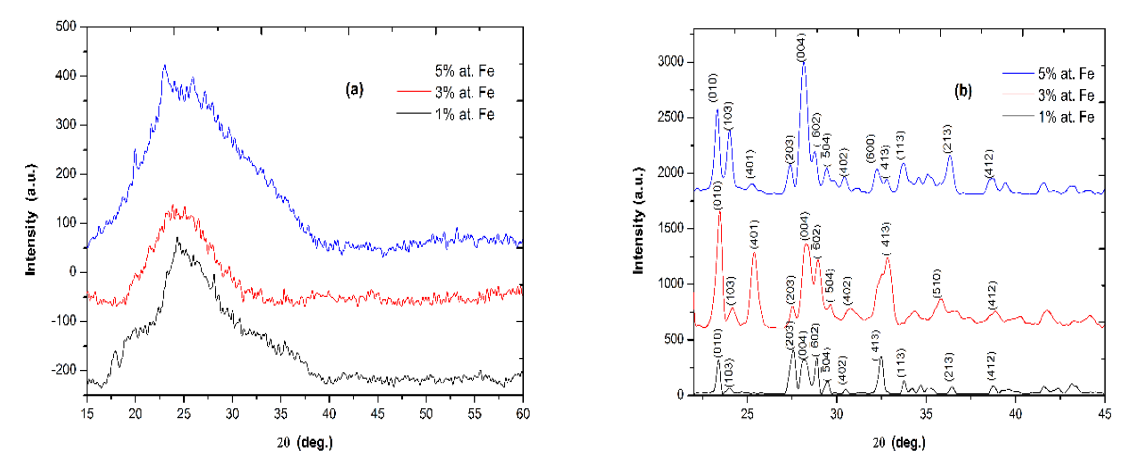


Fig. 2. GIXRD diagrams of $WO_{2.72}$:Fe films with different doping concentrations; before (a) and after (b) annealing at 550 °C for 4 hours

The thin films are of polycrystalline nature, all peaks appearing are attributed to WO_{2.72} of monoclinic structure, identified using the ICDD card N°36-0101. No. Fe diffraction peak or other phases, is detected which indicates that the thin films are well crystallized. Table 4 indicates the Bragg angles θ , the relative intensities of the diffraction peaks and the Miller indices (*hkl*) for different doping concentrations. All the spectra of WO_{2.72}:Fe thin films represent the same peaks of the planes (103), ($\overline{6}$ 02), ($\overline{5}$ 04), (402), ($\overline{4}$ 13) and (412) which are considerably lower and wider peaks, but the most intense peak was attributed to the orientations (203), (010) and (004), with doping concentrations 1, 3 and 5 %, respectively. Usually, the sharp diffraction peaks require the lowest formation energy. In addition, with an increase in the doping concentration 1, 3 and 5 %, the grains preferential orientation changes from (203), (010) and (004), respectively,

indicating a change in the growth mechanism of these thin films, from a direction parallel to the surface of the substrate (010) to a perpendicular direction (004). The peak at orientation (010) is attributed to $WO_{2.72}$ of monoclinic structure as reported in previous works [19], the diffraction angles corresponding to this orientation with doping concentrations at 1, 3 and 5 % were 23.49°, 23.37° and 23.34°, respectively. These results show slight shifts of this diffraction peak towards lower angles. This suggests that the crystal structure is modified during Fe doping due to the very similar ion radius of Fe and W ions [20]. In addition, the incorporation of Fe doesn't change the phase type of $WO_{2.72}$ and no new peak has appeared, indicating the Fe homogeneous incorporation into the lattice of $WO_{2.72}$ [20].

Table 4. The peak positions, the relative intensities and the Miller indices of $WO_{2.72}$: Fe thin films for different
doping concentrations

1 %		3 %		5 %	(64)	
2θ, deg.	I, %	2θ, deg.	I, %	2θ, deg.	I, %	(hkl)
23.49	77	23.37	100	23.34	86	(010)
24.12	17	24.08	47	24.03	80	(103)
27.67	100	27.44	48	27.42	69	(203)
28.29	77	28.36	82	28.19	100	(004)
28.99	82	28.87	74	28.79	73	$(\overline{6}02)$
29.58	30	29.55	49	29.46	68	$(\overline{5}04)$
30.61	13	30.67	47	30.46	66	(402)
32.59	86	32.76	75	32.82	65	$(\overline{4}13)$
38.86	21	38.79	46	38.72	65	(412)

The lattice parameters have been deduced using the relations below:

$$\begin{cases}
\frac{1}{d_{hkl}^2} = \frac{1}{\cos^2 \beta} \left(\frac{h^2}{a^2} + \frac{k^2 \sin^2 \beta}{b^2} + \frac{l^2}{c^2} - \frac{2 \text{hk} \cos \beta}{ab} \right) \\
d_{hkl} = \frac{\lambda}{2 \sin \theta}
\end{cases}, (2)$$

where d_{hkl} is the inter-reticular distance.

The FWHM (Full Width at Half Maximum) of the peaks were calculated by Warren relation: $(FWHM)^2 = B^2 - b^2$, (3)

where *B* is the observed widening, which is given directly by the data processing software of the diffractometer and *b* is instrumental broadening which is equal to 0.08° in our case.

The average grain size *D* was determined using Scherrer formula [21]:

$$D = 0.9 \frac{\lambda}{EWHM \cos \theta},\tag{4}$$

where λ is the X-rays wavelength. Table 5 indicates the lattice parameters a, b, c and β , the full width at half maximum *FWHM* of the most intense peak, the average grain size D, the unit cell volume V, the lattice strain ε and the dislocation density δ .

The *FWHM* of the most intense peaks decreased with the increase in the dopant level up to about 3 % at first, which implies an increase in the grain size and improved crystal quality (Table 5). Tungsten typically exists in the +6 (W $^{+6}$) oxidation state. When iron, which can be in the +2 (Fe $^{+2}$) or +3 (Fe $^{+3}$) oxidation state, is introduced, a charge imbalance occurs, resulting in electrostatic instability. To restore this balance within the crystal structure, oxygen atoms may be released, creating oxygen vacancies. The charge difference between tungsten and iron ions provides the energy needed for these

146 E. Ouadah, N. Hamdadou

vacancies to form. These vacancies serve as low-energy active sites, around which atoms can cluster to form larger and more uniform crystalline grains. Thus, increasing the number of oxygen vacancies can enhance the size and regularity of the crystalline grains [22], which is considered very beneficial for gas detection application. In addition, the presence of oxygen vacancies would generally give the material better conductivity [23]. On the other hand, beyond 3 %, there is an increase in the *FWHM* of the peaks, which is reflected by deterioration in the crystal quality and a reduction in the grain size, or this leads to a significant increase in the specific surface area of grain boundaries [16]. In addition, the change in the grain size depends on the change in the density of the nucleation centers, created just at the time of thin film growth. The greater the density of the nucleation centers, the smaller the grain size and vice versa.

Table 5. Structural parameters values of WO_{2.72}:Fe thin films after annealing at 550 °C for 4 h: the lattice parameters a, b, c and β , FWHM is the full width at half maximum of the most intense peak, D is the grain size, V is the unit cell volume, ε is the lattice strain, δ is the dislocation density

Fe-doping,		Lattice p	arameter		FWHM,	D nm	V, Å ³	٤,	δ,
%	a, Å	b, Å	c, Å	β, °	deg.	D, nm	V, A	× 10 ⁻³	lines/µm²
1	19.8952	3.7830	14.4234	119.06	0.23962	33.92	424.9	1.02	869.1
3	18.6829	3.8018	14.0615	116.58	0.17943	45.31	428.3	0.76	487.1
5	18.7784	3.8068	14.2880	117.69	0.23904	34.00	456.9	1.02	865.0

It can be seen in Table 5 that the lattice parameters are varied with increasing Fe concentration. This variation may be attributed to the incorporation of Fe^{3+} ions into the system of $WO_{2.72}$:Fe because the Fe^{3+} ion can perform the same coordination as that of W^{6+} .

The dislocation density δ of the film defines the length of the dislocation lines per crystal volume unit. This parameter was calculated using the following relation:

$$\delta = \frac{1}{R^2},\tag{5}$$

where D is the average grain size evaluated from the XRD data. The cell deformation varies proportionally with the stress, which is the resultant of the internal forces in matter. The strain \mathcal{E} in the studied films was evaluated using the following equation:

$$\varepsilon = \frac{FWHM\cos\theta}{4}.\tag{6}$$

Table 5 shows the results of stain variation and dislocation density of thin films of $WO_{2.72}$:Fe for different doping concentrations. Strain and dislocation density decrease with increasing dopant concentration from 1 to 3 %, then increase for the dopant concentration from 3 to 5 %, these results agree well with the variation observed in the grain size. The smaller dislocation density values for the doped thin films indicate the homogeneous nucleation growth in the formation of $WO_{2.72}$ thin films, the reduction of the lattice imperfections concentration and the formation of thin films with high crystallinity. Consequently, these observations confirmed that the increase in the grain size is linked to the reduction in deformation and therefore to the reduction in the dislocation density in these films. Moreover, when iron is incorporated into the thin films of $WO_{2.72}$, it can substitute for tungsten atoms in the crystal lattice. This substitution leads to the formation of new equilibrium sites within the lattice, which helps reorganize the network to achieve greater stability. So, iron doping can also contribute to the redistribution of stresses arising from tungsten defects, thereby reducing distortions [24,25].

Optical analysis

The spectrophotometry measurements were performed at room temperature. With the increase in the wavelength, Fig. 3(a) shows a strong decrease in absorption in the ultraviolet from 1.4 to 0.2 a.u. and an average decrease in the visible range from 0.2 to 0.1 a.u. There is no absorption band in the visible region. It can be seen that the prepared thin films had a much higher absorption capacity in the ultraviolet region than in the visible region, which should behave as a UV protective material, which is in good agreement with the result reported by Morankar PJ et al. [16], and similar results were also found for the tungsten bronze compounds of Cs_xWO_3 and K_xWO_3 [26]. On the other hand, the thin films of $WO_{2.72}$:Fe doped at 1 % have the lowest absorbance in the visible region, on the other hand, the highest absorbance was observed for those doped at 5 %.

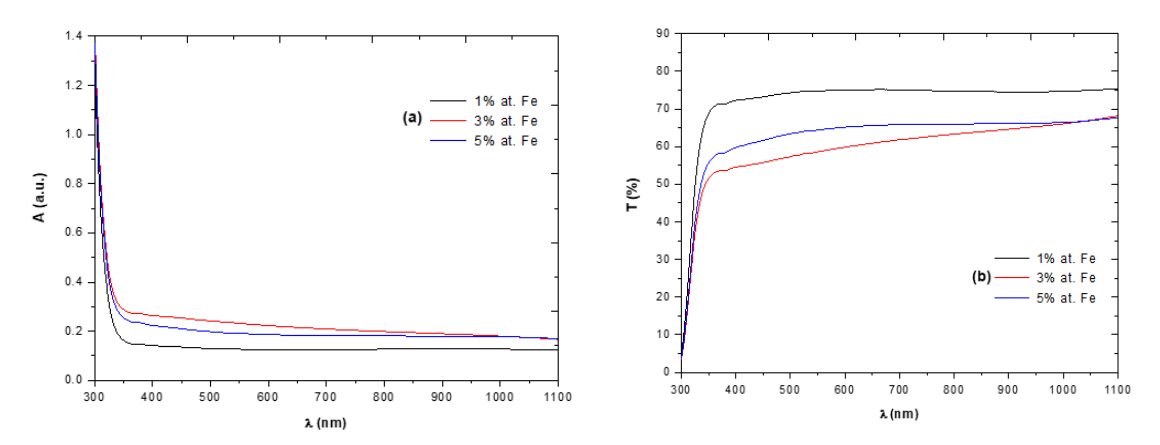


Fig. 3. Absorbance (a) and transmittance spectra (b) of WO_{2.72}:Fe thin films

The transmittance of a thin film is influenced by factors such as surface roughness, scattering of grain boundaries, optical inhomogeneity, etc. From Fig. 3(b), we can notice that, the WO_{2.72}:Fe thin films having a higher transmittance in the visible range, on the other hand, in the ultraviolet range it is weaker. That is why we can say that the WO_{2.72}:Fe thin films have an optical selectivity, because it reaches different optical transmittance for the visible region and the ultraviolet region, of which the WO_{2.72} thin films give an interesting optical characteristic, thus, it can transmit most of the Vis light and mask almost all of the UV light [27], and similar results have been found in the UV-Vis domain for the $WO_{2,72}$ bulk [11,12], $K_xWO_{3+x/2}$ [26] and the tungsten bronze compounds of Cs_xWO_3 and K_xWO_3 [26]. As a consequence, the $WO_{2,72}$: Fe thin films can be used as sun filters in the UV-Vis range. In addition, the transmittance of thin films doped at 1 % reaches the greatest value 75 % in the visible domain and decreases to 68 and 67 % with the increase in doping concentration from 3 to 5 % respectively, this decrease can be attributed to the propagation losses at the grain's boundaries and oxygen vacancies. When introducing iron (Fe) as a dopant into $WO_{2.72}$ material, it leads to the formation of "impurity energy levels" or "defect levels" within the original energy bandgap of the material. When light with appropriate energy strikes this material, it is absorbed more effectively due to the transfer of this required energy to the newly formed energy levels. This enhances the absorption of light in certain energy ranges and reduces the optical transmittance in the visible region [28].

148 E. Ouadah, N. Hamdadou

The absorption coefficient α was calculated from the transmission data using the equation: $\alpha = \frac{1}{e} ln(\frac{100}{T}),$ (7)

where e represents the thickness (cm) and T is the optical transmittance (%).

Figure 4 shows the variation of the optical absorption coefficient of WO_{2.72}:Fe thin films. The optical absorption coefficient values reached $\sim 0.64~10^4$, $\sim 0.81~10^4$ and $\sim 2.32~10^4$ cm⁻¹ for the doping concentrations 1, 3 and 5 % respectively. In other words, they increase proportionally with the doping concentration. This confirms that doping has an effect on the optical absorption coefficient.

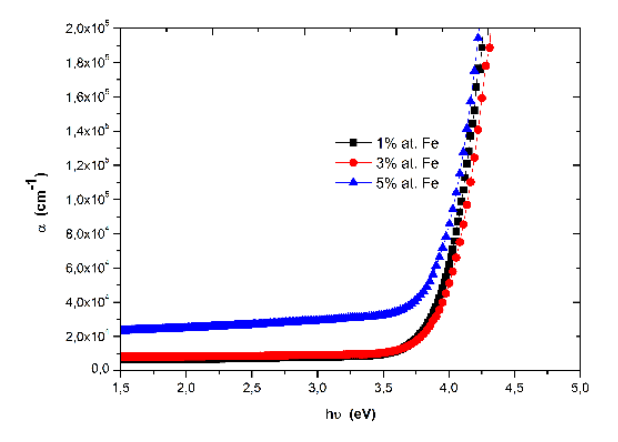


Fig. 4. Variation of the optical absorption coefficient of WO_{2.72}:Fe thin films

To determine the band gap energy, we have used Tauc formula, which is given as follow [29]: $\alpha hv = A(hv - E_a)^n$, (8)

where A is a constant, h is the Planck constant, v is the frequency of the incident light. The constant n = 1/2 in the case of a direct optical transition and n = 2 in the case of an indirect optical transition. E_g is deduced from the plot $(\alpha hv)^2 = f(hv)$ by linear extrapolation to the abscissa axis.

Figures 5(a) and 5(b) show the plots for direct and indirect allowed optical transitions in the thin films, respectively.

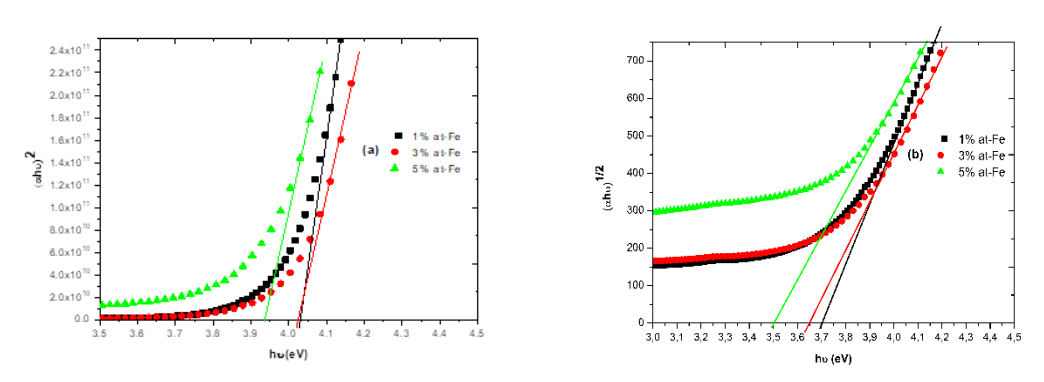


Fig. 5. Direct (a) and indirect (b) optical transitions of WO_{2.72}:Fe thin films

The extrapolation of the linear parts of these curves yields the value of the optical band gap (E_g^{\parallel} is the direct optical band gap, E_g^{\parallel} is the indirect optical band gap). Table 6 resumes the obtained values for WO_{2.72}:Fe thin films. The band gap energy in the direct

and indirect case of the $WO_{2.72}$:Fe thin films decreases by increasing the doping concentration. This would present a similar result for the nanowires of Ti doped $WO_{2.72}$ [30]. The bandgap of $WO_{2.72}$ is primarily formed by the 2p orbitals of oxygen, which constitute the valence band, and the 5d orbitals of tungsten, which constitute the conduction band. When iron is introduced, its 3d orbitals, which have energy levels situated between the valence and conduction bands, participate. The interaction between the 2p orbitals of oxygen, the 5d orbitals of tungsten, and the 3d orbitals of iron leads to the formation of new intermediate energy levels. This interaction results in the reduction of the effective bandgap [31].

Table 6 Energy b	and gaps and Urbach energ	ay of WO Ea thin films	after appealing a	+ 550 °C for 1 h
Table 6. Energy b	and dabs and Urbach ener	av of wusze:re thin films	arter anneaund a	IT 550 °C for 4 fi

Fe-doping, %	Egl, eV	Eg", eV	E _u , meV
1	4.03	3.70	0.226
3	4.02	3.65	0.257
5	3.93	3.50	0.249

Figure 6(a) shows the $Ln \alpha$ plots of the absorption coefficient as a function of photon energy. In this region, called the Urbach region. The following relation gives the absorption coefficient:

$$\alpha = \alpha_0 \exp(\frac{hv}{E_y}) \tag{9}$$

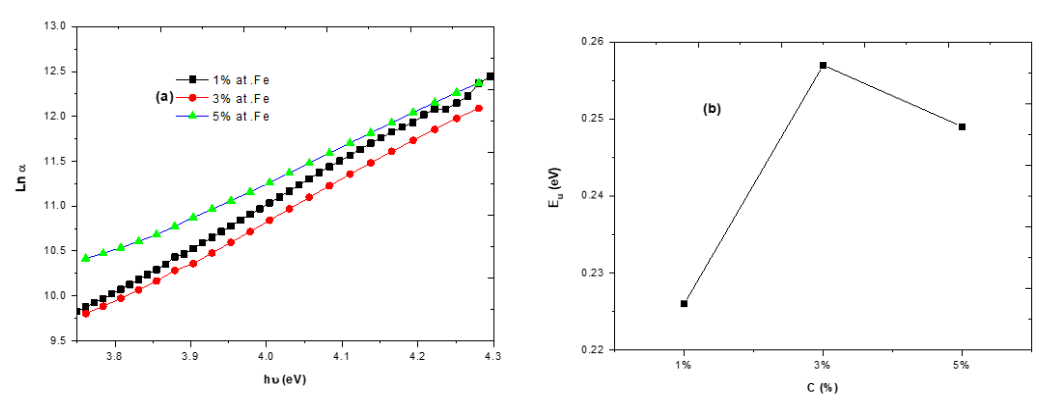


Fig. 6. Urbach energy determination (a) and values (b) of WO_{2.72}:Fe thin films

Therefore:

$$L n \alpha = L n \alpha_0 + \frac{h \nu}{E_u}, \tag{10}$$

where α_0 is a constant and E_u is the Urbach energy.

To measure the width of tail states, the Urbach energy E_u was calculated from the equation:

$$E_u = \left\{ \frac{d(L \, n \, \alpha)}{d(hv)} \right\}^{-1}. \tag{11}$$

The Urbach energy values of WO_{2.72}:Fe thin films annealed at 550 °C for 4 hours are gathered in Table 6. Figure 6(b) shows the variation of the Urbach energy with Fe-doping. It is observed that E_u increases indicating the widening of the tail's states. Moreover, E_u is sensitive to disorder and the increase of the crystallinity in the films, which is believed to explain the variation, observed for the prepared thin films.

150 E. Ouadah, N. Hamdadou

Conclusion

The Fe-doped WO_{2.72} thin films were synthesized on glass substrates by the reactive chemical spraying technique in liquid phase (spray-pyrolysis) using ammonium tungstate (NH₄)₁₀H₂(W₂O₇)₆ as a precursor with a concentration 0.005 M. The dopant concentrations were 1, 3 and 5 % at. After deposition, the thin films were annealed at 550 °C for 4 h. The GIXRD analysis shows that all the samples obtained before the annealing are amorphous; on the other hand, the thin films obtained after annealing at 550 °C for 4 h are polycrystalline in nature, with a monoclinic structure of WO_{2.72}. The surface profiles are reduced by the increase of doping. The thickness of the WO_{2.72}:Fe thin films varies between 245 and 396 nm. The average grain size goes from 33.92 to 45.31 nm and 34.00 nm for Fe doping at 1, 3 and 5 %, respectively. The films obtained have a large number of defects such as oxygen vacancies, which are responsible for their high optical selectivity in the UV-Vis range. The films have direct and indirect electronic transitions, where the energy of the authorized indirect electronic transition is shifted to the red in all samples due to doping with Fe.

References

- 1. Kumar KN, Sattar SA, Ashok Reddy GV, Jafri RI, Premkumar R, Meera MR, Ahamed AA, Muthukrishnan M, Dhananjaya M, Tighezza AM. Structural, optical, and electrochromic properties of RT and annealed sputtered tungsten trioxide (WO₃) thin films for electrochromic applications by using GLAD technique. *Journal of Materials Science: Materials in Electronics*. 2023;34(28): 1934.
- 2. Nabeel MI, Hussain D, Ahmad N, Najam-ul-Haq M, Musharraf SG. Recent Advancements in Fabrication and Photocatalytic Applications of Graphitic Carbon Nitride-Tungsten Oxide Nanocomposites. *Nanoscale Advances*. 2023;5: 5214–5255.
- 3. Zeb S, Sun G, Nie Y, Xu H, Cui Y, Jiang X. Advanced developments in nonstoichiometric tungsten oxides for electrochromic applications. *Materials Advances*. 2021;2(21): 6839–6884.
- 4. Boruah PJ, Khanikar RR, Bailung H. Synthesis and characterization of oxygen vacancy induced narrow bandgap tungsten oxide (WO_{3-x}) nanoparticles by plasma discharge in liquid and its photocatalytic activity. *Plasma Chemistry and Plasma Processing*. 2020;40(4): 1019–1036.
- 5. Wu R, Cheng LH, Ma CQ, Yuan ZT, Song J. Enhancing the sensing performance of $WO_{2.72}$ toward n-butanol via loading CeO_2 nanoparticles. *Journal of Materials Chemistry A.* 2024;12(24): 5678–5687.
- 6. Qiu H, Chen Q, An X, Liu Q, Xie L, Zhang J, Yao W, Luo Y, Sun S, Kong Q, Chen J. WO₂ nanoparticles with oxygen vacancies: a high-efficiency electrocatalyst for the conversion of nitrite to ammonia. *Journal of Materials Chemistry A*. 2022;10(47): 24969–24974.
- 7. Zhang M, Sun H, Guo Y, Wang D, Sun D, Su Q, Ding S, Du G, Xu B. Synthesis of oxygen vacancies implanted ultrathin WO_{3-x} nanorods/reduced graphene oxide anode with outstanding Li-ion storage. *Journal of Materials Science*. 2021;56: 7573–7586.
- 8. Wu CM, Naseem S, Chou MH, Wang JH, Jian YQ. Recent advances in tungsten-oxide-based materials and their applications. *Frontiers in Materials*. 2019;6: 49.
- 9. Gutpa J, Shaik H, Kumar KN, Sattar SA. PVD techniques proffering avenues for fabrication of porous tungsten oxide (WO₃) thin films: A review. *Materials Science in Semiconductor Processing*. 2022;143: 106534. 10. Ouadah E, Hamdadou N., Ammari A. Morphological, Structural and Optical Properties of Fe-Doped WO₃ Films Deposited by Spray-Pyrolysis. *Journal of Electronic Materials*. 2022;51(1): 356–369.
- 11. Xi Z, Erdosy DP, Mendoza-Garcia A, Duchesne PN, Li J, Muzzio M, Li Q, Zhang P, Sun S. Pd nanoparticles coupled to WO_{2.72} nanorods for enhanced electrochemical oxidation of formic acid. *Nano Letters*. 2017;17(4): 2727 2731.
- 12. Shang Y, Cui Y, Shi R, Yang P, Wang J, Wang Y. Regenerated WO_{2.72} nanowires with superb fast and selective adsorption for cationic dye: Kinetics, isotherm, thermodynamics, mechanism. *Journal of Hazardous Materials*. 2019;379: 120834.

- 13. Kahattha C, Noonuruk R, Pecharapa W. Effect of titanium dopant on physical and optical properties of WO₃ thin films prepared by sol-gel method. *Suranaree Journal of Science & Technology*. 2019;26(1): 37–43. 14. Al-Kuhaili MF, Drmosh QA. Investigating the structural and optoelectronic properties of co-sputtered Fe-doped WO₃ thin films and their suitability for photocatalytic applications. *Materials Chemistry and Physics*. 2022;281:125897. 15. Mak AK, Tuna Ö, Sezgin N, Üstün AM, Yılmaz Ş, Öztürk O, Karabulut M. Effect of Al do on the electrochromic properties of WO₃ thin films. *Thin Solid Films*. 2022;751: 139241.
- 16. Morankar PJ, Amate RU, Teli AM, Beknalkar SA, Chavan GT, Ahir NA, Jeon CW. Nanogranular advancements in molybdenum-doped tungsten oxide for superior electrochromic energy storage. *Journal of Energy Storage*. 2024;84: 110978. 17. Haroon A, Anwar K, Ahmed AS. Visible light-driven photo remediation of hazardous cationic dye via Cedoped WO₃ nanostructures. *Journal of Rare Earths*. 2024;42(5): 869−878.
- 18. Shaheen N, Warsi MF, Zulfiqar S, Althakafy JT, Alanazi AK, Din MI, Abo-Dief HM, Shahid M. La-doped WO₃AgCN Nanocomposite for Efficient degradation of cationic dyes. *Ceramics International*. 2023;49(10): 15507–15526.
- 19. Chalotra S, Kaur P, Kaur S, Kandasami A, Kaur P, Singh DP. Influence of implantation assisted Ni do on structural and optical properties of WO_{2.72} films. *Optical Materials*. 2023;136: 113479.
- 20. Wang JC, Shi W, Sun XQ, Wu FY, Li Y, Hou Y. Enhanced photo-assisted acetone gas sensor and efficient photocatalytic degradation using Fe-doped hexagonal and monoclinic WO₃ Phase–Junction. *Nanomaterials*. 2020;10(2): 398.
- 21. Habieb H, Hamdadou N. Preparation and characterization of undoped and antimony doped tin oxide thin films synthesized by spray pyrolysis. *Materials Physics and Mechanics*. 2022;48(3): 367–378.
- 22. John J, Pillai. S S, Philip R, Pillai VM. Effect of Fe doping on the structural, morphological, optical, magnetic and dielectric properties of BaSnO₃. *Journal of Materials Science: Materials in Electronics*. 2021;32: 11763–11780.
- 23. Bootchanont A, Phacheerak K, Fongkaew I, Limpijumnong S, Sailuam W. The pressure effect on the structural, elastic, and mechanical properties of orthorhombic MgSiN₂ from first-principles calculations. *Solid State Communications*. 2021;336: 114318.
- 24. Osiac M, Cioatera N, Jigau M. Structural, morphological, and optical properties of iron doped WO₃ Thin film prepared by pulsed laser deposition. *Coatings*. 2020;10(4): 412.
- 25. Reddy GV A, Naveen Kumar K, Sattar SA, Shetty HD, Guru Prakash N, Imran Jafri R, Devaraja C, Manjunatha BC, Kaliprasad CS, Premkumar R, Ansar S. Effect of post annealing on DC magnetron sputtered tungsten oxide (WO₃) thin films for smart window applications. *Physica B Condensed Matter*. 2023;664: 414996.
- 26. Taha TA, Ahmed EM, El-Tantawy AI, Azab AA. Investigation of the iron do on the structural, optical, and magnetic properties of Fe-doped ZnO nanoparticles synthesized by sol-gel method. *Journal of Materials Science: Materials in Electronics*. 2022;33(9): 6368–6379.
- 27. Gao H, Zhu L, Peng X, Zhou X, Qiu M. Fe-doped WO₃ nanoplates with excellent bifunctional performances: Gas sensing and visible light photocatalytic degradation. *Applied Surface Science*. 2022;592: 153310.
- 28. Kalanur SS. Structural, optical, band edge and enhanced photoelectrochemical water splitting properties of tin-doped WO₃. *Catalysts*. 2019;9(5): 456.
- 29. Betkar MM, Bagde GD. Structural and optical properties of spray deposited CdSe thin films. *Materials Physics and Mechanics*. 2012;14(1): 74–77.
- 30. İloğlu O, Yurtsever HA. The effects of annealing temperature on the thickness, morphology, band gap energy, and photocatalytic performance of ZIF-8-derived ZnO/TiO₂ thin films. *Journal of Materials Science: Materials in Electronics*. 2024;35(18): 1211.
- 31. Thirumoorthi G, Gnanavel B, Kalaivani M, Ragunathan A, Venkatesan H. Suitability of iron (Fe)-doped tungsten oxide (WO₃) nanomaterials for photocatalytic and antibacterial applications. *International Journal of Nanoscience*. 2021;20(05): 2150042.

About Authors

Elaid Ouadah 🗓

PhD, Researcher (Ecole Nationale Polytechnique d'Oran, Oran, Algérie)

Nasr Eddine Hamdadou (DSC)

PhD, Professor (Ecole Nationale Polytechnique d'Oran, Oran, Algérie)

Submitted: March 14, 2024 Revised: May 6, 2024 Accepted: May 28, 2024

Fiberglass thermal barrier for building safety

S.V. Fedosov ¹, A.A. Lazarev ², A.N. Maltsev ², M.V. Toropova ³, I.A. Bogdanov ²

- ¹ National Research Moscow State University of Civil Engineering, Moscow, Russia
- ² Ivanovo Fire and Rescue Academy, Ivanovo, Russia
- ³ Ivanovo State Polytechnic University, Ivanovo, Russia
- [™] malec-37@mail.ru

ABSTRACT

The state of the issue of fire protection from landscape fires is studied and discussed. We set tasks to evaluate the recovered samples of two rolled fiberglass systems by modifying them in various ways: "fiberglass + refractory foam" and "fiberglass + aluminum foil". The first method involves applying a single layer of refractory foam Penosil Premium to the exposed surface of the samples. The second method is to modify the exposed surface by wrapping a layer of aluminum foil. The possibility of resisting an impacting landscape fire with a certain heat flux density was studied. We described the methods of conducting bench tests of a difficult-to-burn material under the influence of a constant heat flow, determine the temperature change of fiberglass from the heating time of the samples, the loss of their mass, determine the reliability of the empirically obtained data. A method for restoring a protective barrier made of fiberglass after damage by a landscape fire is proposed. At the same time, the temperature of the back side of the samples recovered using aluminum foil is reduced by half in relation to samples with refractory foam on the surface and is 173.2 °C (with the application of a single layer of foam 337.1 °C).

KEYWORDS

landscape fire • protective barrier • weakly combustible fiberglass • bench tests

Citation: Fedosov SV, Lazarev AA, Maltsev AN, Toropova MV, Bogdanov IA. Fiberglass thermal barrier for building safety. *Materials Physics and Mechanics*. 2024;52(4): 152–162. http://dx.doi.org/10.18149/MPM.5242024_13

Introduction

Fires at buildings and structures protection facilities can occur when dry grassy and other vegetation ignites. They lead to serious environmental consequences and the failure of expensive equipment [1-7]. Fire is presented as a complex physical and chemical process. At the same time, intense heat generation occurs. This is followed by catastrophic consequences for humans and the environment. The analysis of fire statistics in Russia for 2019 - 2022 is carried out [8]. The data are presented in Table 1.

In Table 1, in the period from 2019 to 2022, there is a tendency to reduce the number of fires in almost every type of facility. Over the past two years, the number of fires in open areas and in residential buildings and adjacent buildings has increased by 8000 cases. Their combined number exceeds 60 % of the total number of fires. The need for measures to ensure the protection of buildings is urgent.

To study this problem in more depth, some available research results are analyzed. In order to increase the limits of fire resistance of equipment, a method for reducing the impact of heat and convective flows on an object is proposed by Fisher R. et al. [9]. This method is based on fencing the protected object with a fire-retardant screen. A coolant

medium is created in the structure of the porous materials of this screen. The process of transferring combustion products during fires over a large area is considered in [10]. Fires in open areas are characterized by a high rate of combustion propagation, where aerodynamics play a major role. Currently, the construction of buildings made of wood is widely popular [11,12]. Prusakov V. et al. [13] paid attention to the issues of studying the fire resistance of structures with a fire-resistant coating based on ultrathin basalt fiber for fire-resistant sealing of joints of reinforced concrete structures [13–21].

Table 1. Fires in Russia at certain facilities in 2019-2022

The chiest of the fire	Nui	mber of fires,	3.6 1.1 1.5 0.	ts.
The object of the fire	2019	2020	2021	2022
Industrial buildings	3.5	3.4	3.6	1.9
Warehouse buildings, structures	1.6	1.5	1.5	0.8
Buildings, structures and premises of trade enterprises	2.8	2.6	2.7	2.4
Educational buildings	0.3	0.3	0.3	0.3
The building of Public Health and Social Services	0.3	0.3	0.3	0.3
Buildings, public service facilities	1.2	1.1	1.2	1.3
Administrative buildings	0.9	0.9	0.8	1.0
Buildings, structures and premises for cultural and leisure activities of the population and religious rituals	0.4	0.3	0.3	0.3
Buildings for temporary stay (residence) of people	0.4	0.3	0.3	0.3
Residential buildings and outbuildings (including an apartment building)	115.4	114.3	114.4	110.7
Buildings and structures for agricultural purposes	0.7	0.7	0.7	0.6
Industrial structures and installations	0.9	0.9	0.9	1.2
Building (structures) under construction (under reconstruction)	17.9	17.1	17.2	15.1
Unused building (structure)	1.7	1.5	1.2	1.2
A place of open storage of substances, materials, agricultural land and other open areas (including garbage), including dry grass (hay, reeds, etc.).	116.0	146.3	122.5	118.9

In [22], it was proposed to isolate the object of protection from the external environment by creating a mesh screen above its surface. A thermal insulation layer is formed on the outside of the screen over its entire area. This method is effective only in case of fire. The "dome" created in this way is local in nature and is carried out using a mobile robot. The engineering and technical solution of the proposed method is very complex in its execution and implies significant material resources for implementation.

The solution described in Fig. 1 is partially similar to [22]. A distinctive feature is the ability of the device to transform into separate modules and into a single fire barrier for installation directly next to the protected object or through its possible environment. This solution is aimed at ensuring the safety of building equipment from the effects of landscape fires at the stages of fire prevention, localization and elimination. When a

landscape fire is exposed to fiberglass at high temperature, the amount of the protective layer of plastic on the surface of the protective cloth decreases. During the operation of damaged fiberglass, its destruction may occur due to negative environmental influences. The damaged surface must be repaired. A comparative analysis of the two methods of such activity allows us to determine the most acceptable option.

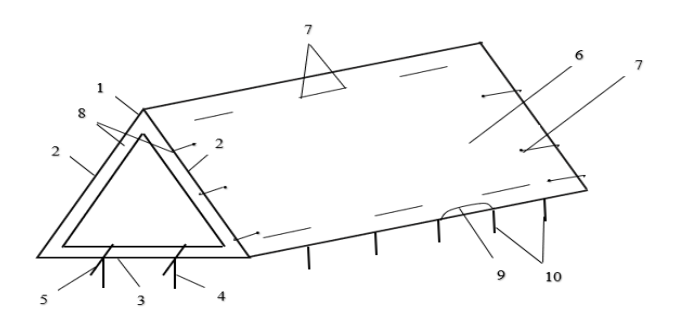


Fig. 1. Device for preventing the spread of landscape fire: 1 – support frame, 2 – sides of the support frame, 3 – base of the support frame, 4 –hooks in the soil, 5 - horizontal supports in the form of plates, 6 – fire–resistant cloth, 7 - fastening elements of the cloth, 8 – connecting devices, 9 – steel cables, 10 – additional hooks in the soil [23,24]

The object of the study is damaged refractory fiberglass and the method of its restoration. The first method involves applying a single layer of refractory foam Penosil Premium to the exposed surface of the samples. The second method is to modify the exposed surface by wrapping a layer of aluminum foil.

The subject of the study is the temperature dynamics of the back side of the studied samples of reconstituted fiberglass, depending on the values of the heat flux density.

The purpose of the work is to study the changes in the basic parameters of fiberglass over time under thermal influence. To achieve the goal of the work, it is necessary to solve a number of tasks:

- 1. to conduct a search for patent and scientific research;
- 2. to propose a methodology for conducting bench tests of samples of damaged refractory fiberglass separately in the first and second ways;
- 3. to determine the pattern of temperature changes on the back of the test samples over time of exposure to the exposed surface of different densities of heat fluxes;
- 4. obtain equations to describe the dynamics of the process under study and determine the reliability of the data based on the results of the study;
- 5. to establish the dependence of the heating time on the loss of mass and temperature changes on the back of the fiberglass using the Statistica software package.

Research methods

To determine the effect of heat flow on fiberglass in its various modifications, a number of bench tests were carried out using a standardized technique, the scope of which is reduced to testing building materials for flammability [25]. For this purpose, samples of weakly combustible fiberglass with a square shape with sides of 16.5×16.5 mm were made. The thickness of all test samples is not more than 0.18 mm. 100 g of fiberglass

contains: fiberglass (the basis of the material) -34 g with the addition of chemical compounds (glycerin -15 g, titanium dioxide -13.6 g, kaolin -19.4 g, epoxy resin -18 g). Tests of each sample were carried out for 10 minutes using an installation for determining the flammability of building structures (Fig. 2).

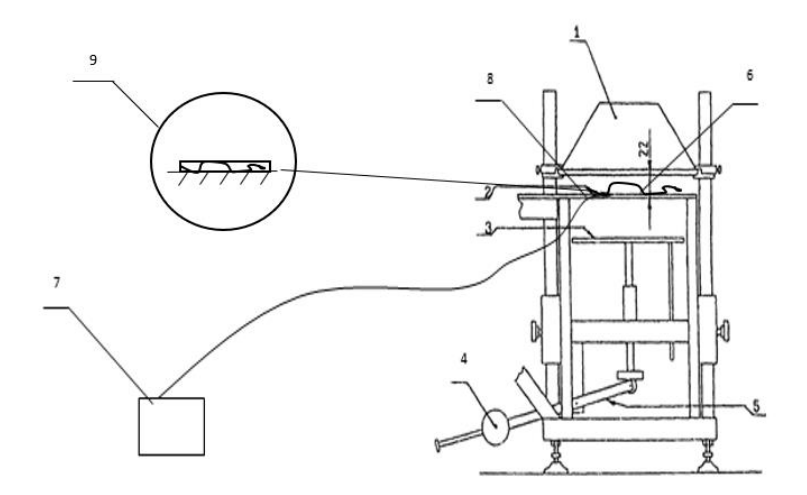


Fig. 2. Installation for determining the temperature of the back of the sample: 1 – radiation panel, 2 – protective plate, 3 – movable platform for the sample, 4 – counterweight, 5 – lever, 6 – test sample, 7 – microprocessor–controlled two-channel regulator 2 TRM 1, 8 – thermocouple, 9 – fiberglass

The studies of the recovered fiberglass were carried out under the same conditions. The heat flow exposure power for the test unit is 39 kW/m². The indoor air temperature is 27.1 °C. To comply with the conditions of the first method, a layer of refractory foam was applied using a metal spatula to the exposed surface. The thickness of the layer was 1.5 mm each. The test sample is shown in Fig. 3(a). According to the second method, the samples were recovered using aluminum foil with a layer thickness of no more than 0.2 mm. A sample for this condition is shown in Fig. 3(b) [24–32].



Fig. 3. Samples of reconstituted weakly combustible fiberglass: (a) the first method; (b) the second method

Three samples were selected for each of the methods for testing. The temperature of the back side of the samples was measured using thermocouples. The determination of this parameter is necessary to prevent the spread of a landscape fire through an obstacle after it is heated to the ignition temperature of dry vegetation. The test facility is calibrated before the start of the research.

Table 2 shows the results of bench tests of refractory fiberglass in the "fiberglass + refractory foam" system. Table 3 shows the results of bench tests of refractory fiberglass in the "fiberglass + aluminum foil" system.

Table 2. Bench tests in the "fiberglass + refractory foam" system

		Fiberglass sample 1		Fiberglass sample 2		Fiberglass sample 3	
Experiment number	Time, min	Temperature of the back of the sample, °C	Sample mass loss Δm, g	Temperature of the back of the sample, °C	Sample mass loss Am, g	Temperature of the back of the sample, °C	Sample mass loss Δm, g
1	1	316.1	2.53	317.2	2.56	315.4	2.54
2	2	337.1	5.15	333.5	5.15	334.6	5.14
3	3	331.0	8.15	330.2	8.14	329.9	8.02
4	4	323.2	11.14	326,1	11.17	327.1	11.01
5	5	321.9	15.05	324.1	15.1	323.3	14.9
6	6	326.1	18.59	324.3	18.58	325.4	18.42
7	7	322.1	21.12	321.8	20.92	323.6	20.99
8	8	319.3	23.54	317.7	23.3	318.2	23.38
9	9	324.0	24.78	322.1	24.49	323.7	24.59
10	10	321.7	25.96	320.2	25.63	321.5	25.76

Table 3. Bench tests in the "fiberglass + aluminum foil" system

Table 5. Benen	CCSCS III (The moengiass i a	tallillalli i	July 3 y 3 t C 1 1 1			
Evporiment	T:	Fiberglass sample 1		Fiberglass sample 2		Fiberglass sample 3	
Experiment number	Time, min	Temperature	Sample	Temperature	Sample	Temperature	Sample
Hamber		of the back of	mass loss	of the back of	mass loss	of the back of	mass loss
		the sample, °C	∆m, g	the sample, °C	∆m, g	the sample, °C	∆m, g
1	1	139.5	0.14	138.4	0.13	137.8	0.12
2	2	163.2	0.29	161.7	0.29	164.5	0.28
3	3	168.4	0.46	166.2	0.43	166.1	0.44
4	4	171.2	0.63	170.8	0.59	173.2	0.63
5	5	171.5	0.83	171.2	0.76	172.7	0.83
6	6	166.8	1.02	164.7	0.95	163.8	1.02
7	7	167.6	1.14	165.1	1.13	168.2	1.2
8	8	166.5	1.25	165.5	1.27	166.1	1.39
9	9	163.1	1.37	162.8	1.42	164.3	1.56
10	10	164.3	1.53	161.8	1.56	160.7	1.71

Results and Discussion

Figure 4 shows photographs of fiberglass samples in various modifications after the end of high-temperature exposure during bench tests. Figure 4 shows the fiberglass recovered by the first and the second methods after repeated high-temperature exposure.

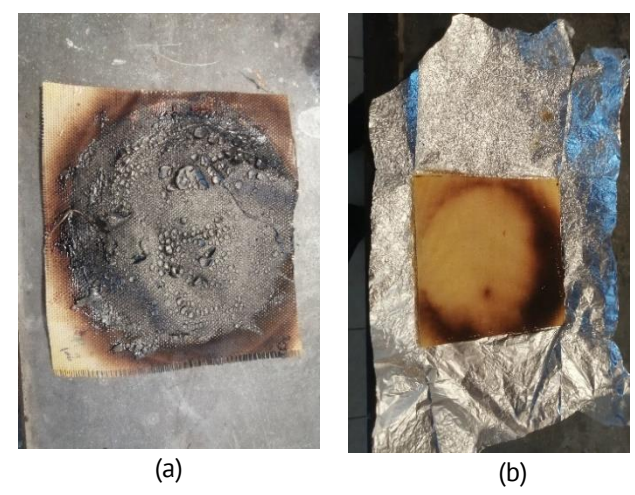


Fig. 4. Samples of recovered fiberglass after repeated high-temperature exposure: (a) recovered by the first method; (b) recovered by the second method

The results of measuring the temperature of the back side of the fiberglass samples recovered by the first method are shown in Fig. 5. After the experimental data were approximated, the coefficient of determination ($R^2 \le 1$) was calculated.

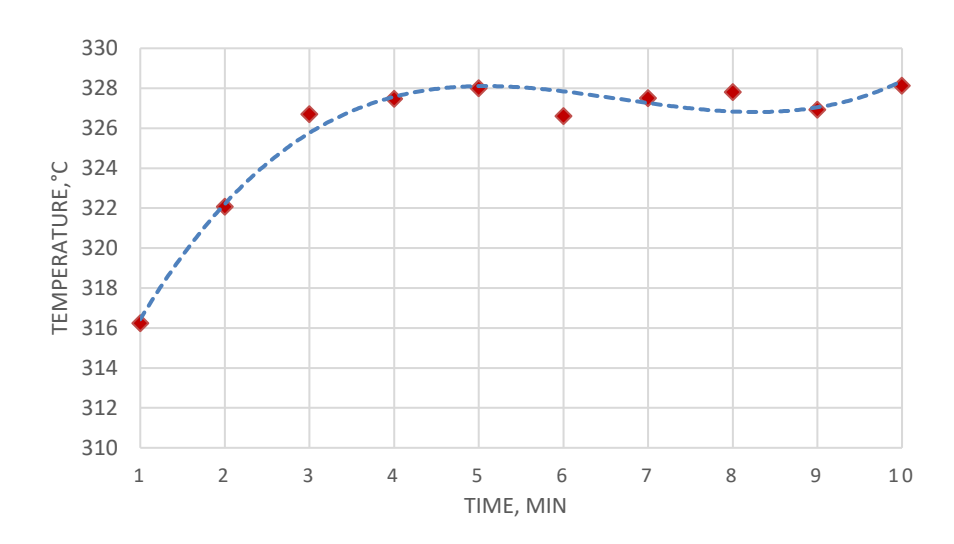


Fig. 5. Dependence of the temperature of the back side of the fiberglass of the samples recovered by the first method on the heating time

To describe the dependence of the temperature change of the back side of fiberglass and the mass loss of the samples recovered by the first method on the heating time, static data processing was performed in Fig. 5 and 6. The data obtained from the results of the experiment were processed using the Statistica software package.

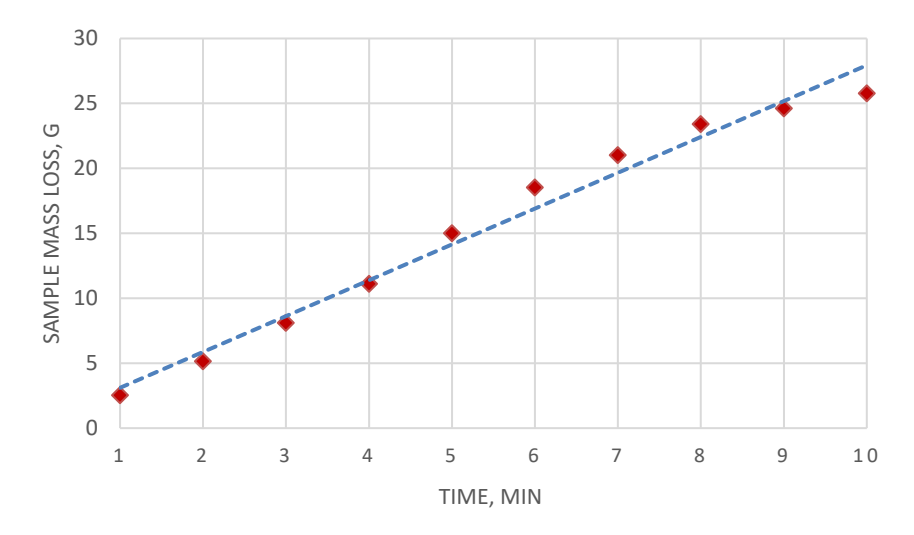


Fig. 6. Dependence of the mass loss of the samples recovered by the first method on the heating time

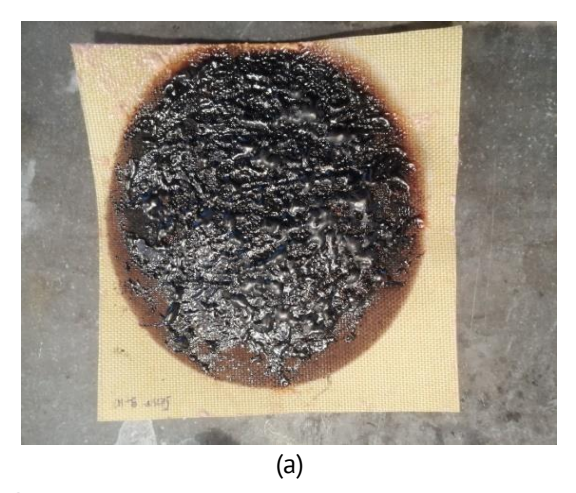
Based on the results of processing the empirically obtained data, the equations are compiled:

$$T_1(\tau) = 0.079 \,\tau^3 - 1.590 \,\tau^2 + 9.994 \,\tau + 307.95,$$
 (1)

where $T_1(\tau)$ is the temperature of the back side of the fiberglass sample recovered by the second method, °C, g, at 0 min $\leq \tau \leq 10$ min, τ is the time of exposure to heat flow on this sample, min. For the dependence of temperature on the time of high-temperature exposure in Fig. 5, the coefficient of determination $R^2 = 0.972$. The approximation error of Eq. (1) is no more than 3 %.

$$m_1(\tau) = 2.759 \ \tau + 0.350,$$
 (2)

where $m_1(\tau)$ is the mass loss of the fiberglass sample recovered by the second method, g, at 0 min $\leq \tau \leq 10$ min, τ is the time of exposure to the heat flux on this sample, min. For the dependence of the mass loss of the sample on the time of high-temperature exposure, the coefficient of determination $R^2 = 0.979$ is shown in Fig. 6. The approximation error of Eq. (2) is no more than 3 %.



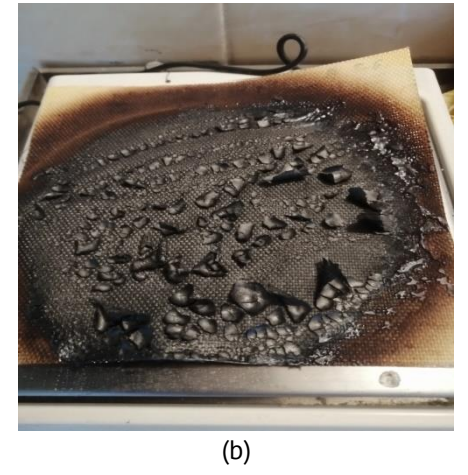


Fig. 7. Samples of reconstituted fiberglass after high-temperature exposure, which lost the greatest mass at the end of high-temperature exposure

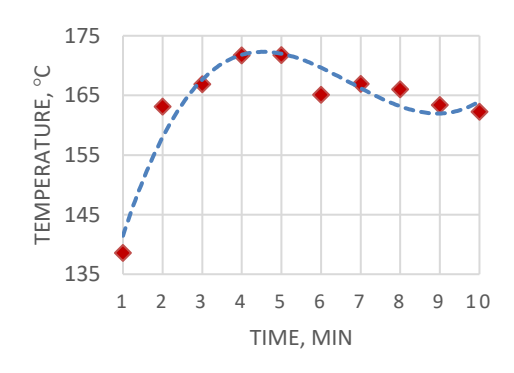
Figure 7 shows photographs of fiberglass samples recovered by the first method. The restoration was carried out using refractory foam. The samples lost the greatest mass at the end of high-temperature exposure during bench tests. Figure 6(a) shows a fiberglass sample 1 recovered with refractory foam after high-temperature exposure. The maximum mass loss of this sample was 3.91 g. At the same time, the temperature of the back side was 321.9 ° C. Figure 6(b) shows a recovered fiberglass sample 2 after high-temperature exposure. The mass loss was 3.93 g. The temperature of the thermocouples was 324.1 °C.

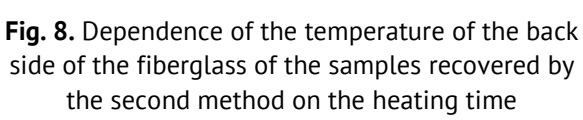
A tensile (rupture) test of fiberglass was performed on the R-5 bursting machine before and after exposure to a radiant heat flux on the sample. The studied fiberglass has almost identical characteristics before and after high-temperature exposure. This indicates its ability to resist high temperatures.

Fiberglass has the following characteristics: the dielectric constant is 1.8-4.6, the tangent of the dielectric loss angle is 0.004-0.0214, the tensile strength at high temperature exposure along and across the fibers are 10.8 and 5.8 MPa, respectively, the tensile strength after high temperature exposure are 10.5 MPa (along the fibers) and 5.2 MPa (across the fibers).

Next, the samples recovered by the second method were examined. The temperature was measured from the back of the samples. The data are shown in Figs. 8 and 9. Data processing was carried out, the coefficient of determination was calculated.

To describe the dependence of the temperature change of the back side of fiberglass and the mass loss of the samples recovered by the second method on the heating time, static data processing was carried out in Figs. 8 and 9.. The data obtained from the results of the experiment were processed using the Statistica software package. A slight decrease in temperature after 5 min in Figs. 6 and 8 is due to the parameters of the installation (Fig. 2). This is due to the operation of the regulator and the need to maintain the set values of the thermal effect.





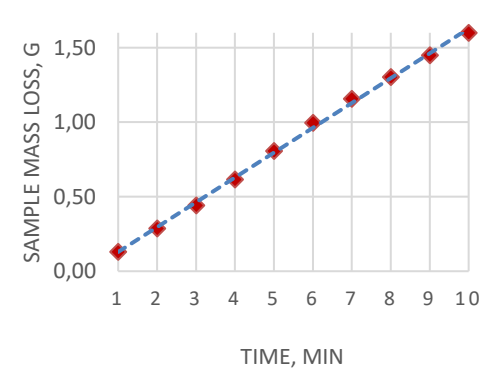


Fig. 9. Dependence of the mass loss of the samples recovered by the second method on the heating time

Based on the results of processing the empirically obtained data, the equations are prepared:

$$T_2(\tau) = 0.243 \ \tau^3 - 4.911 \ \tau^2 + 29.571 \ \tau + 116.55,$$
 (3)

where $T_2(\tau)$ is the temperature of the back side of the fiberglass sample recovered by the second method, °C, g, at 0 min $\leq \tau \leq$ 10 min, τ is the time of exposure to heat flow on this sample, min. For the dependence of temperature on the time of high-temperature exposure in Fig. 8, the coefficient of determination $R^2 = 0.912$. The approximation error of Eq. (3) is no more than 9 %.

$$m_2(\tau) = 0.167 \ \tau - 0.037,$$
 (4)

where $m_2(\tau)$ is the mass loss of the fiberglass sample recovered by the second method, g, at 0 min $\leq \tau \leq$ 10 min, τ is the time of exposure to the heat flux on this sample, min. For the dependence of the mass loss of the sample on the time of high-temperature exposure in Fig. 9, the coefficient of determination R^2 = 0.993. The approximation error of Eq. (2) is no more than 1 %.

After comparing the results of the study and their comparative analysis for fiberglass samples recovered by two methods, it should be noted the advantages of the second method over the first. According to the results of bench tests, the layer of refractory foam is significantly destroyed within 10 minutes. This leads to a loss of mass of the sample. The restoration of samples using aluminum foil is a fairly effective tool. This application significantly reduces the temperature on the back of the sample by half. This method makes it possible to increase the fire protection of buildings from landscape fires in case of fire of dry grass and shrubs [11-17].

Conclusion

The fiberglass protective barrier requires restoration after damage by a landscape fire. An experiment was carried out to establish the regularity of the effect of heat flux density on fiberglass recovered in various ways. The results of this experiment allowed us to draw the following conclusions:

- 1. a search for patent and scientific research has been conducted;
- 2. a method for conducting bench tests of fiberglass samples restored after damage by a landscape fire is proposed;
- 3. the dependence of the temperature change of the back side of fiberglass and the mass loss for the recovered in each of the two methods is determined;
- 4. equations (1)–(4) are obtained to establish with a certain degree of reliability the parameters for the use of fiberglass in fire barriers in order to protect against landscape fires; 5. the advantage of the second method of recovering fiberglass samples over the first method has been established. As a result of high-temperature heating for 10 min, the layers of refractory foam are significantly destroyed. This leads to a loss of mass of the sample. The restoration of samples using aluminum foil is a fairly effective tool.

References

- 1. Fedosov S, Nikolay V, Lazarev A, Malichenko V, Toropova M. The fire-resistant construction for building safety. In: In: Anatolijs B, Nikolai V, Vitalii S. (eds.) *Proceedings of EECE 2019. EECE 2019. Lecture Notes in Civil Engineering, vol 70.* Cham: Springer; 2020. p.319–327.
- 2. Fedosov S, Lazarev A. The Use of Markov Chain Theory for the Organization of Fire Safety Control during Construction. *AIP Conf. Proc.* 2023;2936(1): 050010.
- 3. Takahashi F. Whole House Fire Blanket Protection From Wild Land Urban interface Fires. *Frontiers in Mechanical Engineering*. 2019;5: 60.

- 4. Lein J, Stump N. Assessing wildfire potential within the wildland urban interface: A southeastern Ohio example. *Applied Geography*. 2009;29(1): 21-34.
- 5. Cohen J. Wildland urban fire a different approach. In: *Conf. Proceedings of the Firefigther Safety Summit. Missoula, MT.* 2001. p.32-54.
- 6. Caballero D, Beltran I, Velasco A. Forest Fires and Wildland Urban interface in Spain: Types and Risk Distribution. In: *IV International Wildland Fire Conference*. Seville: Spain; 2007. p.1-14.
- 7. Mutsh R, Rogers M, Scott St, Gill A. Protecting Lives and Property in Wildland Urban interface: Communities in Montana and Southern California Adopt Australian Paradigm. *Fire Technology*. 2011;47: 357–377.
- 8. Goncharenko V, Chechetina T, Sibirko V, Nadtochiy O, Polekhin P, Kozlov A, Gribanov A. *Information and analytical collection Statistics of fires and their consequences*. Balashikha: Fires and fire safety; 2023. (In Russian)
- 9. Fisher R, Lewis B, Price O, Pickford A. Barriers to fire spread in Australian tropical savannas, deriving fire edge metrics from long term high frequency fire histories. *Journal of Environmental Management*. 2022;301: 113864.
- 10. Gostintsev YuA, Kopylov NP, Khasanov IR. Aerodynamics and Combustion Products Transfer by Large Area Fires. In: *Combustion, Detonation, Shock Waves: Proceeding of the Zel'dovich Memorial, Int. Conf. on Combustion.* Moscow; 1994. p.252-254. (In Russian)
- 11. Arlet J. Innovative Carpentry and Hybrid Joints in Contemporary Wooden Architecture. *Arts.* 2021;10(3): 64. 12. Li H, Wang L, Wei, Y, Wang, B, Jin H. Bending and Shear Performance of Cross-Laminated Timber and Glued-Laminated Timber Beams: A Comparative Investigation. *Journal of Building Engineering*. 2022;45: 103477.
- 13. Prusakov V, Gravit M, Simonenko Ya. Superthin Basalt Fiber as the Base of a Matrix of the Fire-Resistant Filling of Deformation Joints in Building Structures. *Glass Physics and Chemistry*. 2023;49(1): 75–80.
- 14. Ohashi H, Igarashi S. and Nagaoka T. Development of Wood Structural Elements for Fire Resistant Buildings. *Journal of Structural Fire Engineering*. 2018;9(2): 126–137.
- 15. Malo K, Abrahamsen R, Bjertnæs M. Some Structural Design Issues of the 14-Storey Timber Framed Building "Treet" in Norway. *European Journal of Wood and Wood Products*. 2016;74: 407–424.
- 16. Gravit M, Serdjuks D, Vatin N, Lazarev Y, Yuminova M. Single burning item test for timber with fire protection. *Magazine of Civil Engineering*. 2020;95(3): 19–30.
- 17. Technical Regulations on Fire Safety Requirements: Federal Law of the Russian Federation No. 123-FZ Dated July 22, 2008 (as Amended by Federal Law No. 538-FZ of December 27, 2018).
- 18. Gravit M, Nedryshkin O, Ogidan O. Transformable fire barriers in buildings and structures. *Magazine of Civil Engineering*. 2018;1: 38–46.
- 19. Gravit M, Dmitriev I. Numerical modeling of basalt roll fire-protection for light steel thin-walled structures. *Magazine of Civil Engineering*. 2022;4(112): 11215.
- 20. Gravit M, Shabunina D, Nedryshkin O. The Fire Resistance of Transformable Barriers: Influence of the Large-Scale Factor. *Fire*. 2023;6: 294.
- 21. Prusakov V, Gravit M, Timofeev N, Simonenko Ya, Gutorov K, Shevchenko AM, K.S. Fire retardant coating for expansion and linear joints in buildings. *Pozharovzryvobezopasnost.* 2018;27(2–3): 45–56. (In Russian)
- 22. Lee D, Ramsey M. *Fire protection system for Runaway Grass and Forest Fires and method for Use*. US2020147423 A1 (Patent), 2020.
- 23. Maly I, Sharabanova I, Maltsev A, Lazarev A, Samoilov D. *A device for preventing the spread of a landscape fire*. RU219622 U1 (Patent), 2023.
- 24. Maly I, Sharabanova I, Maltsev A, Lazarev A, Ivanov V. *A device for preventing the spread of a landscape fire*. RU 221505 U1 (Patent), 2023.
- 25. The interstate standard 30402 96. Building materials. ignitability test method. (In Russian).
- 26. Kesawan S, Mahendran M. A review of parameters influencing the fire performance of light gauge steel frame walls. *Fire Technology*. 2018;54(1): 3-35.
- 27. Pereira D, Viegas C, Panão M. Heat transfer model of fire protection fiberglass thermal barrier coated with thin aluminium layer. *International Journal of Heat and Mass Transfer*. 2022;184: 122301.
- 28. Viegas C, Batista R, Albino A, Coelho M, Andrade J, Alves D, Viegas D. Active barrier combining fire-resistant fiberglass fabric and water sprinkler system for protection against forest fires. *Fire Technol.* 2021;57: 189-206.
- 29. Tao Y, Mahendran M. Fire tests and thermal analyses of LSF walls insulated with silica aerogel fibreglass blanket. *Fire Safety Journal*. 2021;122.
- 30. Ariyanayagam A, Mahendran M. Influence of cavity insulation on the fire resistance of lidght gauge steel framed walls. *Construction and Building Materials*. 2019;203: 687-710.

- 31. Gunalan S, Kolarkar P, Mahendran M. Experimental study of load bearing cold-formed steel wall systems under fire conditions. *Thin-Walled Structures*. 2013;65: 72-92.
- 32. Fedosov S, Lazarev A, Tsvetkov D. On the Problem of Studying the Diffusion of Flame Retardants in Wood. *AIP Conf. Proc.* 2023;2936(1): 020005.

About Authors

Sergey V. Fedosov D Sc

Doctor of Technical Sciences Professor (National Research Moscow State University of Civil Engineering, Moscow, Russia)

Aleksandr A. Lazarev 📵 Sc

Candidate of Technical Sciences Head of the Department (Ivanovo Fire and Rescue Academy, Ivanovo, Russia)

Aleksey N. Maltsev 🗓

Adjunct (Ivanovo Fire and Rescue Academy, Ivanovo, Russia)

Maria V. Toropova D Sc

Candidate of Technical Sciences Associate Professor (Ivanovo State Polytechnic University, Ivanovo, Russia)

Iliya A. Bogdanov 🗓

Adjunct (Ivanovo Fire and Rescue Academy, Ivanovo, Russia)

Submitted: September 7, 2023 Revised: May 28, 2024 Accepted: July 11, 2024

Quasi-static thermal response of a circular plate due to the influence of memory-dependent derivatives

N.K. Lamba [⊠] 🗓

Shri Lemdeo Patil Mahavidyalaya, Mandhal, Nagpur, India

[™] navneetkumarlamba@gmail.com

ABSTRACT

In this paper, the thermal deformation response of a circular plate due to the influence of memory-dependent derivatives (MDD) is analyzed using a quasi-static approach. The top, bottom, and curved surfaces of the plate experience convective boundaries with heat flow on the outer curved radii, and additional cross-sectional heating is prescribed on the top and bottom plate surfaces. Integral transformation methods are used to solve the memory-dependent heat transfer model. Due to the complex nature of the analytical analyses, the Laplace transform is numerically inverted. The rate of change in temperature and thermal deflection is dependent on past changes, making it more suitable for studying physical problems. Numerical calculations of the obtained thermal results are performed for a copper plate and presented graphically.

KEYWORDS

memory-dependent derivatives • circular plate • temperature • thermal deflection • integral transform

Citation: Lamba NK. Quasi-static thermal response of a circular plate due to the influence of memory-dependent derivatives. *Materials Physics and Mechanics*. 2024;52(4): 163–172.

http://dx.doi.org/10.18149/MPM.5242024_14

Introduction

The fractional order theory of thermoelasticity is an integral part of fractional calculus, which falls well under the branch of mathematics. Fractional-order thermoelastic problems have been a hot topic for mathematicians and researchers in recent decades due to their practical application. The results of various investigations based on modelling fractional thermoelasticity have been successfully studied and illustrated by many renowned researchers [1–10].

Wang and Li [11] first proposed the concept of memory-dependent deductions in 2011, and compared to Caputo derivations, it proves to be more suitable for modelling problems based on memory. Since MDD may represent memory-dependent derivatives in a variety of physical processes, it has emerged as a new area of fractional calculus that is constantly growing. The fractional derivative (FD) mostly reflects local change, even though it is stated on an interval. Compared to FD, MDD's physical significance is noticeably more apparent. The kernel function reflects the memory-dependent weight, and the time delay shows how long the memory effect lasts. For temporal modeling, which is helpful in explaining the thermal effect of solid bodies, the memory-related derivative is more appropriate, according to the research that is currently available. In the domains of thermoelasticity, thermoelectricity, particle physics, vibration mechanics, etc., memory-dependent derivatives can serve as a helpful substitute for fractional derivatives. Karamany and Ezzat [12] developed a new generalized concept of thermoelasticity with

164 N.K. Lamba

the effect of time delay and applied it to the solution of one-dimensional half-spaces with free choice of kernel function. Memory-based differentiation was utilized by Purkait et al. [13] to investigate the issue in an infinite space. Sun and Wang [14] recreate the MDD heat transfer model and use first-order memory-dependent advance differentiation to analyze the one-dimensional heat transmission problem. The temporal thermal stress problem associated with a hollow cylinder with underlying surface cracking subjected to a temperature shock at its interior was resolved by Xue et al. [15]. Ma and Gao [16] investigated the dynamic response of a generalized thermoelastic problem in an infinite cylindrical body due to thermal shock and the memory effect.

Sur et al. [17] investigated the innovative mathematical framework for generalized thermoelasticity in the background of memory-related heat transfer. Karamany and Ezzat [18] developed fundamental equations for thermoelastic diffusion in various solids. Qi et al. [19] investigated nonclassical continuum mechanics in a micro/nano-scale system with a memory-based effect. From a mathematical perspective, Verma et al. [20] developed the hygrothermoelasticity theory with fractional order theory.

Othman and Mondal [21] introduced phase-lag models and calculated the displacement and stress functions for generalized thermoelasticity. Awwad et al. [22] studied the thermoelastic response with temperature-dependent properties for a cylindrical hole. Mondal [23] discussed transient phenomena in a rod considering a moving heat source with memory response in generalised thermoelasticity. Abouelregal et al. [24] successfully investigated MDD's response with time delay by constructing a new thermal model and studying its effect graphically. Using the Laplace transform, Abouelregal et al. [25] determined the solution for temperature, bending moment, and displacement for a thermomechanically rotating size-dependent nanobeam. A dynamically bar was the subject of an investigation into the memory phenomenon and discussion of thermo-mechanical performance by Abouelregal et al. [26]. To understand the memory phenomenon in solid objects under thermoelasticity, Lamba [27] recently studied the memory effects of an internal heat source by taking a cylindrical, thick shape under the impact of radiation boundaries. Also, some other renowned authors contributed their work to the field, as reflected in [28–36]. Lamba and Deshmukh [37] conducted a recent analytical and numerical study to examine the impact of time delay on the temperature, displacement, and thermal heat transfer stress histories in an infinitely long thermoelastic solid circular cylinder.

Compared to fractional-order derivatives, the concept of MDD proves to be superior and suitable for describing the memory effect. This inspired the author to create a mathematical model of a solid object to study the thermal effect.

In the present work, a two-dimensional boundary value problem of a circular plate with ranges $0 \le r \le b$; $-h \le z \le h$ is considered to investigate the thermal response due to the effects of MDD on the temperature and deflection distribution (the geometry of the problem is as shown in Fig. 1). The top, bottom and curved surfaces of the plate are subject to convective heat transfer with heat flux on the outer curved boundary, and additional cross-sectional heating is prescribed on the top and bottom plate surfaces. The integral transform method is used to solve the governing heat equation with memory-based derivative.

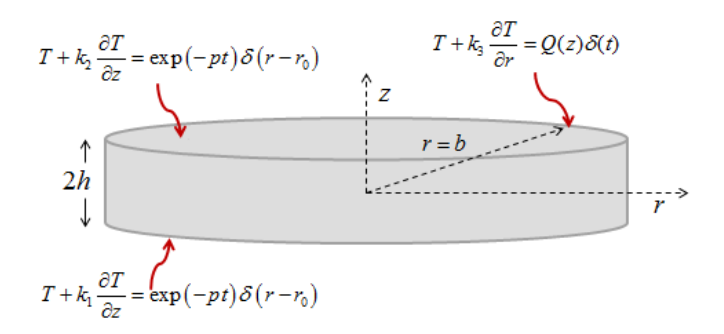


Fig. 1. Geometrical shape of the memory-based circular plate

Investigators working on the development and design of the novel structural material may find the present work to be helpful as it adds to the collection of knowledge in the subject of thermoelasticity.

Modelling of thermoelastic problem

Heat conduction with MDD

The new concept of memory-based Cattaneo and Vernotte (CV) modelling is developed by introducing first-order MDD as in [28]:

$$q + \tau D_{\omega} q = -k \nabla T. \tag{1}$$

If there is no heat inside the body, the equation of thermal equilibrium is expressed as [31]:

$$\nabla q = -\rho_m c_E \frac{\partial T}{\partial t} \tag{2}$$

where ρ_m and c_E are, respectively, mass density and specific heat capacity.

For an axially symmetric circular plate in cylindrical coordinates with influence of memory dependent derivative, the governing equation of heat conduction is obtained by transforming Eq. (1) into Eq. (2) as:

$$k\nabla^2 T = \rho_m c_E (1 + \tau D_\omega) \frac{\partial T}{\partial t}.$$
 (3)

A list of variables is shown below in without dimensions form for ease of use: $r' = \frac{r(t',\tau',\omega')}{r_0} = \frac{1}{\rho_m c_E r_0^2}(t,\tau,\omega), \quad z' = \frac{z(t',\tau',\omega')}{z_0} = \frac{1}{\rho_m c_E r_0^2}(t,\tau,\omega), \quad T' = \frac{T}{T_0}.$ Using the above dimensionless variables, Eq. (3) takes the following form (omitting the prime numbers for simplicity):

$$\nabla^2 T = (1 + \tau D_\omega) \frac{1}{k} \frac{\partial T}{\partial t},\tag{4}$$

where the function's memory dependent derivative is a weighted integral of its common integer-order derivative on an interval that slips, which is denoted by [11]:

$$D_{\omega}T(t) = \frac{1}{\omega} \int_{t-\omega}^{t} K(t-\xi) \frac{\partial T(\xi)}{\partial \xi} d\xi.$$
 (5)

For any function T(t) that is m times differentiable with respect to t, the memory-dependent derivative of order m of T(t) is:

$$D_{\omega}^{m}T(t) = \frac{\partial^{m-1}}{\partial t^{m-1}}D_{\omega}T(t) = \frac{1}{\omega}\int_{t-\omega}^{t}K(t-\xi)\frac{\partial^{m}T(\xi)}{\partial \xi^{m}}d\xi,$$
(6)

where the time delay ω and kernel function $K(t - \xi)$ are arbitrary choices made to reflect the actual behaviours of the materials.

166 N.K. Lamba

Kernel functions, in particularly, can be selected as:

$$K(t - \xi) = 1 - \frac{2l_2}{\omega}(t - \xi) + \frac{l_1^2}{\omega^2}(t - \xi)^2, \tag{7}$$

where l_1 and l_2 are constants.

The function of the kernel usually falls between 0 and 1. Also $\xi \in [t-\omega,t]$ and $|D_{\omega}T(r,z,t)| \leq \left|\frac{\partial T(r,z,t)}{\partial t}\right|$.

Quasi-static deflection based on thermal moment

The deflection function's differential formulation is given in [29].

$$\nabla^4 W = \frac{-\nabla^2 M_T}{\Omega(1-\nu')},\tag{8}$$

where M_T is the plate's thermal moment, which is stated as:

$$M_T = a_t E' \int_{-h}^{h} T(r, z, t) z \ dz, \tag{9}$$

where Ω is the disc's rigidity,

$$\Omega = E'h^3/12(1-v'^2),\tag{10}$$

where a_t , E' and v' represents the disc's material linear thermal expansion coefficient, the Young's modules, and Poisson's ratio, respectively.

For an annular disc's edge to be fixed and clamped, one must write:

$$W(b, z, t) = \frac{\partial W(b, z, t)}{\partial r} = 0, \tag{11}$$

$$W(t=0)=0. (12)$$

Boundary and initial constraints

The differential form of heat transfer Eq. (4) of a circular plate under the impact of MDD is subjected to the following constraints:

$$\left[T + k_3 \frac{\partial T}{\partial r}\right]_{(r=b)} = Q(z)\delta(t),\tag{13}$$

$$\left[T + k_1 \frac{\partial T}{\partial z}\right]_{(z=-h)} = \exp(-pt) \,\delta(r - r_0), \tag{14}$$

$$\left[T + k_2 \frac{\partial T}{\partial z}\right]_{(z=h)} = \exp(-pt) \,\delta(r - r_0),\tag{15}$$

$$T(r, z, t) = 0, t = 0,$$
 (16)

where, $exp(-pt) \, \delta(r-r_0)$ denotes the additional sectional heating applied at the bottom and top surfaces of plate and $Q(z)\delta(t)$ is the heat flux at outer radii. Also, k_1 and k_2 denotes the radiation constants on the plate plane surfaces and k_3 on the outer curved surface, respectively.

The problem under examination is mathematically formulated in Eq. (4) through Eq. (16).

Solution of the modeling

Evaluation of temperature function

To determine the integral of the heat transfer memory-related differential Eq. (4), first we write the formula of the finite Marchi-Fasulo transform and its inverting formula for any function F(r, z, t) as [30].

$$\overline{F}(r,\Lambda_n,t) = \int_{z=-h}^h F(r,z,t) L_n(z) dz, \tag{17}$$

$$F(r,z,t) = \sum_{n=1}^{\infty} \frac{\overline{F}(\Lambda_n)}{\lambda_n} L_n(z), \tag{18}$$

where

$$L_n(z) = M_n \cos(\Lambda_n z) - N_n \sin(\Lambda_n z),$$

$$M_n = \Lambda_n(\gamma_1 + \gamma_2)\cos(\Lambda_n h) + (\eta_1 - \eta_2)\sin(\Lambda_n h),$$

$$N_n = (\eta_1 + \eta_2)\cos(\Lambda_n h) + (\gamma_2 - \gamma_1)\Lambda_n\sin(\Lambda_n h),$$

$$\lambda_n = \int_{z=-h}^{h} L_n^2(z) dz = h \left[M_n^2 + N_n^2 \right] + \frac{\sin(2\Lambda_n h)}{2\Lambda_n} \left[M_n^2 - N_n^2 \right],$$

where the solutions to the equation below are satisfied by the Eigen values Λ_n .

$$[\eta_1 \sin(\Lambda h) + \gamma_1 \Lambda \cos(\Lambda h)] \times [\gamma_2 \Lambda \sin(\Lambda h) + \eta_2 \cos(\Lambda h)] =$$

$$= [-\eta_2 \sin(\Lambda h) + \gamma_2 \Lambda \cos(\Lambda h)] \times [-\gamma_1 \Lambda \sin(\Lambda h) + \eta_1 \cos(\Lambda h)], \tag{19}$$

where $\gamma_1, \gamma_2, \eta_1$ and η_2 are the constants.

On utilizing Eq. (17) to Eq. (4) using Eqs. (14) and (15), one obtains:

$$\frac{\partial^2 \bar{T}}{\partial r^2} + \frac{1}{r} \frac{\partial \bar{T}}{\partial r} - \Lambda_n^2 \bar{T} + \left[\frac{L_n(h)}{k_2} - \frac{L_n(-h)}{k_1} \right] exp(-pt) \, \delta(r - r_0) = (1 + \tau D_\omega) \frac{1}{k} \frac{\partial \bar{T}}{\partial t}, \tag{20}$$

where \bar{T} represents the integral transform of T.

With transformed boundaries as:

$$\left[\bar{T}(r=b) + k_3 \frac{\partial \bar{T}(r=b)}{\partial r}\right] = \overline{Q}(\Lambda_n)\delta(t), \ t > 0, \tag{21}$$

$$\bar{T}(r, \Lambda_n, t) = 0, t = 0, \tag{22}$$

here $\overline{Q}(\Lambda_n) = \int_{z=-h}^h Q(z) L_n(z) dz$.

Secondly, we state the finite Hankel transform formula and its inversion for \bar{F} which satisfies convective boundary conditions [31]:

$$\hat{\bar{F}}(\mu_m, n, t) = \int_0^b r \bar{F}(r, n, t) K_0(\mu_m, r) dr,$$
(23)

$$\bar{F}(r,n,t) = \sum_{m=1}^{\infty} \hat{\bar{F}}(\mu_m, n, t) K_0(\mu_m, r), \tag{24}$$

where $K_0(\mu_m, r) = \frac{\sqrt{2}}{b} \frac{\mu_m k_3}{[1 + k_3^2 \mu_m^2]^{\frac{1}{2}}} \frac{J_0(\mu_m, r)}{J_0(\mu_m, b)}$, here μ_m denotes the root of the below equation:

$$k_3\mu J_0(\mu,b) + J_0(\mu,b) = 0,$$
 (25)

where \hat{T} represents \bar{T} 's Hankel transform.

Now, applying the integral method of transformation defined above in Eq. (23) to Eq. (20) with transformed boundary conditions (21), one obtains:

$$-(\mu_m^2 + \Lambda_n^2)\hat{\bar{T}} + \frac{bK_0(\mu_m, b)}{k_3}\delta(t)\overline{Q}(\Lambda_n) + \left[\frac{L_n(h)}{k_2} - \frac{L_n(-h)}{k_1}\right] exp(-pt) r_0 f_0(\mu_m, r_0) = (1 + \tau D_\omega) \frac{1}{k} \frac{\partial \hat{\bar{T}}}{\partial t}.$$
 (26)

and transformed initial condition:

$$\hat{T}(\mu_m, \Lambda_n, t) = 0, \ t = 0.$$
 (27)

Next, taking Laplace transformation of Eq. (26) and utilizing transformed initial boundary (27), one get:

$$\widehat{\bar{T}}^*(\mu_m, \Lambda_n, s) = \frac{bkK_0(\mu_m, b)}{k_3\{(1+G)s + k(\mu_m^2 + \Lambda_n^2)\}} \overline{Q}(\Lambda_n) + \frac{k\psi_1(h)\psi_2(r_0)}{(s+p)\{(1+G)s + k(\mu_m^2 + \Lambda_n^2)\}},$$
(28)

where
$$\left[\frac{L_n(h)}{k_2} - \frac{L_n(-h)}{k_1}\right] = \psi_1(h)$$
, $r_0 f_0(\mu_m, r_0) = \psi_2(r_0)$ and $G = \frac{\tau}{\omega} \left\{ (1 - e^{-s\omega}) \left(1 - \frac{2l_2}{\omega s} + \frac{2l_1^2}{\omega^2 s^2} \right) - \left(l_1^2 - 2l_2 + \frac{2l_1^2}{\omega s} \right) e^{-s\omega} \right\}$.

Finally, inverting the integral transforms in Eq. (28) by using inversion formula defined in Eqs. (24) and (18), one obtains the expression of temperature distribution in Laplace transform domain as below:

$$T^* = \sum_{m=1}^{\infty} \sum_{n=1}^{\infty} \frac{1}{\lambda_n} K_0(\mu_m, r) L_n(z) \left[\frac{bkK_0(\mu_m, b)}{k_3 \{ (1+G)s + k (\mu_m^2 + \Lambda_n^2) \}} \overline{Q}(\Lambda_n) + \frac{k\psi_1(h)\psi_2(r_0)}{(s+p) \{ (1+G)s + k (\mu_m^2 + \Lambda_n^2) \}} \right].$$
 (29)

168 N.K. Lamba

Determination of thermal deflection

Equations (8), (9) and (11) can be rewriting in the Laplace transform domain as:

$$\nabla^4 W^* = \frac{-\nabla^2 M_T^*}{\Omega(1-\nu')},\tag{30}$$

$$M_T^* = a_t E' \int_{z=-h}^{h} T^*(r, z, s) z \ dz, \tag{31}$$

$$W^* = \frac{\partial W^*}{\partial r} = 0, \text{ at } r = b. \tag{32}$$

Equation (31), which incorporates the value of the temperature (29), yields the equation for heat based moments in the Laplace transform domain as:

$$M_{T}^{*} = a_{t} E' \frac{\sqrt{2}}{b} \sum_{m=1}^{\infty} \sum_{n=1}^{\infty} \frac{\mu_{m} k_{3}}{\left[1 + k_{3}^{2} \mu_{m}^{2}\right]^{\frac{1}{2}}} \frac{J_{0}(\mu_{m}, r)}{J_{0}(\mu_{m}, b)} \left[\frac{bk K_{0}(\mu_{m}, b)}{k_{3} \left\{(1 + G)s + k(\mu_{m}^{2} + \Lambda_{n}^{2})\right\}} \left(\int_{z=-h}^{h} Q(z) L_{n}(z) dz \right) + \frac{k \psi_{1}(h) \psi_{2}(r_{0})}{(s+p) \left\{(1 + G)s + k(\mu_{m}^{2} + \Lambda_{n}^{2})\right\}} \right] \times \int_{-h}^{h} \frac{z L_{n}(z)}{\lambda_{n}} dz.$$
(33)

Assuming that Eq. (30) has a solution that satisfies condition (32) in the domain of the Laplace transform:

$$W^*(r,s) = \sum_{m=1}^{\infty} c_n^*(s) [2bJ_0(\mu_m,r) - 2bJ_0(\mu_m,b) + \mu_m(r^2 - b^2)J_1(\mu_m,b)].$$
As a result, the condition (32) is satisfied by the solution (34):

$$\nabla^4 W^* = \left(\frac{\partial^2}{\partial r^2} + \frac{1}{r} \frac{\partial}{\partial r}\right)^2 \sum_{m=1}^{\infty} c_n^*(s) [2bJ_0(\mu_m, r) - 2bJ_0(\mu_m, b) + \mu_m(r^2 - b^2)J_1(\mu_m, b)]. \tag{35}$$

Using well-known result $\left[\frac{1}{r}\frac{\partial}{\partial r}\left(r\frac{\partial}{\partial r}\right)\right]J_0(\mu_m r)=-\mu_m^2J_0(\mu_m r)$, Eq. (35) can be rewritten as:

$$\nabla^4 W^* = \sum_{m=1}^{\infty} c_n^*(s) [2b\mu_m^4 J_0(\mu_m r) + 2\mu_m J_1(\mu_m, b)]$$
 (36)
Also,

$$\begin{split} \nabla^2 M_T^* &= -a_t E' \frac{\sqrt{2}}{b} \sum_{m=1}^{\infty} \sum_{n=1}^{\infty} \frac{k_3}{\left[1 + k_3^2 \mu_m^2\right]^{\frac{1}{2}}} \frac{\mu_m^3 J_0(\mu_m r)}{J_0(\mu_m, b)} \left[\frac{bk K_0(\mu_m, b)}{k_3 \left\{ (1 + G)s + k \left(\mu_m^2 + \Lambda_n^2 \right) \right\}} \left(\int_{z=-h}^{h} Q(z) L_n(z) dz \right) + \\ &+ \frac{k \psi_1(h) \psi_2(r_0)}{(s+p) \left\{ (1 + G)s + k \left(\mu_m^2 + \Lambda_n^2 \right) \right\}} \right] \times \int_{-h}^{h} \frac{z L_n(z)}{\lambda_n} dz \end{split} \tag{37}$$

Equations (36) and (37) combined with Eq. (30) yield

$$c_n^*(s) = a_t E' \frac{\sqrt{2}}{b\Omega(1-v')} \sum_{m=1}^{\infty} \sum_{n=1}^{\infty} \frac{k_3}{[1+k_2^2 \mu_m^2]^{\frac{1}{2}}} \frac{\mu_m^3 J_0(\mu_m r)}{J_0(\mu_m, b)[2b\mu_m^4 J_0(\mu_m r) + 2\mu_m J_1(\mu_m, b)]} \times$$

$$\times \left[\frac{bkK_0(\mu_m,b)}{k_3\{(1+G)s+k(\mu_m^2+\Lambda_n^2)\}} \left(\int_{z=-h}^h Q(z)L_n(z)dz \right) + \frac{k\psi_1(h)\psi_2(r_0)}{(s+p)\{(1+G)s+k(\mu_m^2+\Lambda_n^2)\}} \right] \int_{-h}^h \frac{zL_n(z)}{\lambda_n} dz. \tag{38}$$

Substituting Eq. (38) into Eq. (34), we get:

$$W^{*}(r,s) = a_{t}E'\frac{\sqrt{2}}{b\Omega(1-v')}\sum_{m=1}^{\infty}\sum_{n=1}^{\infty}\frac{k_{3}\mu_{m}^{3}J_{0}(\mu_{m}r)[2bJ_{0}(\mu_{m},r)-2bJ_{0}(\mu_{m},b)+\mu_{m}(r^{2}-b^{2})J_{1}(\mu_{m},b)]}{[1+k_{3}^{2}\mu_{m}^{2}]^{\frac{1}{2}}J_{0}(\mu_{m},b)[2b\mu_{m}^{4}J_{0}(\mu_{m}r)+2\mu_{m}J_{1}(\mu_{m},b)]}\times \left[\frac{bkK_{0}(\mu_{m},b)}{k_{3}\{(1+G)s+k(\mu_{m}^{2}+\Lambda_{n}^{2})\}}\left(\int_{z=-h}^{h}Q(z)L_{n}(z)dz\right)+\frac{k\psi_{1}(h)\psi_{2}(r_{0})}{(s+p)\{(1+G)s+k(\mu_{m}^{2}+\Lambda_{n}^{2})\}}\right]\int_{-h}^{h}\frac{zL_{n}(z)}{\lambda_{n}}dz.$$
(39)

In the Laplace transform domain, the mathematical formula for temperature and thermal deflection has thus been found. So, for the purpose of numerical inversion algorithm proposed by Brancik [32,33] is adopted.

Numerical results

Dimension

Let the radius of circular plate varies from r=0 to r=1 m and having thickness h=0.1 m. Fixing $Q(z)=z^2\times(z^2-h^2)^2$.

Material properties

Following material properties of copper metal plate is considered for the purpose of numerical computations.

Table 1. Thermo-mechanical properties

$k = 112.34 \times 10^{-6} m/s^2$	v' = 0.35
$a_t = 16.5 \times 10^{-6} K$	$\mu = 26.67GPa$
$\rho = 8954kg/m^3$	$c_p = 383J/(kgK)$

Graphical presentation

This part is primarily concerned with the time delay's influence on how temperatures are distributed and thermal deflection fluctuates in a circular plate. All the plots presented below are made considering dimensionless quantities. For the graphical computation, the dimensionless thickness of the plate is chosen as z=0.2 and the dimensionless time is chosen as t=0.5. Figures 2 and 3 show the graphically plotted temperature and deflection flow radially under the influence of the time delay parameter $\omega=0,0.01,0.02,0.03$ for thin copper plates.

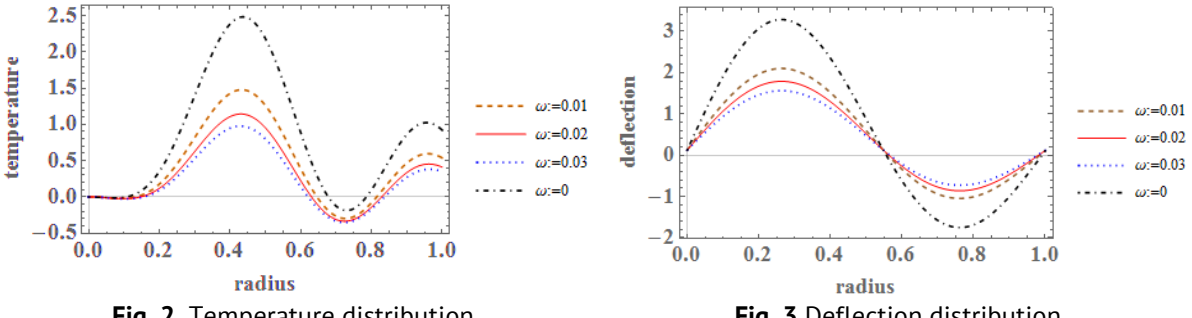


Fig. 2. Temperature distribution with impact of time delay

Fig. 3 Deflection distribution with impact of time delay

For various time delay parameters $\omega=0,0.01,0.02,0.03$, Fig. 2 shows the dimensionless temperature behaviour along radii at t=0.5. At the inner radii, the temperature is initially zero, while at the outer radii it is nonzero due to the applied heat flux. The maximum temperature distribution is found in the middle of the radial direction, which may be due to the effect of additional cross-sectional heating on the bottom and top plate surfaces. When the time delay is shortened and $K(t-\xi)=1$, the present heat transfer model reduces to the model of Cattaneo and Vernotte (CV). Further observations show that the temperature distribution changes smoothly for large values of the time delay values, implying that the temperature flow depends on the values of the time delay variation. Also, depending on the time delay parameters, the thermal waves vary

170 N.K. Lamba

continuously, uniformly, and strongly. As a result, the time delay factor can be crucial in the classification and design of new structural materials.

Figure 3 shows the deflection function along radii at t=0.5 for different $\omega=0,0.01,0.02,0.03$. It is observed that the variation in thermal deflection is zero at the internal and external radii, which fulfills the applied boundary condition mathematically defined in Eq. (11). Also, the variations in the deflection curve are observed at the transition from inner to outer radii, which may be due to the effect of the additional cross-sectional heating at the top and bottom surfaces of the plate. A smooth and continuous variation of the deflection curves is also observed for large time delay parameters. Moreover, the curve shows finite wave propagation characteristics compared to the diffusive characteristics of the Fourier model.

It follows that the temperature and deflection behaviour in a circular body is considerably affected by the time delay and depends on the past changes, which makes this study more suitable for the study of the physical problems associated with the development of novel materials.

Conclusions

The governing equation of the memory-dependent heat transmission equation for a circular plate with certain boundary conditions is solved analytically by employing the Marchi-Fasulo, Hankel, and Laplace transformations. The effect of the time delay parameters on the temperature distribution and thermal deflection (based on thermal moment) is successfully investigated.

The following important findings are highlighted from the graphical investigations: 1. The change in the past affects the instantaneous rate of temperature change and thermal deflection, which is more suitable for the study of physical problems and has applications in the real world.

- 2. The rate of finite wave propagation can be seen from the change in temperature and deflection curves.
- 3. For different time delay parameters, a significant difference in the temperature and deflection curves is observed.
- 4. For large time delays, a uniform distribution of temperature and deflection is observed. It can be concluded that temperature and deflection are considerably affected by the time delay parameter.

As a result, the time delay factor plays an important role in both the development and categorisation of new structural materials. Moreover, the present work is useful for mathematicians and researchers working on the development of fractional and memory theory by considering mathematical modelling of various solids.

References

- 1. Caputo M. Vibrations on an infinite viscoelastic layer with a dissipative memory. J. Acoust. Soc. Am. 1974;56(3): 897 904.
- 2. Caputo M, Mainardi F. A new dissipation model based on memory mechanism. Pure Appl. Geophys. 1971;91:134–147.
- 3. Povstenko YZ. Fractional heat conduction equation and associated thermal stresses. *Journal of Thermal Stresses*. 2005;28(1): 83–102.
- 4. Povstenko YZ. Non-axisymmetric solutions to time-fractional diffusion-wave equation in an infinite cylinder. *Fract. Calc. Appl. Anal.* 2011;14(3): 418–435.
- 5. Ezzat MA, EL-Karamany AS. Fractional order theory of a perfect conducting thermoelastic medium. *Can. J. Phys.* 2011;89: 311–318.
- 6. Hussein EM. Fractional order thermoelastic problem for an infinitely long solid circular cylinder. *Journal of Thermal Stresses*. 2015;38(2): 133–145.
- 7. Abouelregal AE. Fractional heat conduction equation for an infinitely generalized thermoelastic long solid cylinder. *International Journal for Computational Methods in Engineering Science and Mechanics*. 2016;17(5–6): 374–381.
- 8. Lamba NK. Thermosensitive response of a functionally graded cylinder with fractional order derivative. *International Journal of Applied Mechanics and Engineering*. 2022;27(1): 107–124.
- 9. Kumar N, Kamdi DB. Thermal behavior of a finite hollow cylinder in context of fractional thermoelasticity with convection boundary conditions. *Journal of Thermal Stresses*. 2020;43(9): 1189–1204.
- 10. Raslan W. Application of fractional order theory of thermoelasticity in a thick plate under axisymmetric temperature distribution. *Journal of Thermal Stresses*. 2015;38(7): 733–743.
- 11. Wang JL, Li HF. Surpassing the fractional derivative: Concept of the memory-dependent derivative. *Computers and Mathematics with Applications*. 2011;62: 1562–1567.
- 12. El-Karamany AS, Ezzat MA. Modified Fourier's law with time-delay and kernel function: application in thermoelasticity. *Journal of Thermal Stresses*. 2015;38(7): 811–834.
- 13. Purkait P, Sur A, Kanoria M. Thermoelastic interaction in a two-dimensional infinite space due to memory-dependent heat transfer. *Int. J. Adv. Appl. Math. and Mech.* 2017;5(1): 28–39.
- 14. Sun WW, Wang JL. Reconstruct the heat conduction model with memory dependent derivative. *Applied Mathematics*. 2018;9: 1072–1080.
- 15. Xue ZN, Chen ZT, Tian XG. Transient thermal stress analysis for a circumferentially cracked hollow cylinder based on memory-dependent heat conduction model. *Theoretical and Applied Fracture Mechanics*. 2018;96: 123–133.
- 16. Ma Y, Gao Y. Dynamic response of a hollow cylinder subjected to thermal shock considering scale effect and memory dependent effect. *Mechanics of Advanced Materials and Structures*. 2021;29(25): 4468–4477.
- 17. Sur A, Pal P, Kanoria M. Modeling of memory-dependent derivative in a fiber-reinforced plate under gravitational effect. *Journal of Thermal Stresses*. 2018;41(8): 973–992.
- 18. Ahmed S, El-Karamany AS, Ezzat MA. Thermoelastic diffusion with memory-dependent derivative. *Journal of Thermal Stresses*. 2016;39(9): 1035–1050.
- 19. Qi Z, Peng W, He T. Investigation on the thermoelastic response of a nanobeam in modified couple stress theory considering size-dependent and memory-dependent effects. *Journal of Thermal Stresses*. 2022;45(10): 773–792.
- 20. Verma J, Lamba NK, Deshmukh KC. Memory impact of hygrothermal effect in a hollow cylinder by theory of uncoupled-coupled heat and moisture. *Multidiscipline Modeling in Materials and Structures*. 2022;18(5): 826–844.
- 21. Othman MIA, Mondal S. Memory-dependent derivative effect on wave propagation of micropolar thermoelastic medium under pulsed laser heating with three theories. *International Journal of Numerical Methods for Heat & Fluid Flow.* 2020;30(3): 1025–1046.
- 22. Awwad E, Abouelregal AE, Soleiman A. Thermoelastic memory-dependent responses to an infinite medium with a cylindrical hole and temperature-dependent properties. *J. Appl. Comput. Mech.* 2021;7(2): 870–882.
- 23. Mondal S. Memory response for thermal distributions moving over a magneto-thermoelastic rod under Eringen's nonlocal theory. *Journal of Thermal Stresses*. 2020;43(1): 72–89.
- 24. Abouelregal AE, Moustapha MV, Nofal TA, Rashid S, Ahmad H. Generalized thermoelasticity based on higher-order memory-dependent derivative with time delay. *Results in Physics*. 2021;20: 103705.
- 25. Abouelregal AE, Atta D, Sedighi HM. Vibrational behavior of thermoelastic rotating nanobeams with variable thermal properties based on memory-dependent derivative of heat conduction model. *Arch. Appl. Mech.* 2023;93: 197–220.
- 26. Abouelregal AE, Askar SS, Marin M, Badahiould M. The theory of thermoelasticity with a memory-dependent dynamic response for a thermo-piezoelectric functionally graded rotating rod. *Sci. Rep.* 2023;13: 9052.

172 N.K. Lamba

27. Lamba N. Impact of memory-dependent response of a thermoelastic thick solid cylinder. *Journal of Applied and Computational Mechanics*. 2023;9(4): 1135–1143.

- 28. Yu YJ, Hu W, Tian XG. A novel generalized thermoelasticity model based on memory-dependent derivative. *Int. J. Eng. Sci.* 2014;81: 123–134.
- 29. Choudhary RSK. A note on quasi-static thermal deflection of a thin clamped circular plate due to ramptype heating on a concentric circular region of the upper face. *J. of the Franklin Institute*. 1973;206: 213–219.
- 30. Marchi E, Fasulo A. Heat conduction in sector of hollow cylinder with radiation. *Atti, della Acc. Sci. di. Torino.* 1967;1: 373–382.
- 31. Ozisik MN. Boundary Value Problem of Heat Conduction. Scranton PA: International Textbook Co.; 1968.
- 32. Brancik L. Programs for fast numerical inversion of Laplace transforms in MATLAB language environment. In: *Proceedings of the 7th conference, MATLAB*'99. Czech Republic, Prague. 1999. p.27 39.
- 33. Brancik L. Utilization of quotient-difference algorithm in FFT-based numerical ILT method. In: *Proceedings of the 11th International Czech-Slovak Scientific Conference, Radioelektronika*. Czech Republic, Brno. 2001. p.352–355.
- 34. Thakare S, Warbhe MS, Lamba N. Time fractional heat transfer analysis in nonhomogeneous thick hollow cylinder with internal heat generation and its thermal stresses. *International Journal of Thermodynamics*. 2020;23(4): 281–302.
- 35. Kumar R, Manthena VR, Lamba NK, Kedar GD. Generalized thermoelastic axi-symmetric deformation problem in a thick circular plate with dual phase lags and two temperatures. *Materials Physics and Mechanics*. 2017;32(2): 123–132.
- 36. Kulkarni V, Deshmukh KC, Bhave A. An inverse mathematical approach for thermal stresses in a solid sphere. *International Journal of Thermodynamics*. 2015;18(3): 206–211.
- 37. Lamba NK, Deshmukh KC. Memory dependent response in an infinitely long thermoelastic solid circular cylinder. *PNRPU Mechanics Bulletin*. 2024;1: 5–12.

About Author

Navneet Kumar Lamba D Sc

PhD, Assistant Professor (Shri Lemdeo Patil Mahavidyalaya, Mandhal, Nagpur, India)

МЕХАНИКА И ФИЗИКА МАТЕРИАЛОВ

52 (4) 2024

Учредители: Санкт-Петербургский политехнический университет Петра Великого,

Институт проблем Машиноведения Российской академии наук

Издание зарегистрировано федеральной службой по надзору в сфере связи,
информационных технологий и массовых коммуникаций (РОСКОМНАДЗОР),

свидетельство ПИ №ФС77-69287 от 06.04.2017 г.

Редакция журнала

Профессор, д.т.н., академик РАН, А.И. Рудской – главный редактор
Профессор, д.ф.-м.н., член-корр. РАН, А.К. Беляев – главный научный редактор
Профессор, д.ф.-м.н. И.А. Овидько (1961 - 2017) – основатель и почетный редактор
Профессор, д.ф.-м.н. А.Л. Колесникова – ответственный редактор
Профессор, д.ф.-м.н. А.С. Семенов – ответственный редактор
Л.И. Гузилова – выпускающий редактор, корректор

Телефон редакции +7(812)552 77 78, доб. 224

E-mail: mpmjournal@spbstu.ru

Компьютерная верстка Л.И. Гузилова

Подписано в печать 30.09.2024 г. Формат 60х84/8. Печать цифровая Усл. печ. л. <u>10,0</u>. Тираж 100. Заказ____.

Отпечатано с готового оригинал-макета, предоставленного автором в Издательско-полиграфическом центре Политехнического университета Петра Великого. 195251, Санкт-Петербург, Политехническая ул., 29.

Тел.: +7(812)552 77 78, доб. 224.

Accelerated degradation by mechanical load of HIT solar cells encapsulated in flexible plastic	1-8
A.V. Bobyl, R.V. Davydov, O.I. Konkov, A.V. Kochergin, D.A. Malevsky, S.E. Nikitin	
MEMS gas sensor of resistive type for detection of hydrogen sulfide down to low concentrations I.M. Komarevtsev, A.S. Kondrateva, A.N. Kazakin, Ya.B. Enns, I.A. Lazdin, P.A. Karaseov, U.D. Akulsk	9-22 nin
First-principles investigations of physical properties of Nd doped FeSi compound A. Kumar, R. Kumar, R. Kumar, A. Kumar, V.K. Nautiyal, N. Iram	23-32
The influence of low frequency electric field on the coalescence of water drops in emulsion shear flow R.R. Galeev, A.I. Mullayanov, A.A. Musin, L.A. Kovaleva	33-40
Surface modification by laser cladding: state-of-the-art and future prospects R. Ranjan, A.K. Das	41-51
Ultrasonic layer-by-layer treatment of PN85Y15 coating as a way to increase wear resistance of friction pair with bronze I.S. Syundyukov, M.A. Skotnikova, A.Yu. Ryabikin	52-62
Thermal analysis of wear of polymer-polymer friction pairs in vacuum and atmosphere conditions A.O. Pozdnyakov, E.B. Sedakova	63-80
Structure and strength of Mg-Zn-Zr alloy subjected to high pressure torsion D.A. Aksenov, M.A. Shishkunova, R.N. Asfandiyarov, Y.R. Sementeeva	81-90
The effect of martensite stabilization in titanium nickelide after various methods of pre-deformation: simulation with a single set of constants A.E. Volkov, F.S. Belyaev, N.A. Volkova, E.A. Vukolov, M.E. Evard, T.V. Rebrov	91-99
Interface shear damage of novel biocomposite materials based on polyhydroxyalkanoates biopolymer matrix A. Mokaddem, M. Belkheir, M. Rouissat, B. Doumi, A. Boutaous	100-113
Hybrid of a nonlinear Maxwell-type viscoelastoplastic model with the linear viscoelasticity constitutive constitutive equation and properties of crossbred creep and stress-strain curves A.V. Khokhlov	114-140
Synthesis of WO2.72:Fe thin films via ammonium tungstate precursor by spray pyrolysis technique and annealing E. Ouadah, N. Hamdadou	141-151
Fiberglass thermal barrier for building safety S.V. Fedosov, A.A. Lazarev, A.N. Maltsev, M.V. Toropova, I.A. Bogdanov	152-162
Quasi-static thermal response of a circular plate due to the influence of memory-dependent derivatives N.K. Lamba	163-172
Comprehensive studies of pipes metal to identify the causes of failure in the gas pipeline of the gas lift system of an oil and gas condensate field	173-182



A.M. Kunakova, V.A. Svintsov, V.A. Olenev, D.A. Gogolev, L.R. Sayfutdinova, M.S. Solodovnikova